



Defense Threat Reduction Agency  
8725 John J. Kingman Road, MS  
6201 Fort Belvoir, VA 22060-6201



DTRA-TR-15-80

# TECHNICAL REPORT

---

## Irreversible Phase-Changes in Nanophase RE-doped M<sub>2</sub>O<sub>3</sub> and their Optical Signatures

Distribution Statement A. Approved for public release; distribution is unlimited.

December 2015

HDTRA1-10-1-0005

Hergen Eilers

Prepared by:  
Washington State University  
1125 NE Washington St.  
Pullman, WA 99164

**DESTRUCTION NOTICE:**

Destroy this report when it is no longer needed.  
Do not return to sender.

PLEASE NOTIFY THE DEFENSE THREAT REDUCTION  
AGENCY, ATTN: DTRIAC/ J9STT, 8725 JOHN J. KINGMAN ROAD,  
MS-6201, FT BELVOIR, VA 22060-6201, IF YOUR ADDRESS  
IS INCORRECT, IF YOU WISH IT DELETED FROM THE  
DISTRIBUTION LIST, OR IF THE ADDRESSEE IS NO  
LONGER EMPLOYED BY YOUR ORGANIZATION.

# REPORT DOCUMENTATION PAGE

*Form Approved  
OMB No. 0704-0188*

Public reporting burden for this collection of information is estimated to average 1 hour per response, including the time for reviewing instructions, searching existing data sources, gathering and maintaining the data needed, and completing and reviewing this collection of information. Send comments regarding this burden estimate or any other aspect of this collection of information, including suggestions for reducing this burden to Department of Defense, Washington Headquarters Services, Directorate for Information Operations and Reports (0704-0188), 1215 Jefferson Davis Highway, Suite 1204, Arlington, VA 22202-4302. Respondents should be aware that notwithstanding any other provision of law, no person shall be subject to any penalty for failing to comply with a collection of information if it does not display a currently valid OMB control number. **PLEASE DO NOT RETURN YOUR FORM TO THE ABOVE ADDRESS.**

<b>1. REPORT DATE (DD-MM-YYYY)</b>			<b>2. REPORT TYPE</b>			<b>3. DATES COVERED (From - To)</b>	
<b>4. TITLE AND SUBTITLE</b>			<b>5a. CONTRACT NUMBER</b>				
			<b>5b. GRANT NUMBER</b>				
			<b>5c. PROGRAM ELEMENT NUMBER</b>				
<b>6. AUTHOR(S)</b>			<b>5d. PROJECT NUMBER</b>				
			<b>5e. TASK NUMBER</b>				
			<b>5f. WORK UNIT NUMBER</b>				
<b>7. PERFORMING ORGANIZATION NAME(S) AND ADDRESS(ES)</b>			<b>8. PERFORMING ORGANIZATION REPORT NUMBER</b>				
<b>9. SPONSORING / MONITORING AGENCY NAME(S) AND ADDRESS(ES)</b>			<b>10. SPONSOR/MONITOR'S ACRONYM(S)</b>				
			<b>11. SPONSOR/MONITOR'S REPORT NUMBER(S)</b>				
<b>12. DISTRIBUTION / AVAILABILITY STATEMENT</b>							
<b>13. SUPPLEMENTARY NOTES</b>							
<b>14. ABSTRACT</b>							
<b>15. SUBJECT TERMS</b>							
<b>16. SECURITY CLASSIFICATION OF:</b>			<b>17. LIMITATION OF ABSTRACT</b>	<b>18. NUMBER OF PAGES</b>	<b>19a. NAME OF RESPONSIBLE PERSON</b>		
<b>a. REPORT</b>	<b>b. ABSTRACT</b>	<b>c. THIS PAGE</b>			<b>19b. TELEPHONE NUMBER (include area code)</b>		

**UNIT CONVERSION TABLE**  
**U.S. customary units to and from international units of measurement\***

U.S. Customary Units	Multiply by ← Divide by <sup>†</sup>	International Units
<b>Length/Area/Volume</b>		
inch (in)	2.54 $\times 10^{-2}$	meter (m)
foot (ft)	3.048 $\times 10^{-1}$	meter (m)
yard (yd)	9.144 $\times 10^{-1}$	meter (m)
mile (mi, international)	1.609 344 $\times 10^3$	meter (m)
mile (nmi, nautical, U.S.)	1.852 $\times 10^3$	meter (m)
barn (b)	1 $\times 10^{-28}$	square meter ( $m^2$ )
gallon (gal, U.S. liquid)	3.785 412 $\times 10^{-3}$	cubic meter ( $m^3$ )
cubic foot ( $ft^3$ )	2.831 685 $\times 10^{-2}$	cubic meter ( $m^3$ )
<b>Mass/Density</b>		
pound (lb)	4.535 924 $\times 10^{-1}$	kilogram (kg)
unified atomic mass unit (amu)	1.660 539 $\times 10^{-27}$	kilogram (kg)
pound-mass per cubic foot ( $lb\ ft^{-3}$ )	1.601 846 $\times 10^1$	kilogram per cubic meter ( $kg\ m^{-3}$ )
pound-force (lbf avoirdupois)	4.448 222	newton (N)
<b>Energy/Work/Power</b>		
electron volt (eV)	1.602 177 $\times 10^{-19}$	joule (J)
erg	1 $\times 10^{-7}$	joule (J)
kiloton (kt) (TNT equivalent)	4.184 $\times 10^{12}$	joule (J)
British thermal unit (Btu) (thermochemical)	1.054 350 $\times 10^3$	joule (J)
foot-pound-force (ft lbf)	1.355 818	joule (J)
calorie (cal) (thermochemical)	4.184	joule (J)
<b>Pressure</b>		
atmosphere (atm)	1.013 250 $\times 10^5$	pascal (Pa)
pound force per square inch (psi)	6.984 757 $\times 10^3$	pascal (Pa)
<b>Temperature</b>		
degree Fahrenheit ( $^{\circ}\text{F}$ )	$[\text{T}({}^{\circ}\text{F}) - 32]/1.8$	degree Celsius ( ${}^{\circ}\text{C}$ )
degree Fahrenheit ( $^{\circ}\text{F}$ )	$[\text{T}({}^{\circ}\text{F}) + 459.67]/1.8$	kelvin (K)
<b>Radiation</b>		
curie (Ci) [activity of radionuclides]	3.7 $\times 10^{10}$	per second ( $s^{-1}$ ) [becquerel (Bq)]
roentgen (R) [air exposure]	2.579 760 $\times 10^{-4}$	coulomb per kilogram ( $C\ kg^{-1}$ )
rad [absorbed dose]	1 $\times 10^{-2}$	joule per kilogram ( $J\ kg^{-1}$ ) [gray (Gy)]
rem [equivalent and effective dose]	1 $\times 10^{-2}$	joule per kilogram ( $J\ kg^{-1}$ ) [sievert (Sv)]

\* Specific details regarding the implementation of SI units may be viewed at <http://www.bipm.org/en/si/>.

<sup>†</sup>Multiply the U.S. customary unit by the factor to get the international unit. Divide the international unit by the factor to get the U.S. customary unit.

## **ABSTRACT**

Luminescent rare-earth doped metal oxides are evaluated as potential temperature sensors that are seeded into explosive fireballs and collected post-detonation for analysis. The sensors consist of amorphous precursors which, once subjected to thermal exposure, undergo irreversible phase transitions such as decomposition, nucleation, grain growth, and phase transformations. The extent and degree of these phase transitions depends on temperature and heating duration. The phase transitions are monitored via spectral changes in the fluorescence of the luminescent rare-earth dopants. The spectral emission of these dopants is very sensitive to the configuration of the oxygen ions surrounding the dopant. As this configuration changes, the spectral emission properties change and this change can be correlated with the temperature the materials were exposed to. The correlation is based upon laboratory-based reference measurements. The functionality of these temperature sensors was demonstrated during several explosion tests. By using two different sensor materials combined with a kinetic analysis, it is possible to simultaneously extract information about temperature and heating duration. Initial results using this approach were demonstrated. Furthermore, luminescent tracking particles were developed to determine the origin of the temperature sensors during an explosion. These tracking particles consist of fully crystallized rare-earth doped metal oxides. Using different dopants with different spectral signatures, provides a means to tag the temperature sensors placed within different locations of the explosive fireball and to track their origin.

## TABLE OF CONTENTS

LIST OF FIGURES .....	v
LIST OF TABLES.....	xiii
ACKNOWLEDGEMENTS .....	xiv
I. SUMMARY .....	1
II. INTRODUCTION .....	3
III. METHODS, ASSUMPTIONS, AND PROCEDURES .....	5
A. Synthesis .....	5
B. Lab-based heating and temperature measurements.....	6
C. Explosion tests .....	13
D. Characterization.....	13
IV. RESULTS AND DISCUSSIONS .....	15
A. Phase Change Modeling.....	15
C. Temperature Sensors .....	27
Eu:Y <sub>2</sub> O <sub>3</sub> .....	27
Eu:ZrO <sub>2</sub> .....	51
D. Temperature/time (Thermal impulse) Sensors .....	61
Initial evaluation of various compounds .....	61
p-Eu:ZrO <sub>2</sub> + c-Ho:ZrO <sub>2</sub> + p-Dy:Y <sub>2</sub> O <sub>3</sub> .....	69
E. Tracking Sensors .....	77
V. CONCLUSIONS.....	79
VI. RECOMMENDATIONS .....	81
VII. PUBLICATIONS AND PRESENTATIONS .....	82
VIII. REFERENCES .....	84
IX. APPENDIX .....	90
A. Alternative Temperature Sensors .....	90
B. Eu:TiO <sub>2</sub> – based materials .....	100
C. Magnetic Core Sensors.....	100

## LIST OF FIGURES

<b>Figure 1.</b>	CDS Analytical pyroprobe heater, heating strip, and heating coil. ....	6
<b>Figure 2.</b>	Actual pyroprobe temperature profiles.....	6
<b>Figure 3.</b>	Actual indirect (left) and direct (right) laser heating temperature profiles. ....	7
<b>Figure 4.</b>	3-color pyrometer.....	7
<b>Figure 5.</b>	Detector voltages as a function of temperature.....	11
<b>Figure 6.</b>	Measured voltage ratios as a function of pyroprobe temperature and fits to Equation 15.....	11
<b>Figure 7.</b>	Difference in calculated and set temperatures as a function of set temperature. As the temperature increases the difference between the set and calculated temperatures drastically decreases and all differences are within uncertainty of zero. ....	12
<b>Figure 8.</b>	Schematic of the fluorescence/ fluorescence-excitation setup.....	13
<b>Figure 9.</b>	Temperature profile as a function of time plotted with the degree of conversion using the full model of Equation 22 and the isothermal model, which ignores heating and cooling.....	16
<b>Figure 10.</b>	Degree of conversion predicted by Equation 23 as a function of time for different heating rates, as well as the isothermal value. Note that as the heating rate decreases the full model diverges more from the isothermal model. ....	16
<b>Figure 11.</b>	Degree of conversion and fractional error as a function of heating rate.....	17
<b>Figure 12.</b>	Fractional error as a function of heating rate for different (left) isothermal times and (right) isothermal temperature.....	18
<b>Figure 13.</b>	Degree of conversion and fractional error as a function of isothermal time for a heating rate of 200 °K/s and an isothermal time of 100 ms.....	18
<b>Figure 14.</b>	Fractional error as a function of isothermal temperature for different isothermal times, $\Delta t$ , and two different heating rates. As the isothermal time decreases the fractional error increases. ....	19
<b>Figure 15.</b>	Temperature and degree of conversion during simulated explosion profile.....	20
<b>Figure 16.</b>	Temperature and degrees of conversion as a function of time for a temperature profile given by Equation 28.....	21
<b>Figure 17.</b>	Two-dimensional mapping of the degree of conversion as a function of temperature and time.....	22
<b>Figure 18.</b>	Degree of conversion as a function of (a) temperature and (b) time. ..	23

<b>Figure 19.</b>	Two-dimensional mappings of the fraction of material in the (a) tetragonal phase and (b) monoclinic phase.....	24
<b>Figure 20.</b>	Normalized spectra of different phases of Eu:ZrO <sub>2</sub> using an excitation wavelength of 355 nm.....	25
<b>Figure 21.</b>	Two-dimensional mapping of the intensity ratio between 592 nm and 613 nm as a function of temperature and time. The red area corresponds to being rich in the tetragonal phase, while the blue area is rich in the monoclinic phase.....	25
<b>Figure 22.</b>	I <sub>592</sub> /I <sub>613</sub> ratio as a function of (a) temperature and (b) time. As the amorphous material changes into the tetragonal phase the ratio increases. Once the material begins to convert into the monoclinic phase the ratio begins to decrease.....	26
<b>Figure 23.</b>	Intensity ratios as a function of isothermal temperature and time.....	26
<b>Figure 24.</b>	(a) TEM image (scale bar is 100 nm), (b) XRD spectrum, and (c) FT-IR spectrum of coprecipitated yttrium carbonate. ....	27
<b>Figure 25.</b>	DSC and TGA curves of the co-precipitated carbonates.....	28
<b>Figure 26.</b>	FT-IR spectra of co-precipitated yttria precursors heat-treated at 300°C, 500°C, 700°C, 900°C, and 1100°C for dwell times of 5 minutes, 30 minutes, and 180 minutes.....	29
<b>Figure 27.</b>	XRD patterns of co-precipitated yttria precursors heat-treated at 300°C, 500°C, 700°C, 900°C, and 1100°C for dwell times of 5 minutes, 30 minutes, and 180 minutes.....	30
<b>Figure 28.</b>	TEM images of co-precipitated carbonates, heat-treated at various temperatures and dwell times. Scale bar is 100 nm. ....	31
<b>Figure 29.</b>	(a) Grain size vs. dwell times for yttrium carbonates, heat-treated at various temperatures and dwell times. (b) Plot of Ln(K) versus 1/T (K-1).....	32
<b>Figure 30.</b>	Excitation spectra of Eu-doped samples calcined at various temperatures for 5 minutes (top), 30 minutes (middle), and 180 minutes (bottom), observed at 611 nm.....	33
<b>Figure 31.</b>	Fluorescence spectra of Eu-doped samples calcined at various temperatures for 5 minutes, 30 minutes, and 180 minutes, and excited within excitation-peaks observed in Figure 30.....	34
<b>Figure 32.</b>	Fluorescence lifetime of Eu-doped samples, heat treated at various temperatures and dwell times.....	35
<b>Figure 33.</b>	Reference measurements of the pyroprobe heater.....	36
<b>Figure 34.</b>	TEM image of co-precipitated precursor. Scale bar = 50 nm.....	37
<b>Figure 35.</b>	DSC and TGA curves of the co-precipitated carbonates.....	37

<b>Figure 36.</b>	FT-IR spectra of (a) precursor and (b)-(f) precursor heated to various temperatures for 1 s, 50 s, and 100 s.....	38
<b>Figure 37.</b>	XRD of (a) precursor and (b)-(f) precursor heated to various temperatures for 1 s, 50 s, and 100 s.....	38
<b>Figure 38.</b>	TEM images of the co-precipitated carbonates heat treated at various temperatures and dwell times. Scale bar is 50 nm.....	39
<b>Figure 39.</b>	Excitation spectra (left) and fluorescence spectra (right) of amorphous and fully crystalline samples (left). Only minimal overlap occurs for the excitation spectra, while significant overlap occurs for the fluorescence spectra of these two samples.....	40
<b>Figure 40.</b>	Excitation spectra (left), monitored at 611 nm, of yttrium carbonate precursor heated for 1 s to various temperatures. Peak wavelength and peak width as a function of heating temperature, (right) based on Gaussian fit.....	40
<b>Figure 41.</b>	Excitation spectra (left), monitored at 620 nm, of yttrium carbonate precursor heated for 1 s to various temperatures. Peak wavelength and peak width as a function of heating temperature, (right) based on Gaussian fit .....	41
<b>Figure 42.</b>	Excitation spectra of yttrium carbonate precursor heated via pyroprobe for dwell times of 25 s, 50 s, 75 s, and 100 s to various temperatures. 42	
<b>Figure 43.</b>	Shift in peak position (left scale) and peak width (right scale) of excitation spectra monitored at 620 nm of yttrium carbonate precursors heated to various temperatures for dwell times of 25 s, 50 s, 75 s, and 100 s.....	43
<b>Figure 44.</b>	Fluorescence spectra, excited at 579 nm (left) and at 580.8 nm (right), of yttrium carbonate pre-cursors heated to various temperatures for 1 s. ....	43
<b>Figure 45.</b>	Fluorescence spectra, excited at 579 nm (left) and at 580.8 nm (right), of yttrium carbonate pre-cursors heated to various temperatures for 100 S.....	44
<b>Figure 46.</b>	Fluorescence spectrum of yttrium carbonate pre-cursors heated for 1 s to 440°C and its deconvoluted spectral fit.....	44
<b>Figure 47.</b>	Fluorescence lifetimes, excited at 532 nm and observed at 611 nm (left) and 620 nm (right), of yttrium carbonate precursors. ....	45
<b>Figure 48.</b>	Setup for explosion testing (left) and temperature measured via thermocouple (right). ....	45
<b>Figure 49.</b>	The as-prepared sample is amorphous and displays broad spectral features, while the heated sample is crystalline and displays narrow spectral features.....	46

<b>Figure 50.</b>	Comparing excitation spectra of Eu:Y <sub>2</sub> O <sub>3</sub> subjected to explosive heating with those of Eu:Y <sub>2</sub> O <sub>3</sub> heated via a pyroprobe (left) and temperature dependence of peak wavelength and peak width.....	46
<b>Figure 51.</b>	Explosion test setup (left) and temperatures measured via thermocouple (right).....	47
<b>Figure 52.</b>	Thermocouple response during the explosions. ....	47
<b>Figure 53.</b>	Photos of post-detonation sensor materials for six explosion test.....	48
<b>Figure 54.</b>	Closed chamber configuration with locations of three thermocouples (left) and photos of debris collected after the explosion (right). ....	50
<b>Figure 55.</b>	Temperature-dependent FWHM of amorphous peak (left) and temperature-dependent crystalline peaks (right).....	50
<b>Figure 56.</b>	(a) TEM image, (b) XRD spectrum, and (c) FTIR spectrum of as-prepared Zr(OH) <sub>4</sub> .....	52
<b>Figure 57.</b>	(a, b) XRD and FTIR spectra of Zr(OH) <sub>4</sub> heat-treated for 3 hours at temperatures between 300 °C and 900 °C. The gray and black histograms mark the positions of monoclinic (PDF No. 072-0597) and tetragonal peaks (PDF No. 088-1007), respectively.....	52
<b>Figure 58.</b>	Fluorescence spectra of Eu:ZrO <sub>2</sub> precursor, furnace-heated for 3 hours to various temperatures. ....	53
<b>Figure 59.</b>	(a, b) XRD and FTIR spectra of Zr(OH) <sub>4</sub> heat-treated at various temperatures, 300-900 °C for 10 s. The gray and black histograms mark the positions of monoclinic (PDF No. 072-0597) and tetragonal peaks (PDF No. 088-1007), respectively.....	54
<b>Figure 60.</b>	TEM micrographs of Zr(OH) <sub>4</sub> calcined at various temperatures for 10 seconds: (a) 420 °C (b) 495 °C (c) 570 °C, (d) 710 °C, and (e) 835 °C. Scale bar is 20 nm.....	55
<b>Figure 61.</b>	Fluorescence spectra of Eu:ZrO <sub>2</sub> precursor, pyroprobe-heated for 10 s to various temperatures.....	56
<b>Figure 62.</b>	Fluorescence spectra of Eu <sub>0.01</sub> Zr <sub>0.99</sub> (OH) <sub>4</sub> heated for three hours to 673 K and 1123 K, respectively (left), and heated for 10 s to 693 K and 1108 K, respectively (right).....	56
<b>Figure 63.</b>	Tetragonal/monoclinic intensity ratios for 3 h furnace heating (left) and 10 s pyroprobe heating (right).....	57
<b>Figure 64.</b>	Excitation spectra of Eu <sub>0.01</sub> Zr <sub>0.99</sub> (OH) <sub>4</sub> heated for 10 s to various temperatures and monitored at 606 nm - tetragonal phase -(left) and 614 nm - monoclinic phase (right) .....	58
<b>Figure 65.</b>	Excitation spectra of Eu <sub>0.01</sub> Zr <sub>0.99</sub> (OH) <sub>4</sub> heated for 1 s to various temperatures and monitored at 606 nm - tetragonal phase – (left) and monitored at 614 nm - monoclinic phase -(right). .....	58

<b>Figure 66.</b>	Fluorescence lifetime of Eu <sub>0.01</sub> Zr <sub>0.99</sub> (OH) <sub>4</sub> heated for 10 s, excited at 536 nm, and monitored at 606 nm (left) and 614 nm (right), respectively.....	60
<b>Figure 67.</b>	Fluorescence spectra of Eu <sub>0.01</sub> Zr <sub>0.99</sub> (OH) <sub>4</sub> heated for 10 s and 1 s to various temperatures (left) and peak ratio (right).....	60
<b>Figure 68.</b>	Temperature dependence up upconverted red and green emission intensities for furnace heating (left) and pyroprobe heating (right)....	61
<b>Figure 69.</b>	Temperature dependent fluorescence spectra (left), corresponding peak intensity ratios (center), and corresponding integrated intensities (right).....	62
<b>Figure 70.</b>	Schematic of c-Tb:ZrO <sub>2</sub> /p-Eu:Y <sub>2</sub> O <sub>3</sub> core/shell design.....	62
<b>Figure 71.</b>	Fluorescence spectra of Tb:ZrO <sub>2</sub> /p-Eu:Y <sub>2</sub> O <sub>3</sub> core/shell nanoparticles heated to various temperatures for 10 s.....	63
<b>Figure 72.</b>	Integrated Eu <sup>3+</sup> $^5D_0 \rightarrow ^7F_2$ fluorescence intensity as a function of temperature.....	63
<b>Figure 73.</b>	Typical temperature profiles of the laser-based heating method employed in this work.....	64
<b>Figure 74.</b>	Relative fluorescence intensity, I <sub>611</sub> /I <sub>543</sub> , versus time for c-Tb:ZrO <sub>2</sub> /p-Eu:Y <sub>2</sub> O <sub>3</sub> core/shell nanoparticles heated to 700 °C, 800 °C, and 900 °C for 2 s – 60 s. ....	64
<b>Figure 75.</b>	Time-dependent asymmetry ratio for various heating temperatures. Higher ratios indicate a larger degree of asymmetry. <sup>45</sup> .....	65
<b>Figure 76.</b>	Plots of normalized fluorescence intensity, I <sub>611</sub> /I <sub>543</sub> , versus time for Tb:ZrO <sub>2</sub> /p-Eu:Y <sub>2</sub> O <sub>3</sub> core/shell nanoparticles that were heated to 700 °C, 800 °C, and 900 °C for 2 s - 60 s fitted with the kinetic model. ....	65
<b>Figure 77.</b>	XRD spectra (left), and fluorescence spectra of p-Eu:ZrO <sub>2</sub> /p-Tb:Y <sub>2</sub> O <sub>3</sub> core/shell nanoparticles excited with 488 nm (center) and 533.6 nm (right), respectively.....	67
<b>Figure 78.</b>	Fluorescence excited with 488 nm (left) and XRD (right) of p-Eu:ZrO <sub>2</sub> /p-Tb:Y <sub>2</sub> O <sub>3</sub> core/shell nanoparticles heated to 600 °C for 10 s compared with those of a fully crystalline Tb:ZrO <sub>2</sub> sample.....	67
<b>Figure 79.</b>	Fluorescence spectra (left) and XRD spectrum (right) of p-Eu:ZrO <sub>2</sub> /p-Tb:Y <sub>2</sub> O <sub>3</sub> core/shell nanoparticles heated to 800 °C for 10 s and reference samples. The spectra can be assigned to the Eu:t-ZrO <sub>2</sub> and Eu:Y <sub>2</sub> O <sub>3</sub> phases. ....	68
<b>Figure 80.</b>	Distinct phases in (T,t) space and resulting phase diagram for 488 nm excitation.....	68
<b>Figure 81.</b>	Distinct phases in (T,t) space and resulting phase diagram for 533.6 nm excitation.....	69
<b>Figure 82.</b>	Individual spectra of unheated c-Ho:ZrO <sub>2</sub> and p-Dy:Y <sub>2</sub> O <sub>3</sub> .....	70

<b>Figure 83.</b>	Spectra of unheated mixtures of c-Ho:ZrO <sub>2</sub> and p-Dy:Y <sub>2</sub> O <sub>3</sub> . The Ho emission is much weaker than the Dy emission. ....	70
<b>Figure 84.</b>	Spectra of heated c-Ho:ZrO <sub>2</sub> +p-Dy:Y <sub>2</sub> O <sub>3</sub> . The Dy peak dominates the emission for all ratios tested. ....	70
<b>Figure 85.</b>	Individual spectra of unheated Eu:ZrO <sub>2</sub> and c-Ho:ZrO <sub>2</sub> /p-Dy:Y <sub>2</sub> O <sub>3</sub> . ...	70
<b>Figure 86.</b>	Spectra of different mixtures of unheated Eu:ZrO <sub>2</sub> and c-Ho:ZrO <sub>2</sub> /p-Dy:Y <sub>2</sub> O <sub>3</sub> . ....	70
<b>Figure 87.</b>	Spectra of heated mixture of Eu:ZrO <sub>2</sub> and c-Ho:ZrO <sub>2</sub> /p-Dy:Y <sub>2</sub> O <sub>3</sub> . The Dy emission dominates the heated spectrum.....	70
<b>Figure 88.</b>	Spectra of heated mixtures of Eu:ZrO <sub>2</sub> +c-Ho:ZrO <sub>2</sub> /p-Dy:Y <sub>2</sub> O <sub>3</sub> for excitation at 355 nm (top left), 365 nm (top right), 488 nm (bottom left), and 532 nm (bottom right).....	71
<b>Figure 89.</b>	Spectra of an equal ratio of Eu:ZrO <sub>2</sub> +c-Ho:ZrO <sub>2</sub> +p-Dy:Y <sub>2</sub> O <sub>3</sub> for different excitation wavelengths. For excitation using 532 nm the Dy peak is unobserved and a residual pump peak is observed even with the notch filter.....	71
<b>Figure 90.</b>	Fluorescence spectra of p-Eu:ZrO <sub>2</sub> + c-Ho:ZrO <sub>2</sub> + p-Dy:Y <sub>2</sub> O <sub>3</sub> heated to 400 °C (top left), 500 °C (top center), 600 °C (top right), 700 °C (bottom left), 800 °C (bottom center), and 900 °C (bottom right) for various times.....	72
<b>Figure 91.</b>	Ratio of fluorescence intensities at 573 nm and 578 nm as a function of time. ....	73
<b>Figure 92.</b>	592/613 Ratio as a function of time for different temperatures.....	73
<b>Figure 93.</b>	Ratio versus time fit parameters as a function of temperature for the 573/541 ratio.....	74
<b>Figure 94.</b>	Ratio versus time fit parameters plotted as a function of temperature for the 592/613 ratio. All three parameters are found to follow a modified Arrhenius fit function. ....	75
<b>Figure 95.</b>	Ratio maps as a function of time and temperature for two 573/541 (left) and 592/613 (right) intensity ratios.....	75
<b>Figure 96.</b>	Fluorescence spectra of potential tracking particles for excitation with 365 nm (left) and 488 nm (right).....	77
<b>Figure 97.</b>	Layout for explosion test of tracking particles.....	77
<b>Figure 98.</b>	Layout for explosion test of tracking particles combined with p-Eu:Y <sub>2</sub> O <sub>3</sub> /c-Tb:Y <sub>2</sub> O <sub>3</sub> temperature sensors. We were unable to measure a response from this sensor material.....	78
<b>Figure 99.</b>	Layout for explosion test of tracking particles combined with p-Eu:ZrO <sub>2</sub> temperature sensors. The measured temperature ranges (°C) are indicated in the layout.....	78

<b>Figure 100.</b>	SEM micrographs of p-Eu:La <sub>2</sub> O <sub>3</sub> synthesized with (a, d) 1/1, (b, e) 1/40, and (c, f) 1/200 salt/urea ratios. In all cases the salt concentration is 20 mM.....	90
<b>Figure 101.</b>	SEM micrographs of p-Eu:La <sub>2</sub> O <sub>3</sub> synthesized with (a) 1/0.05, (b) 1/0.10, (c) 1/0.25, and (d) 1/0.50 salt/citric acid ratio. In all cases the salt/urea ratio is 1/40. The salt concentration is 20 mM.....	91
<b>Figure 102.</b>	SEM micrographs of p-Eu:La <sub>2</sub> O <sub>3</sub> synthesized using various salt concentrations: (a) 5 mM (b) its corresponding size distributions, (c) 20 mM, and (d) 80 mM. The salt/citric acid/urea ratio is fixed at 1/0.25/40. ....	92
<b>Figure 103.</b>	DSC/TGA graph of (a) p-Eu:La <sub>2</sub> O <sub>3</sub> and (b) p-Tb:Y <sub>2</sub> O <sub>3</sub> nanoparticles..	93
<b>Figure 104.</b>	(a, c) XRD and (b, d) fluorescence of (a, b) p-Eu:La <sub>2</sub> O <sub>3</sub> and (c, d) p-Tb:Y <sub>2</sub> O <sub>3</sub> heated to: (Uncalcined, 300, 500, 600, 700, 900) °C/3 h. Markers in (a) and (c) correspond to: m-La <sub>2</sub> O <sub>2</sub> CO <sub>3</sub> (black), h-La(OH) <sub>3</sub> (magenta), h-La <sub>2</sub> O <sub>3</sub> (blue), and c-Y <sub>2</sub> O <sub>3</sub> phase (gray).....	94
<b>Figure 105.</b>	SEM micrographs of the polycrystalline Eu:La <sub>2</sub> O <sub>3</sub> (a, b, c) and polycrystalline Tb:Y <sub>2</sub> O <sub>3</sub> (d, e, f) nanoparticles heat treated at (a, d) 600 °C/3 h, (b, e) 700 °C/3 h, and (c, f) 900 °C/3 h.....	96
<b>Figure 106.</b>	SEM micrographs of p-Eu:La <sub>2</sub> O <sub>3</sub> synthesized (a) in the presence and (b) in the absence of citric acid. Respectively, the salt/citric acid/urea ratio are 1/0.25/40 and 1/0/40. ....	97
<b>Figure 107.</b>	SEM and TEM micrographs of (a, b) p-Eu:La <sub>2</sub> O <sub>3</sub> /p- Tb:Y <sub>2</sub> O <sub>3</sub> and (c, d) p-Tb:Y <sub>2</sub> O <sub>3</sub> /p-Eu:La <sub>2</sub> O <sub>3</sub> core/shell nanoparticles, and (e, f) corresponding EDS spectra.....	97
<b>Figure 108.</b>	(a, c) XRD and (b, d) fluorescence of p-Eu:La <sub>2</sub> O <sub>3</sub> /p-Tb:Y <sub>2</sub> O <sub>3</sub> (a, b) and p-Tb:Y <sub>2</sub> O <sub>3</sub> /p-Eu:La <sub>2</sub> O <sub>3</sub> (c, d) heated to: (uncalcined, 300, 500, 600, 700, and 900) °C/3 h. Markers in (a) and (c) correspond to p-La <sub>2</sub> O <sub>3</sub> (gray) and the p-Y <sub>2</sub> O <sub>3</sub> phase (black).....	98
<b>Figure 109.</b>	TEM micrographs of the polycrystalline Eu:La <sub>2</sub> O <sub>3</sub> /Tb:Y <sub>2</sub> O <sub>3</sub> (a, b, c) and Tb:Y <sub>2</sub> O <sub>3</sub> /Eu:La <sub>2</sub> O <sub>3</sub> (d, e, f) nanoparticles heat treated at 600 °C/3 h (left), 700 °C/3 h (center), and 900 °C/3 h (right).....	99
<b>Figure 110.</b>	Normalized fluorescence spectra (left) and peak intensity ratio (right) for Eu:TiO <sub>2</sub> excited at 464 nm.....	100
<b>Figure 111.</b>	Debris from explosion tests. Only a very small percentage of the debris is actual sensor material.....	101
<b>Figure 112.</b>	SEM of Fe <sub>3</sub> O <sub>4</sub> /Y <sub>2</sub> O <sub>3</sub> core/shell nanoparticles. ....	101
<b>Figure 113.</b>	Images of Fe <sub>3</sub> O <sub>4</sub> /Eu:Y <sub>2</sub> O <sub>3</sub> core/shell nanoparticles in the presence of a magnet. Precursor (left), heated to 600 °C and 700 °C (center), and heated to 800 °C and 950 °C (right). All samples are magnetic, except the one heated to 950 °C. ....	101

<b>Figure 114.</b>	Fluorescence spectra of Fe <sub>3</sub> O <sub>4</sub> /Eu:Y <sub>2</sub> O <sub>3</sub> core/shell nanoparticles heated to various temperatures for 5 s.....	102
--------------------	---	-----

## LIST OF TABLES

<b>Table 1.</b>	Calculated intensity ratios, and their percent differences, for different filter bandwidths at six different temperatures. The percent difference represents that percentage that the ratio changes if we make the single wavelength approximation.....	10
<b>Table 2.</b>	Calibration parameters determined for pyrometer using pyroprobe heating and predicted b value from theory.....	11
<b>Table 3.</b>	Measured voltage ratios at different pyroprobe temperatures and calculated temperature from pyrometer.....	12
<b>Table 4.</b>	Calculated isothermal temperature and time for different explosion temperature profiles with different peak temperatures and peak widths. Also tabulated are the asymptotic values of $\alpha_1$ and $\alpha_2$ as calculated using Equation 23. ....	21
<b>Table 5.</b>	Fitting parameters for relaxation equation.....	33
<b>Table 6.</b>	Grain size of samples heated to 640°C, 720°C, and 850°C for dwell times of 50 s and 100 s. ....	39
<b>Table 7.</b>	Comparison of temperatures measured via particulate sensors based upon FWHM at 611 nm and thermocouples (TC).....	49
<b>Table 8.</b>	Characteristics of the furnace-heated ZrO <sub>2</sub> crystalline phases.....	53
<b>Table 9.</b>	Characteristics of the pyroprobe-heated ZrO <sub>2</sub> crystalline phases. ....	55
<b>Table 10.</b>	Analysis result for five blind samples. ....	76
<b>Table 11.</b>	Calculated and measured mass loss assuming that the starting compound is MOHCO <sub>3</sub> ·H <sub>2</sub> O.....	93
<b>Table 12.</b>	Irreducible representations for <sup>7</sup> F <sub>J</sub> levels in La <sub>2</sub> O <sub>3</sub> and La(OH) <sub>3</sub> .....	95
<b>Table 13.</b>	Irreducible representations for <sup>7</sup> F <sub>J</sub> levels in Y <sub>2</sub> O <sub>3</sub> .....	95

## **ACKNOWLEDGEMENTS**

I would like to acknowledge the following persons for their contributions to this project: Dr. Suhithi Peiris for the initiation of this program at DTRA and her support throughout the project duration; Drs. Ray Gunawidjaja, Helena Diez-y-Riega, Benjamin Anderson, Thandar Myint, Gediminas Markevicius, and Mr. Patrick Price for their contributions to the synthesis, characterization, and development of the sensors; Drs. James Lightstone, Forrest Svingala, Amber Daniels, Christopher Milby, Demitrios Stamatis, James Carney, and Jillian Horn for the explosive testing of our sensors; Dr. Nick Glumac and his group members for shock tube experiments; and Drs. Eduardo Yukihara, Joseph Talghader, and Liping Huang for stimulating discussions.

## I. SUMMARY

The Defense Threat Reduction Agency (DTRA) is developing the science and technologies to defeat weapons of mass destruction such as biological agents. Developing such weapons requires knowledge of the temperature and heating duration inside the fireball of an explosion. Current approaches rely on the use of thermocouples (TCs) for such measurements. However, TCs are limited in their response time and tend to get destroyed during the explosion. As such, DTRA is supporting the development of alternative sensors that are capable of measuring and recording temperature and heating duration under extreme conditions to ensure that the temperatures reached in a post-detonation fireball is sufficiently high to destroy biological agents. In order to be relevant for this specific application, DTRA expects these sensors to be of about the same size as biological agents. Furthermore, DTRA needs the means to map the spatial temperature profile within the fireball (i.e. the movement of the temperature sensors needs to be tracked).

Our approach is based upon monitoring irreversible phase changes (e.g. decomposition, nucleation, grain growth, and phase transformations) that occur during heating of precursor of metal oxides. These phase changes are probed by rare-earth (RE) dopants via changes in their optical spectra (i.e. spectral changes due to heating-induced rearrangements of the local environment of the RE dopants). Laboratory-based reference measurements in which the sensor material is heated for specific times to various temperatures are used for calibration. Changes in the spectral peak width, peak position, relative peak intensities, etc. can then be used to determine the temperature. By using two different sensor materials and performing a kinetic analysis, it is possible to extract temperature and heating duration. In addition, fully crystalline particles can be added to the temperature sensors as references and for tracking purposes.

Modeling of the heating process and response of the temperature sensors has highlighted the importance of a fast laboratory-based heating technique. If the effective ramp time is too long compared to the actual isothermal heating duration, significant changes will occur in the sensor material that could lead to misinterpretation of the results.

Our initial laboratory-based reference measurements were performed using pyroprobe heating combined with TC-based temperature measurements. However, heating of the temperature sensors was limited by heat conductivity and it took several seconds for the temperature sensors to reach their final temperature even though the heating coil reached its final temperature within a few milliseconds. Next, we used indirect heating via a CO<sub>2</sub> laser. The temperature sensors were embedded between graphite sheets and the sheets were then illuminated by the laser. This approach led to much faster heating times, but still not fast enough to compare with conditions in an explosive fireball. Finally, we changed to direct laser heating using a CO<sub>2</sub> laser and monitoring the temperature via 3-color pyrometry. This approach allowed us to perform our reference measurements using sufficiently fast and high-enough temperature rises.

Different types of our temperature sensors were tested during actual explosion tests at the Naval Surface Warfare Center, Indian Head Explosive Ordnance Disposal Technology Division (NSWC IHEODTD) under various conditions. These tests were performed in open air and closed-chamber settings using non-aluminized and aluminized charges.

After each explosion, the debris including our temperature sensors was collected and returned to our lab for analysis.

Early results showed that precursor Eu-doped yttria ( $p\text{-Eu:Y}_2\text{O}_3$ ) and precursor Eu-doped zirconia ( $p\text{-Eu:ZrO}_2$ ) are suitable temperature sensor materials. Because of its hypersensitive transition, europium is uniquely useful for monitoring temperature-induced structural changes. Both sensor materials were successfully tested during actual explosion tests. The optical analysis of these materials was based upon changes in the full-width half-maximum (FWHM) for  $\text{Eu:Y}_2\text{O}_3$  and on changes in fluorescence and fluorescence-excitation peak position and relative peak intensities for  $\text{Eu:ZrO}_2$ .

The more recent analysis of sensor materials has focused on using changes in relative peak intensities instead of changes to FWHM and shifts in peak position. Combining temperature sensor materials with tracking sensors, with crystalline (c-) reference materials, or mixing two different sensor material for combined temperature and heating duration analysis can lead to spectral interferences from the different emission sources, and we found that using the relative fluorescence peak intensities as indicators is less sensitive to spectral interferences. Also, fluorescence measurements are less time consuming and require simpler experimental setups than fluorescence-excitation measurements – an important consideration for the development of potential portable analysis equipment.

Time-dependent measurements using  $p\text{-Eu:ZrO}_2$  showed that the material response to a heating event is very fast (millisecond timescale and possibly faster) and, dependent on the temperature, the changes in the material can be completed within a few hundred milliseconds. A mixture of  $p\text{-Eu:ZrO}_2$ , c-Ho:ZrO<sub>2</sub>, and  $p\text{-Dy:Y}_2\text{O}_3$  combined with a kinetic analysis approach is currently being used to extract temperature and heating time information. We have used this mixture in combination with direct laser heating to demonstrate that we can measure heating durations as short as 100 ms.

The following materials were evaluated as potential tracking sensors:  $\text{Eu:Y}_2\text{O}_3$ ,  $\text{Tb:Y}_2\text{O}_3$ ,  $\text{Dy:Y}_2\text{O}_3$ ,  $\text{Sm:Y}_2\text{O}_3$ ,  $\text{Er,Yb:Y}_2\text{O}_3$ ,  $\text{Ho:Y}_2\text{O}_3$ ,  $\text{Pr:Y}_2\text{O}_3$ ,  $\text{Nd:Y}_2\text{O}_3$ , and  $\text{Tm:Y}_2\text{O}_3$ , with several of them tested during explosion tests. We found that the critical selection criteria for tracking particles is the spectral overlap between the tracking materials and the temperature sensors, as the tracking particles are found to have a much higher fluorescence intensity than the temperature sensors. Based upon a careful evaluation,  $\text{Dy:Y}_2\text{O}_3$ ,  $\text{Ho:Y}_2\text{O}_3$ ,  $\text{Pr:Y}_2\text{O}_3$ ,  $\text{Nd:Y}_2\text{O}_3$ , and  $\text{Tm:Y}_2\text{O}_3$  appear to be the most promising tracking sensor materials in combination with temperature sensors such as  $\text{Eu:Y}_2\text{O}_3$  and  $\text{Eu:ZrO}_2$ . However, when combined with the  $p\text{-Eu:ZrO}_2$ , c-Ho:ZrO<sub>2</sub>, and  $p\text{-Dy:Y}_2\text{O}_3$  mixture,  $\text{Dy:Y}_2\text{O}_3$  and  $\text{Ho:Y}_2\text{O}_3$  cannot be used.

Temperature-induced phase changes in RE-doped precursor metal-oxides have been successfully demonstrated as temperature sensors in explosive fireballs. The temperature readings from these sensors are always higher than the readings from TCs, which is expected due to their faster response time. The response time of these sensor material is at least as fast as a few milliseconds and possibly faster. Extracting temperature and heating duration requires the simultaneous use of two sensor materials combined with a kinetic analysis. The temperature sensors can be combined with tracking particles to identify the location of their origin.

## **II. INTRODUCTION**

According to DTRA, its “*... counter-WMD mission includes research and development of weapons, in particular Agent Defeat weapons. Such weapons utilize a combination of explosive, thermal and chemical kill mechanisms, to create high temperatures of critical duration to neutralize biological weapon agents. When such a weapon is deployed, the resultant turbulence creates a complex heterogeneous environment of bursting vessels, fragmenting equipment and aerosolized liquids within the blast radius. We need to characterize this spatially and temporally non-uniform thermal environment under extreme conditions such as at hundreds of kilopascals of pressure (100 KPa), and in very transient atmospheres that change every microsecond (1  $\mu$ s). Current technologies cannot provide the desired information, but exploration of thermo-properties of nanomaterials could lead to revolutionary new ways to measure temperature in these extreme environments.*” “*Possible research directions can include the creation and study of nano-composite particles that change and maintain material phases after a thermal event; micro-encapsulated materials that when exposed to a thermal event releases the encapsulated material for analysis, etc.*”<sup>1</sup>

DTRA’s objective for this research topic was “*to support fundamental research to identify and characterize the means and materials that will measure the temperature and perhaps also retain the complete thermal history of events (1 to 180 seconds) involving extreme conditions ranging from tens to hundreds of kilopascals of pressure (100 KPa), hundreds of degrees of temperature (maximum 700 °C), and microsecond (1  $\mu$ s) changes of these conditions.*”<sup>1</sup>

In response to this challenge, we proposed to characterize and evaluate temperature-induced irreversible phase changes in metal-oxide nanoparticles as potential temperature sensors for use in explosive fireballs. The expected phase changes are often relatively subtle and require sensitive means for read-out. As such, we proposed to dope these materials with rare-earth ions such as europium (Eu) whose optical spectra are very sensitive to their local environment.

The scope of this project included:

- development, characterization, and testing of several temperature sensor materials and demonstration of their suitability for measuring and recording temperature inside an explosive fireball
- demonstration that these sensor materials respond at least as fast as a few milliseconds and possibly faster
- development of a laser-based heating and 3-color pyrometer-based temperature recording system
- initial demonstration of a kinetic analysis approach based upon using two different temperature sensor materials to extract temperature and heating duration information
- development and demonstration of tracking particles to monitor the origin of the sensors during explosions

Our approach included:

- identifying the most appropriate synthesis techniques for the preparation of metal-oxide precursors in a specific state
- identifying how these precursors react (i.e. undergo irreversible phase transitions) under thermal exposure
- developing a heating technique that is capable of reaching temperatures with heating rates comparable to those occurring in an explosion in a controlled manner
- measuring the temperature with a fast enough resolution and provide feedback to the heating mechanism

The results gained from this investigation provide the required information to develop further the kinetic approach in combination with appropriate sensor mixtures to extract temperature and heating duration. Besides the use as a development tool for c-WMD, the technique might find more general applications during heating events such as fire and arson investigations. We also envision the development of a portable analysis unit for field testing.

### **III. METHODS, ASSUMPTIONS, AND PROCEDURES**

#### **A. Synthesis**

This section summarizes the synthesis techniques used for the preparation of the sensor and tracking materials. The techniques are described using specific example materials, but are also applicable to other materials.

##### **p-Eu:Y<sub>2</sub>O<sub>3</sub>**

Irregular sized nanoparticles of precursor of Eu-doped yttria, p-Eu:Y<sub>2</sub>O<sub>3</sub>, with dimensions in the 20-50 nm range are synthesized by co-precipitation. An aqueous mixture of ammonium hydroxide and ammonium bicarbonate (1:1 mole ratio, 1.25 M) is drop wise added into an aqueous solution of europium nitrate/yttrium nitrate solution (1:99 mole ratio) until the pH of the mixture solution reaches 7.5 - 8.0. The resulting white precipitate is left to age for 3 h. Subsequently, it is washed with deionized water and rinsed with acetone before it is placed in vacuum to dry overnight followed by heat drying at 150 °C for 12 h. The dried white cake is crushed into powder, and run through a 100 mesh sieve.<sup>2</sup> The europium dopant may be substituted with other rare earth elements. For the preparation of tracking particles, p-Eu:Y<sub>2</sub>O<sub>3</sub> is heated to 1400 °C for 30 min.

##### **p-Eu:ZrO<sub>2</sub>**

Irregular sized nanoparticles of precursor of Eu-doped zirconium oxide, p-Eu:ZrO<sub>2</sub>, is obtained by adding aqueous solution of europium nitrate/zirconium(IV) oxychloride (1:99 mole ratio, 0.15 M), drop-wise to an aqueous solution of ammonium hydroxide (2.5 vol.%) until a pH of 10.00 is reached. A white gel forms and is aged for 4 h. Subsequently, the gel undergoes multiple cycles of centrifugation and redispersion in deionized water. The washed gel is then rinsed twice with acetone, dried in vacuum, and then dried at 150 °C for 12 h. Finally, the white dried cake is crushed into powder with mortar and pestles, and run through a 100 mesh sieve.<sup>3</sup> The europium dopant may be substituted with other rare earth elements.

##### **RE<sub>1</sub>:ZrO<sub>2</sub>/p-RE<sub>2</sub>:Y<sub>2</sub>O<sub>3</sub> Core-shell**

Spherically-shaped nanoparticles of precursor of RE-doped zirconium oxide, p-RE<sub>1</sub>:ZrO<sub>2</sub>, with about 300 nm diameters are obtained via forced hydrolysis and serve as the core. RE salt/zirconium(IV) oxychloride (1:99 mole ratio, 0.2 M) dissolved in an isopropanol/water mixture (5:1 vol/vol) containing hydroxypropyl cellulose (1.5 g/L) is heated quickly in a microwave, and then held isothermally in a hot bath at 75-80 °C for 30 min. The formed spherical nanoparticles are stabilized by adding ammonium hydroxide solution **to neutralize the solution's pH. The nanoparticles are then washed with deionized water, rinsed with acetone, dried in vacuum, and then dried at 150 °C for 12 h. The nanoparticles are then heated to 1000 °C for 30 min to transform them into metallic oxides.**

The precursor of RE-doped yttrium oxide, p-RE<sub>2</sub>:Y<sub>2</sub>O<sub>3</sub>, is grown via homogeneous precipitation using urea in the presence of RE<sub>1</sub>:ZrO<sub>2</sub> (5 mg/mL concentration) to yield the RE<sub>1</sub>:ZrO<sub>2</sub>/p-RE<sub>2</sub>:Y<sub>2</sub>O<sub>3</sub> core-shell nanoparticles. The total metallic salt concentration is 5 mM and the urea concentration is 0.2 M. The homogeneous precipitation is done at 90 °C for 3 h. The obtained nanoparticles are then washed with deionized water, rinsed with acetone, dried in vacuum, and the dried at 150 °C for 12 h.<sup>4</sup>

## B. Lab-based heating and temperature measurements

### Furnace

Initially, irreversible phase transitions of the precursors, placed in crucibles, were induced by heating in a box furnace (Lindberg Blue). This heating method allowed us to subject the precursors to well-defined conditions and to follow the phase changes over time. The precursors which typically consist of amorphous carbonates or hydroxides undergo a thermal decomposition process that leads to the formation of oxides. This process can occur over several steps. Depending on the intermediary products, nucleation may occur while decomposition is still undergoing, or nucleation may start only after the decomposition process is complete. Under continued heating, the nucleated particles will then start to grow into larger structures.

### Pyroprobe

In order to identify phase changes that occur under much faster heating rates, we used a Pyroprobe-1000 (CDS Analytical, Inc.), see Figure 1. This pyroprobe is capable of heating rates from 10 °C/s up to 20000 °C/s, temperatures up to 1400 °C, and heating durations from 0.01 s up to 99.99 s. The sample material can be placed on a heating strip or inside a quartz tube which is then inserted into a heating coil. Placing our material on the heating strip did not work well. The material would typically come off during the heating and thus heating durations were not well defined. The development of gas products such as CO<sub>2</sub> during the thermal decomposition is probably responsible for this effect.



**Figure 1.** CDS Analytical pyroprobe heater, heating strip, and heating coil.

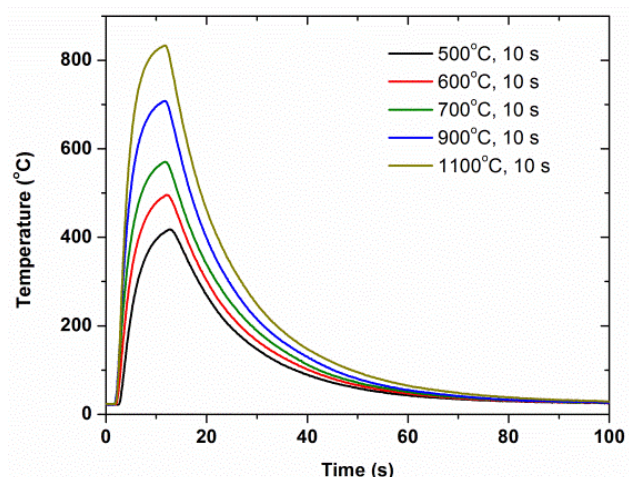


**Figure 2.** Actual pyroprobe temperature profiles.

While placing our material into the quartz tubes and heating it in the coil kept the material in place, we noticed that heating the material at the center of the tube to the set temperature often took a significant amount of time. We embedded a thermocouple (Omega CHAL-005) with a fast response time into the sensor material and monitored the temperature during the heating process. Even though we used a heating rate of 20000 °C/s, the actual heating process took much longer, see Figure 2. With a heating duration of 10 s, none of the samples reached the set temperature.

## Laser heating

In order to achieve faster heating rates, we used a CO<sub>2</sub> laser (Synrad f100). Initially, we enclosed our sample material between graphite sheets to hold the material in place. Using this approach, we improved our heating process and achieved effective heating rates as fast as 400 °C/s, see Figure 3.

To further increase the heating rate while keeping the sample in place, we are cold-pressing the sensor material into a pellet, place it into a sample holder, and cover it with an IR transparent window such as ZnSe. We then use the CO<sub>2</sub> laser and a 3-color pyrometer with home-build control unit and feedback loop to heat the sample in a controlled manner. Using this approach, we are able to reach heating rates up to 26600 °C/s, see Figure 3. At this rate, it takes about 30 ms to reach 1000 K. A fixable problem with the controller is currently limiting the isothermal heating time and causes fluctuations in the temperature value.

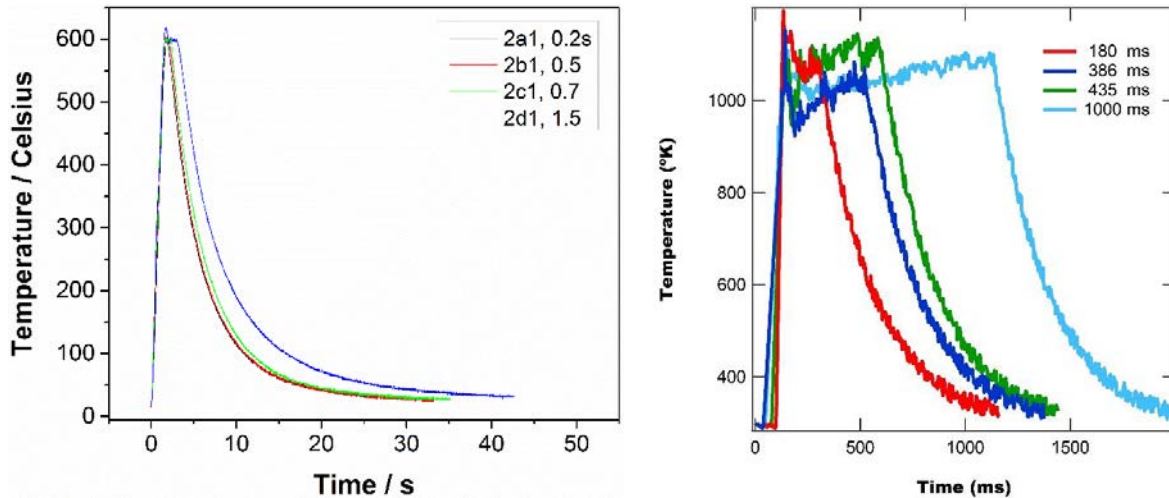


**Figure 3.** Actual indirect (left) and direct (right) laser heating temperature profiles.

## Pyrometer

Our 3-color pyrometer is shown in Figure 4. Fundamentally a pyrometer works based on Planck's law of blackbody radiation, which states that the emitted spectral radiance of a black body at wavelength  $\lambda$  and temperature  $T$  is given by:

$$I(\lambda, T) = \frac{2hc^2}{\lambda^5} \frac{1}{e^{hc/\lambda kT} - 1}, \quad (1)$$

where  $h$  is Planck's constant,  $c$  is the speed of light, and  $k$  is Boltzmann's constant. While Equation 1 holds for a perfect black body, in reality most materials are actually 'grey-bodies' meaning that they have a wavelength and temperature dependent emissivity  $\epsilon(\lambda, T)$ . Additionally, what we measure experimentally is not the spectral radiance, but a photodiode voltage which is proportional to the spectral radiance integrated over a narrow wavelength range, with the proportionality constant

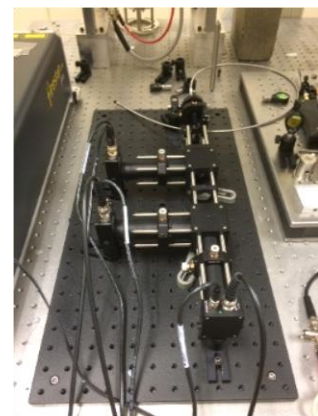


**Figure 4.** 3-color pyrometer.

depending on geometry, optical properties of the pyrometer, and the quantum efficiencies of the photodiodes. For simplicity we lump the various wavelength responses into one function  $S_i(\lambda)$ . Taking into account the emissivity, wavelength response of the pyrometer, and spectral integration we find that the voltage measured by one of the photodiodes at temperature  $T$  is

$$V_i(T) = \int_{\lambda_i - \Delta/2}^{\lambda_i + \Delta/2} \frac{2hc^2}{\lambda^5} \frac{S(\lambda)\epsilon(\lambda, T)}{e^{hc/\lambda kT} - 1} d\lambda. \quad (2)$$

While Equation 2 describes the photodiode voltage measured for a sample at temperature  $T$ , what we want in practice is to invert Equation 2 to find the temperature as a function of the photodiode voltage.

In its current form Equation 2 is too computationally intensive to implement a simple inversion algorithm, which is necessary for the pyrometer to function quickly. We therefore make several approximations to drastically simplify the computation required. First we assume that  $\lambda kT \ll hc$  such that Planck's law can be replaced by Wien's approximation:

$$I(T) = 2hc^2\lambda^{-5}e^{-hc/\lambda kT}. \quad (3)$$

This approximation is valid for our wavelength and temperature range, as the maximum deviation between Equation 1 and 3 is only 0.22 % in our experimental regime.

Next we assume that for the wavelength range we use the emissivity depends only on temperature, which is a fairly good assumption for ceramics and the narrow wavelength range we are using. With these approximations Equation 2 becomes

$$V_i(T) = 2hc^2\epsilon(T) \int_{\lambda_i - \Delta/2}^{\lambda_i + \Delta/2} S(\lambda)\lambda^{-5}e^{-hc/\lambda kT} d\lambda. \quad (4)$$

Finally we assume that the filter bandwidth is negligible such that the signal at each detector is due to a single wavelength.

To calculate the approximate temperature we take the ratio of the voltage at the first and second detector:

$$r_{12} = \frac{V_1}{V_2} = \frac{S_1}{S_2} \left( \frac{\lambda_2}{\lambda_1} \right)^5 \exp \left[ \frac{hc}{kT} \frac{\lambda_2 - \lambda_1}{\lambda_1 \lambda_2} \right], \quad (5)$$

Where  $S_1$  and  $S_2$  are the detector response constants of the first and second detector respectively. Rearranging Equation 5 we find the inverse temperature as a function of the voltage ratio:

$$\frac{1}{T} = \frac{k}{hc} \frac{\lambda_1 \lambda_2}{\lambda_2 - \lambda_1} \ln \left[ \frac{r_{12} S_2}{S_1} \left( \frac{\lambda_1}{\lambda_2} \right)^5 \right]. \quad (6)$$

Equation 6 relates the inverse temperature to the ratio of the detector voltages with the assumption that the emissivity does not change with wavelength. This assumption is not necessarily valid and therefore to increase our accuracy we move to the next order of approximation, which is to include an approximate emissivity wavelength dependence. One model of the wavelength dependent emissivity is an exponential expansion given by:

$$\epsilon(\lambda, T) = \exp(-a_0 - a_1\lambda - a_2\lambda^2 - \dots) \quad (7)$$

Where  $a_0$  defines the magnitude of the emissivity and the higher order terms determine the emissivities spectral shape. Since we are using a relatively narrow wavelength range, it is sufficient to only use the first two orders, which gives a wavelength dependent emissivity of the form:

$$\begin{aligned} \epsilon(\lambda, T) &\approx e^{-a_0} e^{-a_1\lambda} \\ &= \epsilon_0 e^{-a_1\lambda} \end{aligned} \quad (8)$$

With this correction we can write the first order single wavelength detector voltage as

$$V_i = 2S_i h c^2 \epsilon_0 \lambda_i^{-5} \exp\{-hc/\lambda_i kT - a_1 \lambda_i\}. \quad (9)$$

Since we now have two unknowns,  $T$  and  $a_1$ , we need to use two separate ratios in order to calculate the temperature from the pyrometer. We therefore use the ratio of detector 1 and 2, and the ratio of detector 1 and 3, which are given by:

$$r_{12} = \frac{V_1}{V_2} = \frac{S_1}{S_2} \left( \frac{\lambda_2}{\lambda_1} \right)^5 \exp \left[ \frac{hc}{kT} \frac{\lambda_2 - \lambda_1}{\lambda_1 \lambda_2} + a_1(\lambda_2 - \lambda_1) \right], \quad (10)$$

$$r_{13} = \frac{V_1}{V_3} = \frac{S_1}{S_3} \left( \frac{\lambda_3}{\lambda_1} \right)^5 \exp \left[ \frac{hc}{kT} \frac{\lambda_3 - \lambda_1}{\lambda_1 \lambda_3} + a_1(\lambda_3 - \lambda_1) \right]. \quad (11)$$

To calculate the inverse temperature we first rearrange Equation 10 to give the inverse temperature dependent on  $a_1$ ,

$$\frac{1}{T} = \frac{k}{hc} \frac{\lambda_1 \lambda_2}{\lambda_2 - \lambda_1} \left( \ln \left[ \frac{r_{12} S_2}{S_1} \left( \frac{\lambda_1}{\lambda_2} \right)^5 \right] + a_1(\lambda_1 - \lambda_2) \right). \quad (12)$$

We then substitute Equation 12 into Equation 11 and solve for  $a_1$ ,

$$a_1 = \frac{\lambda_3}{\lambda_3 - \lambda_2} \left\{ \frac{1}{\lambda_3 - \lambda_1} \ln \left[ \frac{r_{13} S_3}{S_1} \left( \frac{\lambda_1}{\lambda_3} \right)^5 \right] - \frac{\lambda_2}{\lambda_3(\lambda_2 - \lambda_1)} \ln \left[ \frac{r_{12} S_2}{S_1} \left( \frac{\lambda_1}{\lambda_2} \right)^5 \right] \right\}. \quad (13)$$

Finally, we substitute Equation 13 into Equation 12 and simplify to give the inverse temperature in terms of the detector voltages:

$$\frac{1}{T} = \frac{k \lambda_1 \lambda_2 \lambda_3}{hc(\lambda_1 - \lambda_2)(\lambda_1 - \lambda_3)(\lambda_2 - \lambda_3)} \left[ (\lambda_1 - \lambda_3) \ln \left[ \frac{V_1 S_2}{V_2 S_1} \left( \frac{\lambda_1}{\lambda_2} \right)^5 \right] + (\lambda_2 - \lambda_1) \ln \left[ \frac{V_1 S_3}{V_3 S_1} \left( \frac{\lambda_1}{\lambda_3} \right)^5 \right] \right]. \quad (14)$$

One of the main assumptions in deriving Equation 5 is that the detectors only measure a single wavelength, which is not true. In order to estimate the error in the voltage ratios due to this assumption we calculate the voltage at each detector for a nonzero filter bandwidth using Equation 4 with the emissivity assumed to be constant. Table 1 tabulates the voltage ratios for a 12 nm and 50 nm filter, as well as the percent difference between the multiwavelength calculations and the single wavelength approximation. From these percent differences we see that ratio errors are less than 1%.

**Table 1.** Calculated intensity ratios, and their percent differences, for different filter bandwidths at six different temperatures. The percent difference represents that percentage that the ratio changes if we make the single wavelength approximation.

<b>T (K)</b>	<b>Wavelength (nm)</b>	<b>Ratio (<math>V_\lambda/V_{1500}</math>)</b>			<b>Percent Difference</b>	
		<b>0 nm</b>	<b>12 nm</b>	<b>50 nm</b>	<b>12 nm</b>	<b>50 nm</b>
473	1550	1.63281	1.63291	1.63117	0.00601	0.10064
	1600	2.57262	2.57262	2.56631	-6E-05	0.24526
673	1550	1.34430	1.34419	1.34343	-0.00814	0.06469
	1600	1.76512	1.76494	1.76345	-0.01015	0.09479
873	1550	1.20990	1.20126	1.20961	-0.71389	0.02385
	1600	1.43926	1.42898	1.43865	-0.7145	0.04251
1073	1550	1.13258	1.13258	1.1325	-0.00053	0.00800
	1600	1.26642	1.26642	1.26625	-0.00066	0.01396
1273	1550	1.08252	1.08253	1.08253	0.00036	-0.0003
	1600	1.16024	1.16024	1.16028	-7.9E-05	-0.00315
1473	1550	1.04758	1.04764	1.04748	0.00472	0.01009
	1600	1.08882	1.0888	1.08887	-0.00274	-0.00353

For the actual implementation of the pyrometer, Equation 14 is problematic due to spectral integration of the detectors and deviations between theory and reality. A more helpful approach is to use an empirical model of the voltage ratios using a fit function of

$$r = Ae^{b/T}, \quad (15)$$

where  $r$  is a given ratio,  $T$  is the temperature, and both  $A$  and  $b$  are fit parameters. We can then invert Equation 15 to find the inverse temperature for a given voltage ratio

$$\frac{1}{T} = \frac{1}{b} \ln\left(\frac{r}{A}\right). \quad (16)$$

In order to use Equation 16 for the pyrometer we must first perform calibration measurements in order to determine  $A$  and  $b$  for each ratio permutation. We therefore measure the emission from a pyroprobe at different temperatures and obtain the detector voltages as a function of temperature<sup>1</sup>, shown in Figure 5. From these voltages we calculate the voltage ratios, shown in Figure 6, and fit them to Equation 15, with Table 2 listing the fit parameters for each ratio permutation.

---

<sup>1</sup> For  $T \leq 923$  °K the detectors use a gain setting of 70 db. For higher temperatures the gain has to be set lower (30 dB) to avoid saturation.

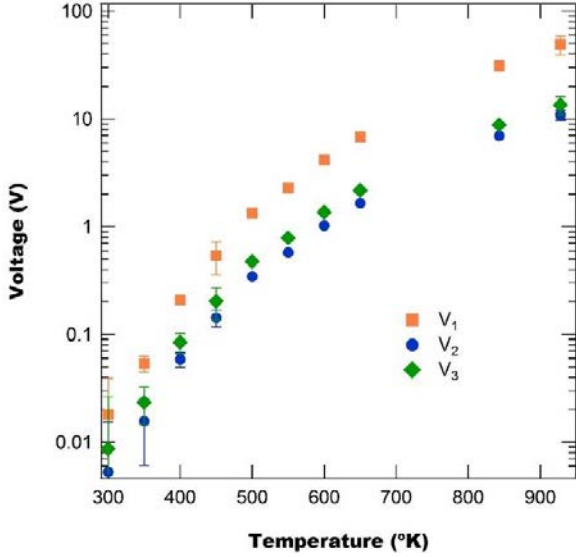


**Figure 5.** Detector voltages as a function of temperature.

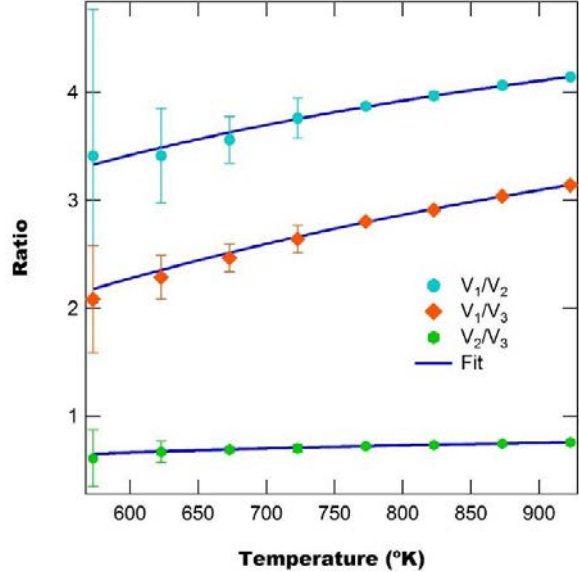


**Figure 6.** Measured voltage ratios as a function of pyroprobe temperature and fits to Equation 15.

**Table 2.** Calibration parameters determined for pyrometer using pyroprobe heating and predicted b value from theory.

	<b>A</b>	<b>B (°K)</b>	<b>b<sub>Th</sub> (°K)</b>
<b>V<sub>1</sub>/V<sub>2</sub></b>	$5.93 \pm 0.20$	$-330 \pm 29$	-309.3
<b>V<sub>1</sub>/V<sub>3</sub></b>	$5.72 \pm 0.15$	$-553 \pm 23$	-599.5
<b>V<sub>2</sub>/V<sub>3</sub></b>	$0.967 \pm 0.035$	$-225 \pm 32$	-289.9

Using Equation 16 and the parameters for each ratio we can compute three temperature values, which can be averaged to give a single temperature. To test this method we use our data from the pyroprobe to calculate the pyroprobes temperature. Table 3 lists the **pyroprobe's set temperature, pyrometer voltage ratios, and the calculate temperature**.

From Table 3 we see that the pyrometer calculates the temperature far more precisely and accurately at high temperatures, which is expected as the signal-to-noise ratio is bigger at higher temperatures. Figure 7 shows the difference magnitude in the calculated and set temperatures as a function of set temperature. From Figure 7 we see that as the set temperature increases the difference drastically decreases to near zero and also that all temperature differences are within uncertainty of zero. The slight increase in the difference at higher temperatures is due to the high T measurements requiring a different detector gain setting.

**Table 3.** Measured voltage ratios at different pyroprobe temperatures and calculated temperature from pyrometer.

T (°K)	V <sub>1</sub> /V <sub>2</sub>	V <sub>1</sub> /V <sub>3</sub>	T <sub>calc</sub> (°K)
523	4.5 ± 2.3	2.22 ± 0.64	708 ± 574
573	3.4 ± 1.4	2.08 ± 0.50	573 ± 126
623	3.41 ± 0.44	2.29 ± 0.20	601 ± 42
673	3.56 ± 0.12	2.465 ± 0.057	652 ± 13
773	3.871 ± 0.024	2.803 ± 0.012	775.3 ± 3.8
823	3.968 ± 0.034	2.912 ± 0.023	821.0 ± 6.3
839	4.004 ± 0.056	2.964 ± 0.041	841 ± 11
873	4.064 ± 0.030	3.038 ± 0.022	874.8 ± 6.4
923	4.143 ± 0.013	3.141 ± 0.010	922.4 ± 3.0
1116	4.429 ± 0.017	3.507 ± 0.013	1130 ± 19
1201	4.511 ± 0.064	3.622 ± 0.051	1210 ± 40
1473	4.724 ± 0.019	3.927 ± 0.015	1470 ± 18

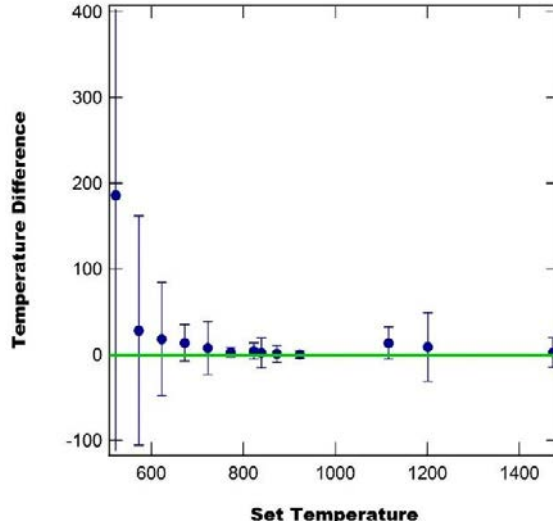


**Figure 7.** Difference in calculated and set temperatures as a function of set temperature. As the temperature increases the difference between the set and calculated temperatures drastically decreases and all differences are within uncertainty of zero.

### C. Explosion tests

During the course of this project, four series of explosion tests were conducted to test the performance of the sensors. These tests were performed at the Naval Surface Warfare Center, Indian Head Explosive Ordnance Disposal Technology Division (NSWC IHEODTD). The tests were conducted either in a large room or inside a smaller steel chamber using aluminized and non-aluminized charges. Since all of the tests were slightly different, the specifics are described in the Results and Discussion section.

### D. Characterization

A variety of optical characterization techniques were used to characterize the optical properties of the sensor materials and to identify appropriate optical signatures that would provide information about the temperature that these sensors were exposed to. The bulk of these measurements was based upon fluorescence and fluorescence-excitation measurements. During fluorescence measurements, the sample material was illuminated at a particular wavelength using a laser or LED source and the light emitted by the sample is monitored as a function of wavelength. In fluorescence-excitation measurements, the monitoring monochromator was set to a specific wavelength and the excitation wavelength (laser) was tuned over a certain range. The resulting spectra were then analyzed with respect to full-width-half-maximum (FWHM) of peaks, peak positions, and relative peak intensities. Figure 8 shows the schematic of the fluorescence/excitation setup. The optical spectroscopy measurements are performed using a Continuum Nd:YAG laser operating at 10 Hz in the 3<sup>rd</sup> harmonic at 355 nm. This laser pumps a Continuum Panther Optical Parametric Oscillator (OPO). Using several mirrors, laser light of about 10 ns pulse length of the desired wavelength is directed onto the sample material which is placed in a vial, see Figure 6 (right). The emitted fluorescence is collected using a 2" diameter lens with a focal length of 15 cm. Using a 2" diameter lens with a focal length of 50 cm, the fluorescence is then focused onto the entrance slit of an Acton 2750 monochromator/spectrometer with PMT and CCD array attached. The excitation spectra are acquired using a SpectraHub (Acton) interface and in-house Labview software. The fluorescence spectra are acquired using the CCD camera and WinSpec software (Princeton Instruments). The lifetimes are measured using a PMT and an oscilloscope (Tektronix TDS3052B). The data is further processed using Origin Pro 8.5.

Additional characterization techniques used during this project include Fourier Transform Infrared (FTIR), x-ray diffraction (XRD); scanning electron microscopy

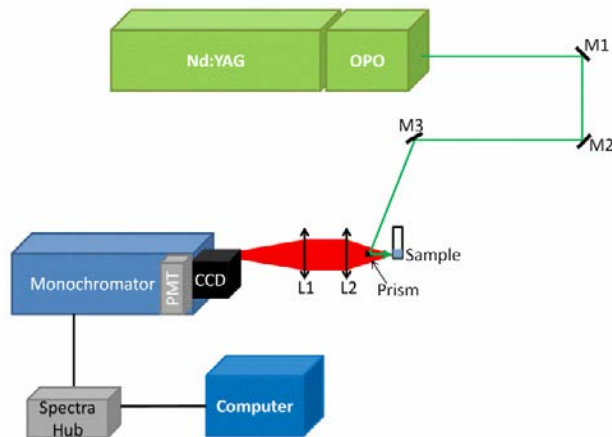


**Figure 8.** Schematic of the fluorescence/excitation setup.

width-half-maximum (FWHM) of peaks, peak positions, and relative peak intensities. Figure 8 shows the schematic of the fluorescence/excitation setup. The optical spectroscopy measurements are performed using a Continuum Nd:YAG laser operating at 10 Hz in the 3<sup>rd</sup> harmonic at 355 nm. This laser pumps a Continuum Panther Optical Parametric Oscillator (OPO). Using several mirrors, laser light of about 10 ns pulse length of the desired wavelength is directed onto the sample material which is placed in a vial, see Figure 6 (right). The emitted fluorescence is collected using a 2" diameter lens with a focal length of 15 cm. Using a 2" diameter lens with a focal length of 50 cm, the fluorescence is then focused onto the entrance slit of an Acton 2750 monochromator/spectrometer with PMT and CCD array attached. The excitation spectra are acquired using a SpectraHub (Acton) interface and in-house Labview software. The fluorescence spectra are acquired using the CCD camera and WinSpec software (Princeton Instruments). The lifetimes are measured using a PMT and an oscilloscope (Tektronix TDS3052B). The data is further processed using Origin Pro 8.5.

(SEM), energy dispersive x-ray spectroscopy (EDS), transmission electron microscopy (TEM), and differential scanning calorimetry (DSC).

Fourier-transform-infrared (FT-IR) spectra are measured using a Cary 680 FTIR (Varian/Agilent). The nanopowder morphologies are characterized using a scanning electron microscope (SEM), NOVA nanoSEM 230 (FEI), and a transmission electron microscope (TEM), Tecnai G2 20 Twin TEM (FEI). The SEM is equipped with X-Max Silicon Drift Detector (SDD) with an 80 mm<sup>2</sup> active area (Oxford Instruments, PLC.) for energy dispersive spectroscopy (EDS) measurements. A PANalytical X’Pert Pro diffractometer (PANalytical B.V.), using Cu-K $\alpha$  radiation ( $\lambda=1.5418\text{ \AA}$ ) and operated at 45 kV and 40 mA, is used to measure x-ray diffraction patterns. Diffraction pattern were measured using a PIXcel<sup>3D</sup> detector (PANalytical B.V.). The x-ray beam was collimated using a fixed divergence slit (FDS) with 0.04 radian Soller slits, 0.5° divergence slit, and a 10 mm mask. The x-ray beam was monochromatized using a X’Celerator monochromator (PANalytical B.V.). Due to the age of the x-ray source, it also contained W-L $\alpha$  and Cu-K $\beta$  radiation that led to small ghost peaks in the XRD spectra.

Transmission electron microscopy (TEM) images are obtained using a Tecnai G2 20 Twin TEM (FEI) or a Philips CM 200 transmission electron microscope (TEM). A Netzch STA 409 PCat, using a ramp rate of 20°C/minute under Ar atmosphere, is used to measure differential scanning calorimetry (DSC) and thermogravimetric analysis (TGA).

## IV. RESULTS AND DISCUSSIONS

This section is divided as follows: Section A describes our modeling results for the kinetics of temperature-induced phase changes; Section B describes various temperature sensors we characterized, but focuses on Eu:Y<sub>2</sub>O<sub>3</sub> and Eu:ZrO<sub>2</sub>, the two most important ones; Section C describes our temperature/time (thermal impulse) sensors; and Section D describes the tracking particles.

### A. Phase Change Modeling

#### General Model

We can model the kinetics of thermal degradation by considering the degree of conversion,  $\alpha$ , which is found to obey the differential equation:<sup>5</sup>

$$\frac{d\alpha}{dt} = h(T)f(\alpha), \quad (17)$$

where  $h(T)$  is an Arrhenius equation,

$$h(T) = A \exp\left[-\frac{E}{kT(t)}\right] \quad (18)$$

and  $f(\alpha)$  can generally be expressed as:

$$f(\alpha) = \alpha^m(1 - \alpha)^n[-\ln(1 - \alpha)]^p \quad (19)$$

where  $m$ ,  $n$ , and  $p$  depend on the reaction mechanism. Substituting Equations 18 and 19 into Equation 17 lets us write the whole kinetic equation as:

$$\frac{d\alpha}{dt} = A \exp\left[-\frac{E}{kT(t)}\right] \alpha^m(1 - \alpha)^n[-\ln(1 - \alpha)]^p. \quad (20)$$

Moving all the  $\alpha$  and  $t$  terms to opposite sides we can solve Equation 20 to give a general solution of:

$$\int_{\alpha_0}^{\alpha} \frac{d\alpha'}{\alpha'^m(1 - \alpha')^n[-\ln(1 - \alpha')]^p} = A \int_{t_0}^t \exp\left[-\frac{E}{kT(t')}\right] dt'. \quad (21)$$

At this point further simplification of the general case cannot be done as both the integrals depend on the specific functional forms, some of which have analytical solutions, and others which require numerical solutions.

As an example of a semi-analytic solution (we leave T(t) in its general form), we use the case of random nucleation and growth, which gives exponent values of  $m = 0$ ,  $n = 1$ ,  $p = 0$ . Assuming that the system begins with no conversion, i.e.  $\alpha_0 = 0$ , we can solve Equation 21 to give the degree of conversion as a function of time as:

$$\alpha(t) = 1 - \exp\left\{-A \int_{t_0}^t \exp\left[-\frac{E}{kT(t')}\right] dt'\right\}. \quad (22)$$

The integral in Equation 22 has no general analytical solutions and typically requires numerical methods to calculate. However, the simplest case of a temperature profile, that of an isotherm, gives an exact analytical solution of

$$\alpha(t) = 1 - \exp \left\{ -A \exp \left[ -\frac{E}{kT_{iso}} \right] (t - t_0) \right\}. \quad (23)$$

## Nucleation and Growth Example

To better understand how different temperature-time profiles affect the degree of conversion, we assume a nucleation and growth mechanism, with the degree of conversion as a function of time given by Equation 22. For our simulations we assume parameter values of  $E = 0.725$  eV and  $A = 10^4$ , which are on the same order of magnitude as those measured by Turmanova *et al.* for a different material.<sup>5</sup> We will first consider the effect of heating rate on the degree of conversion and then consider an estimated explosion temperature profile.

### Effect of Heating Rate

We simulate the effect of the heating rate,  $g$ , on the degree of conversion by assuming a heating profile consisting of a linear ramp from 273 °K to 873 °K, followed by a 1 s isotherm and then an exponential cooling profile with a time constant of  $\tau = 1$  min. For the ramp rates we use 200 °K/s, 400 °K/s, 600 °K/s, and 2400 °K/s, with the ramping time varying such that the final temperature is always 873 °K. Figure 9 shows the temperature profile and degree of conversion as a function of time for the 600 °K/s heating rate, with the degree of conversion given both by Equation 22 and by the isothermal model.

From Figure 9 we see that for the isothermal model the degree of conversion only changes during the isothermal time, neglecting the effects of heating and cooling. By comparing the full model to the isothermal model we see that the heating and cooling works to increase the degree of conversion further than just for the isothermal period.

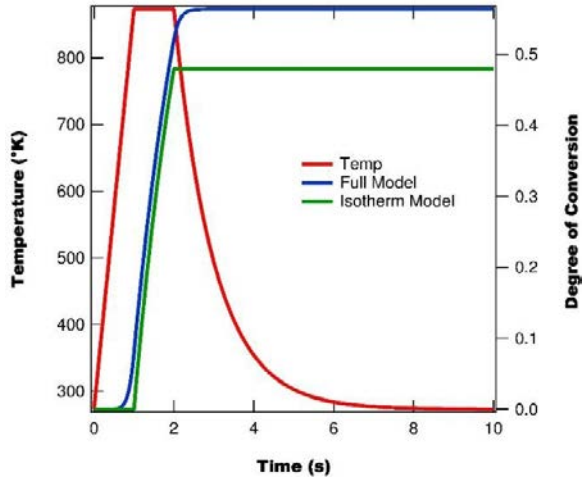


**Figure 9.** Temperature profile as a function of time plotted with the degree of conversion using the full model of Equation 22 and the isothermal model, which ignores heating and cooling.

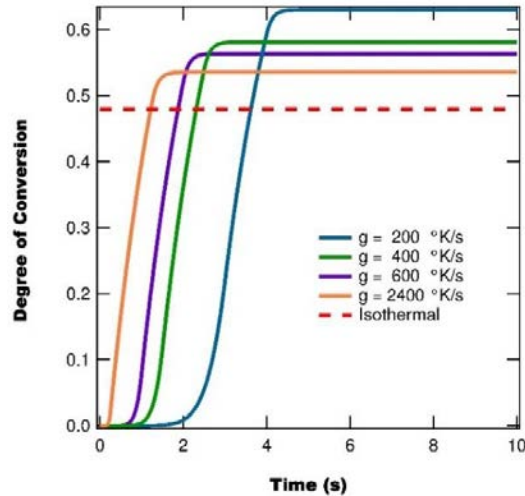


**Figure 10.** Degree of conversion predicted by Equation 23 as a function of time for different heating rates, as well as the isothermal value. Note that as the heating rate decreases the full model diverges more from the isothermal model.

Next we plot the degree of conversion from Equation 22 for different ramp rates as shown in Figure 10, as well as the full isotherm value. From Figure 10 we find that as the ramp rate increases, the final degree of conversion begins to approach the isothermal value. This can be understood as the isothermal calculation essentially assumes an infinite ramp rate and cooling rate. This implies that the heating time and cooling time will increase the degree of conversion and that slower heating/cooling rates will have a larger impact on the degree of conversion.

Additionally, Figure 10 shows that there is an error associated with the degree of conversion when neglecting the heating rate and only assuming an isothermal profile. To better understand this error and how different experimental parameters affect it, we define the fractional error between the isothermal assumption and full model to be:

$$FE = \frac{\alpha_{Full} - \alpha_{iso}}{\alpha_{Full}} \quad (24)$$

where  $\alpha_{Full}$  is the degree of conversion calculated by the full model and  $\alpha_{iso}$  is the degree of conversion calculated using the isothermal assumption. Equation 24 essentially gives us a measure of how good, or poor, the isothermal assumption is. As an example, Figure 11 shows the degree of conversion for the isothermal assumption and the full model as a function of ramp rates and overlayed is the fractional error. From Figure 11 we see that as the ramp rate increases the fractional error decreases, which is consistent with the observations in Figure 10.

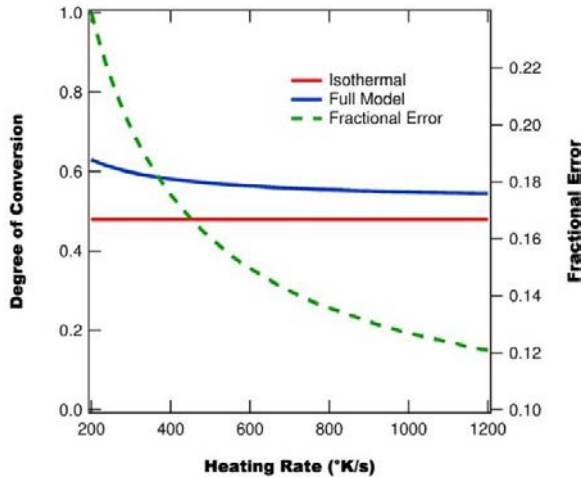


**Figure 11.** Degree of conversion and fractional error as a function of heating rate.

Furthermore, in Figure 12 we plot the fractional error as a function of ramp rates for different (a) isothermal times and (b) isothermal temperatures. From Figure 12 we find that for long times and high temperatures the fractional error is small. However, for short times, or lower temperatures the fractional error can be substantial, up to 82%.

From these results it is obvious that achieving the highest possible ramp rate is of utmost importance to obtain an accurate degree of conversion.

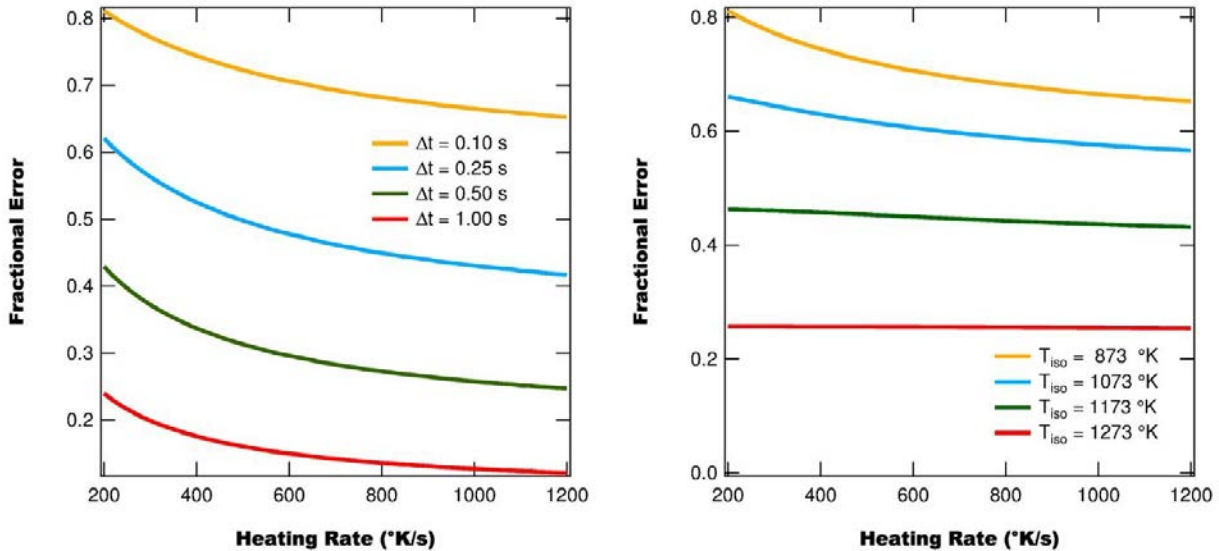


**Figure 12.** Fractional error as a function of heating rate for different (left) isothermal times and (right) isothermal temperature.

### Effect of Isothermal Time

In addition to considering the effect of the heating rate on the degree of conversion, we also consider how changing the isothermal time affects the degree of conversion and the fractional error due to the isothermal approximation. Figure 13 shows the degree of conversion for the full model and isothermal model, as well as the fractional error as a function of isothermal temperature for a heating rate of 200 °K/s and an isothermal time of 100 ms.

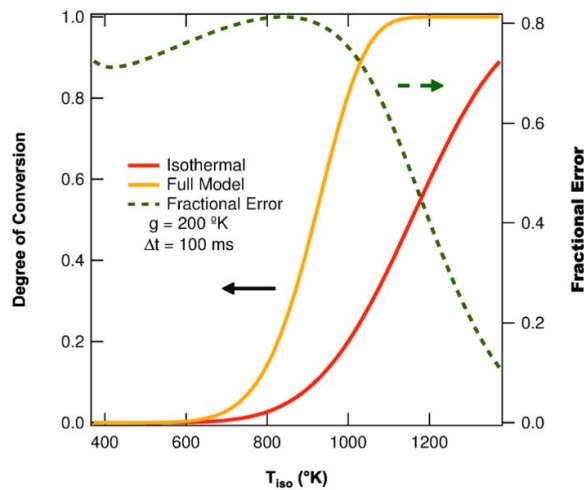


**Figure 13.** Degree of conversion and fractional error as a function of isothermal time for a heating rate of 200 °K/s and an isothermal time of 100 ms.

From Figure 13 we see that for low isothermal temperatures ( $T < 900$  °K) the fractional error is in between 0.7 and 0.8, but decreases rapidly as the temperature exceeds 900 °K. The fractional error remains above 0.1 until around 1300 °K, implying that for isothermal temperatures below 1300 °K the isothermal approximation is poor.

To more fully get a sense of the effect of the isothermal time we consider the fractional error as a function of isothermal temperature for different times and heating rates, as shown in Figure 14.

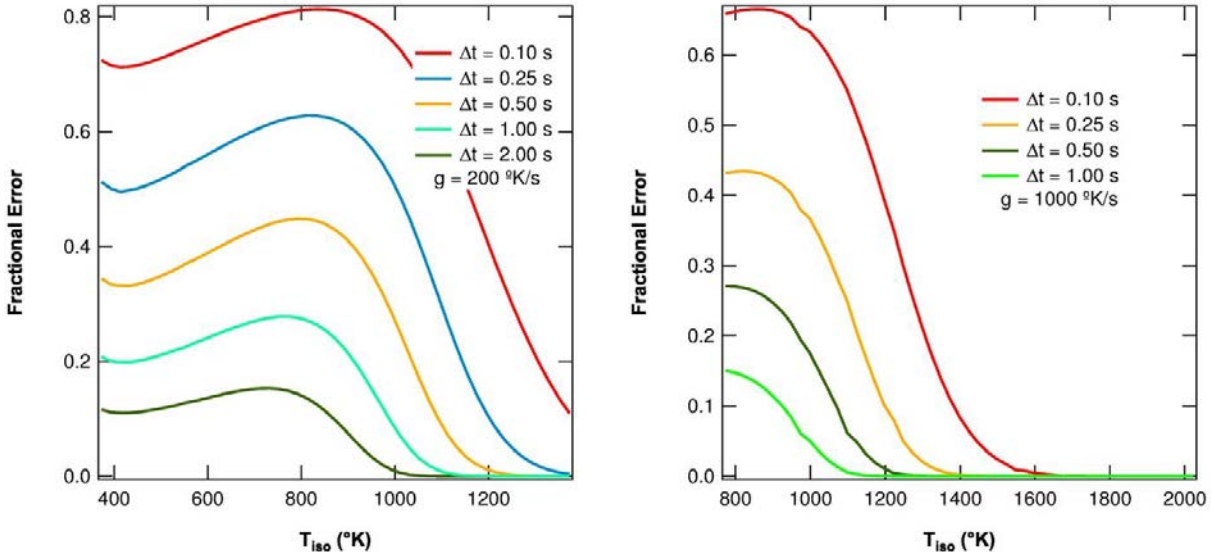


**Figure 14.** Fractional error as a function of isothermal temperature for different isothermal times,  $\Delta t$ , and two different heating rates. As the isothermal time decreases the fractional error increases.

### “Exact” Solution

For a temperature profile consisting of a linear ramp from  $T_0$  to  $T_{iso}$  at a rate  $g$ , followed by an isotherm of time  $\Delta t$  and concluding with an instantaneous cooling, we can solve Equation 19 exactly, albeit with special functions. We begin with Equation 22

$$\alpha(t) = 1 - \exp \left\{ -A \int_0^{t_1} \exp \left[ -\frac{E}{k(T_0 + gt')} \right] dt' - A \exp \left[ -\frac{E}{kT_{iso}} \right] \Delta t_{iso} \right\}. \quad (25)$$

where the integral in Equation is given by,

$$\begin{aligned} & \int_{t_0}^t \exp \left[ -\frac{E}{k(T_0 + gt')} \right] dt' \\ &= \frac{1}{kg} \left\{ k(T_0 + gt) \exp \left[ -\frac{E}{k(T_0 + gt)} \right] - Ei \left( \frac{1}{k(T_0 + gt)} \right) - kT_0 \exp \left[ -\frac{E}{kT_0} \right] + Ei \left( \frac{1}{kT_0} \right) \right\}, \\ &= \frac{1}{kg} \left\{ kT_{iso} \exp \left[ -\frac{E}{kT_{iso}} \right] - Ei \left( \frac{1}{kT_{iso}} \right) - kT_0 \exp \left[ -\frac{E}{kT_0} \right] + Ei \left( \frac{1}{kT_0} \right) \right\}. \end{aligned} \quad (26)$$

where the function  $Ei(x)$  is the exponential integral function.

$$\alpha(t) = 1 - \exp \left\{ -\frac{A}{kg} \left( kT_{iso} \exp \left[ -\frac{E}{kT_{iso}} \right] - Ei \left( \frac{-1}{kT_{iso}} \right) - kT_0 \exp \left[ -\frac{E}{kT_0} \right] + Ei \left( \frac{-1}{kT_0} \right) \right) - A \exp \left[ -\frac{E}{kT_{iso}} \right] \Delta t_{iso} \right\}. \quad (27)$$

## Explosion Temperature Profile

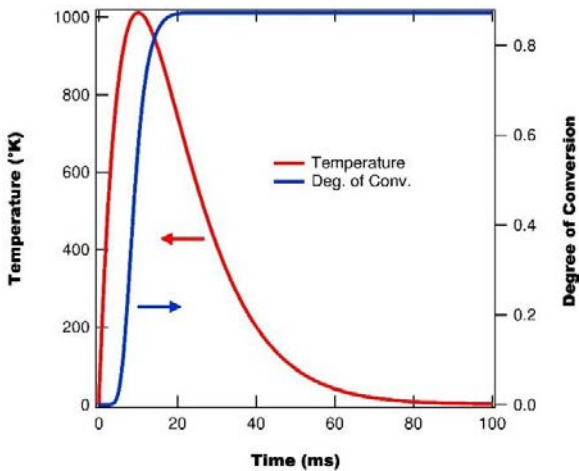


**Figure 15.** Temperature and degree of conversion during simulated explosion profile.

To simulate the degree of conversion as a function of time during an explosion, we assume an explosion temperature profile of,

$$T(t) = T_0 + t\Delta T e^{-t/\tau}, \quad (28)$$

Where  $T_0$  is the initial temperature,  $t$  is the time,  $\Delta T$  is an amplitude term, and  $\tau$  is a decay time. We also use the same  $A$  and  $E$  values used in the previous section. Figure 15 shows the temperature profile and degree of conversion as a function of time during the explosion. From Figure 15 we see that the majority of the change in the degree of conversion occurs during heating and slightly into the cool down.

## Temperature and Time for Isothermal Nucleation and Growth

The proposed goal for this project is to be able to extract a temperature and time from thermally induced changes in our samples. What this means precisely for an explosion is ambiguous as in explosion the temperature is constantly changing. However, for simplistic modeling purposes, we can assume an isothermal temperature-time profile with the temperature instantly becoming  $T_{iso}$  for a period of time  $\Delta t$ , after which it instantly cools back to ambient temperature. Assuming that we have two materials in our samples (with nucleation and growth parameters  $A_1, E_1$  and  $A_2, E_2$ ) we can write the isothermal degree of conversion for the two materials as:

$$\alpha_1(t) = 1 - \exp \left\{ -A_1 \exp \left[ -\frac{E_1}{kT_{iso}} \right] \Delta t \right\} \quad (29)$$

$$\alpha_2(t) = 1 - \exp \left\{ -A_2 \exp \left[ -\frac{E_2}{kT_{iso}} \right] \Delta t \right\} \quad (30)$$

Performing some simple algebra on Equations 29 and 30 we can eliminate the time dependence and determine the isothermal temperature in terms of the materials parameters and the measured degree of conversion, with the inverse isothermal temperature given by:

$$\frac{1}{T_{iso}} = \frac{k}{E_2 - E_1} \ln \left[ \frac{A_2 \ln(1 - \alpha_1)}{A_1 \ln(1 - \alpha_2)} \right]. \quad (31)$$

Finally, by substituting Equation 31 into Equation 29 and rearranging we can find the isothermal time as,

$$\Delta t = -\ln(1 - \alpha_1) A_1 \exp \left\{ \frac{E_1}{E_2 - E_1} \ln \left[ \frac{A_2 \ln(1 - \alpha_1)}{A_1 \ln(1 - \alpha_2)} \right] \right\}. \quad (32)$$

## Example Calculation

To better understand what happens when we apply the isothermal approximation to a non-isothermal temperature profile we start with the temperature profile given by

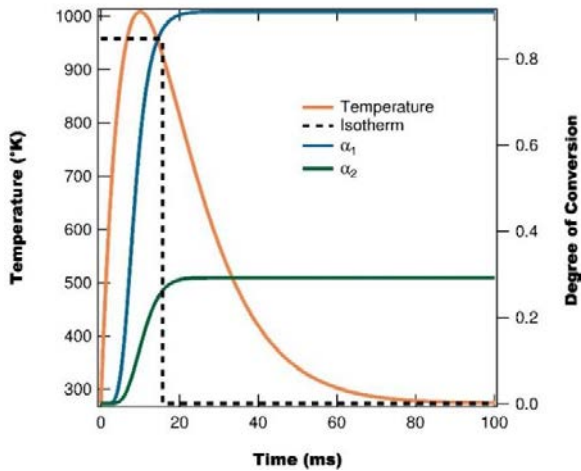


**Figure 16.** Temperature and degrees of conversion as a function of time for a temperature profile given by Equation 28.

Equation 28, with the parameters varied to give different peak temperatures and peak widths. We then calculate asymptotic values of  $\alpha_1$  and  $\alpha_2$  for the temperature profiles, from which we use Equations 31 and 32 to calculate the isothermal temperature and time. Figure 16 shows an example temperature,  $\alpha_1$ , and  $\alpha_2$  as a function of time, with the isothermal “pulse” overlayed to demonstrate the profile calculated by Equations 31 and 32. Note that the isothermal temperature slightly less than the peak and the isothermal time is about 65% the FWHM of the peak. We also perform these calculations for different peak temperatures and peak widths, with the results tabulated in Table 4.

**Table 4.** Calculated isothermal temperature and time for different explosion temperature profiles with different peak temperatures and peak widths. Also tabulated are the asymptotic values of  $\alpha_1$  and  $\alpha_2$  as calculated using Equation 23.

Peak T (°K)	FWHM (ms)	$\alpha_1$	$\alpha_2$	T <sub>iso</sub> (°K)	Δt (ms)
456.9	25.35	9.52E-05	1.20E-06	445.5	15.1
640.75	25.35	0.018114	0.000826	619.4	14.5
861	25.35	0.425829	0.055041	823.9	15.1
1008	25.35	0.90945	0.29236	957.7	15.7
1008	36.85	0.972596	0.404128	957.6	23.5
1008	48.95	0.9918	0.499249	957.8	31.4
1008	67	0.999254	0.645362	957.7	47.1
1008	95	0.99993	0.748766	959.0	61.8

From Table 4 we find that using the isothermal approximation leads to the calculated temperature being slightly less than the peak temperature (approx. 95%) and the isothermal time being approximately 65% the peak width.

## B. Isothermal Conversion Calculation

In the previous sections we considered different heating profiles and their effects on the degree of conversion. Additionally, we considered how the isothermal assumption compared to the results of the full model and found that they diverge for low temperatures and short isothermal times. These results suggest that a fast heating rate is necessary to accurately use isothermal temperature-time calibration curves. In this section we assume an essentially infinite heating rate and consider how temperature and time effect the degree of conversion, using the same model of nucleation as used above. We begin by considering a single phase system (similar to Eu:Y<sub>2</sub>O<sub>3</sub>), then a two-phase system (similar to Eu:ZrO<sub>2</sub>), and finally we use experimental data for Eu:ZrO<sub>2</sub> to determine the  $A$  and  $E$  constants and compute the nucleation model based on these parameters.

### Single Phase

For our single phase model we assume that only nucleation and growth occur with the descriptive differential equation given by Equation 20 with  $m = 0$ ,  $n = 1$ , and  $p = 0$ . The calculations are performed assuming a rate parameter of  $A = 10000$  and an energy barrier of  $E = 0.75$  eV. Figure 17 shows a two-dimensional mapping of the degree of conversion as a function of isothermal time and temperature. From Figure 17 we find that for low temperatures the degree of conversion is negligible, even at large isothermal times, and that as the temperature increases the time to full conversion shortens. To better demonstrate these effects we plot the degree of conversion as a function of temperature for different isothermal times in Figure 18 (a) and the degree of conversion as a function of isothermal time for different temperatures in Figure 18 (b). The degree of conversion is found to be exponential in time and a sigmoid function in temperature. From calculations using different values for  $A$  and  $E$ , we find that  $E$  determines the half-conversion temperature of the sigmoid function and  $A$  is the primary parameter for the rate constant when considering the isothermal time.

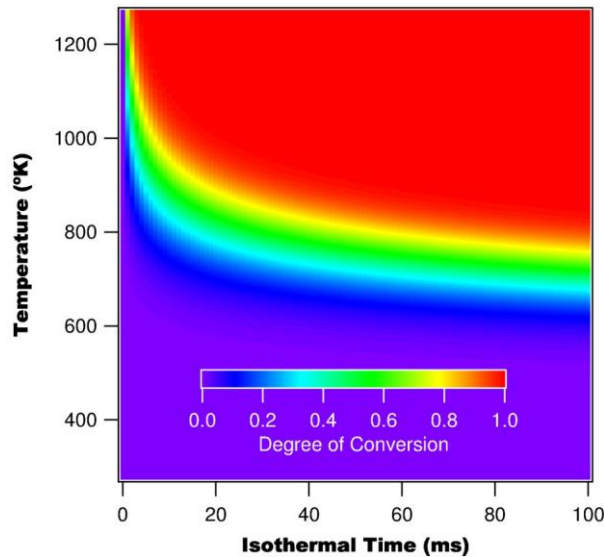


**Figure 17.** Two-dimensional mapping of the degree of conversion as a function of temperature and time.

Additionally from Figure 17 we find that there exists different combinations of temperature and time which produce the same degree of conversion. Rearranging Equation 23 we find that the iso-conversion curves to be defined by the relation:

$$\frac{\ln(\Delta t)}{T_{iso}} = -\frac{k}{E} \ln \left[ -\frac{1}{A} \ln(1 - \alpha) \right] \quad (33)$$

where  $\Delta t$  is the isothermal time and  $T_{iso}$  is the isothermal temperature.

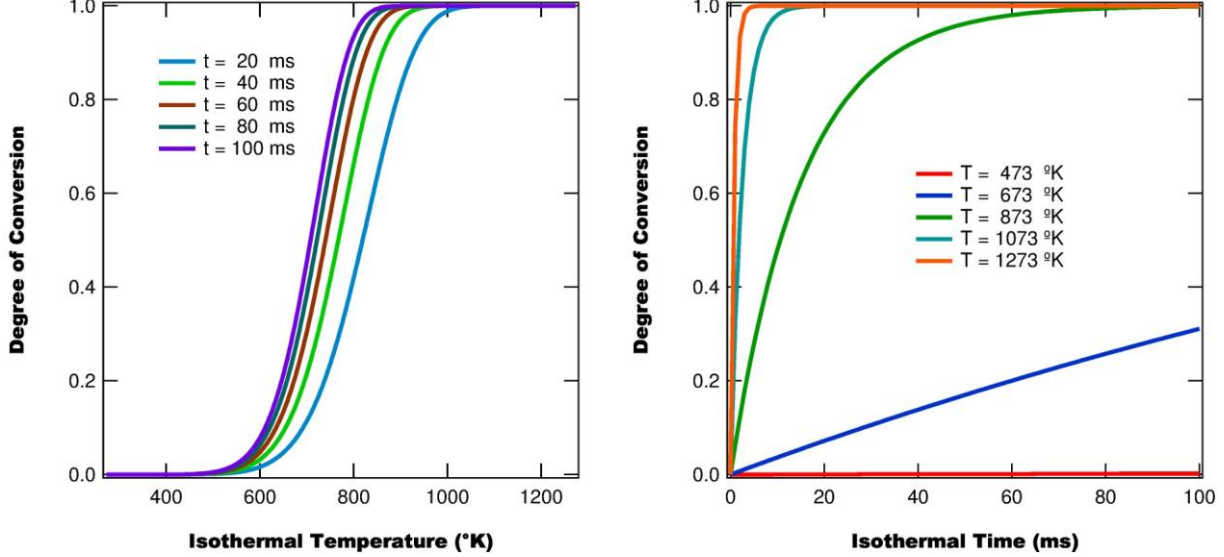


**Figure 18.** Degree of conversion as a function of (a) temperature and (b) time.

## Two-Phases

While  $\text{Y}_2\text{O}_3$  is known to only have the one crystalline phase,  $\text{ZrO}_2$  has two crystalline phases: tetragonal and monoclinic. From experiments we know that the Tetragonal phase forms first and only after the tetragonal phase is formed does the monoclinic phase form. Additionally, we know that for temperatures below approximately 400 °C the monoclinic phase doesn't form. Based on these facts and using the same nucleation model for both phases we can write a set of couple differential equations describing the fraction of material that is in the tetragonal phase  $\alpha_T$ , and in the monoclinic phase  $\alpha_M$ :

$$\frac{d\alpha_T}{dt} = A_T \exp \left\{ \frac{E_T}{kT(t)} \right\} [1 - \alpha_T(t) - \alpha_M(t)] \quad (34)$$

$$\frac{d\alpha_M}{dt} = \begin{cases} 0 & T < T_1 \\ A_M \exp \left\{ \frac{E_M}{kT(t)} \right\} \alpha_T(t), & T \geq T_1 \end{cases} \quad (35)$$

where  $T_1$  is the minimum temperature required for the formation of the monoclinic phase.

With Equations 34 and 35 we model the tetragonal and monoclinic fractions as a function of isothermal temperature and time. Figure 19 (a) shows a 2D mapping of the tetragonal fraction as a function of temperature and time, while Figure 19 (b) shows a 2D mapping of the monoclinic fraction as a function of temperature and time. From Figure 19 we find

that at low temperatures and times the tetragonal fraction plot is similar to the one phase model, but as the time and/or temperature increases the tetragonal fraction begins to decrease as the monoclinic fraction forms, eventually dominating the sample.

### Intensity Ratio

While we calculated the tetragonal and monoclinic fraction above, what we measure experimentally is the fluorescence intensity, and more specifically the ratio between peaks. In order to get a better sense of how the two phases affect the spectrum we calculate an estimated intensity ratio between the peak at 592 nm and 613 nm for Eu:ZrO<sub>2</sub>. We begin by calculating the experimental intensity ratio from fully amorphous ( $r_a = 0.22$ ), tetragonal ( $r_T = 0.5715$ ), and monoclinic ( $r_M = 0.0476$ ) Eu:ZrO<sub>2</sub>.

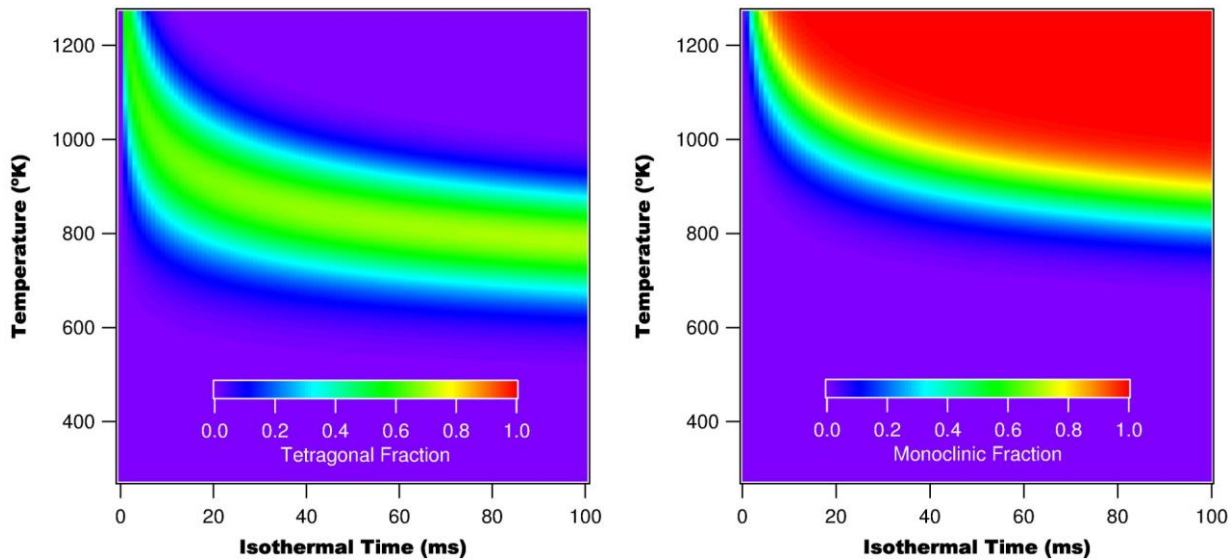


**Figure 19.** Two-dimensional mappings of the fraction of material in the (a) tetragonal phase and (b) monoclinic phase.

Using the experimental values and a simplistic model of the intensity ratios we can write the measured intensity ratio for a mixture of the three phases as

$$r_{mix} = (1 - \alpha_T - \alpha_M)r_a + \alpha_T r_T + \alpha_M r_M \quad (36)$$

With Equation 36 and the fractions computed in the previous section we determine the intensity ratio as a function of temperature and time, which is shown in Figure 21. As the material becomes more rich in the tetragonal phase the ratio between 592 nm and 613 nm grows, but then as the monoclinic phase begins growing the ratio rapidly decreases as the material becomes rich in the monoclinic phase, which is characterized by a large peak at 613 nm. To get a better sense of this functional form we plot the intensity ratio as a function of temperature at different isothermal times in Figure 22 (a), and as a function of isothermal time at different temperature in Figure 22 (b). From Figure 23 we find that the ratio as a function of temperature and time goes through an inflection point as the sample changes from being rich in the tetragonal phase to being rich in the monoclinic phase. The location of the inflection point depends on the isothermal time and temperature.

## Modeling with Experimentally Determined Parameters

Thus far we have performed phase change modeling using arbitrary values which are on the order of magnitude of those found in the literature. At this point we turn to looking at experimental data to determine estimates of the rate constant and energy barrier of Eu:ZrO<sub>2</sub>. To begin we set  $E=(0.131\pm 0.010)$  eV and  $A= 8.5(\pm 1.3) \times 10^{-2}$  ms<sup>-1</sup>. Figure 20 shows the normalized fluorescence spectra of amorphous, tetragonal, and monoclinic Eu:ZrO<sub>2</sub>. While all the spectra are dominated by the Eu<sup>3+</sup>  $^5D_0 \rightarrow ^7F_J$  transitions, there are clear differences in peak positions and relative peak intensities. When amorphous Eu:ZrO<sub>2</sub> is heated up, it first transforms into the tetragonal form and then into the monoclinic form for higher temperatures and longer heating times, see Figure 21.

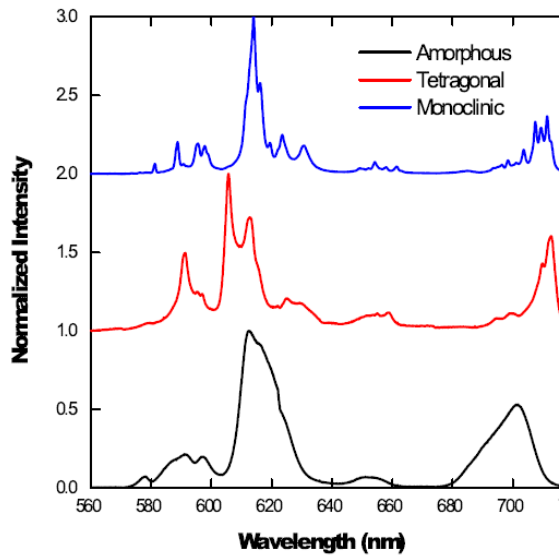


**Figure 20.** Normalized spectra of different phases of Eu:ZrO<sub>2</sub> using an excitation wavelength of 355 nm.

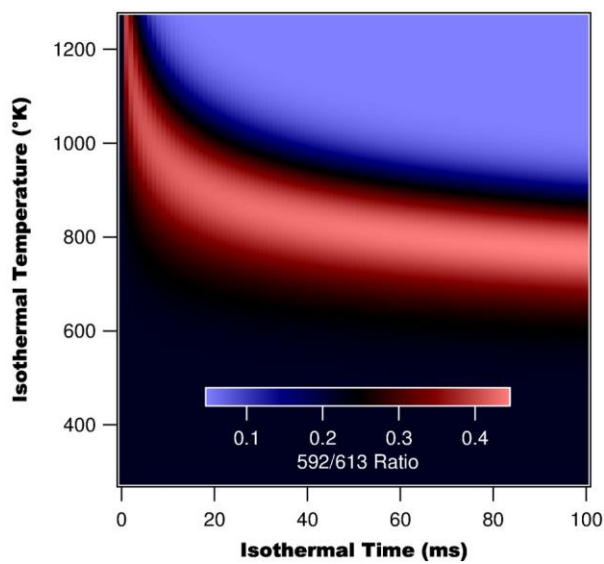


**Figure 21.** Two-dimensional mapping of the intensity ratio between 592 nm and 613 nm as a function of temperature and time. The red area corresponds to being rich in the tetragonal phase, while the blue area is rich in the monoclinic phase.

Figure 22 shows the calculated ratio between the two phases as a function of isothermal temperature for various heating times, and as a function of heating times for various isothermal temperatures. Initially, the ratio increases, indicating the increasing amount of the tetragonal phase. However, once the monoclinic phase starts to form, the ratio starts to decrease. Figure 23 shows the experimental intensity ratios as a function of isothermal temperature and isothermal heating time and fits to the data.

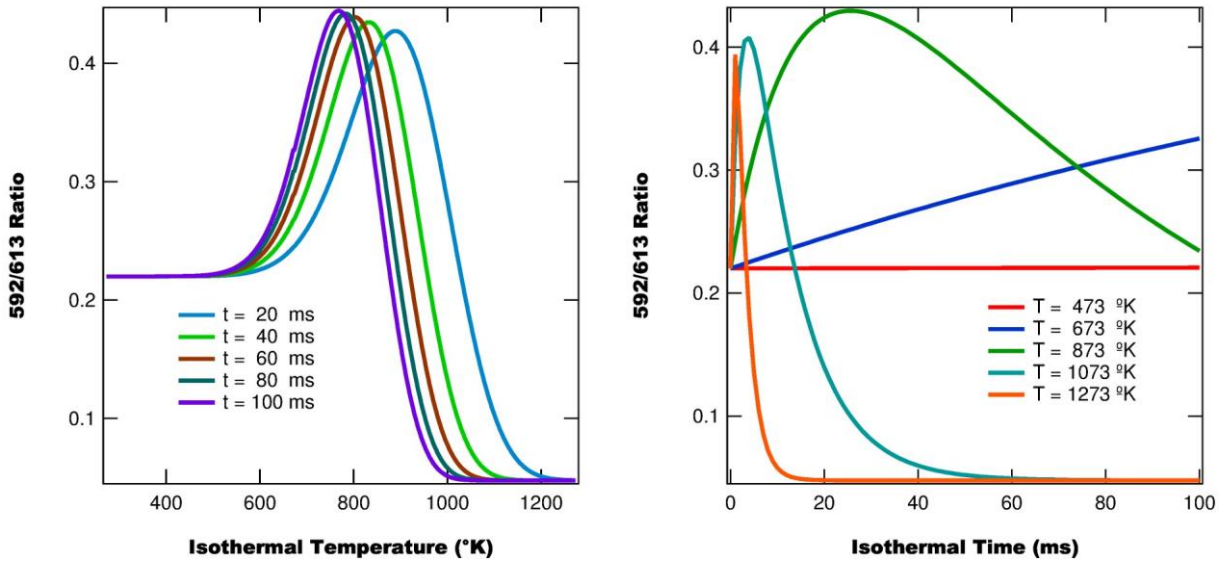


**Figure 22.**  $I_{592}/I_{613}$  ratio as a function of (a) temperature and (b) time. As the amorphous material changes into the tetragonal phase the ratio increases. Once the material begins to convert into the monoclinic phase the ratio begins to decrease.

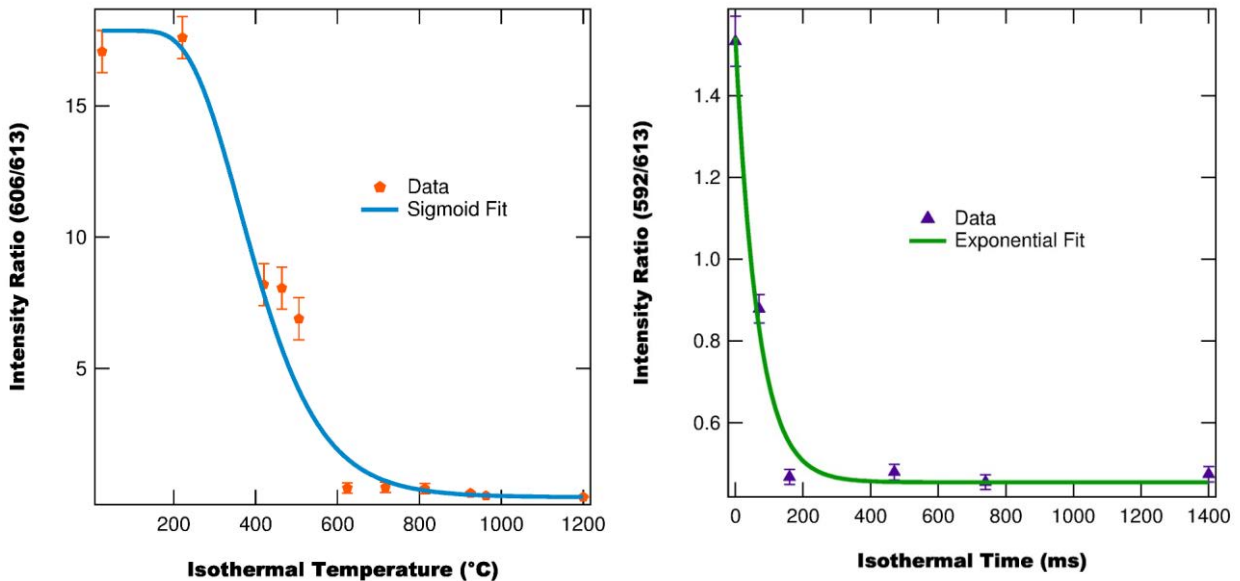


**Figure 23.** Intensity ratios as a function of isothermal temperature and time.

### C. Temperature Sensors

Initially, a variety of potential sensor materials consisting of individual and core/shell rare-earth-doped metal-oxides including precursors of Eu:Y<sub>2</sub>O<sub>3</sub>, Eu:Gd<sub>2</sub>O<sub>3</sub>, Eu:Y(GdO<sub>3</sub>, Er,Yb:Y<sub>2</sub>O<sub>3</sub>, Tm,Yb:Y<sub>2</sub>O<sub>3</sub>, SiO<sub>2</sub>/Eu:Y<sub>2</sub>O<sub>3</sub>, Eu:ZrO<sub>2</sub>, Yb<sub>2</sub>O<sub>3</sub>/Er:Y<sub>2</sub>O<sub>3</sub>, Er<sub>2</sub>O<sub>3</sub>/Yb:Y<sub>2</sub>O<sub>3</sub>, Eu:ZrO<sub>2</sub>/Er,Yb:Y<sub>2</sub>O<sub>3</sub>, and Tb:ZrO<sub>2</sub>/Eu:Y<sub>2</sub>O<sub>3</sub> were synthesized, characterized, and evaluated. It quickly became apparent that Eu:Y<sub>2</sub>O<sub>3</sub> and Eu:ZrO<sub>2</sub> were the most promising sensor materials as they showed the best sensitivity with respect to temperature-induced changes. As such, they will be described here in more detail.

#### **Eu:Y<sub>2</sub>O<sub>3</sub>**

##### Characterization of as-synthesized material

Precursor europium-doped yttria (p-Eu:Y<sub>2</sub>O<sub>3</sub>) is synthesized using co-precipitation, resulting in a white powder. The use of mixed precipitants, ammonium hydroxide and ammonium bicarbonate, leads to the formation of nanosized morphologies, see Figure 24 (a). Since the nanoparticles tend to aggregate, it is not possible to accurately measure the particle size. The particles have irregular shapes with dimensions in the 20 – 50 nm range. Nanoparticles prepared in this manner are known to favor the formation of de-agglomerable (soft agglomerate) oxide powders upon calcination <sup>6</sup>. X-ray diffraction measurements show that the as-prepared precipitate is amorphous, as seen from the broad halo curve in Figure 24 (b). It is worth noting that at a pH greater than 9.0, the nanosized particles are known to form two-dimensional microstructures. However, this formation was avoided in this work by keeping the pH at a lower value. According to Huang et al. <sup>7</sup>, at a lower pH the precipitate consists of Y<sub>2</sub>(CO<sub>3</sub>)<sub>3</sub>·nH<sub>2</sub>O, while at higher pH the Y<sub>2</sub>(CO<sub>3</sub>)<sub>3</sub>·nH<sub>2</sub>O species transform into Y(OH)CO<sub>3</sub>. The hydroxyl group in Y(OH)CO<sub>3</sub> is capable of forming oxo-bridges that lead to the formation of micron-sized aggregates. As they spontaneously assemble into micro-aggregates, the yttrium hydroxide nanoparticles tend to assemble more rapidly in the direction perpendicular to the resulting plane of two-dimensional micro-structures. Upon calcination, Y(OH)CO<sub>3</sub> powders form hard agglomerate <sup>7</sup>. However, because of the lower pH used, the likelihood for the presence of Y(OH)CO<sub>3</sub> in our samples is low.

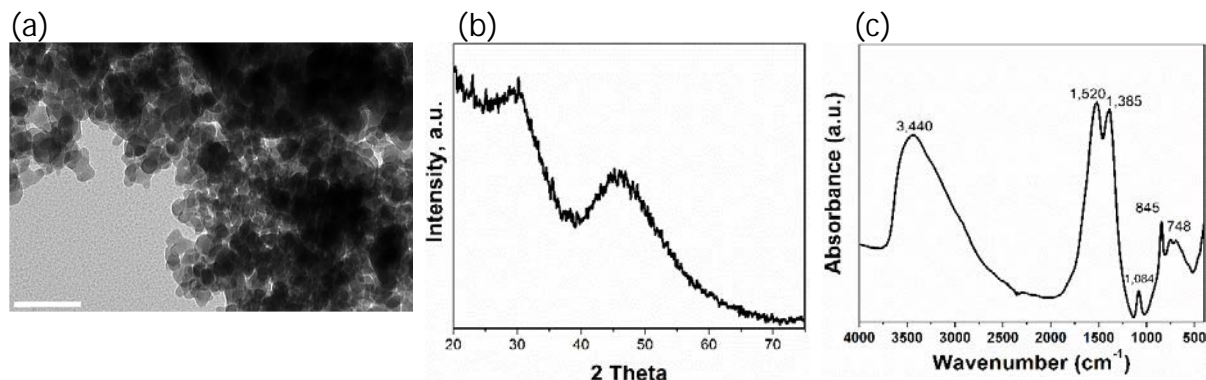


**Figure 24.** (a) TEM image (scale bar is 100 nm), (b) XRD spectrum, and (c) FT-IR spectrum of coprecipitated yttrium carbonate.

Figure 24 (c) shows the FT-IR spectrum of the amorphous precursor. The broad absorption peak at 3,440 cm<sup>-1</sup> is due to the O-H stretching mode, indicating the presence of hydroxide ions. The absorption peaks at 1,520 cm<sup>-1</sup> and 1,385 cm<sup>-1</sup> are due to the

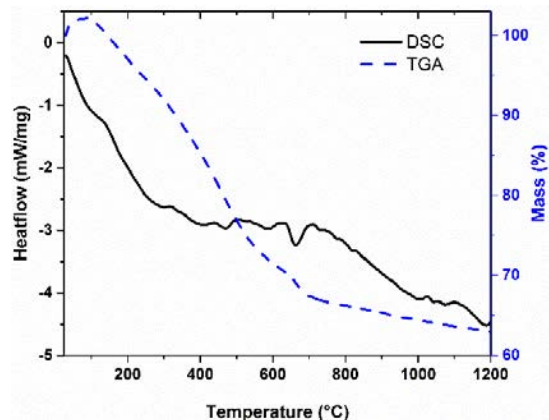
asymmetric stretching of C-O, and the absorption peaks at  $1,084\text{ cm}^{-1}$  and  $845\text{ cm}^{-1}$  are due to the symmetric and deformation vibration of C-O, respectively, indicating the presence of carbonate ions. The bands between  $800\text{ cm}^{-1}$  and  $650\text{ cm}^{-1}$  are due to the deformation of  $\text{CO}_3^{2-}$  and O-H<sup>-</sup>.

### **Characteristics of the heat-treated yttria precursor**

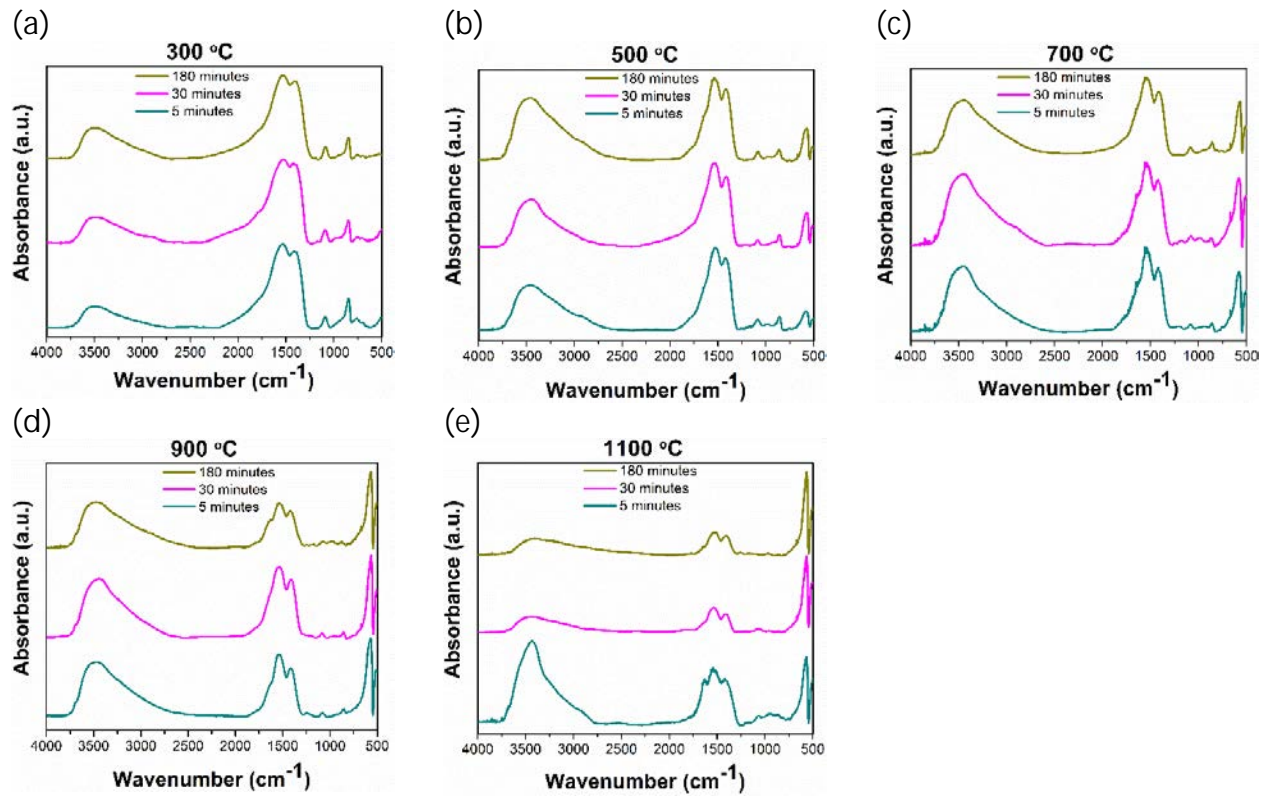
Between room temperature and  $700^\circ\text{C}$ , the TGA curve shows a continuous mass loss of up to about 33 wt%, see Figure 25. This large mass loss indicates that the yttria precursor

is indeed a carbonate rather than a pure hydroxide.<sup>8</sup> The DSC curve shows an exothermic transition that has been attributed to the formation of  $\text{Y}_2\text{O}_3$  following the decomposition of yttrium carbonate at  $665.7^\circ\text{C}$ .<sup>9</sup> Above this temperature, the rate of mass loss is significantly reduced, indicating an almost completed formation of the  $\text{Y}_2\text{O}_3$  phase. Due to prior drying (see section 2), no apparent endothermic transitions in the  $100$ - $150^\circ\text{C}$  range, corresponding to loss of water, were observed. The overall decomposition steps for yttrium carbonate precursors have been reported previously.<sup>7</sup> The decomposition begins with the loss of water, physisorbed, chemisorbed, and molecular water, followed by the release of  $\text{CO}_2$  resulting in  $\text{Y}_2\text{O}(\text{CO}_3)_2$ . Due to further release of  $\text{CO}_2$ ,  $\text{Y}_2\text{O}(\text{CO}_3)_2$  decomposes into  $\text{Y}_2\text{O}_2\text{CO}_3$ , which finally transforms into  $\text{Y}_2\text{O}_3$  under loss of  $\text{CO}_2$ . As such, the main expected decomposition processes (under release of  $\text{CO}_2$ ) is:  $\text{Y}_2(\text{CO}_3)_3 \rightarrow \text{Y}_2\text{O}(\text{CO}_3)_2 \rightarrow \text{Y}_2\text{O}_2\text{CO}_3 \rightarrow \text{Y}_2\text{O}_3$ .

The initial formation of  $\text{Y}_2\text{O}_3$  is corroborated by the appearance of an FT-IR absorption peak at  $570\text{ cm}^{-1}$ , which is indicative of Y-O bonds, see Figure 26 (a)-(e). The earliest appearances of the Y-O bond can be seen for heating to  $500^\circ\text{C}$  for 5 minutes, see Figure 3 (b). The continuous loss of water and decomposition towards the formation of  $\text{Y}_2\text{O}_3$  is apparent by the relative increase in intensity of the Y-O peak at  $570\text{ cm}^{-1}$  compared to the O-H and C-O peaks. However, some remnants of the peaks corresponding to C-O and O-H bonds are still visible even after furnace heating to  $1100^\circ\text{C}$  for 180 minutes. These peaks are due to surface hydroxyl and carbonate groups that form when  $\text{Y}_2\text{O}_3$  reacts with ambient water and carbon dioxide, respectively.<sup>10</sup>

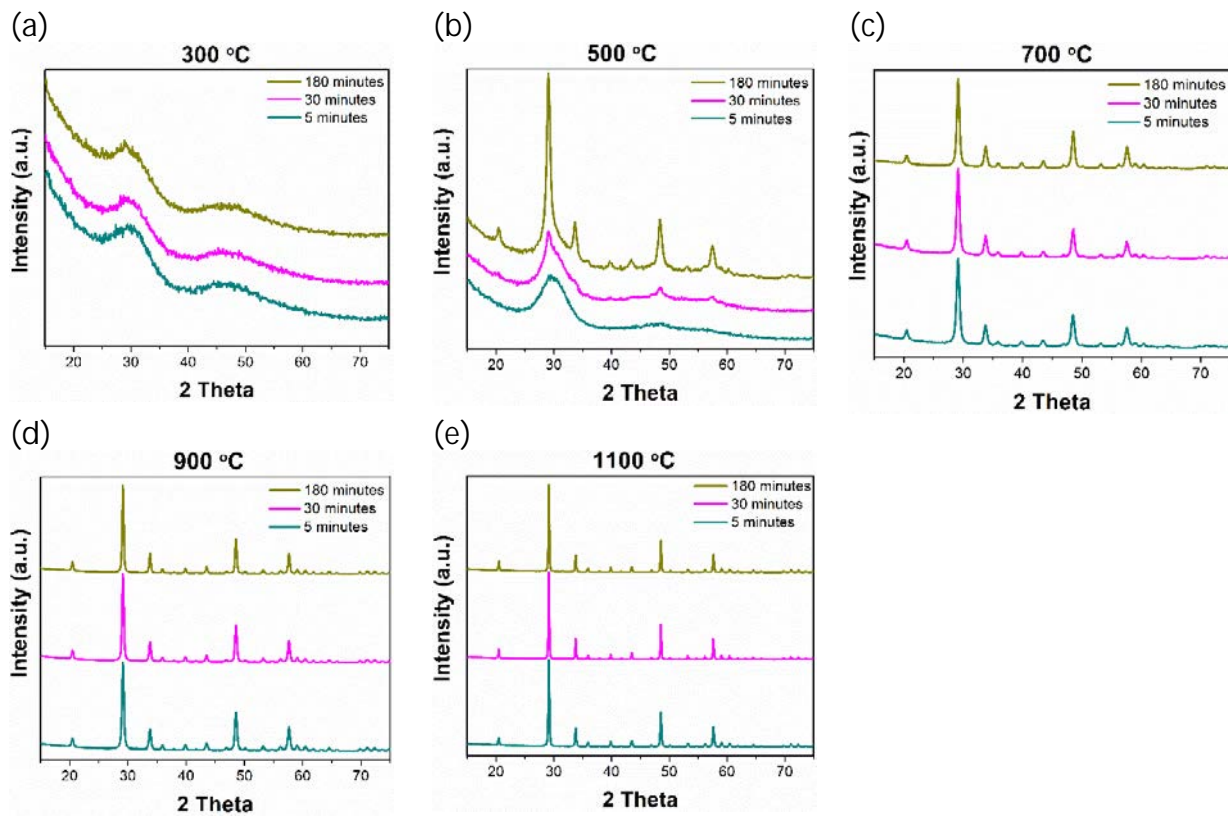


**Figure 25.** DSC and TGA curves of the co-precipitated carbonates.



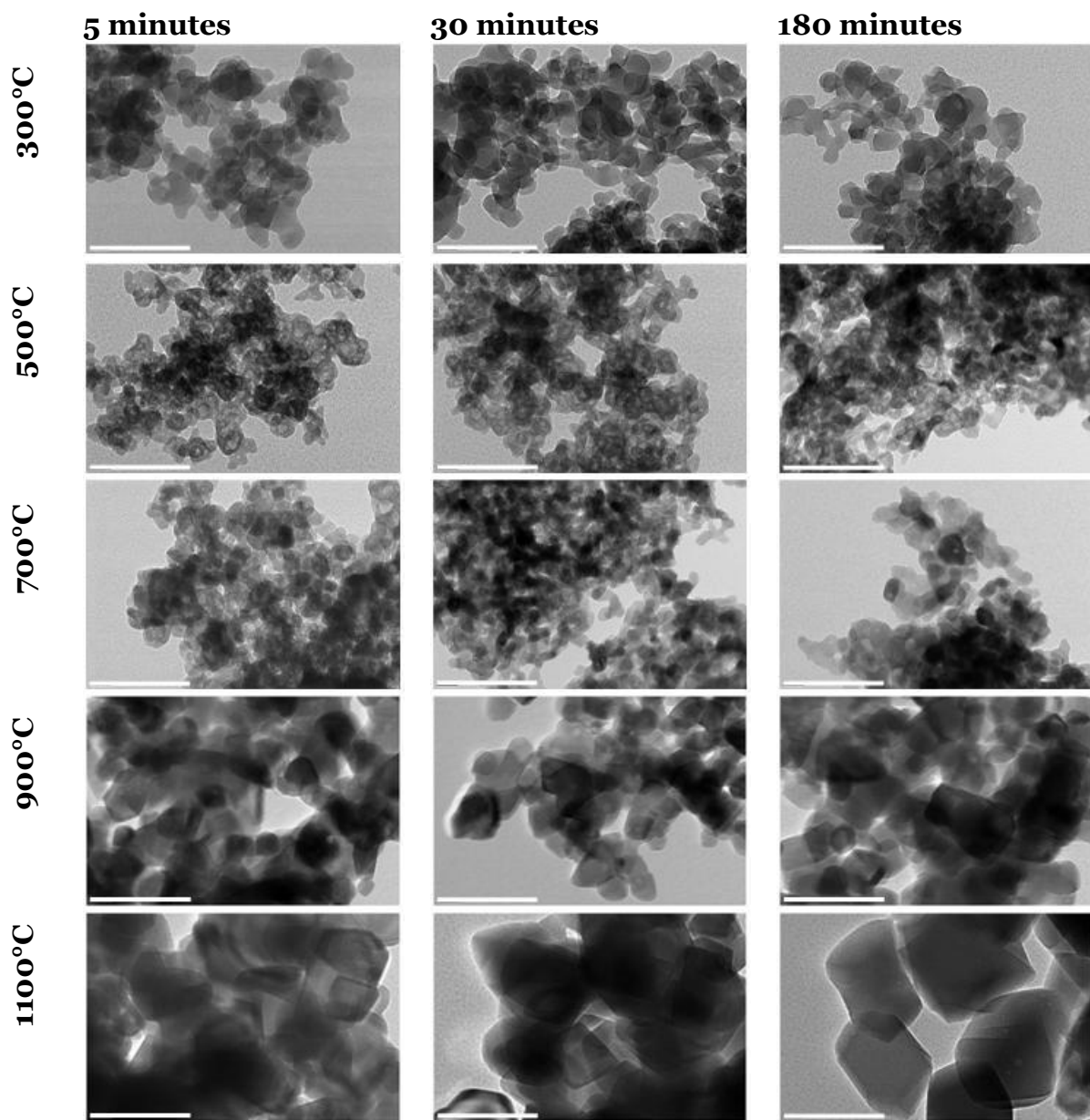
**Figure 26.** FT-IR spectra of co-precipitated yttria precursors heat-treated at 300°C, 500°C, 700°C, 900°C, and 1100°C for dwell times of 5 minutes, 30 minutes, and 180 minutes.

Figure 27 shows XRD spectra of yttria precursors heat-treated at various temperatures and dwell times. Figure 27 (a) shows that at 300°C the matrix remains amorphous even for dwell times of 180 minutes. The influence of dwell time on the crystal quality is best demonstrated in Figure 27 (b). As the dwell time increases at 500°C, the peaks become narrower, indicating the formation of crystalline cubic Y<sub>2</sub>O<sub>3</sub>. The three highest intensity x-ray diffraction peaks, matching the crystalline cubic Y<sub>2</sub>O<sub>3</sub> phase (JCPDS# 98-010-7439) **at  $2\theta = 29.1^\circ$ ,  $48.5^\circ$ , and  $57.6^\circ$ , start to appear for the sample heated to 500°C for 30 minutes.** The presence of the cubic crystalline phase of Y<sub>2</sub>O<sub>3</sub> is apparent in the spectra of samples heated to 700°C and above, see Figure 27 (c)-(e). Since Y<sub>2</sub>O<sub>2</sub>CO<sub>3</sub> is thermally stable only up to 470°C, the crystalline peaks seen for heating to 500°C for 30 minutes are likely to correspond to Y<sub>2</sub>O<sub>3</sub>.<sup>11</sup> After a dwell time of 180 minutes the peaks can be unambiguously matched to the cubic Y<sub>2</sub>O<sub>3</sub> phase.



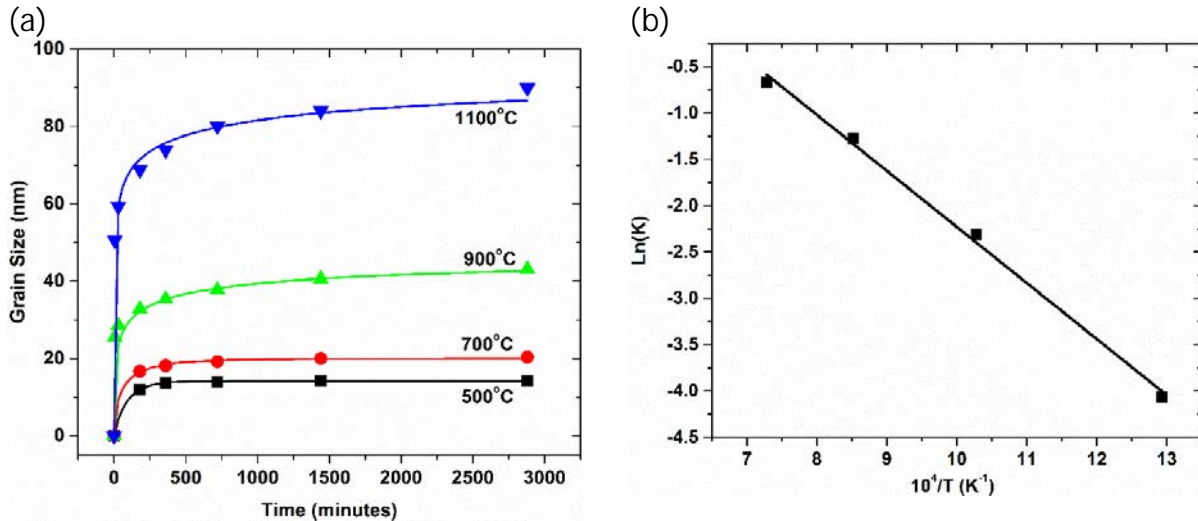
**Figure 27.** XRD patterns of co-precipitated yttria precursors heat-treated at 300°C, 500°C, 700°C, 900°C, and 1100°C for dwell times of 5 minutes, 30 minutes, and 180 minutes.

Figure 28 shows the TEM images of the heated samples. The images show that the samples heated to 500°C have a perforated appearance, which may be attributed to the carbonate decomposition resulting in the release of carbon dioxide. This decomposition results in smaller particle sizes for samples heated to 700°C for dwell times of 5 minutes, 30 minutes, and 180 minutes. Above 700°C, these crystalline particles grow in size with increasing temperature — up to 70 – 80 nm in diameter for heating to 1100°C for 180 minutes. The particle size of this sample, as determined from the TEM image is comparable to the grain size determined from the XRD spectrum, indicating complete crystallization. These particles have polyhedral geometry and are loosely agglomerated.



**Figure 28.** TEM images of co-precipitated carbonates, heat-treated at various temperatures and dwell times. Scale bar is 100 nm.

Figure 29 (a) shows the grain size (determined from XRD data) vs. dwell time for various heating temperatures. The trend in the crystalline growth is characteristic for nanosized particles.<sup>12</sup> Initially, the grains grow rapidly within a short period of annealing time. This period is followed by a period of substantially slower growth rate, and finally a period in which the growth levels off. During the last stage, the grain size approaches its limiting grain size for a given temperature. No crystalline domain is observed at 300°C. At all higher temperatures, the grain growth slows down considerably after about two hours.



**Figure 29.** (a) Grain size vs. dwell times for yttrium carbonates, heat-treated at various temperatures and dwell times. (b) Plot of  $\ln(K)$  versus  $1/T$  ( $K^{-1}$ ).

Fitting of the above data using the conventional grain growth equation:<sup>12</sup>

$$D^n - D_0^n = Kt \quad (37)$$

with  $D$  being the average grain size after annealing,  $D_0$  being the initial grain size,  $n$  being the grain growth exponent,  $t$  being the annealing time, and  $K$  being a constant proportional to  $\exp(-Q/RT)$  with  $Q$  being the activation energy,  $R$  being the gas constant, and  $T$  being the calcination temperature, yielded different values for the grain growth exponent  $n$  for the various calcinations temperatures.

Fitting our data to a structural relaxation equation yielded more consistent results<sup>12</sup>. While all data points for the 900 and 1100°C isothermals could be fitted to this equation, for the 500 and 700°C isothermals the data points for dwell times of 5 minutes and 30 minutes could not be fitted and were left out. It may be that a different process occurs for the shorter dwell times at lower temperatures. The relaxation equation:

$$\frac{D - D_0}{D_m - D_0} = 1 - e^{-Kt^m} \quad (38)$$

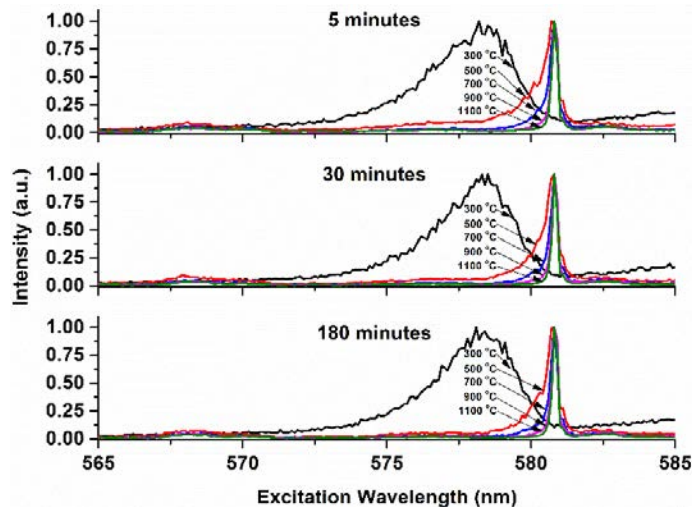
with  $D$  being the grain size,  $D_0$  being the initial grain size,  $D_m$  being the limiting grain size,  $t$  being the annealing time,  $m$  being the relaxation order ( $=1$  for linear relaxation), and  $K$  being the rate constant proportional to  $\exp(-Q/RT)$  with  $Q$  being the activation energy,  $R$  being the gas constant, and  $T$  being the calcination temperature, describes crystalline **growth due to gradual ordering of the bond lengths and bond angles at the nanoparticles' interface**<sup>12</sup>. This model has been successfully used to describe isothermal growth of sol-gel synthesized nanoparticles. Figure 29 (b) shows the plot of the log of the rate constant vs. inverse temperature. Fitting of this data set provides the activation energy for the grain growth process. Table 5 shows the fitted parameters for each temperature. The fitted activation energy of 50.3 KJ/mol is on par with values reported in the literature for nanosized particles.<sup>12</sup>

**Table 5.** Fitting parameters for relaxation equation.

Temperature (°C)	K	D <sub>m</sub>	m	X <sup>2</sup>
500	0.017	14.1	0.90	0.009
700	0.099	20.0	0.55	0.075
900	0.280	46.0	0.28	0.033
1100	0.509	98.0	0.18	4.32

### Optical properties

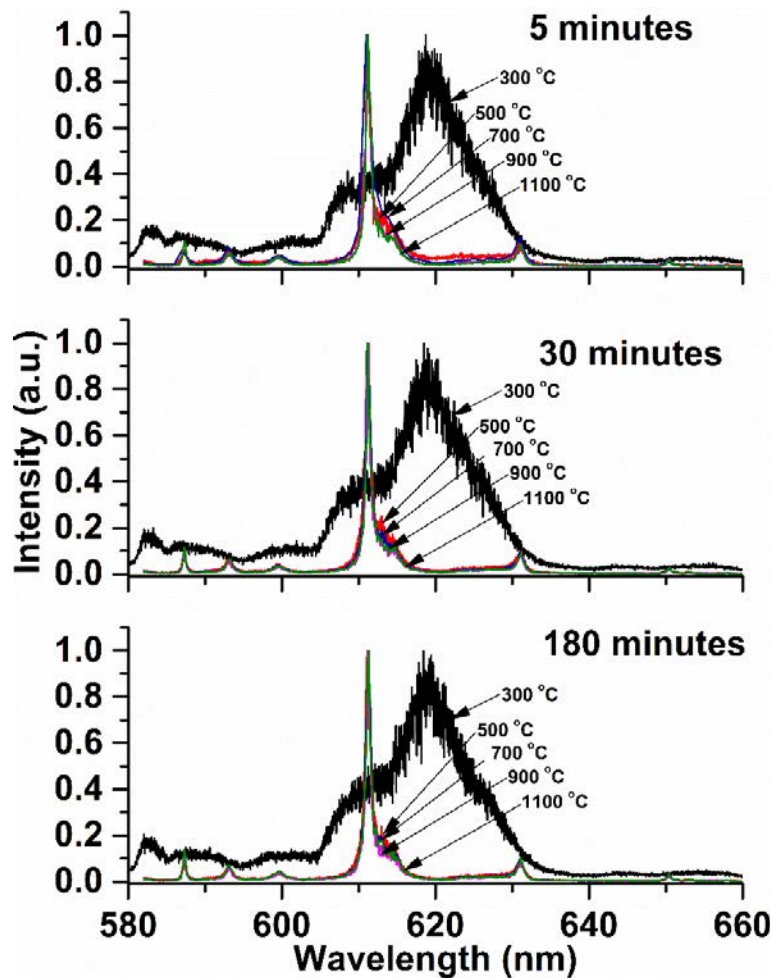
Eu<sup>3+</sup> dopants can be used to monitor the structural properties of their host and to gain information about how these properties change in response to stimuli.<sup>13</sup> For example, if the europium ion is located in a site with inversion symmetry, electric dipole transitions are forbidden.<sup>14, 15</sup> As the site symmetry is lowered, electric dipole transitions become allowed and the optical spectra change from being dominated by magnetic dipole transitions to being dominated by electric dipole transitions. Also, when the host is amorphous, a variety of sites are available for the europium ions, leading to inhomogeneous broadening of the optical spectra. As the material changes from an amorphous phase to a crystalline phase, the spectra become narrower, indicating the more homogeneous nature of the host material.



**Figure 30.** Excitation spectra of Eu-doped samples calcined at various temperatures for 5 minutes (top), 30 minutes (middle), and 180 minutes (bottom), observed at 611 nm.

Figure 30 shows the excitation spectra of europium-doped nanoparticles, monitored at 611 nm and heated to various temperatures (300°C, 500°C, 700°C, 900°C, and 1100°C) for dwell times of 5 minutes, 30 minutes, and 180 minutes. The excitation spectra of the samples heated to 300°C for all dwell times show a broad peak centered at about 578.3 nm. As the temperature increases, this broad peak decreases rapidly and instead, a sharp peak centered at about 580.8 nm (<sup>7</sup>F<sub>0</sub> → <sup>5</sup>D<sub>0</sub>) and some weak double peaks at about 568 nm and 570 nm appear. The broad excitation peak centered at about 578.5 nm disappears

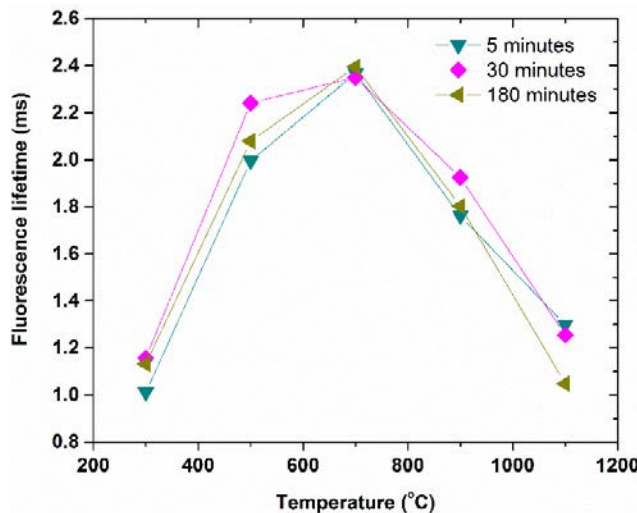
with increasing temperature. This disappearance is due to the decomposition of the amorphous yttrium carbonate phase. As seen in Figure 30, the full-width-half-max (FWHM) of the narrow peak at 580.8 nm, representing the formation of the crystalline  $\text{Y}_2\text{O}_3$  phase, continues to decrease with increasing temperature.<sup>16</sup> No obvious distinctions are apparent in the excitation spectra of samples heated for different dwell times.



**Figure 31.** Fluorescence spectra of Eu-doped samples calcined at various temperatures for 5 minutes, 30 minutes, and 180 minutes, and excited within excitation-peaks observed in Figure 30.

The fluorescence spectra of the samples heated to 300°C, 500°C, 700°C, 900°C, and 1100°C for dwell times of 5 minutes, 30 minutes, and 180 minutes are shown in Figure 31. The samples heated to 300°C were excited at 577 nm, in the broad excitation peak for the amorphous phase. This excitation resulted in broad emission lines centered at about 620 nm. The samples heated to 500°C, 700°C, 900°C, and 1100°C were excited at 580.8 nm, leading to emission centered at about 611 nm, typical for crystalline  $\text{Y}_2\text{O}_3:\text{Eu}$ . The peaks between 585 nm and 605 nm are due to the  ${}^5\text{D}_0 \rightarrow {}^7\text{F}_1$  transition, the peaks between 610 nm and 635 nm are due to the  ${}^5\text{D}_0 \rightarrow {}^7\text{F}_2$  transition, and the peaks around 650 nm are due to the  ${}^5\text{D}_0 \rightarrow {}^7\text{F}_3$  transition.<sup>17</sup> While the FWHM of the excitation peak of the crystalline  $\text{Y}_2\text{O}_3$  phase continues to decrease with temperature, the FWHM of the  ${}^5\text{D}_0 \rightarrow {}^7\text{F}_2$  fluorescence of the crystalline  $\text{Y}_2\text{O}_3$  phase does not show any apparent decrease. This

difference is due to the fact that for the excitation spectra, monitored at 611 nm, the amorphous phase and the crystalline phase both emit, but the amorphous phase disappears with increasing temperature, reducing the FWHM. For the fluorescence spectra however, 580.8 nm excites only the crystalline phase and not the amorphous phase. Similar to the excitation spectra, no obvious distinctions are apparent in the fluorescence spectra of samples heated for different dwell times.



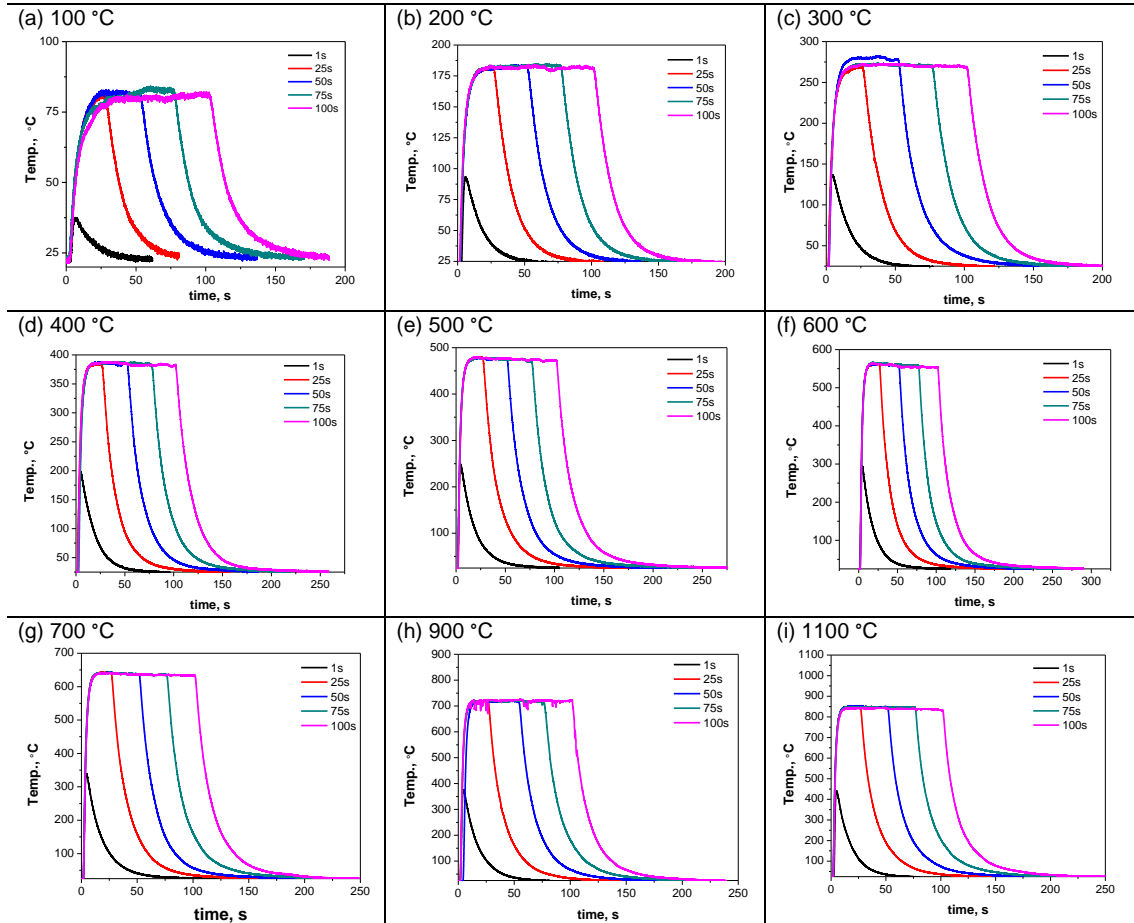
**Figure 32.** Fluorescence lifetime of Eu-doped samples, heat treated at various temperatures and dwell times.

Figure 32 shows the fluorescence lifetimes of the various europium-doped samples. In each case, a single exponential was used to fit the data. The traces for the three furnace-heated samples (5 minutes, 30 minutes, and 180 minutes) are very close to each other. Samples heated to low temperatures start out at about 1-1.2 ms. As the temperature of the samples is increased, the fluorescence lifetime increases and reaches a maximum of about 2.4 ms at 700°C. Samples heated to higher temperatures show a decrease in fluorescence lifetime. As already seen before, the samples undergo a phase transition at around 665°C and convert into a crystalline cubic oxide phase. As more and more of the sample material undergoes this transition, the fluorescence lifetime settles at a value of about 1.2 ms, which is typical for cubic Eu:Y<sub>2</sub>O<sub>3</sub>. The fluorescence lifetimes observed at lower temperatures reflect the various decomposition products present in the material. The dwell time at each temperature setting does not appear to affect the fluorescence lifetime very much.

### Pyroprobe-heated Y<sub>2</sub>O<sub>3</sub>:Eu

In the lab, samples were heated via a CDS Analytical Pyroprobe 1000. The nanopowders were placed in a quartz tube, which was sealed at both ends. Subsequently, the quartz tube was placed inside a coil heater and heated to various temperatures and dwell times using a ramp rate of 20000°C/s. However, these setting are based upon heating of the coil heater, not the material inside the quartz tube. Reference measurements were performed using a thermocouple placed inside the quartz tube. Figure 33 shows the results.

As can be seen from the data in Figure 10, for short heating times of 1 s, the maximum temperature reached was less than 50% of the set temperature, while for longer heating times, the maximum temperature is 10-25% below the set temperature. Also, the observed ramp rate is significantly slower than the set ramp rate. For the further analysis, the measured temperatures were used.



**Figure 33.** Reference measurements of the pyroprobe heater.

Figure 34 shows a TEM image of the co-precipitated and dried precursor. The particles are about 20 – 50 nm in diameter and appear to be agglomerated. Calcination of this precursor is known to lead to the formation of  $\text{Y}_2\text{O}_3:\text{Eu}$  powders characterized by soft agglomeration.<sup>6</sup> Figure 35 shows the DSC and TGA curves of the precursor. Between room temperature and 700°C, the TGA curve shows a continuous mass loss of up to about 33 wt%. This large mass loss indicates that the yttria precursor is indeed a carbonate rather than a pure hydroxide.<sup>8</sup> According to Zhuang et al.,<sup>7</sup> the precipitate is expected to consist of  $\text{Y}_2(\text{CO}_3)_3 \cdot n\text{H}_2\text{O}$ . The DSC curve shows an exothermic transition at 665.7°C, which has been attributed to the formation of crystalline  $\text{Y}_2\text{O}_3$  following the decomposition of yttrium carbonate.<sup>9</sup> Above this temperature, the rate of mass loss is significantly reduced, indicating an almost completed formation of the  $\text{Y}_2\text{O}_3$  phase. Because of prior drying (see section 2), no apparent endothermic transitions in the 100-150°C range, corresponding to loss of water, are observed.

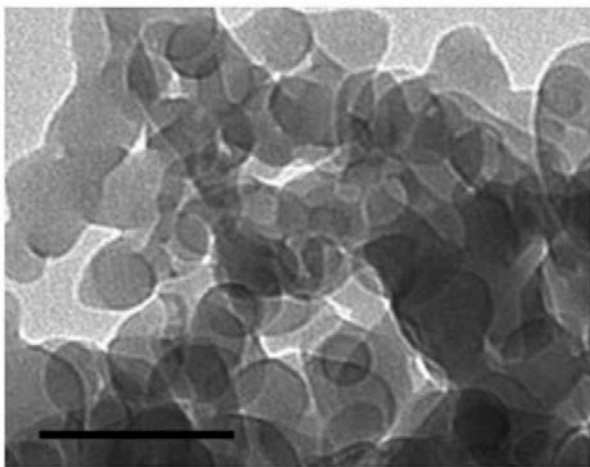


**Figure 34.** TEM image of co-precipitated precursor. Scale bar = 50 nm.

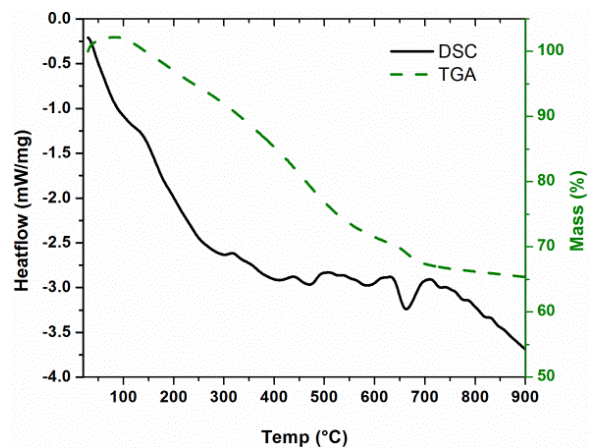
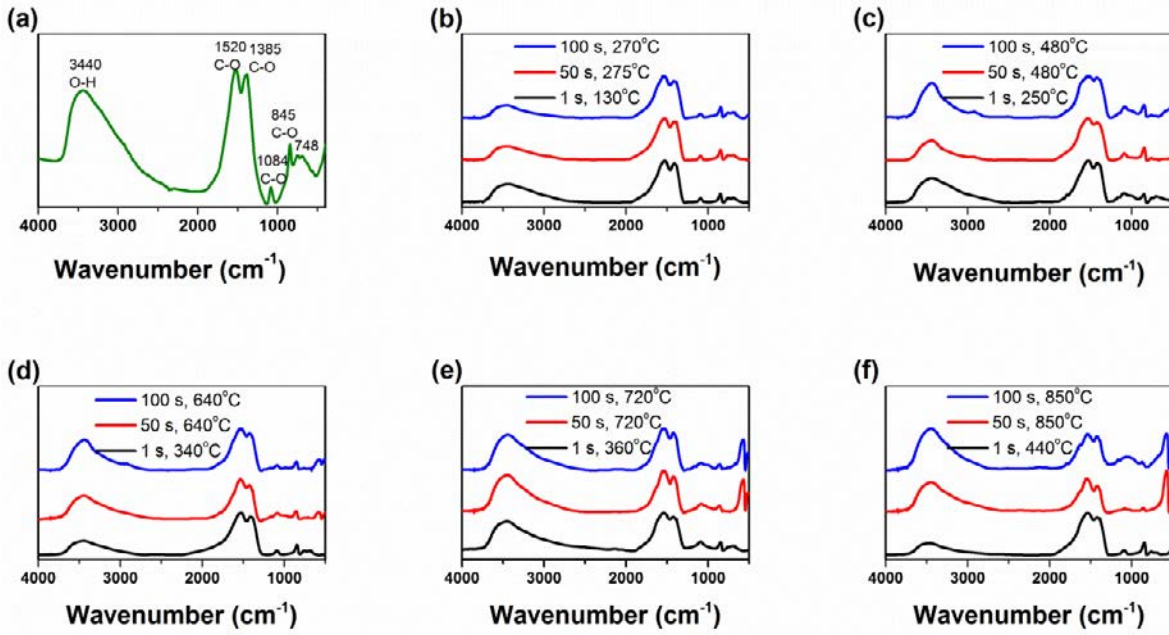


**Figure 35.** DSC and TGA curves of the co-precipitated carbonates.

The overall decomposition steps have been reported for yttrium carbonate precursors.<sup>7</sup> The decomposition begins with the loss of water, physisorbed, chemisorbed, and molecular water, followed by the release of CO<sub>2</sub> resulting in Y<sub>2</sub>O(CO<sub>3</sub>)<sub>2</sub>. Due to further release of CO<sub>2</sub>, Y<sub>2</sub>O(CO<sub>3</sub>)<sub>2</sub> decomposes into Y<sub>2</sub>O<sub>2</sub>CO<sub>3</sub>, which finally transforms into Y<sub>2</sub>O<sub>3</sub> under further loss of CO<sub>2</sub>. As such, the main expected decomposition process (under release of CO<sub>2</sub>) is: Y<sub>2</sub>(CO<sub>3</sub>)<sub>3</sub> → Y<sub>2</sub>O(CO<sub>3</sub>)<sub>2</sub> → Y<sub>2</sub>O<sub>2</sub>CO<sub>3</sub> → Y<sub>2</sub>O<sub>3</sub>. According to Husslein, Y<sub>2</sub>(CO<sub>3</sub>)<sub>3</sub> transforms into Y<sub>2</sub>O(CO<sub>3</sub>)<sub>2</sub> and Y<sub>2</sub>O<sub>2</sub>CO<sub>3</sub> at 375°C and 400°C, respectively.<sup>18</sup>

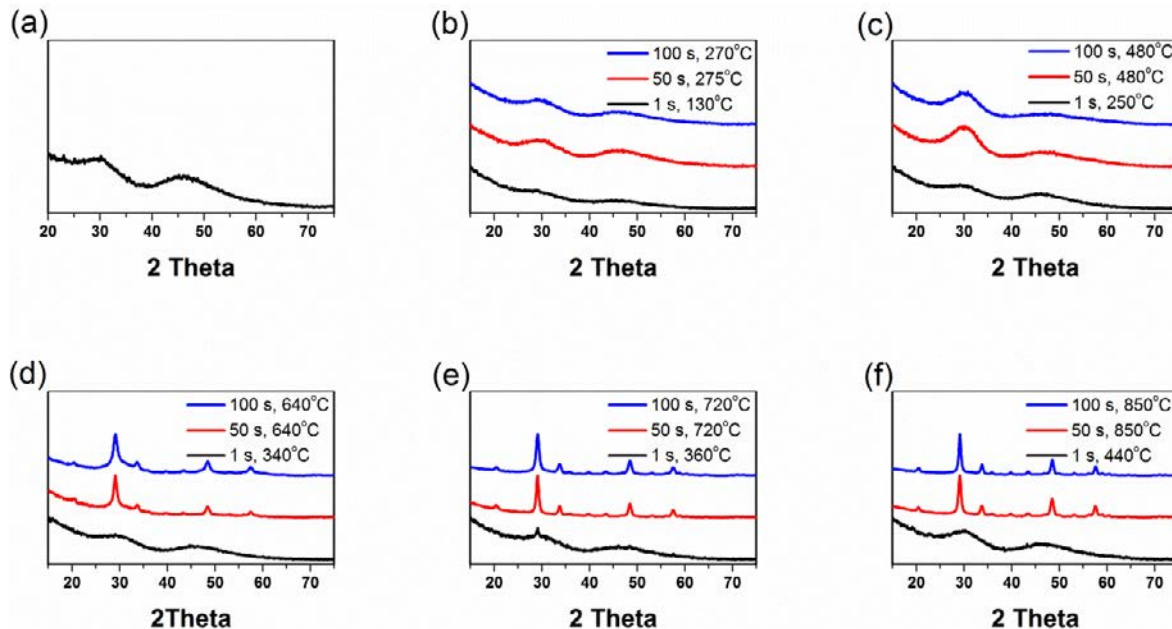
Figure 36 shows the FT-IR spectra of the precursor and samples heated to various temperatures for dwell times of 1 s, 50 s, and 100 s. The precursor spectrum, shown in Figure 36 (a), is consistent with the presence of hydroxyl and carbonate groups. The O-H stretching mode is responsible for the broad peak at 3440 cm<sup>-1</sup> and the asymmetric stretching of C-O is responsible for the peaks at 1520 cm<sup>-1</sup> and 1385 cm<sup>-1</sup>. The C-O symmetric and deformation vibrations absorb at 1084 cm<sup>-1</sup> and 845 cm<sup>-1</sup>. Absorption peaks between 800 cm<sup>-1</sup> and 650 cm<sup>-1</sup> are due to deformation vibrations of CO<sub>3</sub><sup>2-</sup> and OH<sup>-</sup>.

Figure 36 (b)-(f) show the FT-IR spectra of the precursor after it has been heated for dwell times of 1 s, 50 s, and 100 s to various temperatures. All spectra indicate the presence of hydroxyl and carbonate groups, which form at the surface when the material reacts with ambient water and carbon dioxide. The presence of Y-O (570 cm<sup>-1</sup>) shows in the spectra of samples heated for 50 s and 100 s to 720°C and 850°C. This observation is consistent with the DSC measurement indicating the formation of Y<sub>2</sub>O<sub>3</sub> at about 665°C.



**Figure 36.** FT-IR spectra of (a) precursor and (b)-(f) precursor heated to various temperatures for 1 s, 50 s, and 100 s.

Figure 37 shows the XRD spectra of the precursor and the heated precursors. A crystalline signature first appears for the sample heated to 640°C for 50 s. The diffraction peaks are consistent with cubic Y<sub>2</sub>O<sub>3</sub> (JCPDS No. 98-010-7439). Table 6 summarizes the grain size of the samples heated to 640°C, 720°C, and 850°C for dwell times of 50 s and 100 s. This data indicates only small changes in grain size heating temperature and dwell time.



**Figure 37.** XRD of (a) precursor and (b)-(f) precursor heated to various temperatures for 1 s, 50 s, and 100 s.

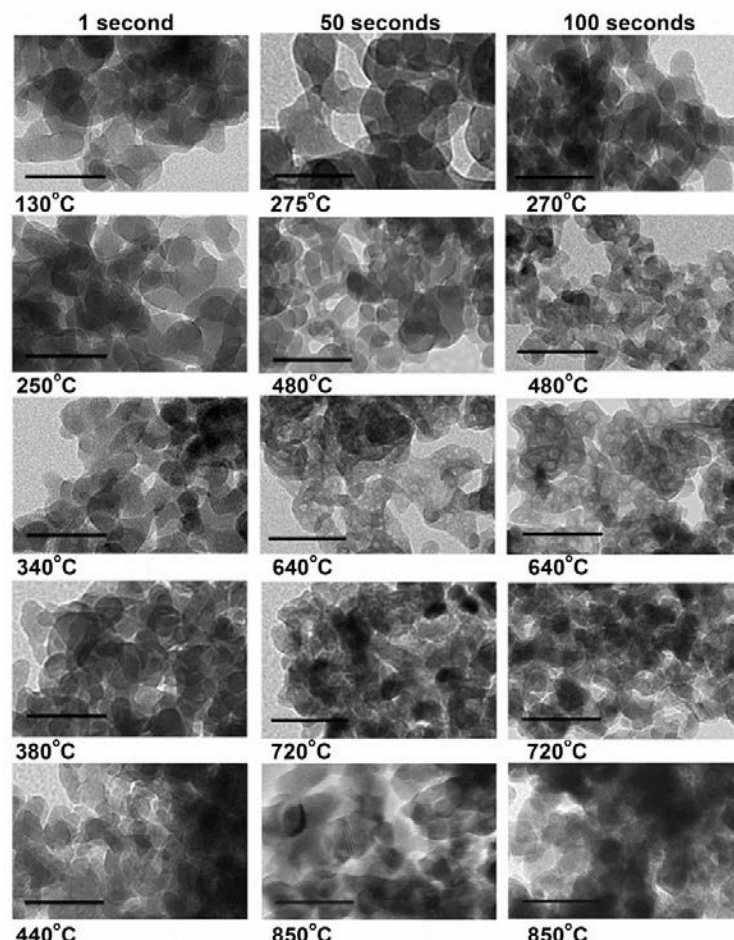
**Table 6.** Grain size of samples heated to 640°C, 720°C, and 850°C for dwell times of 50 s and 100 s.

Time (s)	Temperature (°C)		
	640	720	850
50	11.5 nm	14.1 nm	14.5 nm
100	13.0 nm	14.5 nm	18.2 nm

While the grain growth kinetics are often described by the conventional grain growth equation or the relaxation equation,<sup>12</sup> these equations are unable to describe any growth occurring at the much shorter time scales described in this work. This inability is due to the multi-step decomposition process that takes place as described in Equation 33.

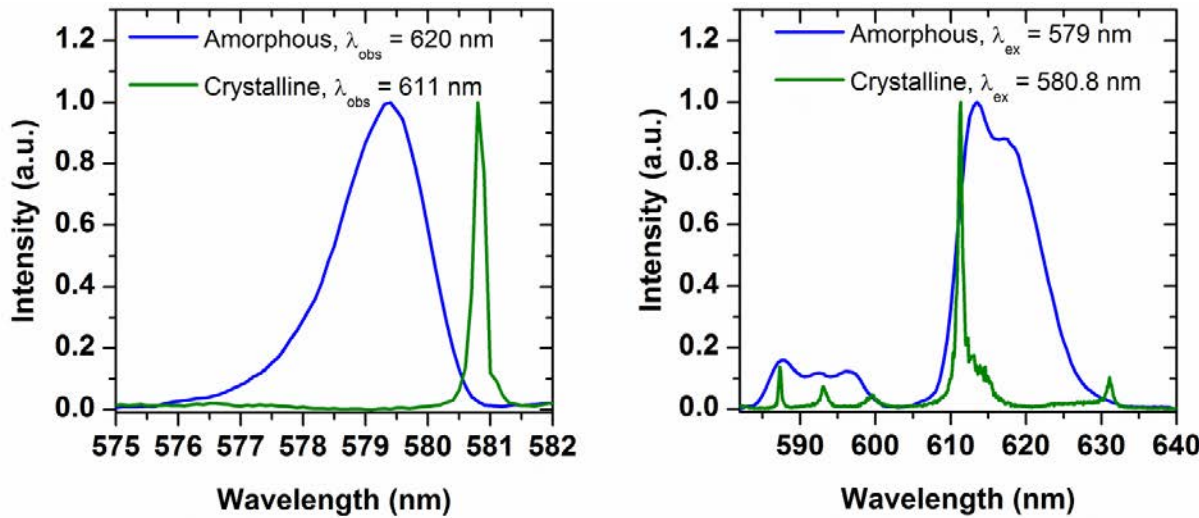
Figure 38 shows the TEM images of samples heated for dwell times of 1 s, 50 s, and 100 s at various temperatures. The samples heated to 640°C for 50 s and 100 s have a perforated appearance, indicating decomposition and release of CO<sub>2</sub> gas. The TEM images of the samples heated to 720°C for 100 s and 850°C for 50 s and 100 s show the crystalline lattice. Due to their tendency to agglomerate, measurement of the particle size from the TEM images is not possible. Also, because the material has mixed amorphous and crystalline phases, the crystallite size derived from XRD spectra does not necessarily correspond to the particle size seen in the TEM images.

Figure 39 shows the excitation spectra and fluorescence spectra of the two extreme cases, amorphous Y<sub>2</sub>(CO<sub>3</sub>)<sub>3</sub>:Eu precursor and fully crystalline Y<sub>2</sub>O<sub>3</sub>:Eu. The excitation peaks are due to the pure electronic <sup>7</sup>F<sub>0</sub>→<sup>5</sup>D<sub>0</sub> transition in the amorphous and crystalline samples, respectively.<sup>19</sup> The fluorescence peaks are due to the <sup>5</sup>D<sub>0</sub>→<sup>7</sup>F<sub>1</sub> (585 nm – 600 nm) and <sup>5</sup>D<sub>0</sub>→<sup>7</sup>F<sub>2</sub> (610 nm – 630 nm) transitions, respectively.<sup>19</sup> The excitation peaks for the amorphous and



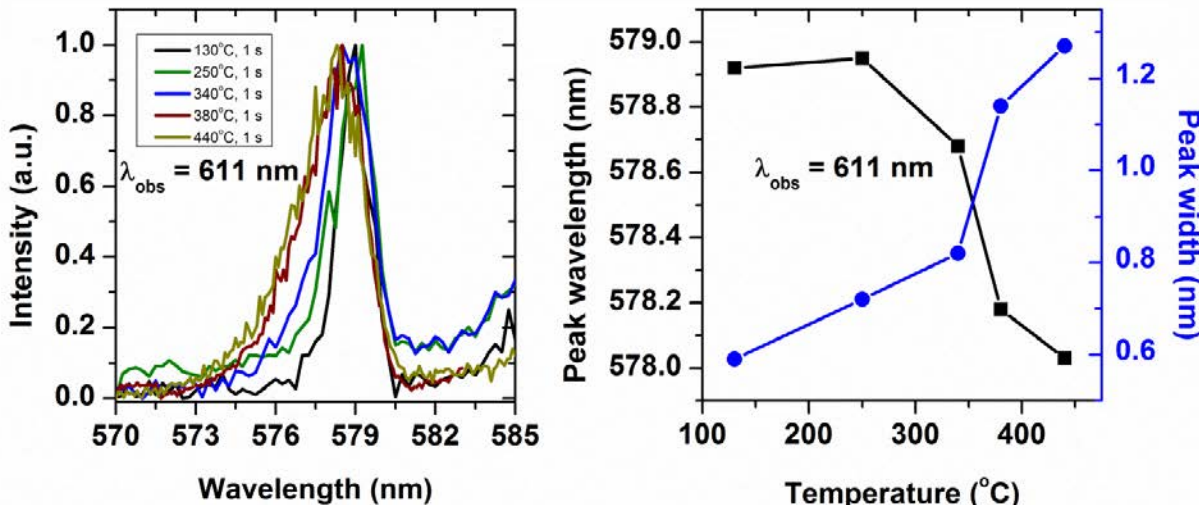
**Figure 38.** TEM images of the co-precipitated carbonates heat treated at various temperatures and dwell times. Scale bar is 50 nm.

crystalline samples are well separated, while the fluorescence peaks for the amorphous and crystalline samples have significant overlap.



**Figure 39.** Excitation spectra (left) and fluorescence spectra (right) of amorphous and fully crystalline samples (left). Only minimal overlap occurs for the excitation spectra, while significant overlap occurs for the fluorescence spectra of these two samples.

Under the influence of temperature and time, the broad excitation peak first shifts toward shorter wavelength while increasing in width. As high enough temperatures are reached for extended dwell times, the crystalline peak appears and increases in strength, while the amorphous peak collapses and disappears. The crystalline peak width continues to decrease with increased heating temperature.<sup>16</sup>



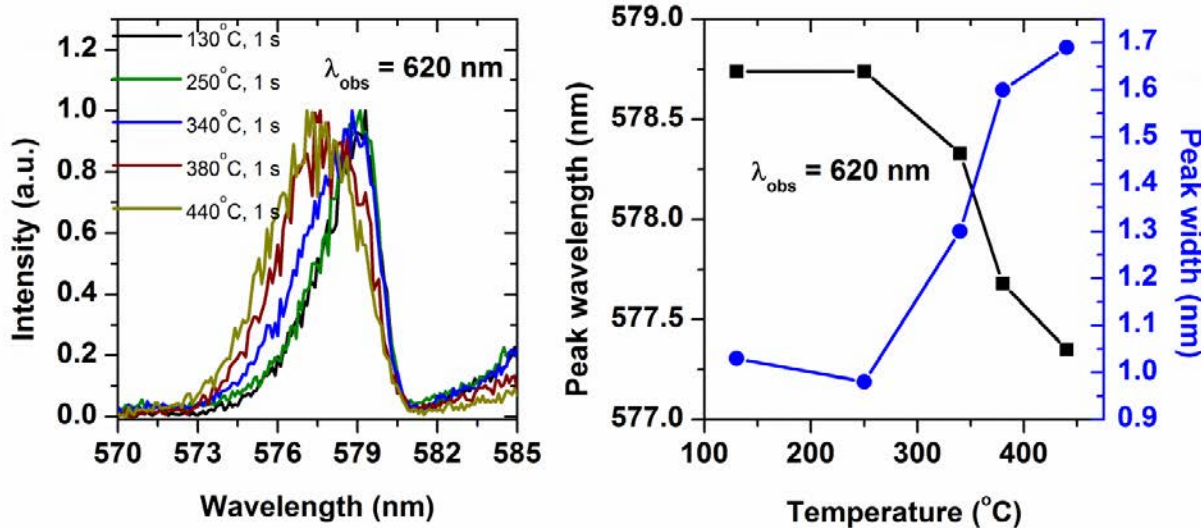
**Figure 40.** Excitation spectra (left), monitored at 611 nm, of yttrium carbonate precursor heated for 1 s to various temperatures. Peak wavelength and peak width as a function of heating temperature, (right) based on Gaussian fit.

Figure 40 shows the excitation spectra, monitored at 611 nm, of yttrium carbonate precursors heated for 1 s to 130°C, 250°C, 340°C, 380°C, and 440°C. The spectra show one broad absorption peak that shifts to shorter wavelength and increases in width as the

temperature is increased. A single Gaussian peak was fitted to the excitation peak, and its peak position and peak width are also shown in Figure 40.

As the original amorphous  $\text{Y}_2(\text{CO}_3)_3$  decomposes with increasing temperature and starts forming  $\text{Y}_2\text{O}(\text{CO}_3)_2$  and  $\text{Y}_2\text{O}_2\text{CO}_3$ , each of these compounds contributes to the excitation spectra, increasing the width of the peak. The decomposition products  $\text{Y}_2\text{O}(\text{CO}_3)_2$  and  $\text{Y}_2\text{O}_2\text{CO}_3$  must have higher crystal field strength than  $\text{Y}_2(\text{CO}_3)_3$  to account for the shift to higher energy (shorter wavelength).

Figure 41 shows the excitation spectra and shifts when monitored at 620 nm instead of 611 nm. In this case, the peak shift is about 35% larger than when monitored at 611 nm. However, the change in peak width is about the same.



**Figure 41.** Excitation spectra (left), monitored at 620 nm, of yttrium carbonate precursor heated for 1 s to various temperatures. Peak wavelength and peak width as a function of heating temperature, (right) based on Gaussian fit.

The larger peak shift is probably due to the overlap of crystalline and amorphous fluorescence components at 611 nm while monitoring almost pure amorphous components at 620 nm. The crystalline peak component is not expected to shift as much as the amorphous peak components.

Figure 42 shows how the excitation spectra of the pyroprobe-heated yttrium carbonate precursor evolve as a function of temperature and time while monitored at 611 nm and 620 nm. The general trend starts out with a broad peak caused by the amorphous phase, which increases in width with increasing temperature until its intensity decreases and a narrow peak due to a crystalline phase appears. The transition from amorphous to crystalline phase occurs earlier in time and temperature for monitoring at 611 nm than monitoring at 620 nm. This difference is because at 620 nm the observed signal is almost exclusively due to the amorphous phase, while at 611 nm the observed signal is due the combination of amorphous and crystalline phase.

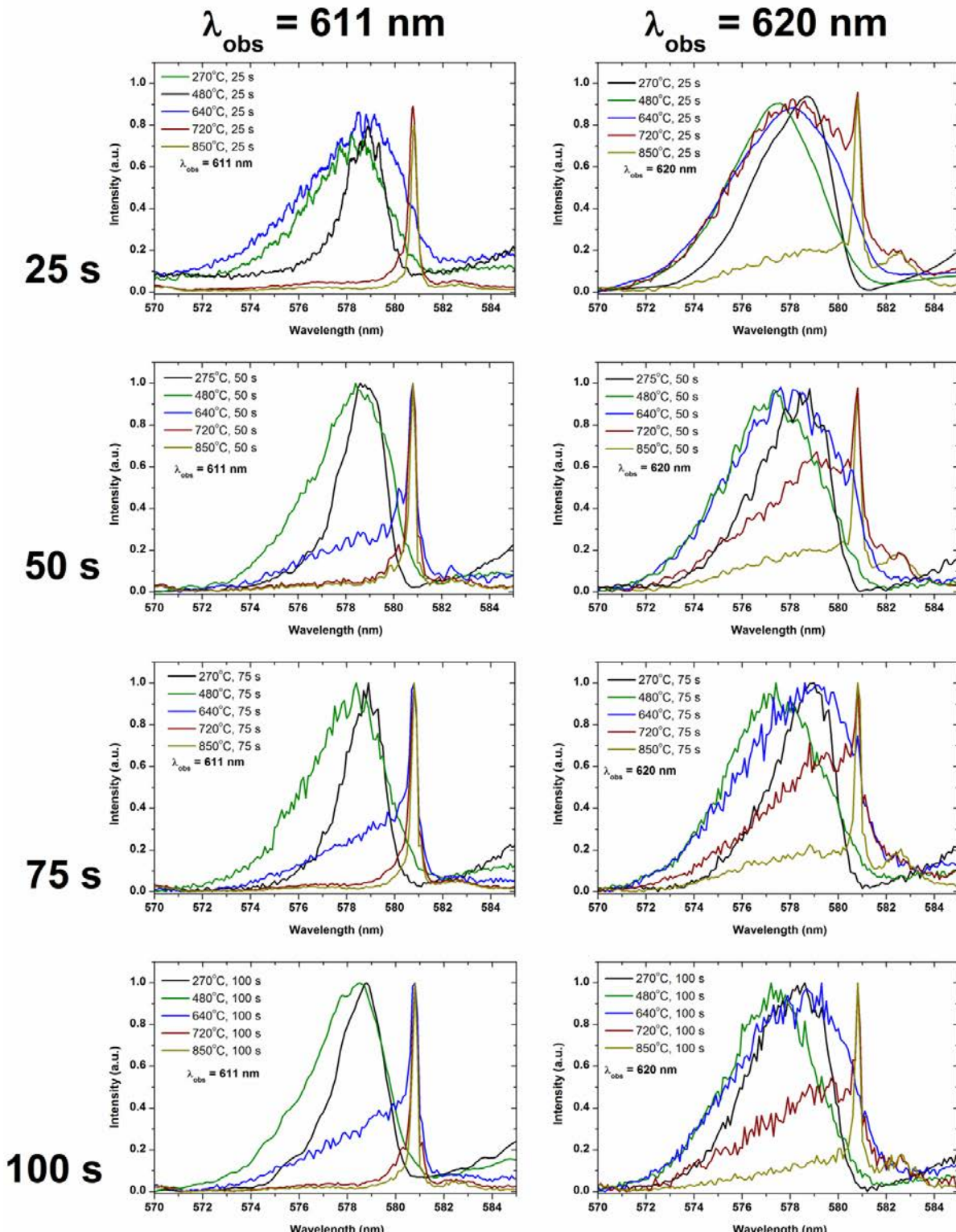


**Figure 42.** Excitation spectra of yttrium carbonate precursor heated via pyroprobe for dwell times of 25 s, 50 s, 75 s, and 100 s to various temperatures.

Figure 43 summarizes the shift in peak wavelength and peak width of the spectra monitored at 620 nm. The initial shift in peak position with increasing temperature is toward shorter wavelength, followed by a shift toward longer wavelength. The shift in peak width is increasing with increasing temperature. Dwell-time does not appear to have much of an influence on the observed shift.

The data shown in Figure 42 for a dwell-time of 1 s, are consistent with the measurements shown in Figure 43. These data represent the shift toward shorter wavelength for temperatures up to about 440°C, as seen in Figure 18 with higher resolution. The minimum peak position, corresponding to the highest energy, occurs at a temperature when most of the sample is expected to be made up of  $\text{Y}_2\text{O}_2\text{CO}_3$ . As such, this material appears to have the highest crystal field strength of the various materials present.

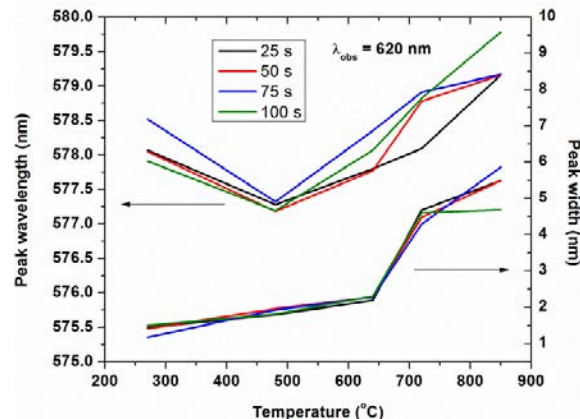


**Figure 43.** Shift in peak position (left scale) and peak width (right scale) of excitation spectra monitored at 620 nm of yttrium carbonate precursors heated to various temperatures for dwell times of 25 s, 50 s, 75 s, and 100 s.

occurs at a temperature when most of the sample is expected to be made up of  $\text{Y}_2\text{O}_2\text{CO}_3$ . As such, this material appears to have the highest crystal field strength of the various materials present.

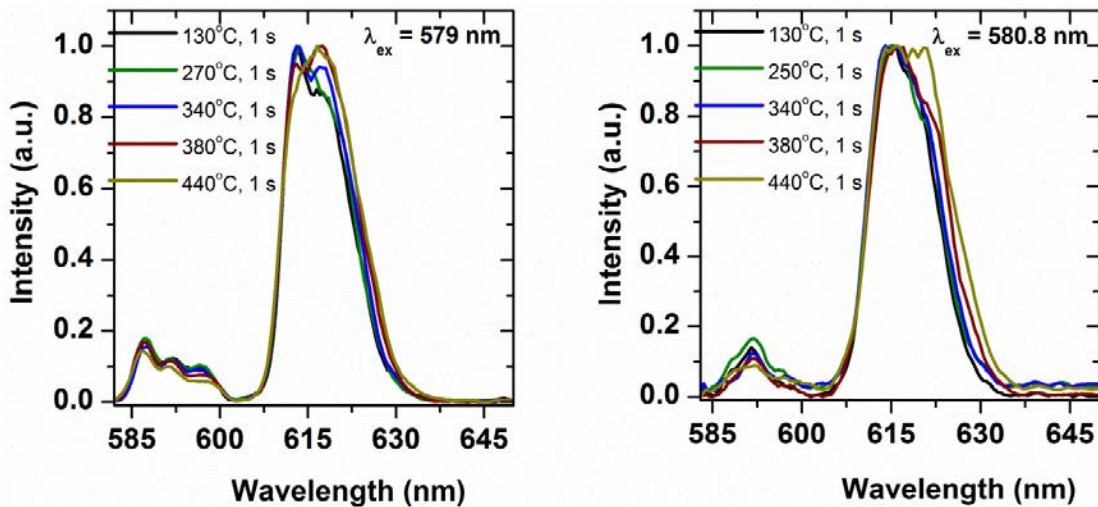


**Figure 44.** Fluorescence spectra, excited at 579 nm (left) and at 580.8 nm (right), of yttrium carbonate pre-cursors heated to various temperatures for 1 s.

Figure 44 shows the fluorescence spectra of yttrium carbonate precursors heated for 1 s to various temperatures for excitation at 579 nm and 580.8 nm, respectively. As the heating temperature increases, the emission peak between about 610 nm and 625 nm increases in width. When excited at 579 nm, the fluorescence appears to have two peaks, centered at about 613 nm and 617 nm. With increasing temperature, the intensity of the former decreases, while the intensity of the latter increases. Also, three peaks, which are due to the  $^5\text{D}_0 \rightarrow ^7\text{F}_1$  transition are located between 585 nm and 600 nm. The fact that the  $^7\text{F}_1$  level splits into three levels indicates the low symmetry of the Eu site. When excited at

580.8 nm, a main peak is located at about 615 nm. Only when the temperature reaches 440°C does the intensity at longer wavelength increase. As opposed to excitation at 579 nm, the spectra for excitation at 580.8 nm show one main peak with two shoulders between 585 nm and 600 nm.

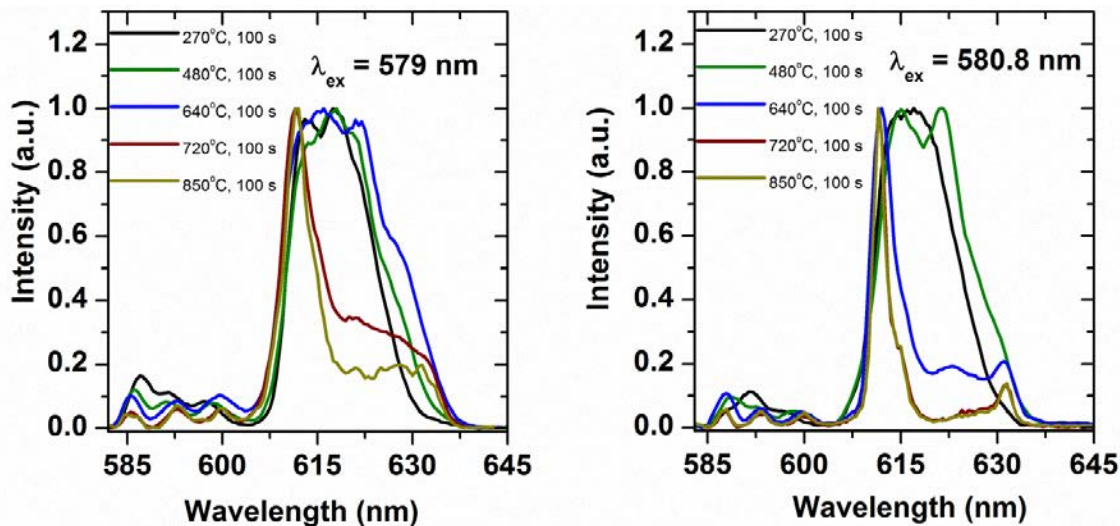


**Figure 45.** Fluorescence spectra, excited at 579 nm (left) and at 580.8 nm (right), of yttrium carbonate pre-cursors heated to various temperatures for 100 s.

The fluorescence spectra for heating of yttrium carbonate precursors for 100 s to various temperatures are shown for excitation at 579 nm and at 580.8 nm in Figure 45. In this case, the heating temperatures are higher than for the spectra shown in Figure 11. Heating to higher temperatures highlights the difference between the samples excited at 579 nm and those excited at 580.8 nm. The higher temperatures lead to the formation of crystalline Y<sub>2</sub>O<sub>3</sub>, which is characterized by a strong emission peak centered at about 611 nm and which has its main excitation at 580.8 nm.

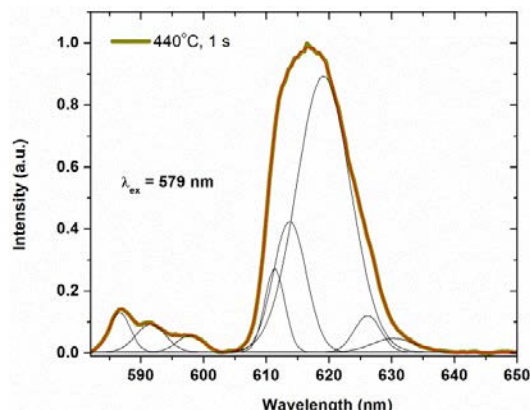


**Figure 46.** Fluorescence spectrum of yttrium carbonate pre-cursors heated for 1 s to 440°C and its deconvoluted spectral fit.

Figure 46 shows the fluorescence spectrum of the sample heated for 1 s to 440°C and its deconvoluted spectral fit. Because of the low symmetry indicated by the three peaks for the <sup>5</sup>D<sub>0</sub>→<sup>7</sup>F<sub>1</sub> transition, five peaks are fitted to the <sup>5</sup>D<sub>0</sub>→<sup>7</sup>F<sub>2</sub> transition.

The fluorescence lifetimes of the heated samples are shown in Figure 47 for excitation at 532 nm and monitoring at 611 nm, and for excitation at 532 nm and monitoring at 620 nm. The samples monitored at 611 nm reach fluorescence lifetimes of about 2 ms when heated to about 850°C, while reaching only about 1.4 ms when heated to 850°C but monitored at 620 nm. This difference reflects the presence of crystalline vs. amorphous phase for the respective observation wavelengths. At 611 nm, a large contribution of the

signal is due to the crystalline phase, while at 620 nm a large contribution is due to the amorphous phase. As expected, the crystalline phase has a longer fluorescence lifetime than the amorphous phase.

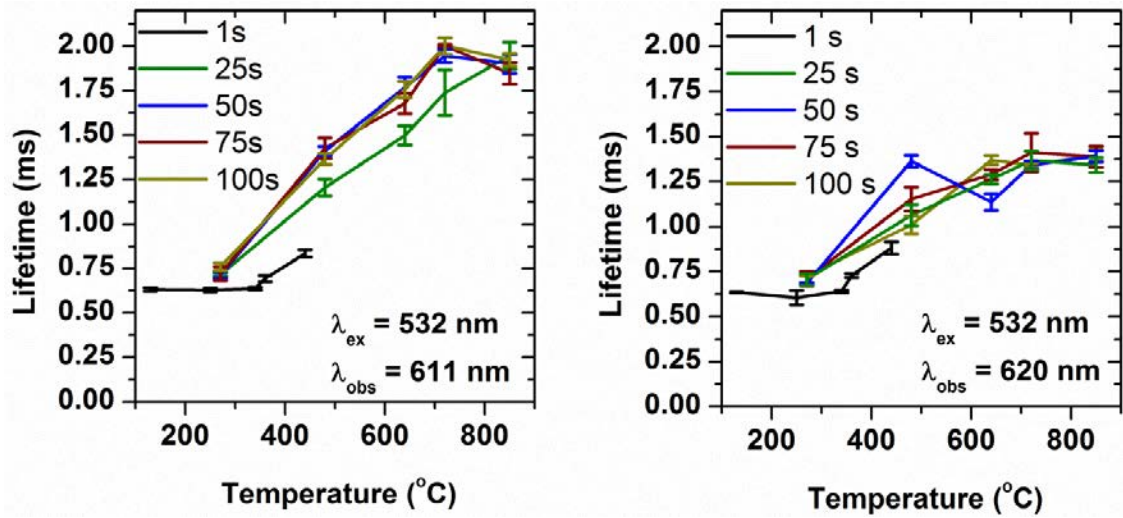


**Figure 47.** Fluorescence lifetimes, excited at 532 nm and observed at 611 nm (left) and 620 nm (right), of yttrium carbonate precursors.

### Explosion tests

The explosion tests were performed in a 450 cm x 450 cm steel plated blast proof chamber at the Sigmund Jacobs Detonation Science Facility located at the Indian Head Division of the Naval Surface Warfare Center in Indian Head, MD, by Dr. James Lightstone and his colleagues, who provided the following information. Figure 48 shows the experimental setup. The sensor particles, placed in small pieces of paper tissue, were hung ~21.5 cm from the center of a charge containing aluminum and HMX. A plastic Imhoff cone with a 10 cm maximum diameter was used to collect the particles. An R-type fast-thermocouple (Omega P13R-002), housed in a small metal cylinder and placed at approximately the same distance from the center of the charge as the particle sample, was used to record the temperature.

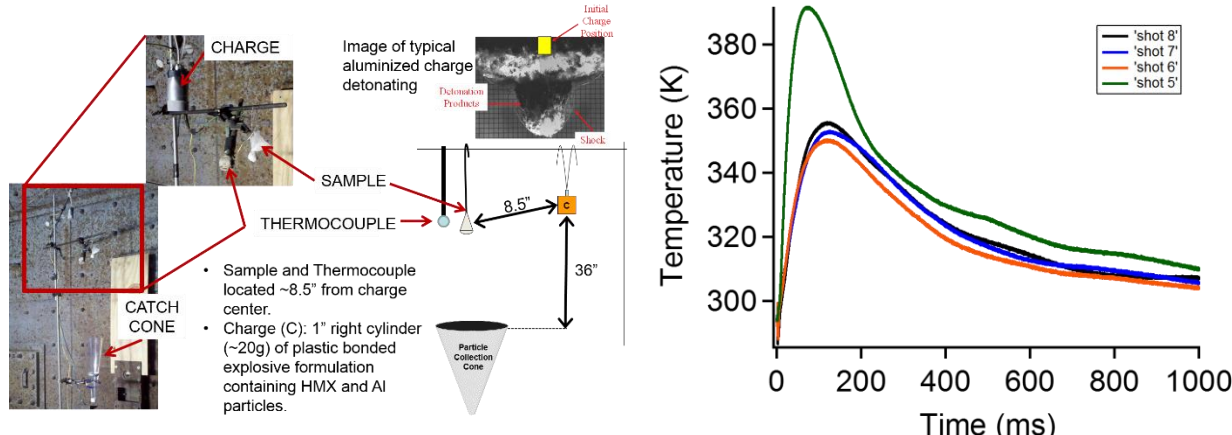


**Figure 48.** Setup for explosion testing (left) and temperature measured via thermocouple (right).

The fluorescence and fluorescence-excitation spectra of amorphous and fully-crystalline Eu:Y<sub>2</sub>O<sub>3</sub> are shown in Figure 49.

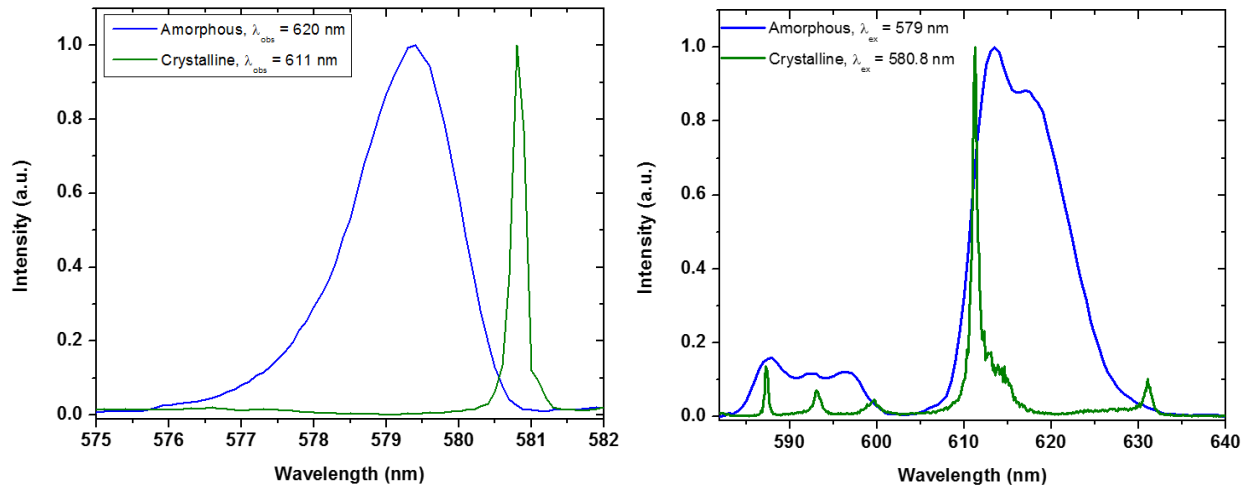


**Figure 49.** The as-prepared sample is amorphous and displays broad spectral features, while the heated sample is crystalline and displays narrow spectral features.

Reference samples were heated using a pyroprobe for 1 s to various temperatures and their spectra were then compared with those of the explosion sample, see Figure 50. This comparison indicates a temperature of about 250 °C (523 K) for the explosion sample. This reading compares with a peak temperature of about 390 K measured by the thermocouple, corresponding to a 34% higher reading. Since thermocouples have a relatively large mass compared to the small particulate sensors, and an explosion represents a very fast heating event, it is fully expected that the Eu:Y<sub>2</sub>O<sub>3</sub> temperature sensors yield higher reading than the relatively slow thermocouple.

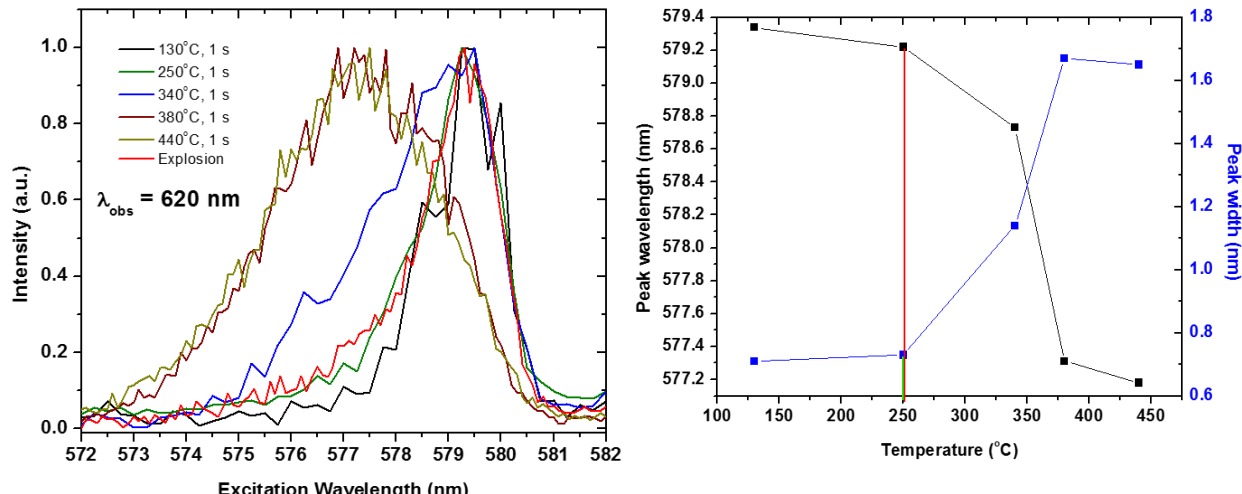


**Figure 50.** Comparing excitation spectra of Eu:Y<sub>2</sub>O<sub>3</sub> subjected to explosive heating with those of Eu:Y<sub>2</sub>O<sub>3</sub> heated via a pyroprobe (left) and temperature dependence of peak wavelength and peak width.

Another explosion test focused on identifying any dependencies for samples collected at different distances from the charge location. The sample material was hung about 8.5" away from an explosive charge. A thermocouple was also placed about 8.5" away from the charge. Several collection bins were placed at different distances from the sample material. Bins labeled "a", "b", and "c" collected materials at 0-18", 12-30", and 24-40", respectively. Figure 51 shows the experimental setup and the temperatures measured by the thermocouple. Six different tests were conducted.

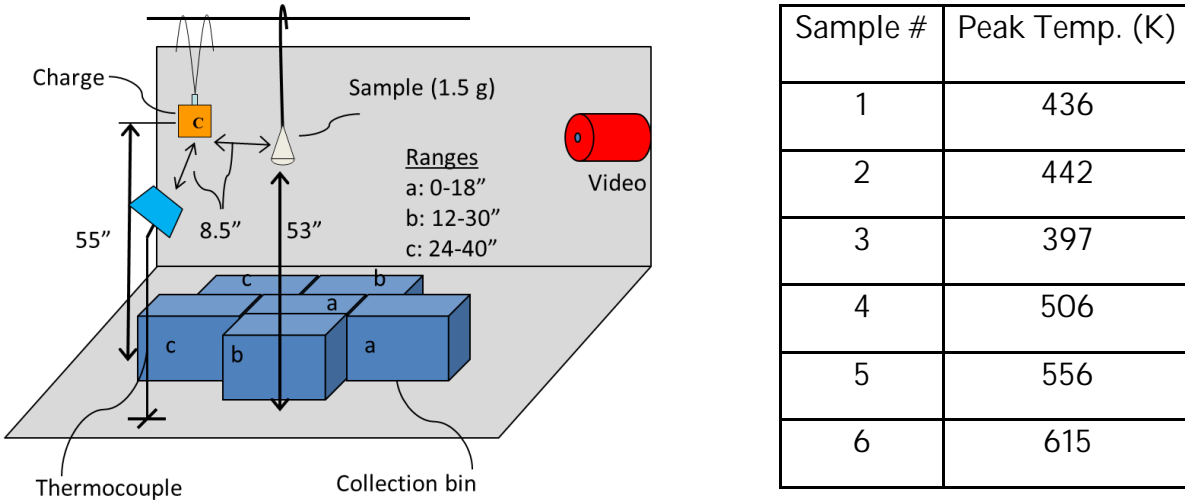


**Figure 51.** Explosion test setup (left) and temperatures measured via thermocouple (right).

The temporal evolution of the temperature measured by the thermocouple is shown in Figure 52. The maximum is reached after about 0.1 s. However, the thermocouple is known to not be able to accurately track the temporal evolution of an explosive fireball, which is significantly faster.

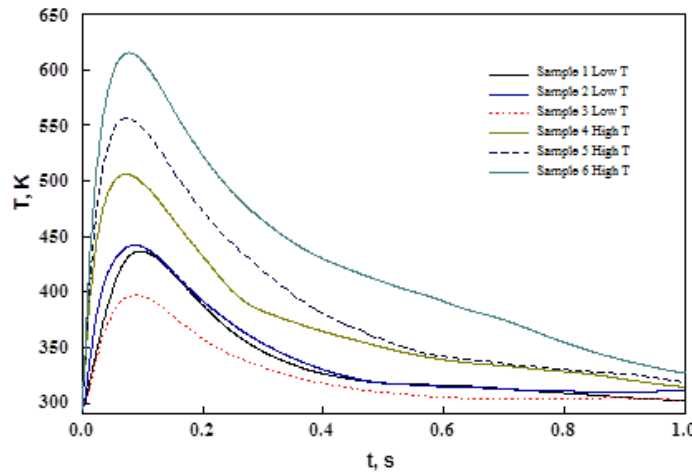


**Figure 52.** Thermocouple response during the explosions.

Figure 53 shows photos of the six post-detonation sensor materials. Vials “a”, “b”, and “c” correspond to the different collection distances. The sensor material samples contain **various impurities from the explosion**. However, in all six cases, samples “b” appear to have the least amount of impurities.



**Figure 53.** Photos of post-detonation sensor materials for six explosion test.

Table 7**Table 7** lists the temperatures determined by the nanophase sensors. Because of the inhomogeneity within each sample, three small sample amounts were extracted from **each vial and measured separately. These samples are labeled “A”, “B”, and “C”**. In addition, Table 7**Table 7** lists the average temperature as well as the temperature measured by the thermocouple.

**Table 7.** Comparison of temperatures measured via particulate sensors based upon FWHM at 611 nm and thermocouples (TC).

	<b>Temperature (K)</b>			<b>Average Temp. (K)</b>	<b>TC Temperature (K)</b>
<b>Sample</b>	<b>A</b>	<b>B</b>	<b>C</b>		
<b>1a</b>	803	721	717	747±49	436
<b>1b</b>	633	652	611	632±21	
<b>1c</b>	751	622	684	686±65	
<b>2a</b>	622	541	687	617±73	442
<b>2b</b>	651	585	613	616±33	
<b>2c</b>	690	624	673	662±34	
<b>3a</b>	551	597	541	563±30	397
<b>3b</b>	536	660	582	593±63	
<b>3c</b>	608	542	553	568±35	
<b>4a</b>	686	653	630	656±28	506
<b>4b</b>	627	544	546	572±47	
<b>4c</b>	803	745	627	725±90	
<b>5a</b>	780	*	864	822±59	556
<b>5b</b>	653	762	691	702±55	
<b>5c</b>	752	789	777	773±19	
<b>6a</b>	824	863	*	844±28	615
<b>6b</b>	598	586	623	602±19	
<b>6c</b>	657	690	802	716±76	

\* Material is fully crystallized, i.e. temperature was too high for this sensor material.

Except for sample 3, the “b” samples always read the lowest temperature. This may be explained with the expected temperature profile within an explosive fireball. Also, in all cases the maximum temperature recorded by the thermocouple is lower than the temperature recorded by the nanosensors. The slow response time of thermocouples prevents them from following a fast temperature profile such as is expected within an explosive fireball. As is apparent from the data in Table 7, the nanosensor materials have a much faster response time. The variation in measured temperature reflects the inhomogeneous temperature distribution within an explosive fireball. The difference

between the two techniques ranges anywhere from 17% to 58%, with the higher temperature measurements showing less of a difference.

A third explosion test was conducted inside a closed chamber, see Figure 54. Also shown are photos of the debris collected from these tests.

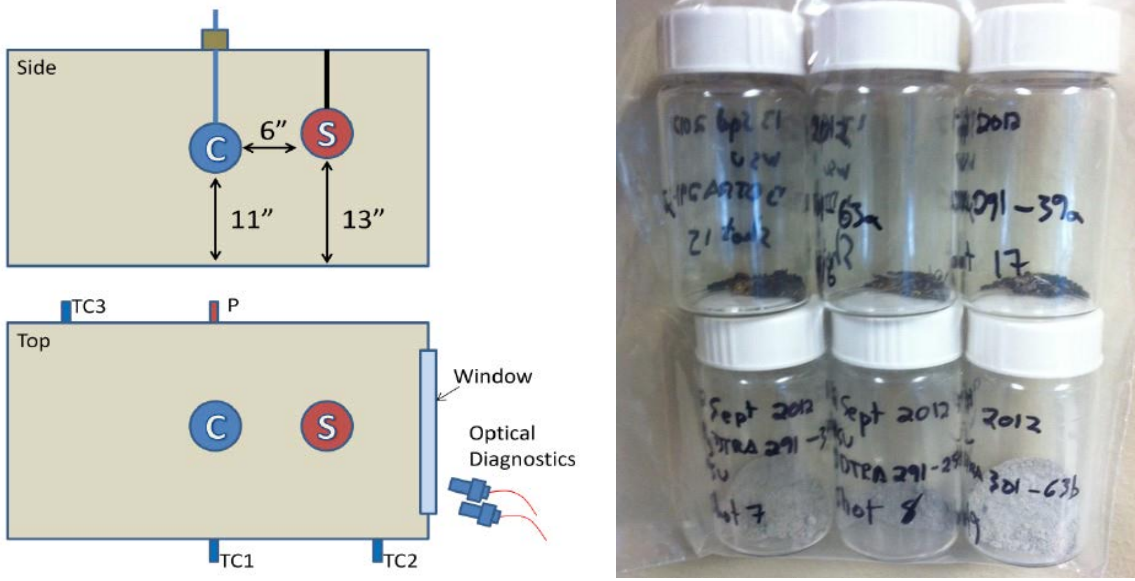


**Figure 54.** Closed chamber configuration with locations of three thermocouples (left) and photos of debris collected after the explosion (right).

In our previous measurements for the open-air tests, we used the FWHM of the amorphous peak to determine the temperature, see Figure 55. The temperature inside the closed chamber was so high that all the temperature sensor material crystallized. As such, we used the FWHM of the crystalline peak to determine the temperature, see Figure 55.

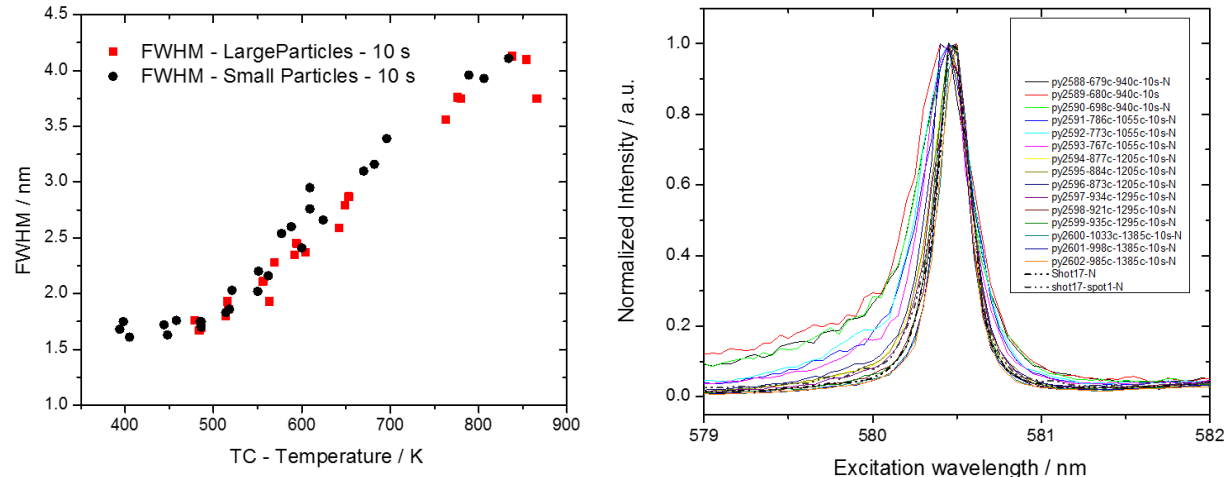


**Figure 55.** Temperature-dependent FWHM of amorphous peak (left) and temperature-dependent crystalline peaks (right).

Using our temperature sensors, we determined a temperature of about 1020 K. The three thermocouples measured 395 K, 750 K, and 1060 K, respectively.

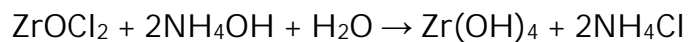
## **Eu:ZrO<sub>2</sub>**

### Characterization of as-synthesized material

Nanophase ZrO<sub>2</sub>:Eu precursor is prepared by precipitation as described by Su et al.<sup>20</sup> ZrO<sub>2</sub> has three polymorphs at ambient pressure, monoclinic phase (m-phase) at low temperatures, tetragonal phase (t-phase) above about 1200 °C, and cubic phase (c-phase) at temperatures above about 2370 °C.<sup>21</sup> Because the tetragonal and cubic phases are of high technological interest, many approaches have been reported in attempting to stabilize either of these phases at ambient conditions.<sup>22</sup> Most of these approaches include doping with trivalent cations leading to the formation of oxygen vacancies. These vacancies are believed to be responsible for the stabilization of the tetragonal or cubic phase.<sup>23</sup> Due to surface energy effects, oxygen vacancies can be stabilized in undoped isolated nanoparticles of less than 10 nm diameter and in aggregated nanoparticles of less than 33 nm diameter.<sup>24</sup> The tetragonal phase can also be stabilized by the presence of anions such as OH<sup>-</sup>.<sup>24</sup> The metastable ZrO<sub>2</sub> phases may also be stabilized by addition of solutes, e.g., Y<sub>2</sub>O<sub>3</sub>, MgO, and Ce<sub>2</sub>O<sub>3</sub>.<sup>25-27</sup>

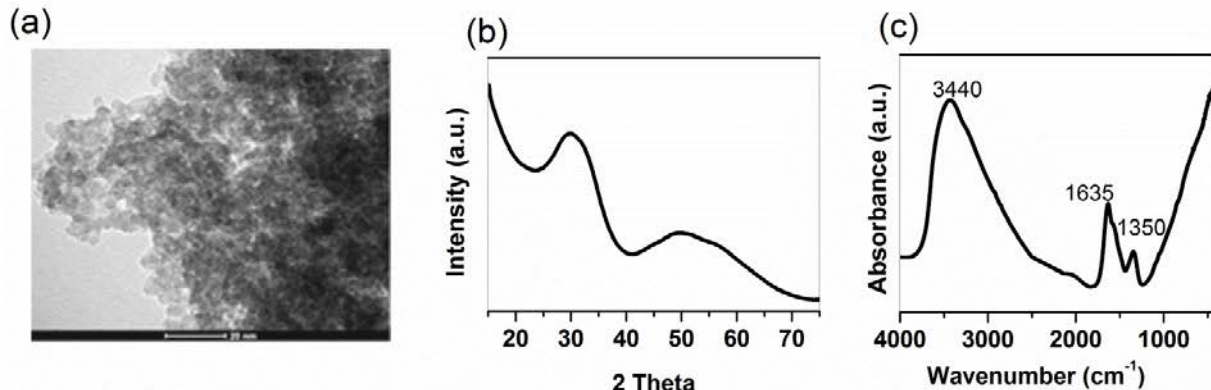
The optical properties of rare-earth-doped ZrO<sub>2</sub> have been characterized by several authors. Of particular interest is the ability to use rare-earth dopants such as Eu<sup>3+</sup> to monitor structural changes.<sup>28-30</sup> For example, the ratio of the electric-dipole allowed <sup>5</sup>D<sub>0</sub>→<sup>7</sup>F<sub>2</sub> transition to the magnetic-dipole allowed <sup>5</sup>D<sub>0</sub>→<sup>7</sup>F<sub>1</sub> transition can be used to extract changes about the symmetry of the Eu<sup>3+</sup> site. The lower the site symmetry, the higher the intensity of the <sup>5</sup>D<sub>0</sub>→<sup>7</sup>F<sub>2</sub> transition and the higher the ratio. Also, the splitting of the Eu<sup>3+</sup> energy levels will be different in monoclinic, tetragonal, and cubic symmetry. Higher symmetry leads to degeneration, while lower symmetry removes the degeneracy and leads to the observation of additional spectral lines.

Processing completeness requires that ZrO<sub>2</sub> nanoparticle precursors, prepared via wet-chemistry techniques, undergo a subsequent calcination step to remove hydrates, carbonates, ammonium, etc., and to induce crystallization. The decomposition and crystallization processes lead to variations in the chemical surrounding of the embedded europium ions in the ZrO<sub>2</sub> precursor matrix. These structural changes affect the optical properties of Eu<sup>3+</sup> as the matrix undergoes various irreversible phase transformation from amorphous to metastable t-phase and to the stable m-phase with increasing temperatures.<sup>31</sup> According to Ray et al, the drop-wise addition of ZrOCl<sub>2</sub>·8H<sub>2</sub>O aqueous solution to NH<sub>4</sub>OH aqueous solution yields Zr(OH)<sub>4</sub>:<sup>32</sup>



The precipitated powder is composed of monodispersed nanosized particles. Due to their tendency to aggregate, precise measurement of the particle size is ambiguous.

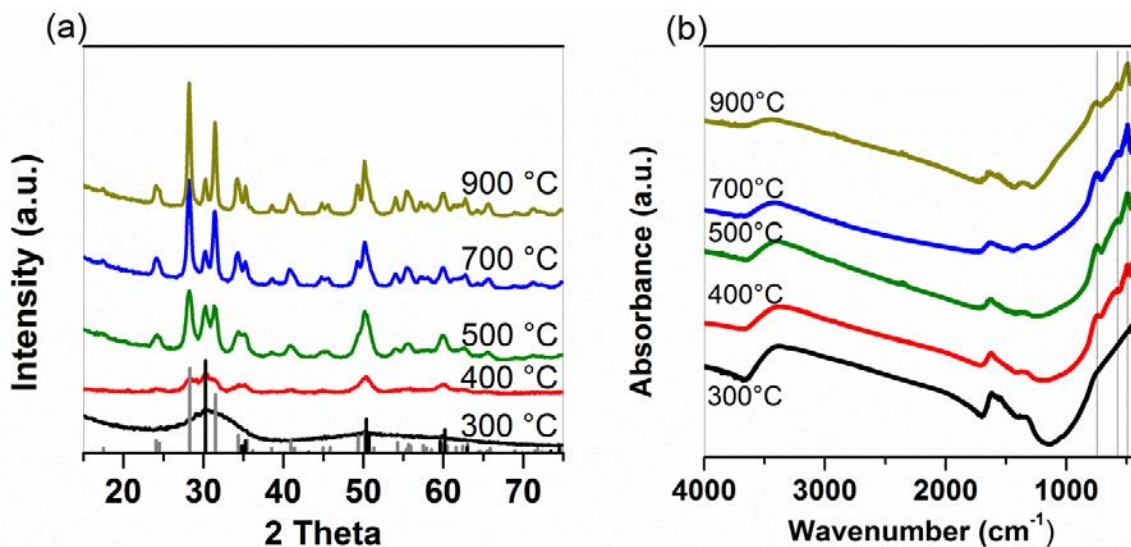
The TEM image shown in Figure 56 (a) suggests a particle diameter of about 2-5 nm. The XRD spectrum, shown in Figure 56 (b), shows broad halo peaks, indicating that the as-prepared precipitated powder is amorphous. The FTIR spectrum of the ZrO<sub>2</sub> precursor, shown in Figure 56 (c), is consistent with the presence of lattice water. The broad peak at 3440 cm<sup>-1</sup> and the narrow peak at 1635 cm<sup>-1</sup> are caused by the symmetric and asymmetric H-O-H stretching and deformation vibrations, respectively.<sup>33</sup> The shoulder at about 1580 cm<sup>-1</sup> and the peak at 1350 cm<sup>-1</sup> are attributed to carbonates that are produced during exposure to CO<sub>2</sub> in the atmosphere.<sup>34</sup>



**Figure 56.** (a) TEM image, (b) XRD spectrum, and (c) FTIR spectrum of as-prepared  $\text{Zr}(\text{OH})_4$ .

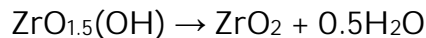
#### Furnace heating

Figure 57 (a) shows the XRD spectra of the  $\text{Zr}(\text{OH})_4$  precursor when heat-treated for 3 hours at temperatures between  $300\text{ }^\circ\text{C}$  and  $900\text{ }^\circ\text{C}$ . Heating to  $300\text{ }^\circ\text{C}$  for 3 hours does not lead to crystallization of the precursor. When heated to  $400\text{ }^\circ\text{C}$  for 3 hours, some XRD peaks become visible, which can be matched to a mixed  $\text{ZrO}_2$  t-phase and m-phase.



**Figure 57.** (a, b) XRD and FTIR spectra of  $\text{Zr}(\text{OH})_4$  heat-treated for 3 hours at temperatures between  $300\text{ }^\circ\text{C}$  and  $900\text{ }^\circ\text{C}$ . The gray and black histograms mark the positions of monoclinic (PDF No. 072-0597) and tetragonal peaks (PDF No. 088-1007), respectively.

Figure 57 (b) shows Zr-O vibrational bands at  $495\text{ cm}^{-1}$ ,  $575\text{ cm}^{-1}$ , and  $745\text{ cm}^{-1}$  (indicated by dashed lines) for samples heated to  $400\text{ }^\circ\text{C}$  and above, confirming the presence of the crystalline  $\text{ZrO}_2$  m-phase and t-phase.<sup>35, 36</sup> Figure 57 (b) also shows that even with heat treatment at  $900\text{ }^\circ\text{C}$ , the presence of OH and  $\text{CO}_3$  groups, due to reactions with the atmosphere, can still be seen. Following calcination,  $\text{Zr}(\text{OH})_4$  has been proposed to undergo continuous dehydroxylation:<sup>37</sup>



The crystallite size and the percent composition of the t-phase with respect to the m-phase, can be estimated from the XRD spectra, see Table 8. As the heating temperature increases from 400 °C to 900 °C, the crystallite size increases from 8 nm to 33 nm for the t-phase, and from 11 nm to 25 nm for the m-phase.

**Table 8.** Characteristics of the furnace-heated  $\text{ZrO}_2$  crystalline phases.

Temperature (°C)	t-phase/m-phase	t-phase/m-phase (%)
	Crystallite size (nm)	m-phase (%)
400	8/11	45/55
500	13/16	28/72
700	18/25	14/86
900	33/25	11/89

At 400 °C, the crystallite sizes are in the range for the t-phase to m-phase transformation for isolated crystallites, 10 nm.<sup>24</sup> The crystallite sizes are slightly smaller for the t-phase which may suggest phase transformation of the t-phase to the m-phase as it grows in size. Indeed, the amount of metastable t-phase decreases with increasing temperatures. As the heat treatment temperature increases from 400 °C to 900 °C, the percent of t-phase composition decreases from 45% to 11% (Table 1). The non-vanishing t-phase indicates that, in addition to its role as an optical probe, the europium dopant might act as stabilizer of this phase.<sup>38</sup>

Figure 58 shows the fluorescence spectra, excited at 536 nm, of  $\text{ZrO}_2:\text{Eu}$  precursors furnace-heated for 3 hours to various temperatures. The peaks at 592 nm and 607 nm can be assigned to the  $^5\text{D}_0 \rightarrow ^7\text{F}_1$  and  $^5\text{D}_0 \rightarrow ^7\text{F}_2$  transitions of the t-phase.<sup>39</sup> The remaining peaks belong to the m-phase, which has a lower symmetry than the t-phase and can lead to splitting of the transitions. At 300 °C only emission from amorphous components are observed. As the temperature increases, a mix of m-phase and t-phase forms, just as observed in the XRD spectra. At 400 °C the percentage of t-phase is significantly higher than at 900 °C, confirming that the t-phase is metastable and converts into the m-phase as the temperature increases.

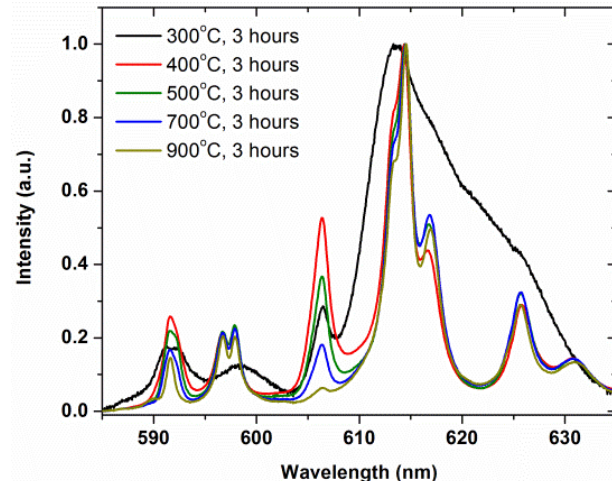


**Figure 58.** Fluorescence spectra of  $\text{Eu:ZrO}_2$  precursor, furnace-heated for 3 hours to various temperatures.

### Rapid pyroprobe heating of Zr(OH)<sub>4</sub>

Figure 59 (a) and (b) show the XRD and FT-IR spectra of Zr(OH)<sub>4</sub> when heat treated for 10 s to temperatures between 420 °C and 835 °C. The samples heated to 420 °C and 495 °C do not show any crystalline ZrO<sub>2</sub> signatures, while samples heated to higher temperatures show clear crystalline signatures. Just as in the case of the furnace-heated samples, the presence of the mixed t-phase and m-phase leads to Zr-O vibrational peaks at 495 cm<sup>-1</sup>, 575 cm<sup>-1</sup>, and 745 cm<sup>-1</sup>, (indicated by dashed lines in Figure 5b).

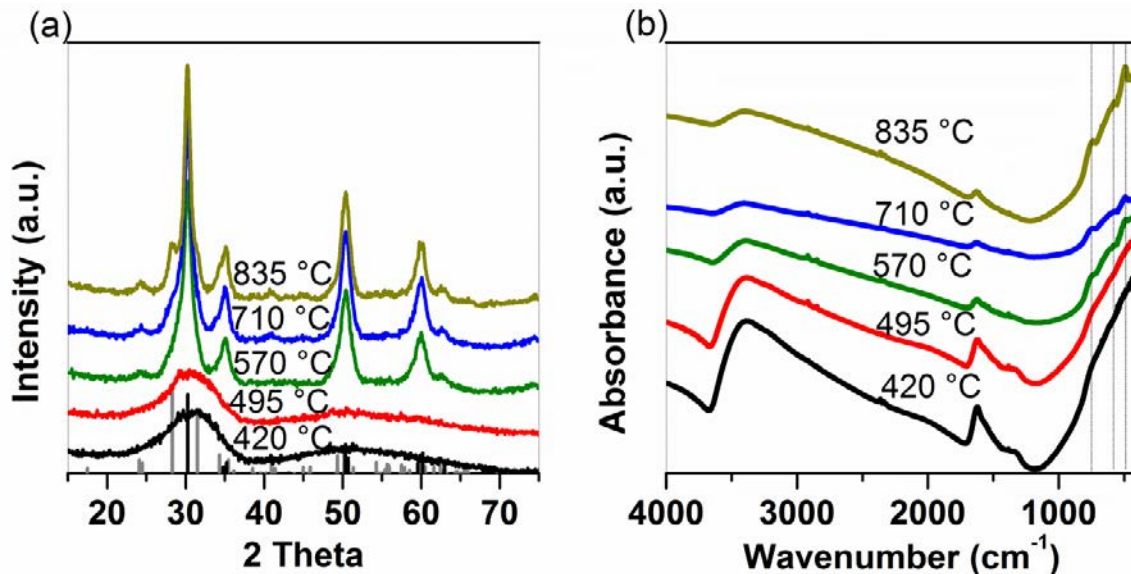


**Figure 59.** (a, b) XRD and FTIR spectra of Zr(OH)<sub>4</sub> heat-treated at various temperatures, 300-900 °C for 10 s. The gray and black histograms mark the positions of monoclinic (PDF No. 072-0597) and tetragonal peaks (PDF No. 088-1007), respectively.

The XRD spectra of Zr(OH)<sub>4</sub> heat treated for 10 s in the pyroprobe differ from those heat treated for 3 hours in the furnace (compare Figure 57 a and Figure 59 a). Both heating procedures result in a mixture of m-phase and t-phase. However, for the pyroprobe-heated samples, the peaks indicate a stronger presence of the metastable t-phase and for the furnace-heated samples, the peaks indicate a stronger presence of the m-phase. In comparison with the furnace-heated samples that are ramped up at a rate of 25 °C/min, the rapidly heated samples (nominal ramping rate of the pyroprobe heated sample is 20000 °C/s) may not have sufficient time to completely dehydroxylate the Zr(OH)<sub>4</sub> compound and to achieve large crystallites. For the matching crystallite sizes of the pyroprobe and the furnace heated samples, the pyroprobe heated sample clearly shows a larger amount of the metastable t-phase. The remaining OH groups may have stabilized the t-phase in the pyroprobe-heated samples (compare Table 8 and Table 9). In contrast to the 3-hours furnace-heated samples, the crystallite sizes of the t-phase are larger than the ones of the m-phase. This observation suggests that for rapid heating the metastable t-phase is favored over the m-phase.

**Table 9.** Characteristics of the pyroprobe-heated ZrO<sub>2</sub> crystalline phases.

Temperature (°C)	t-phase/m-phase	t-phase/m-phase (%)
	Crystallite size (nm)	
570	10/6	68/32
710	11/6	68/32
835	14/11	64/36

TEM images confirm the significant role of temperature on the ZrO<sub>2</sub> crystallite growth, even at heating times as short as 10 s (Figure 60). The observed particle sizes are on par with those estimated from the XRD spectra. It is worth noting that the particle sizes do not necessarily correspond to the crystallite size due to its polycrystalline nature.

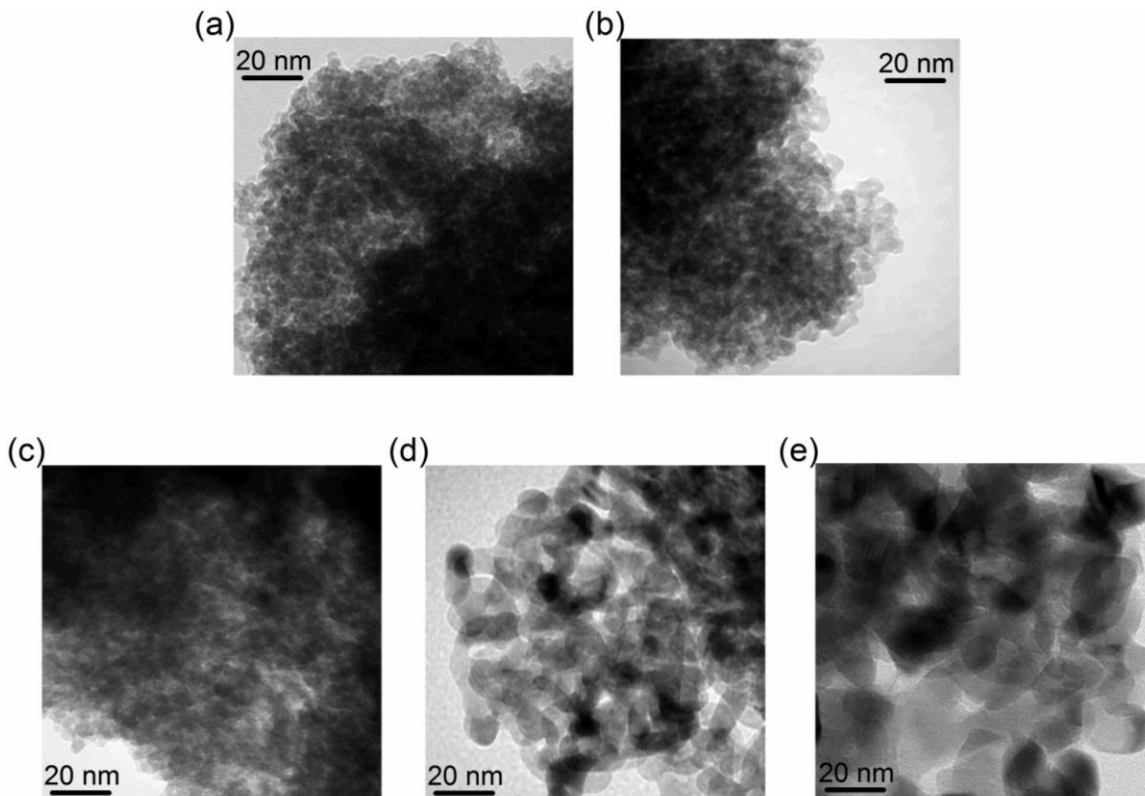
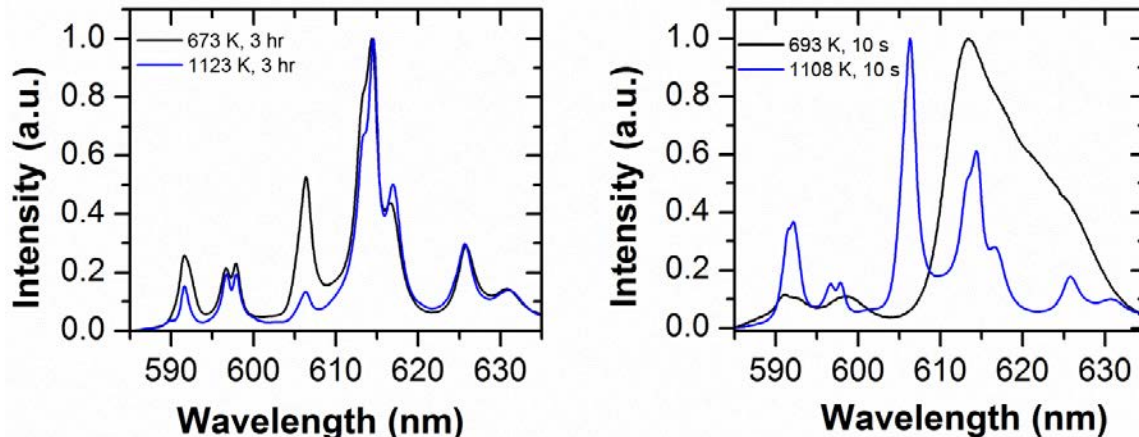
**Figure 60.** TEM micrographs of Zr(OH)<sub>4</sub> calcined at various temperatures for 10 seconds: (a) 420 °C (b) 495 °C (c) 570 °C, (d) 710 °C, and (e) 835 °C. Scale bar is 20 nm.

Figure 61 shows the fluorescence spectra, excited at 536 nm, of ZrO<sub>2</sub>:Eu precursors pyroprobe-heated for 10 s to various temperatures. At the two lowest temperatures, only amorphous components are present and emit light. As the temperature reaches 570 °C, crystalline emission peaks appear, which show the presence of the t-phase and m-phase. Compared to the furnace-heated samples, the t-phase has a much stronger presence in these samples. Again, the peaks at 592 nm and 607 nm can be assigned to the  ${}^5D_0 \rightarrow {}^7F_1$  and  ${}^5D_0 \rightarrow {}^7F_2$  transitions of the t-phase, and the remaining peaks to the m-phase. As the

temperature reaches 835 °C, the signal for the m-phase increases compared to those at lower temperatures.

Besides Eu-doped  $\text{Y}_2\text{O}_3$ , we recently also presented some initial results for Eu-doped  $\text{ZrO}_2$ .<sup>3</sup> The synthesis, morphological characterization, and pyroprobe heating of the Eu-doped  $\text{Zr}(\text{OH})_4$  nanoparticles is described elsewhere.<sup>3</sup> Briefly, an aqueous solution of  $\text{ZrOCl}_2 \cdot 8 \cdot \text{H}_2\text{O}$  and  $\text{Eu}(\text{NO}_3)_3 \cdot 5 \cdot \text{H}_2\text{O}$  is added to an aqueous solution of ammonium hydroxide to reach a pH of 10. The white gel that forms is aged for 2 h and is then several times centrifuged and redispersed in ionized water. Subsequently, the material is rinsed in acetone, dried for 12 h at 80 °C, and then crushed into a powder. Using this approach,  $\text{Eu}_{0.01}\text{Zr}_{0.99}\text{O}_2$  was synthesized and used for the following characterization.

We previously determined that the  $\text{Eu}_{0.01}\text{Zr}_{0.99}(\text{OH})_4$  nanoparticles crystallize into tetragonal and monoclinic phases upon heating.<sup>3</sup> Figure 62 (left) shows the fluorescence spectra of  $\text{Eu}_{0.01}\text{Zr}_{0.99}(\text{OH})_4$  samples that have been heated for three hours in a furnace at 673 K and at 1123 K, respectively.



**Figure 61.** Fluorescence spectra of Eu:ZrO<sub>2</sub> precursor, pyroprobe-heated for 10 s to various temperatures.

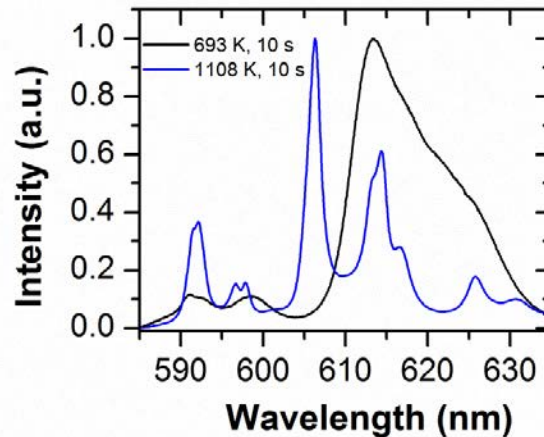
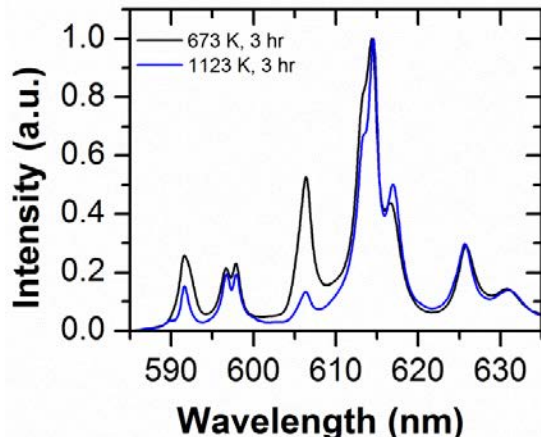


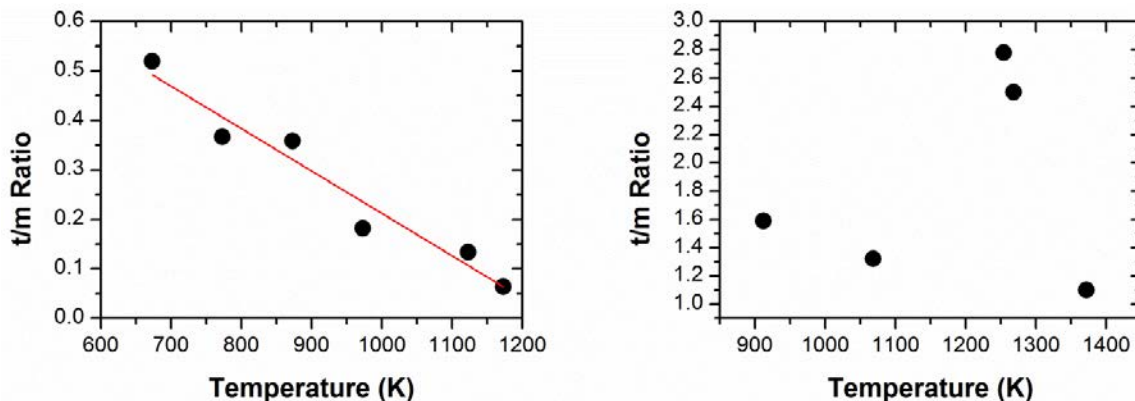
**Figure 62.** Fluorescence spectra of  $\text{Eu}_{0.01}\text{Zr}_{0.99}(\text{OH})_4$  heated for three hours to 673 K and 1123 K, respectively (left), and heated for 10 s to 693 K and 1108 K, respectively (right).

While the spectra are normalized with respect to each other, it should be kept in mind that the emission intensity of the sample heated to 1123 K is significantly stronger than the emission intensity of the sample heated to 673 K. These two spectra show some of the main features of Eu ions embedded in  $\text{ZrO}_2$ . The peaks at about 592 nm and at about 606 nm correspond to the  $^5\text{D}_0 \rightarrow ^7\text{F}_1$  and  $^5\text{D}_0 \rightarrow ^7\text{F}_2$  transitions of Eu ions ( $\text{D}_{2d}$  site symmetry) in tetragonal  $\text{ZrO}_2$  ( $\text{P}42/\text{n m c}$ ), respectively.<sup>40</sup> The remaining peaks at about 597 nm and

610 nm through 635 nm correspond to the  $^5D_0 \rightarrow ^7F_1$  and  $^5D_0 \rightarrow ^7F_2$  transitions of Eu ions (C<sub>1</sub> site symmetry) in monoclinic ZrO<sub>2</sub> (P1 21/c 1).<sup>40</sup>

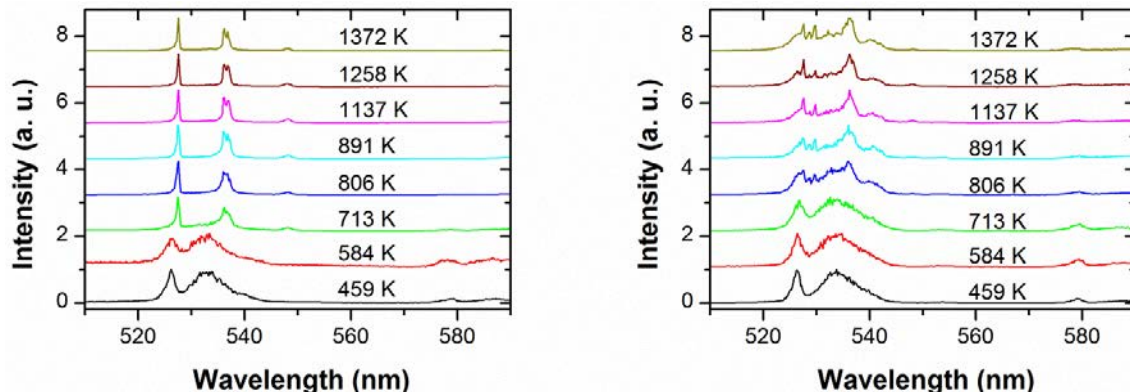
Shown in Figure 62 (right) are the spectra of Eu<sub>0.01</sub>Zr<sub>0.99</sub>(OH)<sub>4</sub> samples heated for 10 s in the pyroprobe heater to 693 K and 1108 K, respectively. The spectral features of the sample heated to 693 K are relatively broad, indicating that most of the sample is still amorphous. The crystalline spectral features become apparent somewhere between 770 K and 840 K.<sup>3</sup> Compared to the furnace-heated samples, the spectrum of the pyroprobe-heated sample (1108 K) shows a stronger signal for the emission peaks of the tetragonal phase compared to the monoclinic phase.<sup>3</sup>

Figure 63 shows the ratio of the intensities of the peaks at 606 nm and 614 nm for a range of temperatures for the 3 h furnace-heated sample and the 10 s pyroprobe-heated sample. For the furnace-heated samples the ratios show a linear dependency with temperature, providing a means to determine temperature based upon the ratio of tetragonal to monoclinic composition. However, no ratio/temperature relationship is apparent for short 10 s pyroprobe heating, see Figure 63 (right). Thus, alternative temperature indicators need to be determined.



**Figure 63.** Tetragonal/monoclinic intensity ratios for 3 h furnace heating (left) and 10 s pyroprobe heating (right).

Our investigation of heated Eu<sub>0.02</sub>Y<sub>1.98</sub>(CO<sub>3</sub>)<sub>3</sub> indicates that the peak width and peak position of excitation spectra are good temperature indicators.<sup>41, 42</sup> Thus, excitation spectra of heated Eu<sub>0.01</sub>Zr<sub>0.99</sub>(OH)<sub>4</sub> are measured between 510 nm and 590 nm for samples heated for 10 s, and between 510 nm and 600 nm for samples heated 1 s to various temperatures, while monitored at 606 nm (tetragonal phase) and 614 nm (monoclinic phase), respectively, see Figure 64 and Figure 65. The samples monitored at 606 nm shows peaks between 520 nm and 550 nm corresponding to the  $^7F_0 \rightarrow ^5D_1$  transitions, and peaks between 575 nm and 590 nm corresponding to the  $^7F_0 \rightarrow ^5D_0$  transitions, respectively. Figure 64 (right) which shows the excitation spectra monitored at 614 nm, shows some of the same peaks as shown in Figure 64 (left) which are monitored at 606 nm, indicating that the emission at 614 nm may not be purely due to the monoclinic phase but may also contain contribution from the tetragonal phase.



**Figure 64.** Excitation spectra of  $\text{Eu}_{0.01}\text{Zr}_{0.99}(\text{OH})_4$  heated for 10 s to various temperatures and monitored at 606 nm - tetragonal phase –(left) and 614 nm - monoclinic phase (right).

Figure 65 shows the excitation spectra of samples heated for 1 s. These spectra are very similar to the spectra of samples heated for 10 s and shown in Figure 64, indicating that even for heating times as short as 1 s some of the material crystallizes. However, the peaks of the samples monitored at 614 nm, see Figure 65 (right) remain relatively broad compared to the samples heated for 10 s and the samples heated to 1 s but monitored at 606 nm. This observation could be explained if the tetragonal phase starts to crystallize before the monoclinic phase. The higher the temperature and the longer the heating time, the more intense the peaks between 520 nm and 540 nm compared to the peaks between 575 nm and 590 nm. This observation is more pronounced for the excitation spectra monitored at 606 nm (tetragonal) than the ones monitored at 614 nm (monoclinic), and is consistent with the fact that the  $^5\text{D}_0 \rightarrow ^7\text{F}_0$  transition is forbidden in  $\text{D}_{2d}$  symmetry (tetragonal) but electric dipole allowed in  $\text{C}_1$  symmetry (monoclinic). However, unlike for heated  $\text{Eu}_{0.02}\text{Y}_{1.98}(\text{CO}_3)_3$ , the excitation spectra of heated  $\text{Eu}_{0.01}\text{Zr}_{0.99}(\text{OH})_4$  do not readily show any apparent changes in peak position or peak width that could be used as a temperature indicator. Therefore, the fluorescence lifetime and fluorescence spectra are evaluated as potential temperature indicators.

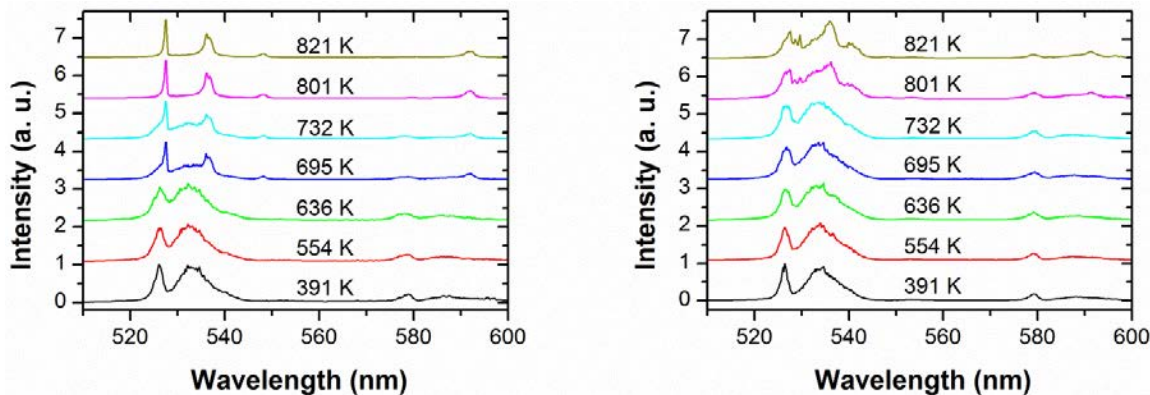


**Figure 65.** Excitation spectra of  $\text{Eu}_{0.01}\text{Zr}_{0.99}(\text{OH})_4$  heated for 1 s to various temperatures and monitored at 606 nm - tetragonal phase – (left) and monitored at 614 nm - monoclinic phase - (right).

Figure 66 shows the fluorescence lifetimes of Eu-doped ZrO<sub>2</sub> heated for 10 s to various temperatures, excited at 536 nm, and monitored at 606 nm and 614 nm, respectively. The decay curves of the samples monitored at 614 nm (monoclinic) show a very short lifetime component as well as a longer lifetime component. These curves are fitted with a single exponential for all temperatures starting at 0.3 ms. The lifetime data for the samples monitored at 606 nm (tetragonal) are fitted with a single exponential for temperatures below 700 K (amorphous phase). Above 700 K, the data are fitted with a double exponential. One of the exponentials is the same as the monoclinic lifetime, indicating that a mixed phase is observed at 606 nm. The second exponential (tetragonal) is the one shown in Figure 66 (left). As expected, at temperatures below about 700 K, when the material is still amorphous, the observed lifetimes are about the same for both observation wavelengths. As the temperature is further increased, the tetragonal phase displays a jump in fluorescence lifetime from about 1 ms to more than 4 ms. Subsequently, the lifetime increases a little more before it drops again to about 3 ms at about 1400 K. The monoclinic phase on the other hand displays a different temperature dependence. The lifetime continues to increase more slowly to a maximum of about 1.6 ms, at which it levels out. Only at temperatures above 1200 K does the lifetime decrease again to about 1.5 ms at about 1300 K. The increase and subsequent decrease of fluorescent lifetime with temperature is not unusual in nanoparticles. A similar behavior is also seen in Eu:Y<sub>2</sub>O<sub>3</sub>,<sup>2</sup> and the concept of this effect was described by Meltzer et al.<sup>43</sup> Equation 35 describes the dependence of the radiative lifetime of an electronic transition:

$$\tau_R = \frac{1.5 \times 10^4}{f(ED)} \frac{\lambda_0^2}{\left[ \frac{1}{3}(n^2 + 2) \right]^2 n} \quad (39)$$

where **f(ED)** is the oscillator strength, **n** is the index of refraction, and **λ** is the wavelength in vacuum. Because the nanoparticles are much smaller than the wavelength of light, their immediate surrounding environment needs to be considered to determine an effective index of refraction. In our case, the nanoparticles start out as Zr(OH)<sub>4</sub> and decompose into ZrO<sub>2</sub> as they are heated. During the decomposition process the size, shape, and surrounding of the particles change, resulting in changes in the radiative lifetime. A more detailed description of this effect can be found in the literature.<sup>2, 43</sup> The fact that the shape of the fluorescence lifetime data for Eu ions in the tetragonal phase is different from the shape of the fluorescence lifetime data of Eu ions in the monoclinic phase indicates that their morphological development must be different during the heating process. Considering the shape of the fluorescence lifetime curves, the data monitored at 614 nm could provide some indication for temperature in the range between about 500 K and about 1100 K.

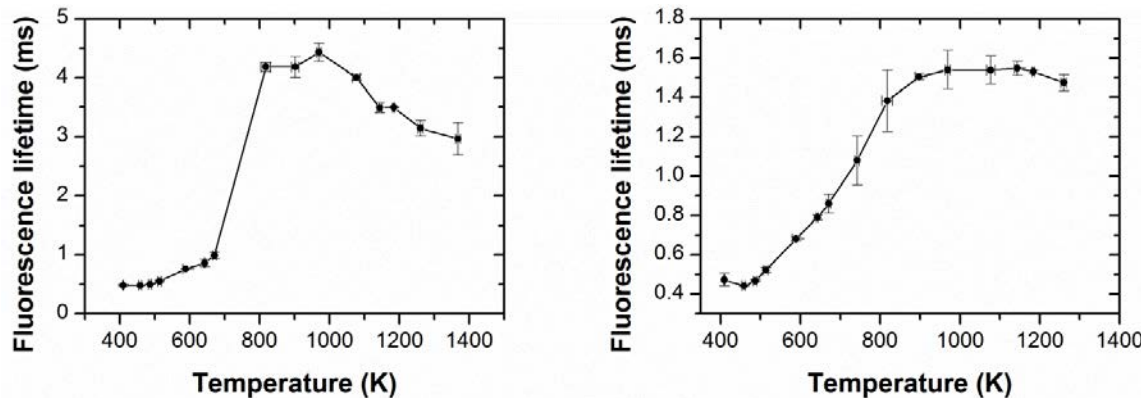


**Figure 66.** Fluorescence lifetime of  $\text{Eu}_{0.01}\text{Zr}_{0.99}(\text{OH})_4$  heated for 10 s, excited at 536 nm, and monitored at 606 nm (left) and 614 nm (right), respectively.

Figure 67 (left) shows a small section with two peaks of the fluorescence spectra of  $\text{Eu}_{0.01}\text{Zr}_{0.99}(\text{OH})_4$  heated for 10 s and 1 s to various temperatures. Both of these peaks have the same fluorescence lifetime, indicating that they are both resulting from the same level of Eu ions in the tetragonal phase. It is apparent that the shorter wavelength peak decreases in intensity as the heating temperature is increased. Figure 67 (right) shows the ratio of the emission peak intensities as a function of temperature. As can be seen, a linear relationship exists between peak ratio and temperature in the range between about 800 K and about 1300 K. At lower temperatures the material is still amorphous and the peaks are not well characterized. At temperatures above about 1300 K, the curve flattens out. The data from the 1 s heating tests overlaps well with the data from the 10 s heating tests.

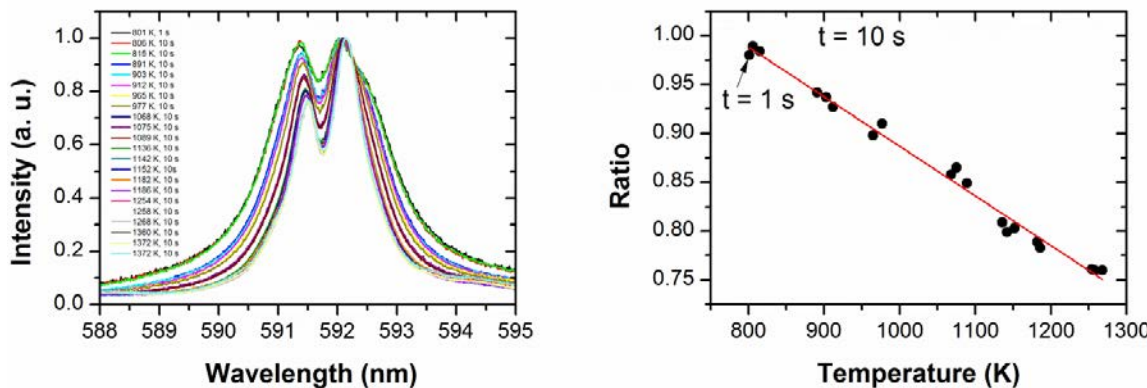


**Figure 67.** Fluorescence spectra of  $\text{Eu}_{0.01}\text{Zr}_{0.99}(\text{OH})_4$  heated for 10 s and 1 s to various temperatures (left) and peak ratio (right).

The changing intensity peak ratio with temperature is most likely due to the continued crystallization process of the tetragonal phase over the observed temperature range. The transition from an amorphous phase to a crystalline phase with higher symmetry leads to the reduction of energy level splittings. This process starts at the crystallization temperature and ends when all material has been crystallized.

## D. Temperature/time (Thermal impulse) Sensors

In order to simultaneously extract information about heating temperature and heating duration, we rely on a kinetic analysis of our sensors. The theoretical background and some modeling information was provided in section A. This approach requires that we use two different sensor materials with sufficiently different kinetic parameters. Ideally, these two sensor materials are physically combined in such a manner that they always measure and record in the same location. We prepared different types of core/shell particles and evaluated different sensing approaches.

### Initial evaluation of various compounds

For our first type of core/shell sensor, we combine the well-known  $\text{ZrO}_2$  and  $\text{Y}_2\text{O}_3$  matrices that work well for crystallization-based changes. However, in order to probe temperature-induced changes in these two materials, we have to use two different rare-earth dopants, and selected  $\text{Er},\text{Yb}:\text{ZrO}_2/\text{Eu}:\text{Y}_2\text{O}_3$  for evaluation. The  $\text{Er},\text{Yb}$  combination yields upconverted light in the red and green spectral regions when excited with infrared 980 nm light. Depending on the Er/Yb molar ratio, the ratio of the red and green emission intensity shows a linear temperature dependence for furnace heating, see Figure 68. However, when heated for short periods of time via a pyroprobe, the temperature dependence was no longer apparent. Furthermore, it appears that the shell prevents the growths of  $\text{ZrO}_2$ , limiting its functionality.

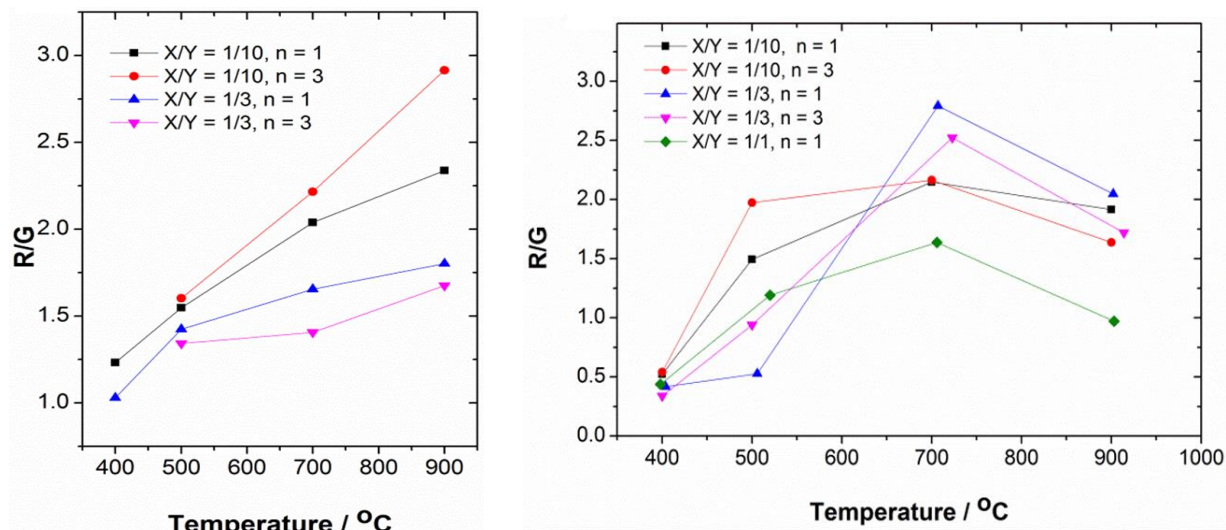


**Figure 68.** Temperature dependence up upconverted red and green emission intensities for furnace heating (left) and pyroprobe heating (right).

Next, we evaluated potential temperature-induced diffusion and resulting upconversion in  $\text{Yb}_2\text{O}_3/\text{Er}:\text{Y}_2\text{O}_3$ . Ytterbium is a well-known activator for upconversion and if enough Yb diffuses from the core into the shell, the shell should show enhance upconversion. Again, we saw this effect occurring for furnace-heated samples, but not for pyroprobe-heated samples.

Finally, we attempted to use an intensity reference. In particular, we used  $\text{Tb}:\text{ZrO}_2/\text{Eu}:\text{Y}_2\text{O}_3$ , in which the core was fully crystalline and the shell was a temperature sensitive precursor. During actual heating events, the core would no longer change and

could be used as a reference. Figure 69 shows the spectra and intensity ratios for pyroprobe-heated samples. These results demonstrate the promising nature of using an intensity reference.

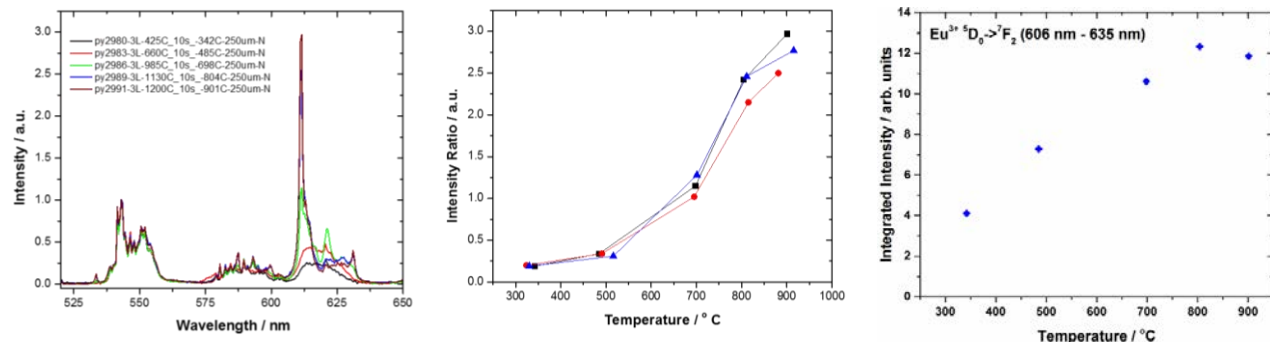


**Figure 69.** Temperature dependent fluorescence spectra (left), corresponding peak intensity ratios (center), and corresponding integrated intensities (right).

Next, we evaluate c-Tb:ZrO<sub>2</sub>/p-Eu:Y<sub>2</sub>O<sub>3</sub>. In order to measure two unknowns, temperature (T) and time (t), the sensor needs to contain two materials with sufficiently different decomposition characteristics. Also, due to potential temperature gradients within the fireball, the two sensor materials need to be able to measure and record in the same location. Furthermore, since the decomposition characteristics are evaluated by the optical emission from rare-earth dopants in the sensor materials, appropriate optical indicators with non-interfering optical spectra need to be identified.

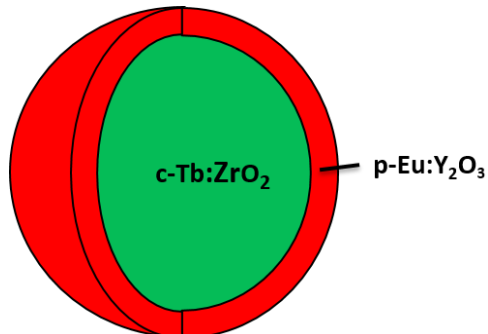
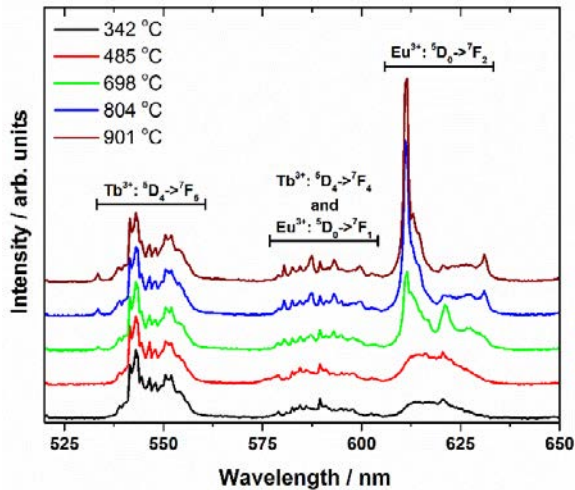


**Figure 70.** Schematic of c-Tb:ZrO<sub>2</sub>/p-Eu:Y<sub>2</sub>O<sub>3</sub> core/shell design.

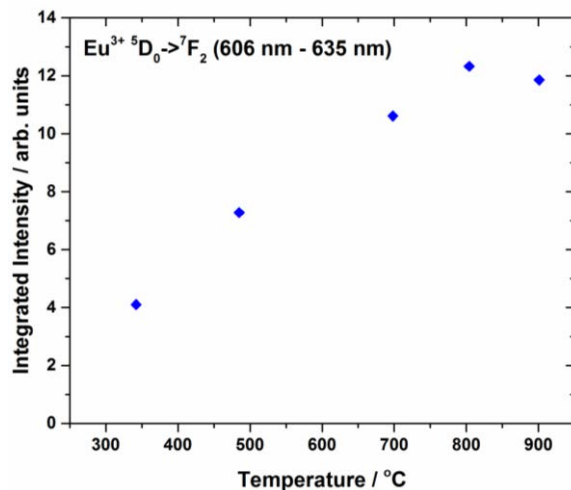
We previously concluded that using sensor materials in a core/shell configuration is the best approach to ensure that they measure and record temperature in the same location within the fireball. Multiple types of core/shell systems based upon a variety of approaches including crystallization, diffusion, and intensity were evaluated. Based upon those measurements, a core/shell/shell system with a built-in fluorescence intensity reference was selected as the most promising approach.

Figure 70 shows a simplified design version that is used to evaluate this approach. These core/shell

nanoparticles are composed of a fully crystalline Tb<sup>3+</sup>-doped ZrO<sub>2</sub> core (calcined at 1000 °C for 30 minutes), and a shell consisting of unheated amorphous Eu:Y<sub>2</sub>O<sub>3</sub> precursors. The shell was prepared by growing three layers of Eu<sup>3+</sup>-doped Y<sub>2</sub>O<sub>3</sub> precursor (p-Eu:Y<sub>2</sub>O<sub>3</sub>) around the crystalline Tb:ZrO<sub>2</sub> core, resulting in Tb:ZrO<sub>2</sub>/p-Eu:Y<sub>2</sub>O<sub>3</sub> core/shell nanoparticles. These core/shell nanoparticles were heated to various temperatures for nominal heating times of 10 s (actual time at maximum temperature was about 1 s) via pyroprobe heating. X-ray diffraction (XRD) spectra show that for high-enough temperatures the p-Eu:Y<sub>2</sub>O<sub>3</sub> shell undergoes an amorphous to crystalline phase changes.



**Figure 71.** Fluorescence spectra of  $\text{Tb:ZrO}_2/\text{p-Eu:Y}_2\text{O}_3$  core/shell nanoparticles heated to various temperatures for 10 s.



**Figure 72.** Integrated  $\text{Eu}^{3+}$   ${}^5\text{D}_0 \rightarrow {}^7\text{F}_2$  fluorescence intensity as a function of temperature.

Figure 71 shows the previously measured fluorescence spectra of these samples for excitation at 488 nm. Since the  $\text{Tb:ZrO}_2$  core is already fully crystallized, its fluorescence intensity is not expected to change due to further heating for short timeframes. The fluorescence spectra were normalized to the intensity of the  $\text{Tb}^{3+}$   ${}^5\text{D}_4 \rightarrow {}^7\text{F}_5$  transition at 543 nm. The integrated fluorescence intensities of the  $\text{Eu}^{3+}$   ${}^5\text{D}_0 \rightarrow {}^7\text{F}_2$  transition from 606 nm to 635 nm are then measured and plotted as a function of temperature, see Figure 72. This integrated fluorescence intensity monotonically increases with temperature until about 800 °C and then slightly decreases.

Continuing with this work, we are evaluating the effect of time on the optical spectra of  $\text{Tb:ZrO}_2/\text{p-Eu:Y}_2\text{O}_3$  core/shell nanoparticles. About 4-7 mg of the core/shell nanoparticles is encapsulated in a 0.0028" thick pyrolytic graphite sheet (Panasonic, Corp.) and heated using a 100 Watt  $\text{CO}_2$  laser, Firestar series f100 (Synrad, Inc.), to 600 °C, 700 °C, 800 °C, and 900 °C. The setpoint temperatures are maintained for holding times between 2 s and 60 s. A high speed PID temperature controller, HA400 (RKC Instruments Inc.), is used to achieve and maintain an isothermal at the setpoint temperature. A type K thermocouple, CHAL005 (Omega Engineering, Inc.) is used to monitor the heating temperature. The heating is performed in a vacuum chamber with reduced atmosphere of about (5–10) Torr to minimize oxidation of the graphite sheet. The heating rate is 200 °C/s. Figure 73 shows typical temperature profiles of the laser-based heating method employed in this work.

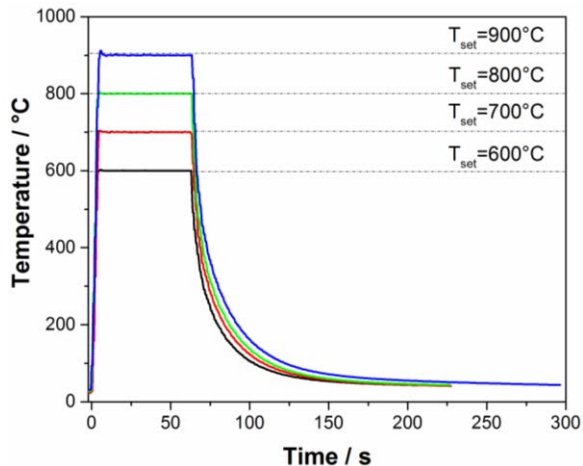


**Figure 73.** Typical temperature profiles of the laser-based heating method employed in this work.

In agreement with our previous data, crystallization of the  $\text{Y}_2\text{O}_3$  phase occurs for heating temperatures of 700 °C, 800 °C, and 900 °C, as indicated by the appearance of the  $\text{Eu}^{3+}$   $^5\text{D}_0 \rightarrow ^7\text{F}_2$  emission peak at 611 nm.<sup>2</sup> Heating to 600 °C is not sufficient to initiate crystallization, even for holding times of 60 s. Figure 74 shows the plots of  $I_{611}/I_{543}$ .

The relative intensity of the  $\text{Eu}^{3+}$  fluorescence, and in particular the intensity of the hypersensitive  $^5\text{D}_0 \rightarrow ^7\text{F}_2$  transition, depends on various parameters. Since the 4f electrons are shielded by outer electrons, interaction with the lattice is minimized. As such, it is mostly the strength of the electric field and the symmetry of the ligands that determine the optical properties of the material.<sup>44</sup> Sharma et al. have reported the effect of solvent, host precursor, dopant concentration, and crystallite size on the fluorescence properties of  $\text{Eu}^{3+}$  doped yttria.<sup>30</sup> In the present case, changes in the intensities can be ascribed to the amorphous to crystalline phase transition, and subsequently nucleation and growth of the crystalline phase. In addition, an initial analysis of the asymmetry R of the Eu sites via comparison of the electric dipole allowed  $^5\text{D}_0 \rightarrow ^7\text{F}_2$  transition and the magnetic dipole allowed  $^5\text{D}_0 \rightarrow ^7\text{F}_1$  transition is shown in Figure 22. These differences indicate that effects due to asymmetry cannot be ruled out.

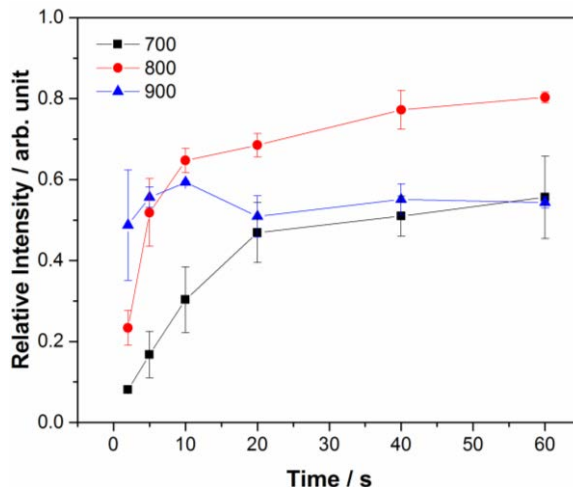


**Figure 74.** Relative fluorescence intensity,  $I_{611}/I_{543}$ , versus time for c-Tb:ZrO<sub>2</sub>/p-Eu:Y<sub>2</sub>O<sub>3</sub> core/shell nanoparticles heated to 700 °C, 800 °C, and 900 °C for 2 s – 60 s.

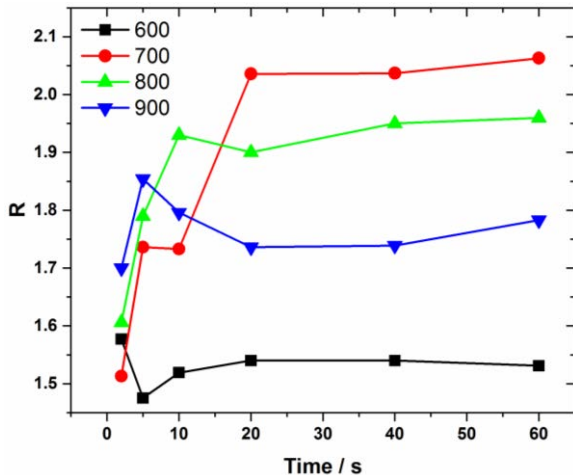


**Figure 75.** Time-dependent asymmetry ratio for various heating temperatures. Higher ratios indicate a larger degree of asymmetry.<sup>45</sup>

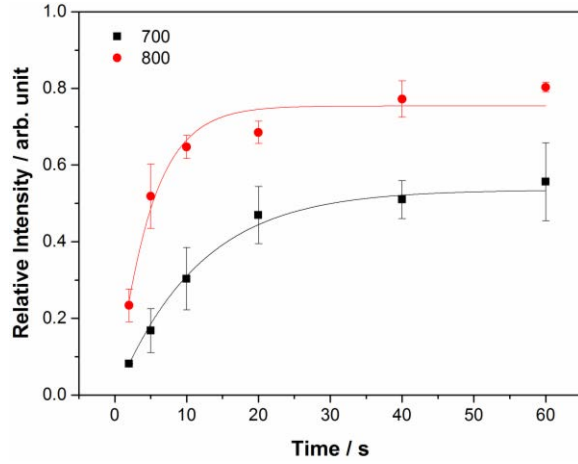


**Figure 76.** Plots of normalized fluorescence intensity,  $I_{611}/I_{543}$ , versus time for  $Tb:ZrO_2/p\text{-}Eu:Y_2O_3$  core/shell nanoparticles that were heated to 700 °C, 800 °C, and 900 °C for 2 s - 60 s fitted with the kinetic model.

Figure 74 shows that for the 2 s heating the fluorescence intensity is directly proportional with temperature. The value is highest for the 900 °C and lowest for the 700 °C heating temperature. Likewise, the equilibrium fluorescence intensity of the samples heated to 800 °C is higher than those that were heated to 700 °C. However, for the samples that were heated to 900 °C, the equilibrium fluorescence intensity is on par with that of the samples heated to 700 °C.

It is believed that the increasing trend in the fluorescence intensity of the  $^5D_0 \rightarrow ^7F_2$  transition in the samples heated to 700 °C, 800 °C, and 900 °C between 2 s and 60 s correspond to nuclei formation of the Eu:Y<sub>2</sub>O<sub>3</sub> phase, and that the fluorescence intensity is directly proportional to the number of nuclei formed. At 900 °C heating temperature, the nucleation stage has quickly reached completion within the 2 s timeframe, and the kinetic mechanism is subsequently dominated by crystallite growth. At this stage, there is little untransformed material for nuclei to form in. Instead, each of the formed nuclei fuse into each other to form larger crystals. It was reported that the fluorescence intensity of the  $^5D_0 \rightarrow ^7F_2$  transition of the Eu<sup>3+</sup> ion is inversely proportional with crystallite size.<sup>30, 46</sup> As such, the lower fluorescence intensity in the samples heated to 900 °C might reflect significantly larger crystallite grain sizes compared to those heated to 700 °C and 800 °C. Alternatively, the reduction in the intensities may be due to the asymmetry effect. As shown in Figure 75, the sample heated to 900 °C has a lower equilibrium R value than the samples heated to 700 °C and 800 °C. A lower R value indicates higher symmetry and lower fluorescence intensity due to the electric dipole nature of this transition.<sup>45</sup>

For the samples heated to 700 °C and 800 °C, where the amorphous to crystalline nucleation mechanism dominates, the trend in the change in the relative intensity of the Eu<sup>3+</sup> fluorescence as a function of time has the characteristics of the well-known Johnson-Mehl-Avrami-Kolmogorov (JMAK) model, which has the following general form:<sup>47-50</sup>

$$\phi(t) = 1 - e^{-kt^n} \quad (40)$$

where,  $k$  and  $n$  are the Avrami constants, and  $\phi(t)$  is the time-dependent fraction of transformation. The major characteristic of the JMAK model is the s-shaped profile that indicates a low rate of transformation at the beginning and at the end of the transformation, but rapid transformation in between. The equation was used to describe **the formation of spherical nuclei having a “ $\beta$ ” phase in a matrix having an “ $\alpha$ ” phase.** The above equation has also been successfully applied to describe the grain growth kinetics of nanocrystalline materials.<sup>2, 12</sup> By assuming that the fluorescence intensity,  $I$ , of the  ${}^5D_0 \rightarrow {}^7F_2$  transition of the Eu<sup>3+</sup> ion for the samples that were heated to 700 and 800 °C is proportional to the fraction of transformed phase, we write Equation 36 as follows:

$$\frac{I - I_0}{I_\infty - I_0} = 1 - e^{-kt^n} \quad (41)$$

where,  $I$  is the instantaneous fluorescence intensity,  $I_0$  is the initial intensity at the start of nucleation, which is taken to be zero, and  $I_\infty$  is the equilibrium (limiting) intensity at that temperature.

At the onset of nucleation the relative fluorescence intensity at 611 nm is close to zero, see Figure 76. Over time, the fluorescence intensity evolves towards a maximum equilibrium (limiting) value. In between the nucleation and the equilibrium stage, the fluorescence intensity increases rapidly. Figure 76 shows that equation 2 fits well to the plot of relative intensity versus temperature of the samples that were heated to 700 °C and 800 °C between 2 s and 60 s. The former yields  $k_{700C}=0.0802$ ,  $n=1.03$ , and  $I_\infty=0.54$  with  $R^2=0.998$ , and the latter yields  $k_{800C}=0.19$  and  $n=1.05$  with  $R^2=0.98$ . It can be seen that  $k_{800C} > k_{700C}$  which is consistent with increased nucleation rate at higher temperature.

Work is underway to verify the suitability of the kinetic model, and to generate additional data in the vicinity of the 700 °C and 800 °C heating temperatures to yield a temperature-dependent Arrhenius plot, which is needed to obtain the complete time-temperature dependent kinetic equation. In addition, the effects of asymmetry and grain size need to be further evaluated. Finally, additional indicators such as excitation spectra need to be evaluated to include lower temperature regimes in the analysis.

As part of this evaluation, we also characterized p-Tb:ZrO<sub>2</sub>/p-Eu:Y<sub>2</sub>O<sub>3</sub> and p-Eu:ZrO<sub>2</sub>/p-Tb:Y<sub>2</sub>O<sub>3</sub>. The spectra shown in Figure 71 indicate that the emission intensity of the Eu<sup>3+</sup>  ${}^5D_0 \rightarrow {}^7F_1$  transition (about 580 – 600 nm range) appears to be constant. This observation is not completely surprising, as this particular transition is magnetic dipole allowed and as such not sensitive to symmetry changes in the host material. It does however indicate that it might be possible to use this particular transition as a built-in intensity reference which would eliminate the need for a separate reference material.

In order to evaluate the potential of using the Eu  ${}^5D_0 \rightarrow {}^7F_1$  transition as a built-in reference, we synthesized p-Tb:ZrO<sub>2</sub>/p-Eu:Y<sub>2</sub>O<sub>3</sub> and p-Eu:ZrO<sub>2</sub>/p-Tb:Y<sub>2</sub>O<sub>3</sub> core/shell nanoparticles and evaluated them for a large (T, t) space using the newly operational laser-heating setup with the goal to perform a kinetic analysis on these sensors. Temperature and times of the (T,t) space include (200, 400, 600, 800, and 950) °C and (2, 5, 10, 20, 40, 60) s, respectively. Excitation wavelength of 488 nm and 533.6 nm were used. 488 nm excites Tb and Eu, while 533.6 nm only excites Eu. Figure 77 shows an XRD spectra and two fluorescence spectra of p-Eu:ZrO<sub>2</sub>/p-Tb:Y<sub>2</sub>O<sub>3</sub> core/shell nanoparticles excited with 488 nm and 533.6 nm, respectively.

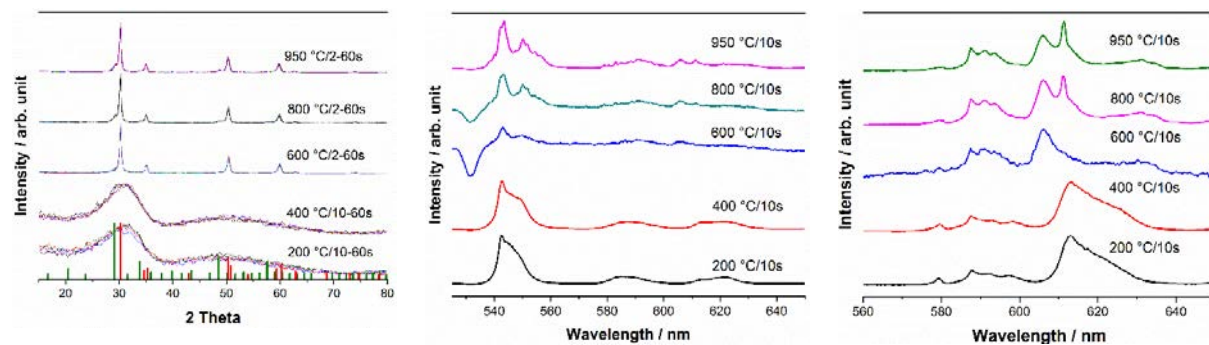


**Figure 77.** XRD spectra (left), and fluorescence spectra of p-Eu:ZrO<sub>2</sub>/p-Tb:Y<sub>2</sub>O<sub>3</sub> core/shell nanoparticles excited with 488 nm (center) and 533.6 nm (right), respectively.

The fluorescence spectra can be correlated with the formations of the tetragonal ZrO<sub>2</sub> (t-ZrO<sub>2</sub>) and cubic Y<sub>2</sub>O<sub>3</sub> (c-Y<sub>2</sub>O<sub>3</sub>) phases. XRD shows that the c-Y<sub>2</sub>O<sub>3</sub> phase is formed at 800 °C and higher temperatures, while the t-ZrO<sub>2</sub> phase is formed at 600 °C and higher temperatures. Similarly, the fluorescence spectra show that Tb is located in a crystalline t-ZrO<sub>2</sub> phase starting at 600 °C, while Eu is located in a c-Y<sub>2</sub>O<sub>3</sub> phase starting at 800 °C.

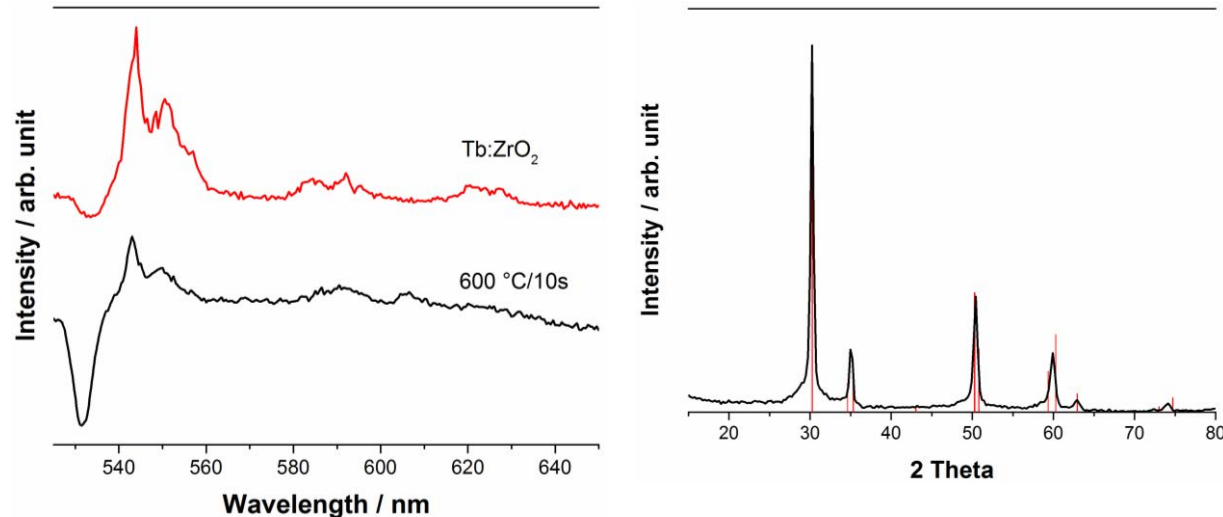


**Figure 78.** Fluorescence excited with 488 nm (left) and XRD (right) of p-Eu:ZrO<sub>2</sub>/p-Tb:Y<sub>2</sub>O<sub>3</sub> core/shell nanoparticles heated to 600 °C for 10 s compared with those of a fully crystalline Tb:ZrO<sub>2</sub> sample.

The optical and XRD spectra of the heated samples can then be compared with reference samples. Figure 78 shows the data for p-Eu:ZrO<sub>2</sub>/p-Tb:Y<sub>2</sub>O<sub>3</sub> core/shell nanoparticles heated to 600 °C for 10 s. Figure 79 shows the fluorescence spectra and XRD spectrum of p-Eu:ZrO<sub>2</sub>/p-Tb:Y<sub>2</sub>O<sub>3</sub> core/shell nanoparticles heated to 800 °C for 10 s and reference samples. The spectra indicate that diffusion across the interface occurs and the spectra can be assigned to the Eu:t-ZrO<sub>2</sub> and Eu:Y<sub>2</sub>O<sub>3</sub> phases.

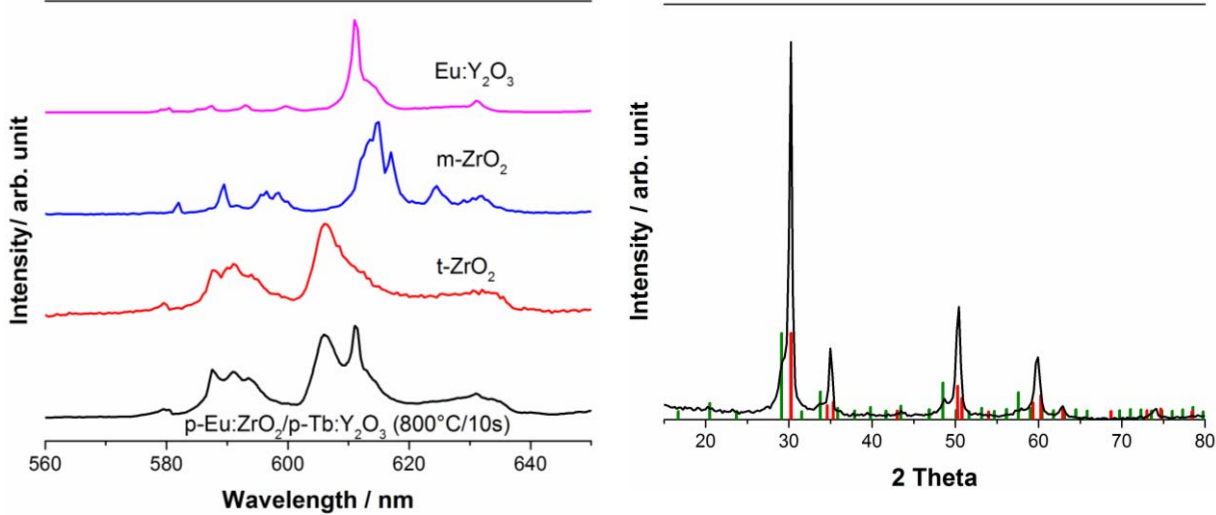


**Figure 79.** Fluorescence spectra (left) and XRD spectrum (right) of p-Eu:ZrO<sub>2</sub>/p-Tb:Y<sub>2</sub>O<sub>3</sub> core/shell nanoparticles heated to 800 °C for 10 s and reference samples. The spectra can be assigned to the Eu:t-ZrO<sub>2</sub> and Eu:Y<sub>2</sub>O<sub>3</sub> phases.

Using the fluorescence spectra, five distinct phases can be identified within the evaluated (T,t) space. However, in some cases (e.g. regions IV and V) the differences are not as conclusive as in other cases. Figure 80 shows the fluorescence spectra, exciting Tb and Eu using 488 nm, belonging to the different regions, as well the resulting phase diagram. Regions I, II, III, IV, and V correspond to the following heat treatments: 200 °C and 400 °C for (10, 20, 30, 45, and 60) s; 600 °C for (10, 20, 30, 45, and 60) s; 800 °C for (2 and 5) s; 800 °C for (10, 20, 30, 45, and 60) s and 950 °C for (2 and 5) s; and 950 °C for (10, 20, 30, 45, and 60) s, respectively.

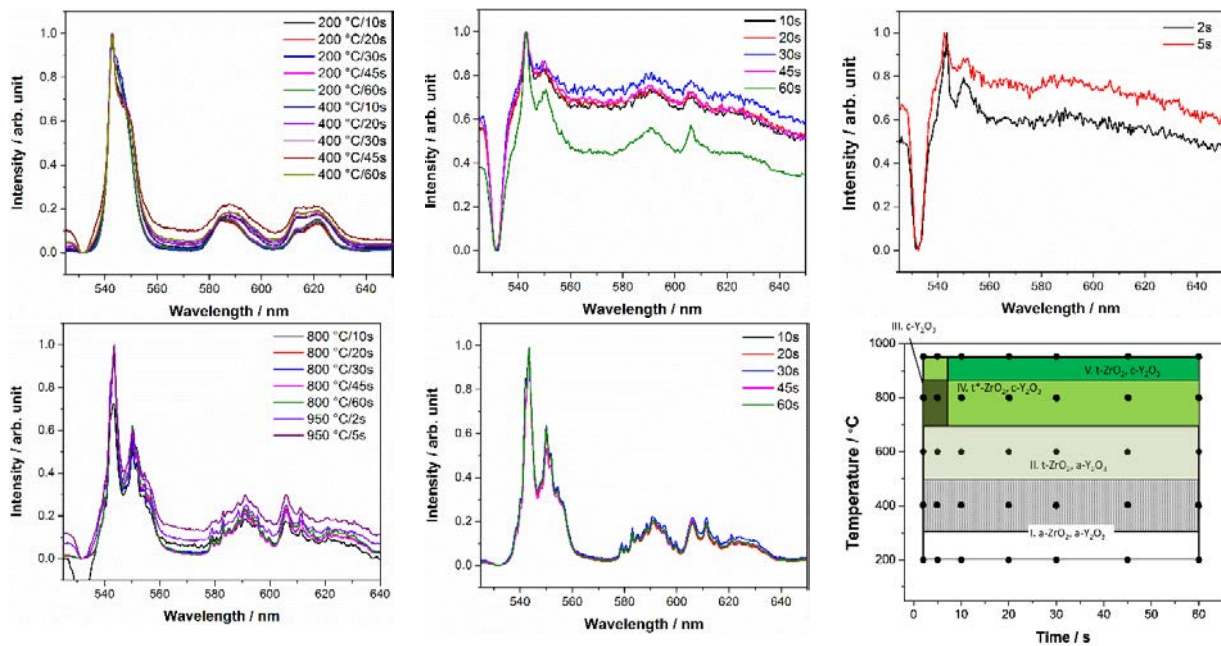


**Figure 80.** Distinct phases in (T,t) space and resulting phase diagram for 488 nm excitation.

Figure 81 shows the spectra, exciting Eu using 533.6 nm, belonging to the different regions, as well the resulting phase diagram. These assignments are somewhat less ambiguous than the ones resulting from excitation at 488 nm. Regions I, II, III, IV, and V correspond to the following heat treatments: 200 °C and 400 °C for (10, 20, 30, 45, and 60) s; 600 °C for (2, 5, 10, 20, 30, 45, and 60) s; 800 °C and 950 °C for (2 and 5) s; 800 °C for (10, 20, 30, 45, and 60) s; and 950 °C for (10, 20, 30, 45, and 60) s, respectively. Depending on the specific excitation wavelength chosen, some emission from the crystalline Tb compound can overlap with the emission from the precursor Eu compound.

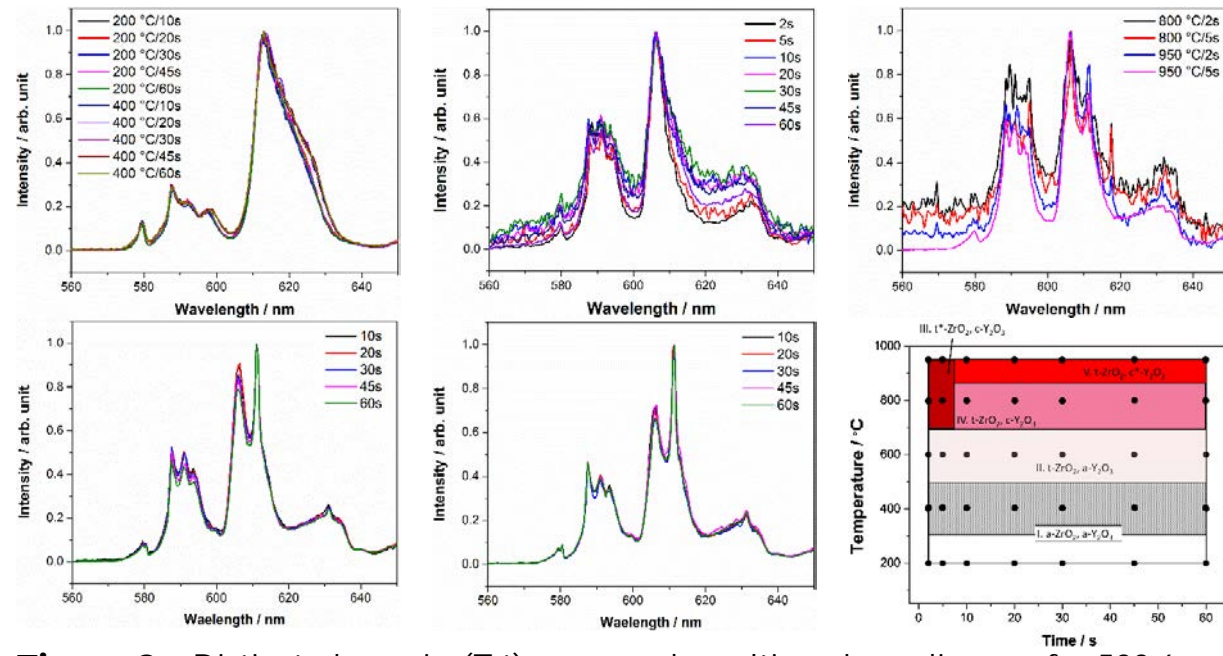


**Figure 81.** Distinct phases in (T,t) space and resulting phase diagram for 533.6 nm excitation.

### p-Eu:ZrO<sub>2</sub> + c-Ho:ZrO<sub>2</sub> + p-Dy:Y<sub>2</sub>O<sub>3</sub>

To minimize spectral overlap issues, the following mixture has been chosen as the most promising compound, even though it requires two measurements using two different excitation wavelength: p-Eu:ZrO<sub>2</sub> + c-Ho:ZrO<sub>2</sub> + p-Dy:Y<sub>2</sub>O<sub>3</sub>.

First, we evaluate a mixture of c-Ho:ZrO<sub>2</sub> and p-Dy:Y<sub>2</sub>O<sub>3</sub>. The emission spectra of the unheated materials for excitation at 355 nm are shown in Figure 82 and Figure 83. Figure 82 shows the spectra of the individual components. While there is some spectral overlap, significant portions of the peaks do not suffer from overlap. Figure 83 shows the spectra of combined mixtures for different ratios. Even though p-Dy:Y<sub>2</sub>O<sub>3</sub> is a precursor material, its emission intensity is very strong compared to the crystalline c-Ho:ZrO<sub>2</sub>. Figure 84 shows the emission spectra of heated (950 °C) c-Ho:ZrO<sub>2</sub> + p-Dy:Y<sub>2</sub>O<sub>3</sub> for several ratios. The spectra are dominated by the Dy emission, indicating that the ratio needs to be adjusted.

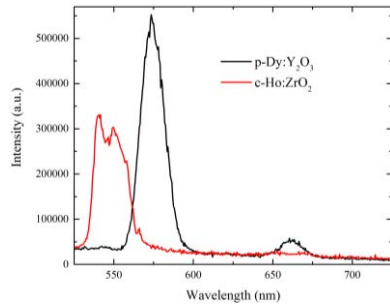


**Figure 82.** Individual spectra of unheated c-Ho:ZrO<sub>2</sub> and p-Dy:Y<sub>2</sub>O<sub>3</sub>.

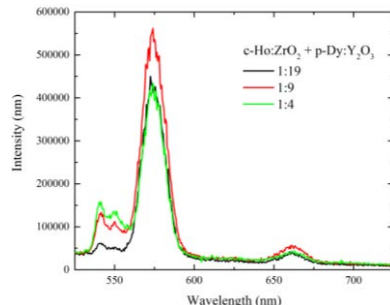


**Figure 83.** Spectra of unheated mixtures of c-Ho:ZrO<sub>2</sub> and p-Dy:Y<sub>2</sub>O<sub>3</sub>. The Ho emission is much weaker than the Dy emission.

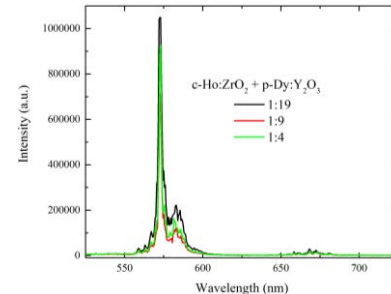


**Figure 84.** Spectra of heated c-Ho:ZrO<sub>2</sub>+p-Dy:Y<sub>2</sub>O<sub>3</sub>. The Dy peak dominates the emission for all ratios tested.

Figure 85 shows the individual spectra of unheated Eu:ZrO<sub>2</sub> and c-Ho:ZrO<sub>2</sub>/p-Dy:Y<sub>2</sub>O<sub>3</sub> core/shell particles excited at 355 nm, and Figure 86 shows the spectra of the unheated mixture for various ratios. Figure 87 shows the spectra of heated (950 °C) mixtures for various ratios. Again, the Dy emission dominates the spectra.

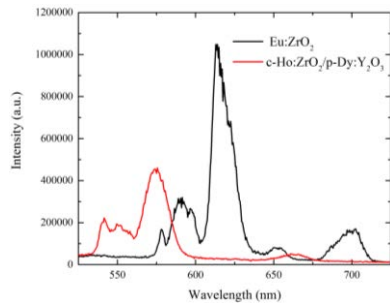


**Figure 85.** Individual spectra of unheated Eu:ZrO<sub>2</sub> and c-Ho:ZrO<sub>2</sub>/p-Dy:Y<sub>2</sub>O<sub>3</sub>.

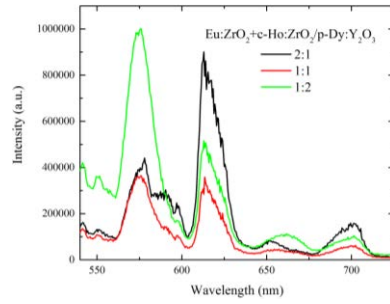


**Figure 86.** Spectra of different mixtures of unheated Eu:ZrO<sub>2</sub> and c-Ho:ZrO<sub>2</sub>/p-Dy:Y<sub>2</sub>O<sub>3</sub>.

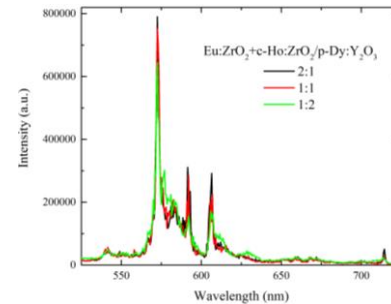


**Figure 87.** Spectra of heated mixture of Eu:ZrO<sub>2</sub> and c-Ho:ZrO<sub>2</sub>/p-Dy:Y<sub>2</sub>O<sub>3</sub>. The Dy emission dominates the heated spectrum.

However, the overall shape of the spectra depends on the excitation wavelength. Figure 88 shows the spectra of heated Eu:ZrO<sub>2</sub> + c-Ho:ZrO<sub>2</sub>/p-Dy:Y<sub>2</sub>O<sub>3</sub> for four different excitation wavelengths, 355 nm, 365 nm, 488 nm, and 532 nm, and Figure 89 shows a direct comparison of the emission spectra of Eu:ZrO<sub>2</sub> + c-Ho:ZrO<sub>2</sub> + p-Dy:Y<sub>2</sub>O<sub>3</sub> in a 1:1:1 ratio. Considering the relative emission intensities of the different compounds and potential corresponding spectral overlap, one possible combination of excitation wavelengths is 355 nm and 532 nm.

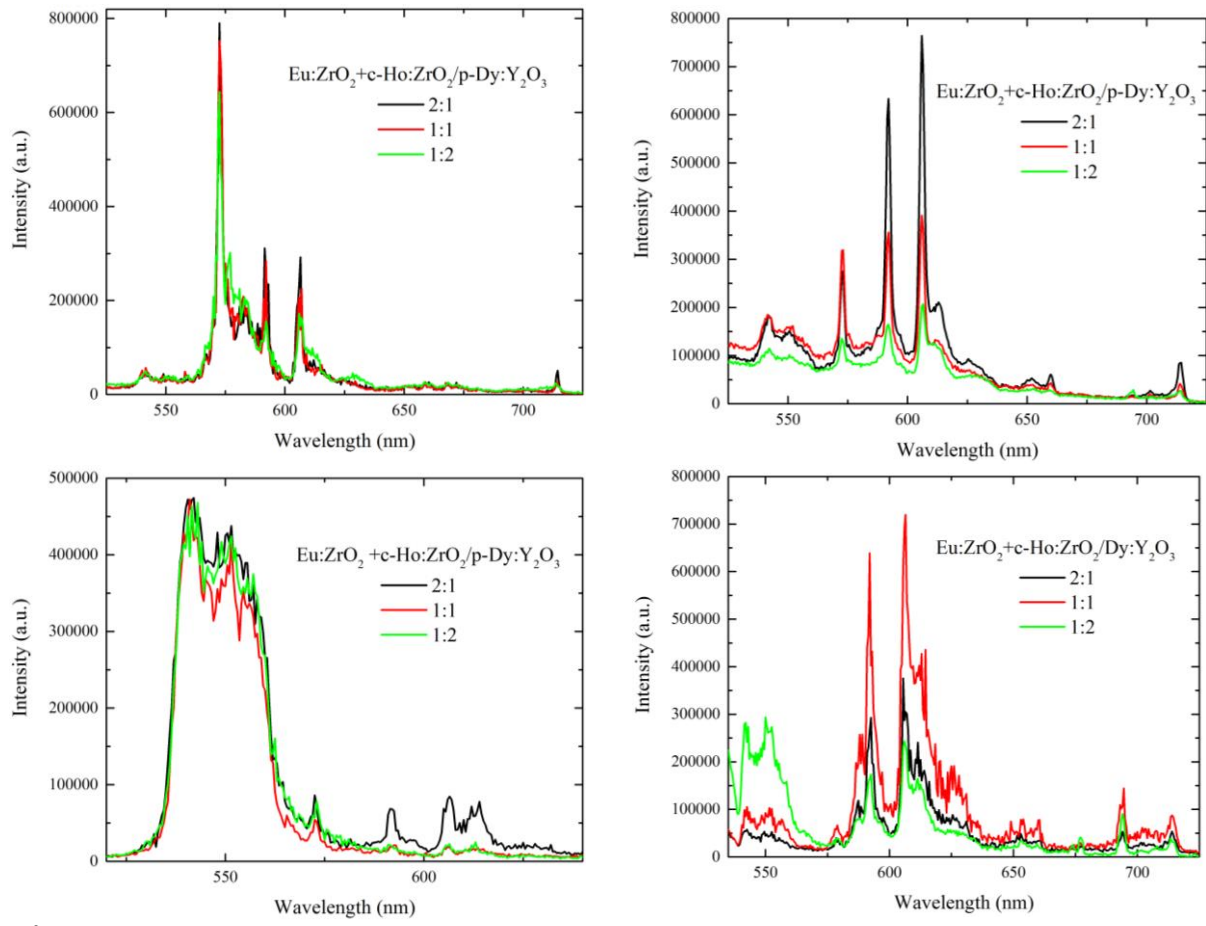


**Figure 88.** Spectra of heated mixtures of  $\text{Eu:ZrO}_2+\text{c-Ho:ZrO}_2/\text{p-Dy:Y}_2\text{O}_3$  for excitation at 355 nm (top left), 365 nm (top right), 488 nm (bottom left), and 532 nm (bottom right).

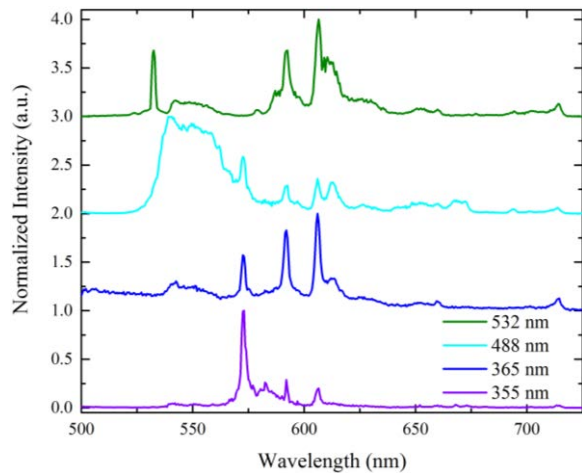


**Figure 89.** Spectra of an equal ratio of  $\text{Eu:ZrO}_2+\text{c-Ho:ZrO}_2+\text{p-Dy:Y}_2\text{O}_3$  for different excitation wavelengths. For excitation using 532 nm the Dy peak is unobserved and a residual pump peak is observed even with the notch filter.

We performed an initial evaluation of the thermal impulse sensor combination p-Eu:ZrO<sub>2</sub> + c-Ho:ZrO<sub>2</sub> + p-Dy:Y<sub>2</sub>O<sub>3</sub>. Using indirect laser heating, sample material was heated to various temperatures for specific isothermal heating durations. The fluorescence spectra of these samples were then measured using pulsed 355 nm laser pulses, see Figure 90.

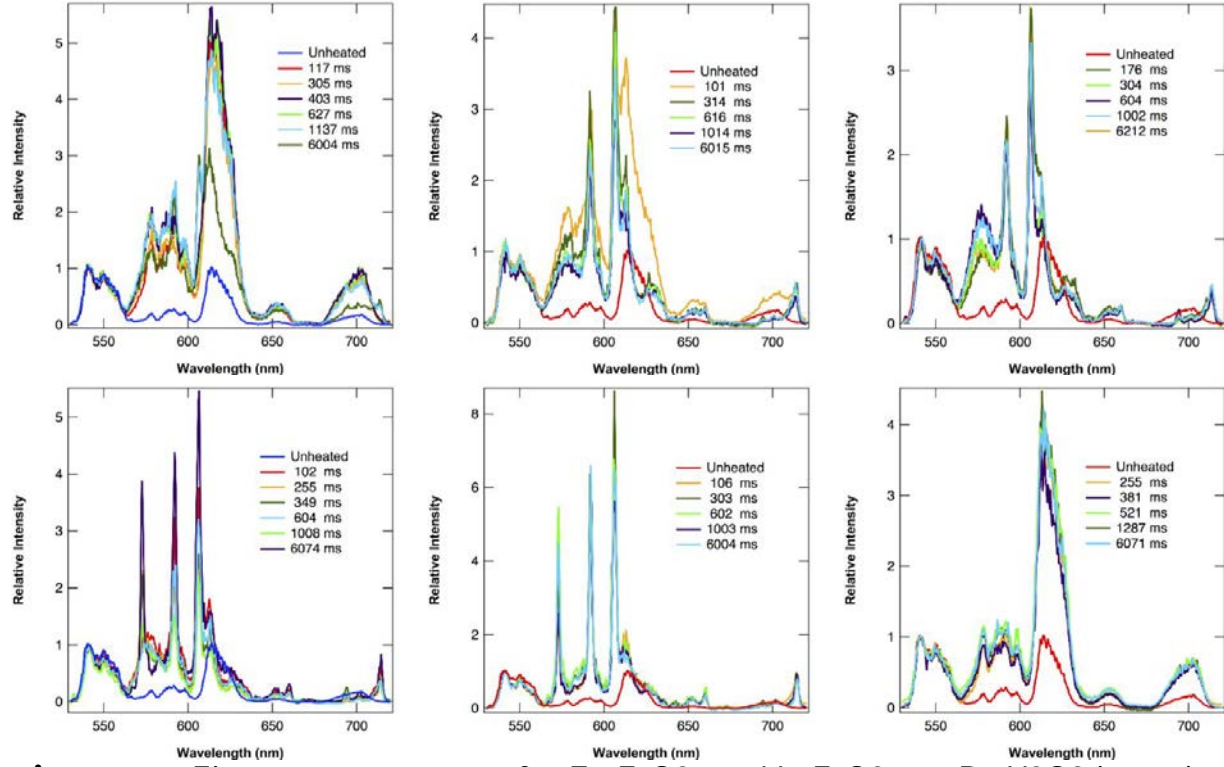


**Figure 90.** Fluorescence spectra of p-Eu:ZrO<sub>2</sub> + c-Ho:ZrO<sub>2</sub> + p-Dy:Y<sub>2</sub>O<sub>3</sub> heated to 400 °C (top left), 500 °C (top center), 600 °C (top right), 700 °C (bottom left), 800 °C (bottom center), and 900 °C (bottom right) for various times.

In addition to using Ho peaks for computing intensity ratios, we also calculate ratios using internal peaks (i.e. different peaks from the same material). For Dy:Y<sub>2</sub>O<sub>3</sub> we use the ratio between the intensity at 573 nm and 578 nm. These wavelengths are chosen because amorphous Dy:Y<sub>2</sub>O<sub>3</sub> is found to have a broad peak centered at 578 nm and crystalline Dy:Y<sub>2</sub>O<sub>3</sub> is found to have a sharp peak at 573 nm. The ratio between the two therefore corresponds to a direct measure of the crystallinity of the Dy:Y<sub>2</sub>O<sub>3</sub>. Figure 91 shows the 573/578 ratio as a function of isothermal time with fits to a simple exponential. From Figure 91 we find that there is a drastic change in the ratios behavior as a function of time between 700 °C and 800 °C. This corresponds to the temperature range in which crystallization can occur.

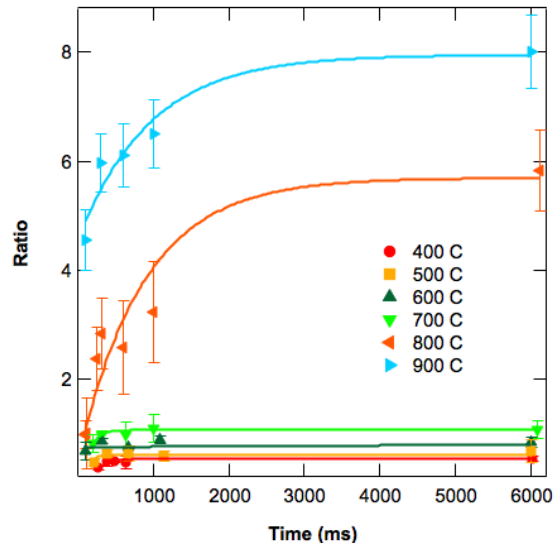


**Figure 91.** Ratio of fluorescence intensities at 573 nm and 578 nm as a function of time.

While Dy:Y<sub>2</sub>O<sub>3</sub> has one very clear and clean intensity ratio to consider for measuring phase changes, Eu:ZrO<sub>2</sub> has multiple peaks which change with temperature and time leading to several different intensity ratios we can use for extracting temperature and time. The main peaks of Eu:ZrO<sub>2</sub> we can use for this purpose are at 592 nm, 606 nm, 613 nm, 631 nm, 660 nm, and 714 nm. Additionally, the intensity at 620 nm drastically changes during crystallization as the 613 nm peaks FWHM collapses. Figure 92 shows the 592/613 ratio as a function of time for various temperatures.

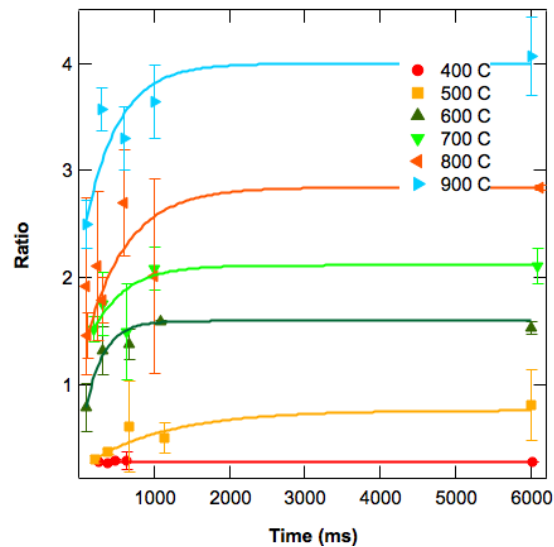


**Figure 92.** 592/613 Ratio as a function of time for different temperatures.

After obtaining the ratio curves as a function of time and temperature we first attempted to fit the fluorescence ratios to the isothermal degree of conversion function and discovered that the single phase model fails to adequately describe the observed phenomenon. Therefore in order to use the calibration data to determine temperature

and time we instead use a phenomenological model. For our phenomenological model we define the ratios as a function of time  $t$ , to follow an exponential function:

$$R(T, t) = R_\infty(T) - [R_\infty(T) - R_0(T)]e^{-g(T)t} \quad (42)$$

where  $g(T)$  is the exponential rate as a function of temperature,  $R_\infty(T)$  is the asymptotic ratio as a function of temperature, and  $R_0(T)$  is the ratio offset as a function of temperature. The ratio offset is related to the effects of slow heating rates.

Using Equation 42, we fit the 573/541 ratio and 592/613 ratio as a function of time for each temperature tested. Figure 93 shows the fit parameters as a function of temperature for the 573/541 ratio and Figure 94 shows the fit parameters as a function of temperature for the 592/613 ratio. The parameters for 592/613 behave as expected, with each parameter increasing with temperature. However, for the 573/541 ratio the exponential rate behaves opposite to what is expected with the rate decreasing with temperature. The nature of this result is currently unknown.

While the basic behavior of the fit parameters as a function of time is as expected, the precise functional form is found to be different than expected. The parameters (aside from the 573/541 rate) are found to follow a modified Arrhenius function given by:

$$f(T) = f_0 + A \exp\left\{-\left(\frac{E}{kT}\right)^\beta\right\} \quad (43)$$

where the stretch parameter  $\beta$  is found to be greater than 1. For fitting the 573/541 rate we use a simple power function.

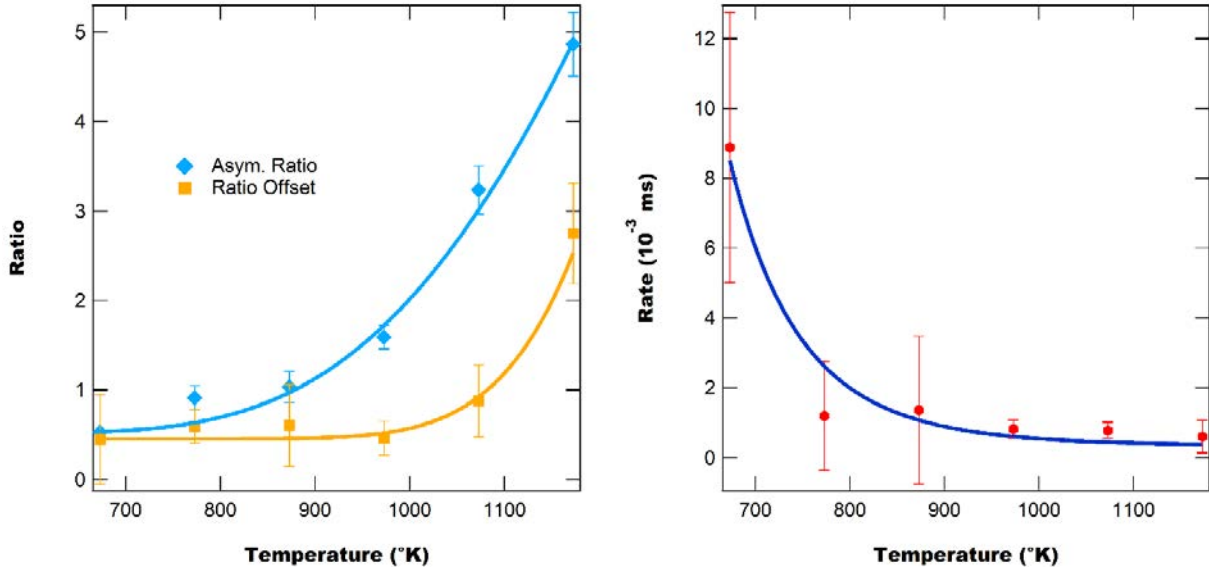


**Figure 93.** Ratio versus time fit parameters as a function of temperature for the 573/541 ratio.

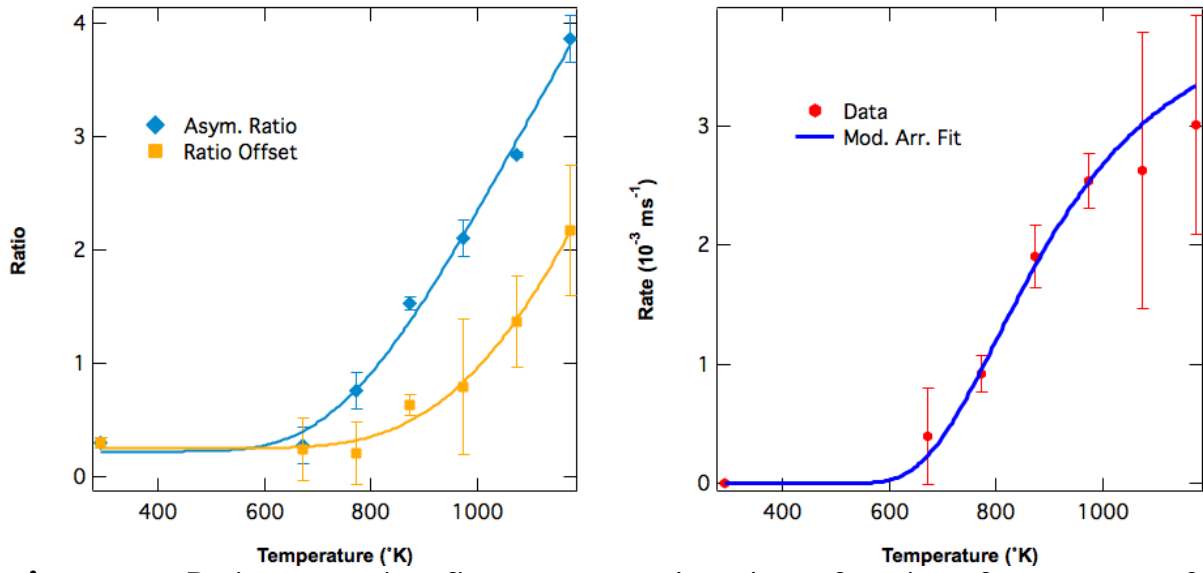


**Figure 94.** Ratio versus time fit parameters plotted as a function of temperature for the 592/613 ratio. All three parameters are found to follow a modified Arrhenius fit function.

Using the parameter curves as a function of temperature – determined from fitting the data shown in Figure 93 and Figure 94 – and using Equation 42, we can determine a functional mapping of the ratios as a function of temperature and time. Figure 95 shows the ratio maps as a function of temperature and time for the 573/541 ratio and 592/613 ratio.

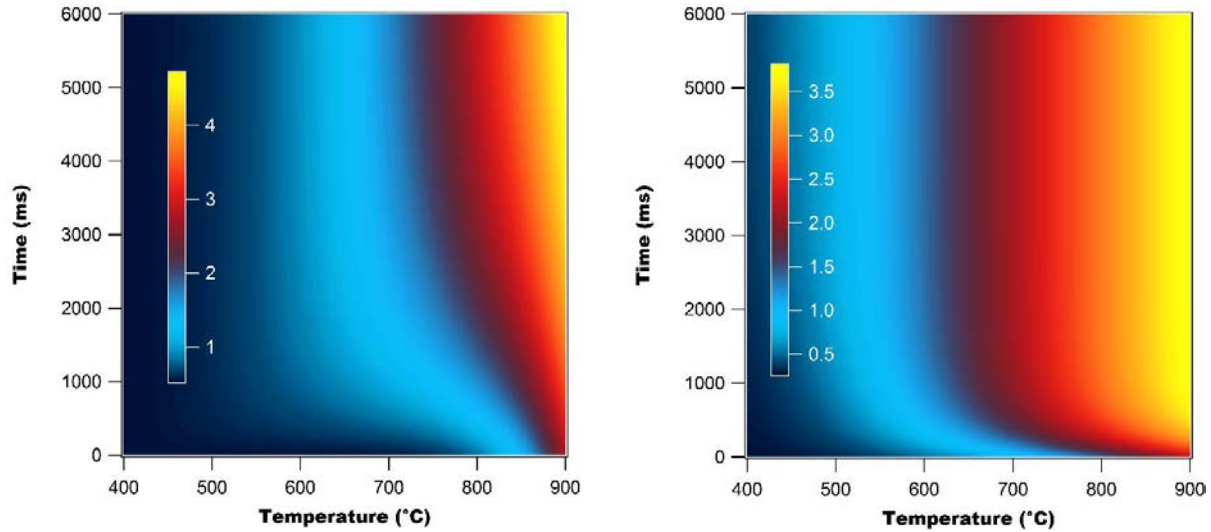


**Figure 95.** Ratio maps as a function of time and temperature for two 573/541 (left) and 592/613 (right) intensity ratios.

The current measurements have relatively large uncertainties. A variety of factors are responsible:

1. The laser profile is spatially and possibly temporally inhomogeneous, showing various hot spots. These hot spots lead to inhomogeneous heating of the samples during direct laser heating.
2. Due to the inhomogeneous laser profile, we are currently working with an indirect laser heating method. This method relies on heat-conductivity (graphite sheets) to spread the heat throughout the sample. The finite heat conductivity leads to temperature gradients across the graphite sheet and the sample material.
3. The indirect laser heating method also limits the heating rate to 300 °C to 400 °C (i.e. a sample heated to 800 °C for 100 ms also experienced 2 s of ramp-up heating).
4. There is some uncertainty due to sample handling during the heating procedure.
5. Shot-to-shot noise during spectral measurements.

The root causes of these uncertainties will be addressed next to improve the accuracy of the combined temperature and heating duration measurements. Meanwhile, an initial test using five blind samples yielded the following results, see Table 10. Addressing the above listed sources of uncertainty, the results are expected to significantly improve.

**Table 10.** Analysis result for five blind samples.

	<b>Heating temperature and duration</b>		<b>Measured heating temperature and duration.</b>	
<b>Sample</b>	<b>T (K)</b>	<b>t (ms)</b>	<b>T (K)</b>	<b>t (ms)</b>
1	673	1003	623 - 723	100 - 6000
2	1173	114	1181 – 1228	350 – 790
3	873	303	888 – 958	100 – 400
4	unheated		unheated	
5	1073	605	1077 – 1159	13 – 185

## E. Tracking Sensors

Since heating in an explosive environment is expected to be spatially inhomogeneous, it is important to know the provenance of the temperature sensors. As such, we prepared and evaluated different tracking particles that can be mix in with the temperature sensors to provide information about their original location. These tracking particles consist of fully crystallized rare-earth doped yttria, including Eu:Y<sub>2</sub>O<sub>3</sub>, Tb:Y<sub>2</sub>O<sub>3</sub>, Dy:Y<sub>2</sub>O<sub>3</sub>, Sm:Y<sub>2</sub>O<sub>3</sub>, Er,Yb:Y<sub>2</sub>O<sub>3</sub>, Ho:Y<sub>2</sub>O<sub>3</sub>, Pr:Y<sub>2</sub>O<sub>3</sub>, Nd:Y<sub>2</sub>O<sub>3</sub>, and Tm:Y<sub>2</sub>O<sub>3</sub>. After preparing these materials, their fluorescence spectra were measured and compared with those of the temperature sensor materials to make sure the spectral emission does not interfere, see Figure 96.

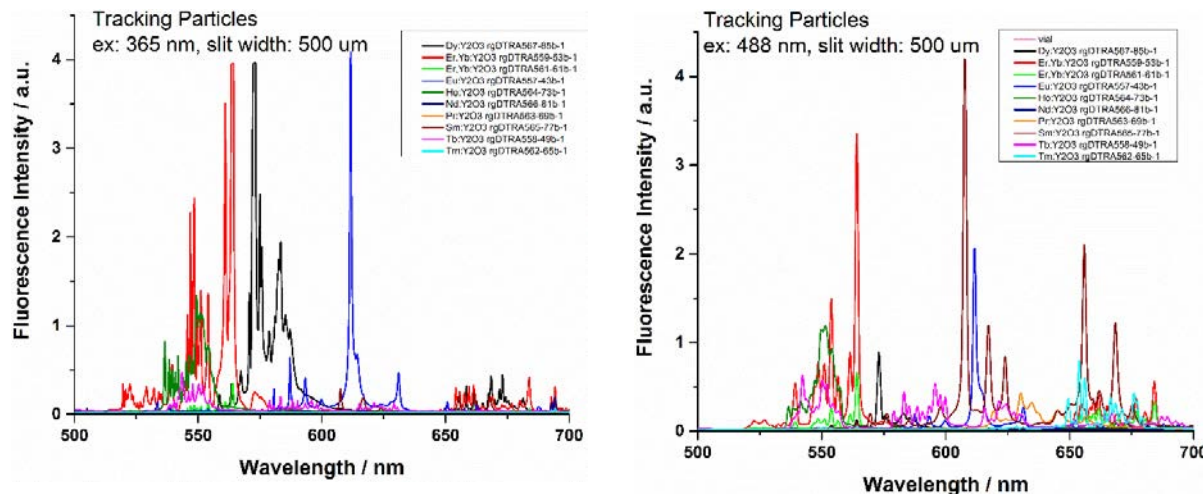


**Figure 96.** Fluorescence spectra of potential tracking particles for excitation with 365 nm (left) and 488 nm (right).

As can be seen from Figure 96, excitation with different wavelengths leads to significantly different fluorescence spectra. Based upon our analysis, we selected Dy:Y<sub>2</sub>O<sub>3</sub>, Sm:Y<sub>2</sub>O<sub>3</sub>, and Er,Yb:Y<sub>2</sub>O<sub>3</sub> for initial explosion testing.

The layout for the explosion testing is shown in Figure 97. A charge was placed in the center of the room and 1.5 g each of the three tracking particles was wrapped in a paper bag and hung from the ceiling at distances of **2'**, **4'**, and **6'**, respectively. Post-detonation, debris samples were collected in the areas marked a through i. Also shown in the figure are the tracking particles detected in those specific area. No tracking particles were detected in area c. Dy:Y<sub>2</sub>O<sub>3</sub> was detected in all other areas, which is probably due to its very strong fluorescence compared to the other samples. Sm:Y<sub>2</sub>O<sub>3</sub> was detected only in areas a and d. Its fluorescence intensity is significantly weaker than that of Dy:Y<sub>2</sub>O<sub>3</sub>. Er,Yb:Y<sub>2</sub>O<sub>3</sub> was detected in five of the areas.

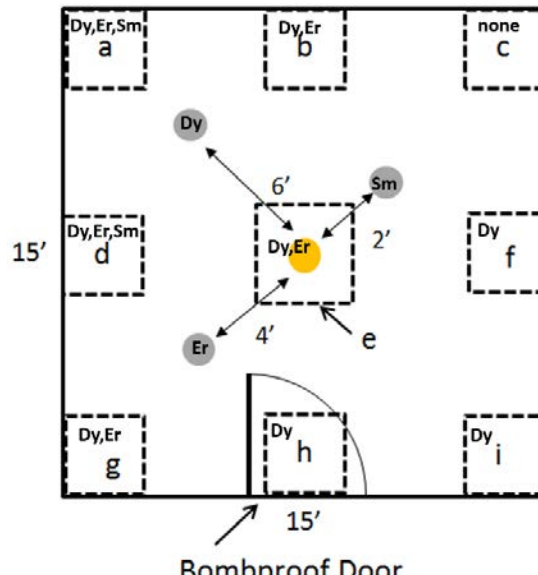


**Figure 97.** Layout for explosion test of tracking particles.

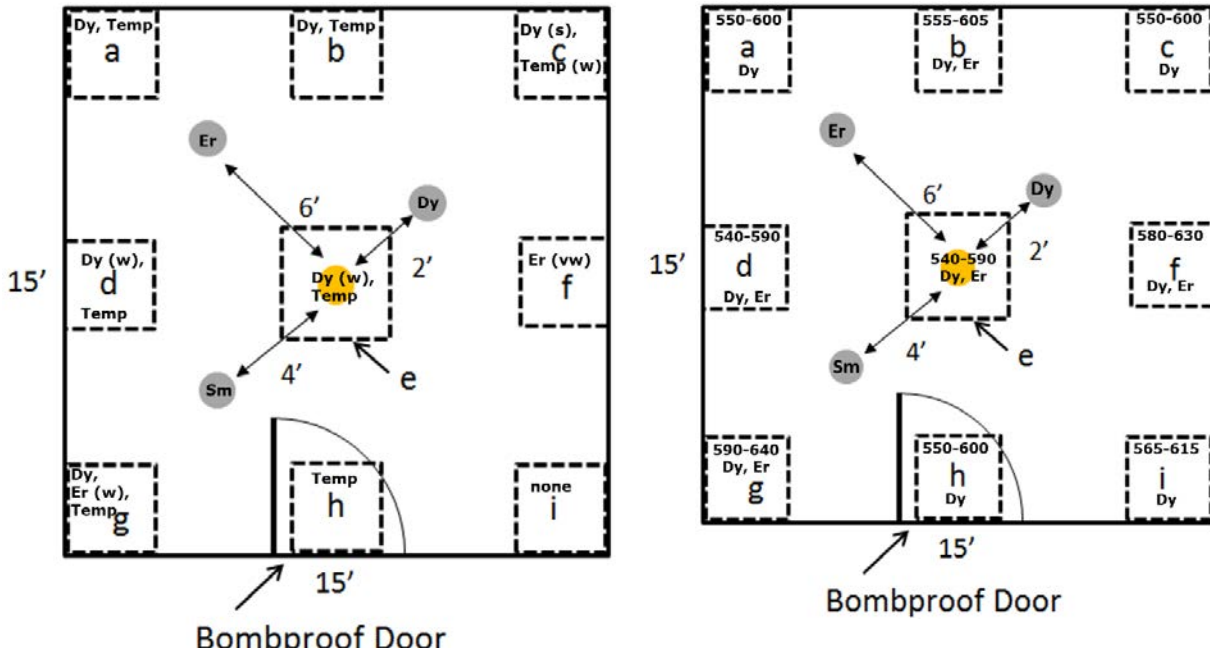


**Figure 98.** Layout for explosion test of tracking particles combined with p-Eu:Y<sub>2</sub>O<sub>3</sub>/c-Tb:Y<sub>2</sub>O<sub>3</sub> temperature sensors. We were unable to measure a response from this sensor material.

The quasi-static temperature, measured via a thermocouple, for shot 2 at a distance of 6'' was 430 °C. This corresponds to a difference of about 17% to 24% between the thermocouple and the temperature sensor measurements, with the temperature sensors measuring the higher values.

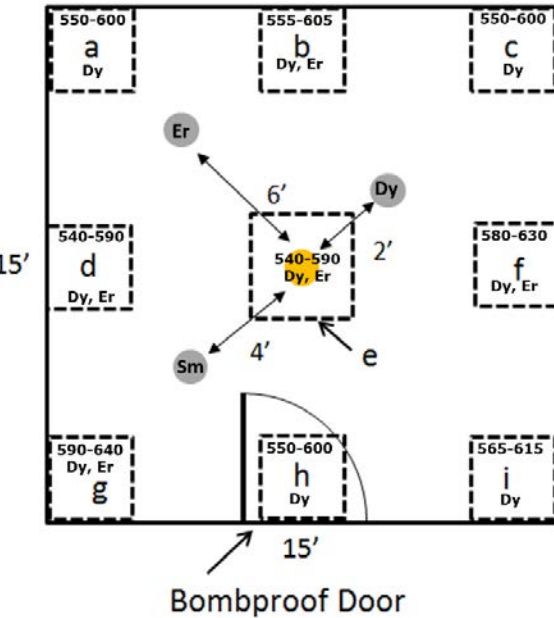


**Figure 99.** Layout for explosion test of tracking particles combined with p-Eu:ZrO<sub>2</sub> temperature sensors. The measured temperature ranges (°C) are indicated in the layout.

## V. CONCLUSIONS

The following conclusions can be drawn from this investigation:

### 1. Temperature Sensors

Modeling of the phase transitions confirms that the effect of time is significantly less than the effect of temperature and that therefore calibration measurements at longer times can be used to extract temperature information. The following materials have been successfully demonstrated:

#### a. p-Eu:Y<sub>2</sub>O<sub>3</sub>

This material works well as a temperature sensors in explosive fireballs. Various spectral signatures can be used to determine the temperature. Below the crystallization temperature, the FWHM and peak wavelength of the fluorescence-excitation peak of the  $^7F_0 \rightarrow ^5D_0$  transition are good indicators for temperature. Above the crystallization temperature, the FWHM of the  $^5D_0 \rightarrow ^7F_0$  fluorescence transition is a good indicator for temperature. In addition, the intensity ratio for the  $^5D_0 \rightarrow ^7F_2$  vs.  $^5D_0 \rightarrow ^7F_1$  fluorescence peaks can be used as an indicator. Furthermore, peak intensities with respect to reference materials can be used to determine temperature.

#### b. p-Eu:ZrO<sub>2</sub>

This material also works very well as a temperature sensor in explosive fireballs. High spectral resolution measurements show that the peak intensity ratio and peak position of the split  $^5D_0 \rightarrow ^7F_1$  fluorescence can be used as indicators for temperature. In addition, the ratio of the tetragonal to monoclinic phases, as well as the intensity ratio compared with reference materials can be used to determine temperature.

In general, fluorescence measurements are easier and faster to perform than fluorescence-excitation measurements, an important parameter for future portable equipment suitable for field operations.

### 2. Thermal impulse sensors

Thermal impulse sensors consist of a mixture of two sensor materials to be able to simultaneously determine temperature and time. The following material has been successfully demonstrated under laboratory conditions:

#### a. p-Eu:ZrO<sub>2</sub> + c-Ho:ZrO<sub>2</sub> + p-Dy:Y<sub>2</sub>O<sub>3</sub>

**This “cocktail” consist of the already demonstrated host materials ZrO<sub>2</sub> and Y<sub>2</sub>O<sub>3</sub>.** While ZrO<sub>2</sub> is still doped with Eu, the dopant for Y<sub>2</sub>O<sub>3</sub> had to be changed to avoid spectral overlap. As such, Dy was chosen as it shows strong emission lines and temperature-induced spectral changes. In addition, c-Ho:ZrO<sub>2</sub> was added as a reference. Using this material combination, we were able to extract temperatures between 400 °C and 900 °C for heating durations as short as 100 ms. Shorter heating durations are possible but

require improved reference measurements. Also, further optimizations of the sensor composition are expected.

### 3. Tracking sensors

Of the currently tested tracking sensors, Dy:Y<sub>2</sub>O<sub>3</sub> appears to be the most promising one as it shows very strong emission intensities. However, this material cannot be used in combination with the current thermal impulse sensor material combinations since it contains the same material. Er,Yb:Y<sub>2</sub>O<sub>3</sub> is the second best material and does not interfere with any of the other materials. Sm:Y<sub>2</sub>O<sub>3</sub> has the weakest emission intensity of the tested materials. Also, depending on the selection of the thermosensor host material, it may interfere with Eu from the thermal sensors.

We have successfully demonstrated that small luminescent particles can be used as temperature sensors during explosions. As expected, the readings from these sensors typically show higher temperatures than the thermocouples. Also, our sensors show a range of temperatures, reflecting the range of temperatures within an explosive fireball, in particular when reactive metals such as aluminum are present. Initial tests of thermal impulse sensors and tracking sensors also look promising.

## **VI. RECOMMENDATIONS**

Given the demonstrated functionality of the temperature sensors and the progress made today, it is clear that the approach works. However, further refinements can be made to the overall design and functionality of the various sensors. In particular, the following is recommended:

1. Refine laboratory-based short-pulse laser heating system.
2. Optimize thermal impulse (TI) sensors for heating durations as short as 1 ms.
3. Optimize tracking sensors to minimize spectral interference with temperature sensors.
4. Develop portable analysis equipment.

## VII. PUBLICATIONS AND PRESENTATIONS

The following is a list of publications and presentations that resulted from this project:

### In preparation (percent completed):

- 1) Ray Gunawidjaja, Helena Diez-y-Riega, Benjamin Anderson, and Hergen Eilers, “Magnetic  $\text{Fe}_3\text{O}_4/\text{p-Eu:Y}_2\text{O}_3$  and  $\text{Eu:ZrO}_2/\text{p-Eu:Y}_2\text{O}_3 + \text{Fe}_3\text{O}_4/\text{p-Y}_2\text{O}_3$  blended core/shell nanoparticles as ex-situ temperature sensors,” (~60% complete).
- 2) Ray Gunawidjaja, Helena Diez-y-Riega, Benjamin Anderson, and Hergen Eilers, “Irreversible phase changes in rapidly heated p-Eu: $\text{TiO}_2$  nanoparticles,” (~60% complete).

### Published:

- 1) Ray Gunawidjaja, Helena Diez-y-Riega, and Hergen Eilers, “Irreversible Phase Transitions due to Laser-Based T-Jump Heating of Precursor  $\text{Eu:ZrO}_2/\text{Tb:Y}_2\text{O}_3$  Core/Shell Nanoparticles,” *J. Solid State Chem.* accepted.
- 2) Ray Gunawidjaja, Helena Diez-y-Riega, and Hergen Eilers, “Synthesis and Characterizations of Spherical Eu: $\text{La}_2\text{O}_3$  and Related Core-Shell Nanoparticles,” *Powder Tech.* 271, 255-261 (2015).
- 3) R. Gunawidjaja, T. Myint, and H. Eilers, “Optical and Morphological Characterization of  $\text{Tb}_{0.01}\text{Zr}_{0.99}\text{O}_2/(\text{precursor } \text{Eu}_{0.02}\text{Y}_{1.98}\text{O}_3)$  Core/Shell Nanoparticles as Temperature Sensors in Fast Heating Events,” *J. Phys. Chem. C*, 118 (10), pp. 5563-5569 (2014).
- 4) R. Gunawidjaja, T. Myint, and H. Eilers, “Temperature dependent phase changes in multi-colored  $\text{Er}_x\text{Y}_y\text{Zr}_{1-x-y}\text{O}_2/\text{Eu}_{0.02}\text{Y}_{1.98}\text{O}_3$  core/shell nanoparticles,” *J. Phys. Chem. C* 117 (27), pp 14427-14434 (2013).
- 5) Hergen Eilers, Thandar Myint, Ray Gunawidjaja, Jillian Horn, James Lightstone, Christopher Milby and Demitrios Stamatis (2013). Nanosized Thermosensors for Use in Explosions. *MRS Proceedings*, 1519, mrsf12-1519-mm02-09 doi:10.1557/opr.2012.1758.
- 6) T. Myint, R. Gunawidjaja, and H. Eilers, “Spectroscopic Properties of nanophase Eu-Doped  $\text{ZrO}_2$  and its Potential Applications for fast Temperature Sensing under Extreme Conditions,” *J. Phys. Chem. C* 116 (40), pp 21629–21634 (2012).
- 7) Thandar Myint, Ray Gunawidjaja, and Hergen Eilers, “Fast Pyroprobe-Heating-Induced Structural Changes of  $\text{Y}_2\text{O}_3:\text{Eu}$  Precursors and their Optical Signatures,” *J. Phys. Chem. C* 116 (2), 1687-1693 (2011).
- 8) Ray Gunawidjaja, Thandar Myint, and Hergen Eilers, “Correlation of Optical Properties and Temperature-Induced Irreversible Phase Transitions in Europium-doped Yttrium Carbonate,” *J. Solid State Chem.* 184, 3280 (2011).
- 9) Ray Gunawidjaja, Thandar Myint, and Hergen Eilers, “Stabilization of tetragonal phase in  $\text{ZrO}_2:\text{Eu}$  by rapid thermal heating,” *Chem. Phys. Lett.*, 515, 122 (2011).

- 10) H. Eilers, R. Gunawidjaja, T. Myint, J. Lightstone and J. Carney, "Irreversible Phase Transitions in Doped Metal Oxides for use as Temperature Sensors in Explosions," **Shock Compression of Condensed Matter – 2011**, AIP Conf. Proc. 1426, 1577-1580 (2012).

Presentations in preparation

- 1) Hergen Eilers, Ray Gunawidjaja, Helena Diez-y-Riega, Benjamin Anderson, Forrest R. Svingala, Amber Daniels, and James M. Lightstone, "Luminescent Sensors for Tracking Spatial Particle Distribution in an Explosion," oral presentation at the APS-SCCM 2015 in Tampa, FL.
- 2) Hergen Eilers, Ray Gunawidjaja, Helena Diez-y-Riega, and Benjamin Anderson, "Sub-Second Laser Heating of Thermal Impulse Sensors," poster presentation at the APS-SCCM 2015 in Tampa, FL.

Presentations

- 1) Hergen Eilers, "Optics for National Security Applications," Invited Presentation, Optics Colloquium, Montana State University, 17 April 2014, Bozeman, MT.
- 2) Hergen Eilers, "Optics for National Security Applications," Invited Presentation, Pacific Northwest Association for College Physics, 28 March 2014, Spokane, WA.
- 3) Hergen Eilers, Ray Gunawidjaja, Thandar Myint, James M. Lightstone, Christopher Milby, Demitrios Stamatis, and Amber L. Daniels, "Luminescent Core/Shell Nanoparticles as Temperature Sensors in Explosions," MRS Fall Meeting 2013, 4 December 2013, Boston, MA.
- 4) Hergen Eilers, Thandar Myint, Ray Gunawidjaja, "Er,Yb:ZrO<sub>3</sub> / Eu:Y<sub>2</sub>O<sub>3</sub> Core/Shell Assemblies as Potential Temperature Sensors in Explosions," APS-SCCM & AIRAPT-24 Joint Conference, 9 July 2013, Seattle, WA.
- 5) Hergen Eilers, Thandar Myint, Ray Gunawidjaja, Jillian Horn, James Lightstone, Christopher Milby, and Demitrios Stamatis, "Nanosized Thermosensors for Use in Explosions," MRS Fall Meeting 2012, Boston, MA.
- 6) H. Eilers, "Luminescent Nanoparticles for Time-Dependent Temperature Measurements," invited presentation at Workshop on Time-Dependent Temperature Measurements in Energy release Processes, October 10-11, 2012, Chicago, IL.
- 7) H. Eilers, "Light/Matter Interactions and Optical Spectroscopy for Sensor Applications," Colloquium Presentation, Department of Physics and Astronomy, WSU, Pullman, WA, 3/20/2012.
- 8) H. Eilers, R. Gunawidjaja, Thandar Myint, and James Lightstone, "Irreversible phase transition in doped metal oxides as temperature sensors in explosions," presented at APS SCCM 2011, Chicago, IL, (June 27, 2011).

## VIII. REFERENCES

- (1) "BROAD AGENCY ANNOUNCEMENT," Enterprise, R. a. D.; Directorate, B. a. A. S.; (C-WMD), B. R. f. C. W. o. M. D., Eds., ed: Defense Threat Reduction Agency, 2008.
- (2) Gunawidjaja, R.; Myint, T.; Eilers, H. Correlation of optical properties and temperature-induced irreversible phase transitions in europium-doped yttrium carbonate nanoparticles. *J. Solid State Chem.* **2011**, *184*, 3280-3288
- (3) Gunawidjaja, R.; Myint, T.; Eilers, H. Stabilization of tetragonal phase in ZrO<sub>2</sub>:Eu by rapid thermal heating. *Chem. Phys. Lett.* **2011**, *515*, 122-126
- (4) Gunawidjaja, R.; Myint, T.; Eilers, H. Optical and Morphological Characterization of Tb<sub>0.01</sub>Zr<sub>0.99</sub>O<sub>2</sub>/(Precursor Eu<sub>0.02</sub>Y<sub>1.98</sub>O<sub>3</sub>) Core/Shell Nanoparticles as Temperature Sensors in Fast Heating Events. *Journal of Physical Chemistry C* **2014**, *118*, 5563-5569
- (5) Turmanova, S. C.; Genieva, S. D.; Dimitrova, A. S.; Vlaev, L. T. Non-isothermal degradation kinetics of filled with rice husk ash polypropene composites. *Express Polym Lett* **2008**, *2*, 133-146
- (6) Saito, N.; Matsuda, S.; Ikegami, T. Fabrication of transparent yttria ceramics at low temperature using carbonate-derived powder. *J. Am. Ceram. Soc.* **1998**, *81*, 2023-2028
- (7) Huang, Z. G.; Sun, X. D.; Xiu, Z. M.; Chen, S. W.; Tsai, C. T. Precipitation synthesis and sintering of yttria nanopowders. *Mater. Lett.* **2004**, *58*, 2137-2142
- (8) Sun, Y.; Qi, L.; Lee, M.; Lee, B. I.; Samuels, W. D.; Exarhos, G. J. Photo luminescent properties of Y<sub>2</sub>O<sub>3</sub> : Eu<sup>3+</sup> phosphors prepared via urea precipitation in non-aqueous solution. *J. Lumin.* **2004**, *109*, 85-91
- (9) Wang, N.; Zhang, X.; Bai, Z.; Liu, Q.; Lu, L.; Mi, X.; Sun, H.; Wang, X. Carbonate-precipitation synthesis of Yb<sup>3+</sup>:Y<sub>2</sub>O<sub>3</sub> nanopowders and its characteristics. *Powder Technol.* **2010**, *203*, 458-461
- (10) Traina, C. A.; Schwartz, J. Surface modification of Y<sub>2</sub>O<sub>3</sub> nanoparticles. *Langmuir* **2007**, *23*, 9158-9161
- (11) Imanaka, N.; Masui, T.; Mayama, Y.; Koyabu, K. Synthesis of crystalline yttrium oxycarbonate in a single phase. *J. Solid State Chem.* **2005**, *178*, 3601-3603

- (12) Shek, C. H.; Lai, J. K. L.; Lin, G. M. Grain growth in nanocrystalline SnO<sub>2</sub> prepared by sol-gel route. *Nanostruct. Mater.* **1999**, *11*, 887-893
- (13) Myint, T.; Gunawidjaja, R.; Eilers, H. Light-induced structural changes in Eu-doped (Pb,La)(Zr,Ti)O<sub>3</sub> ceramics. *Appl Phys Lett* **2011**, *98*, 171906
- (14) Binnemans, K. Lanthanide-Based Luminescent Hybrid Materials. *Chem. Rev.* **2009**, *109*, 4283-4374
- (15) Binnemans, K.; Gorllerwalrand, C. A Simple-Model for Crystal-Field Splittings of the <sup>7</sup>F<sub>1</sub> and <sup>5</sup>D<sub>1</sub> Energy-Levels of Eu<sup>3+</sup>. *Chem. Phys. Lett.* **1995**, *245*, 75-78
- (16) Bihari, B.; Eilers, H.; Tissue, B. M. Spectra and Dynamics of Monoclinic Eu<sub>2</sub>O<sub>3</sub> and Eu<sup>3+</sup>:Y<sub>2</sub>O<sub>3</sub> Nanocrystals. *J. Lumin.* **1997**, *75*, 1-10
- (17) Cascales, C.; Zaldo, C. Crystal-field analysis of Eu<sup>3+</sup> energy levels in the new rare-earth R BiY<sub>1-x</sub>R<sub>x</sub>GeO<sub>5</sub> oxide. *J. Solid State Chem.* **2003**, *171*, 262-267
- (18) Hussein, G. A. M. Formation of High-Surface-Area Yttrium-Oxide by the Thermal-Decomposition of Different Inorganic Precursors. *Thermochim. Acta* **1994**, *244*, 139-151
- (19) Munoz-Santiuste, J. E.; Rodriguez-Mendoza, U. R.; Gonzalez-Platas, J.; Lavin, V. Structural study of the Eu<sup>3+</sup> environments in fluorozirconate glasses: Role of the temperature-induced and the pressure-induced phase transition processes in the development of a rare earth's local structure model. *J. Chem. Phys.* **2009**, *130*, -
- (20) Su, C. L.; Li, J. R.; He, D. H.; Cheng, Z. X.; Zhu, Q. M. Synthesis of isobutene from synthesis gas over nanosize zirconia catalysts. *Applied Catalysis a-General* **2000**, *202*, 81-89
- (21) Gupta, T. K.; Bechtold, J. H.; Kuznicki, R. C.; Cadoff, L. H.; Rossing, B. R. Stabilization of tetragonal phase in polycrystalline zirconia. *Journal of Materials Science* **1977**, *12*, 2421-2426
- (22) Caracoche, M. C.; Dova, M. T.; Garcia, A. R. L. Stabilization and Hyperfine Characterization of Metastable Tetragonal Zro<sub>2</sub>. *J. Mater. Res.* **1990**, *5*, 1940-1947
- (23) Fabris, S.; Paxton, A. T.; Finnis, M. W. A stabilization mechanism of zirconia based on oxygen vacancies only. *Acta Mater.* **2002**, *50*, 5171-5178

- (24) Shukla, S.; Seal, S. Mechanisms of room temperature metastable tetragonal phase stabilisation in zirconia. *Int. Mater. Rev.* **2005**, *50*, 45-64
- (25) Kim, H. C.; Shon, I. J.; Jeong, I. K.; Ko, I. Y. Rapid sintering of nanocrystalline 8 mol.%Y<sub>2</sub>O<sub>3</sub>-stabilized ZrO<sub>2</sub> by high-frequency induction heating method. *Mater-Int* **2006**, *12*, 393-398
- (26) Armelao, L.; Barreca, D.; Bottaro, G.; Gasparotto, G.; Tondello, E.; Ferroni, M.; Polizzi, S. Innovative approaches to oxide nanosystems: CeO<sub>2</sub>-ZrO<sub>2</sub> nanocomposites by a combined PE-CVD/sol-gel route. *Chem. Vap. Deposition* **2004**, *10*, 257-264
- (27) Muoto, C. K.; Jordan, E. H.; Gell, M.; Aindow, M. Phase Homogeneity in MgO-ZrO<sub>2</sub> Nanocomposites Synthesized by a Combined Sol-Gel/Thermal Decomposition Route. *J. Am. Ceram. Soc.* **2010**, *93*, 3102-3109
- (28) Blasse, G. The Eu<sup>3+</sup> luminescence as a measure for chemical bond differences in solids. *Chem. Phys. Lett.* **1973**, *20*, 573-574
- (29) Reisfeld, R.; Zigansky, E.; Gaft, M. Europium probe for estimation of site symmetry in glass films, glasses and crystals. *Mol. Phys.* **2004**, *102*, 1319-1330
- (30) Sharma, P. K.; Nass, R.; Schmidt, H. Effect of solvent, host precursor, dopant concentration and crystallite size on the fluorescence properties of Eu(III) doped yttria. *Opt. Mater.* **1998**, *10*, 161-169
- (31) Moon, B. K.; Kwon, I. M.; Jeong, J. H.; Kim, C. S.; Yi, S. S.; Kim, P. S.; Choi, H.; Kim, J. H. Synthesis and luminescence characteristics of Eu<sup>3+</sup>-doped ZrO<sub>2</sub> nanoparticles. *J. Lumin.* **2007**, *122*, 855-857
- (32) Ray, J. C.; Park, D. W.; Ahn, W. S. Chemical synthesis of stabilized nanocrystalline zirconia powders. *Journal of Industrial and Engineering Chemistry* **2006**, *12*, 142-148
- (33) Socrates, G. *Infrared and Raman characteristic group frequencies : tables and charts*, pp., 3rd ed. Chichester, West Sussex, England ; New York: Wiley, 2001.
- (34) Morterra, C.; Orio, L. Surface Characterization of Zirconium-Oxide .2. The Interaction with Carbon-Dioxide at Ambient-Temperature. *Mater. Chem. Phys.* **1990**, *24*, 247-268

- (35) Ali, A. A. M.; Zaki, M. I. Thermal and spectroscopic studies of polymorphic transitions of zirconia during calcination of sulfated and phosphated  $\text{Zr}(\text{OH})_4$  precursors of solid acid catalysts. *Thermochim. Acta* **1999**, *336*, 17-25
- (36) Phillipi, C. M.; Mazdiyasni, K. S. Infrared and Raman Spectra of Zirconia Polymorphs. *J. Am. Ceram. Soc.* **1971**, *54*, 254-258
- (37) Sarkar, D.; Mohapatra, D.; Ray, S.; Bhattacharyya, S.; Adak, S.; Mitra, N. Nanostructured  $\text{Al}_2\text{O}_3$ - $\text{ZrO}_2$  composite synthesized by sol-gel technique: powder processing and microstructure. *Journal of Materials Science* **2007**, *42*, 1847-1855
- (38) Hemmer, E.; Soga, K.; Konishi, T.; Watanabe, T.; Taniguchi, T.; Mathur, S. Influence of the Host Phase on the Vibrational Spectra of Europium-Doped Zirconia Prepared by Hydrothermal Processing. *J. Am. Ceram. Soc.* **2010**, *93*, 3873-3879
- (39) Chen, L. M.; Liu, Y. N.; Li, Y. D. Preparation and characterization of  $\text{ZrO}_2 : \text{Eu}^{3+}$  phosphors. *J. Alloys Compd.* **2004**, *381*, 266-271
- (40) Li, L.; Yang, H. K.; Moon, B. K.; Choi, B. C.; Jeong, J. H.; Jang, K. W.; Lee, H. S.; Yi, S. S. Structure, Charge Transfer Bands and Photoluminescence of Nanocrystals Tetragonal and Monoclinic  $\text{ZrO}_2:\text{Eu}$ . *Journal of Nanoscience and Nanotechnology* **2011**, *11*, 350-357
- (41) Eilers, H.; Gunawidjaja, R.; Myint, T.; Lightstone, J.; Carney, J. Irreversible Phase Transitions in doped Metal Oxides for use as Temperature Sensors in Explosions. In *APS SCCM 2011*, Chicago, IL, **2011**
- (42) Myint, T.; Gunawidjaja, R.; Eilers, H. Fast Pyroprobe-Heating-Induced Structural Changes of  $\text{Y}_2\text{O}_3:\text{Eu}$  Precursors and Their Optical Signatures. *J Phys Chem C* **2012**, *116*, 1687-1693
- (43) Meltzer, R. S.; Feofilov, S. P.; Tissue, B.; Yuan, H. B. Dependence of fluorescence lifetimes of  $\text{Y}(2)\text{O}(3):\text{Eu}^{(3+)}$  nanoparticles on the surrounding medium. *Phys Rev B* **1999**, *60*, 14012-14015
- (44) Guan, J. B.; Chen, B.; Sun, Y. Y.; Liang, H.; Zhang, Q. J. Effects of synergetic ligands on the thermal and radiative properties of  $\text{Eu}(\text{TTA})(3)n\text{L}$ -doped poly(methyl methacrylate). *J. Non-Cryst. Solids* **2005**, *351*, 849-855
- (45) Myint, T.; Gunawidjaja, R.; Eilers, H. Light-Induced Structural Changes in Eu-doped  $(\text{Pb},\text{La})(\text{Zr},\text{Ti})\text{O}_3$  Ceramics. *Appl. Phys. Lett.* **2011**, *98*, 171906

- (46) Sharma, P. K.; Jilavi, M. H.; Nass, R.; Schmidt, H. Tailoring the particle size from  $\mu\text{m}$  -> nm scale by using a surface modifier and their size effect on the fluorescence properties of europium doped yttria. *J. Lumin.* **1999**, *82*, 187-193
- (47) Avrami, M. Kinetics of Phase Change I. General Theory. *1939*, *7*, 1103-1112
- (48) Avrami, M. Kinetics of Phase Change II. Transformation-Time Relations for Random Distribution of Nuclei. *1940*, *8*, 212-224
- (49) Johnson, W. A.; Mehl, R. F. Reaction kinetics in processes of nucleation and growth. *1939*, *135*, 416-458
- (50) Kolmogorov, A. N. A statistical theory for the recrystallization of metals. *1937*, *3*, 355-359
- (51) Tang, B.; Ge, J. C.; Zhuo, L. H. The fabrication of  $\text{La}(\text{OH})_3$  nanospheres by a controllable-hydrothermal method with citric acid as a protective agent. *Nanotechnology* **2004**, *15*, 1749-1751
- (52) Li, G. G.; Peng, C.; Zhang, C. M.; Xu, Z. H.; Shang, M. M.; Yang, D. M.; Kang, X. J.; Wang, W. X.; Li, C. X.; Cheng, Z. Y.; Lin, J. Eu<sup>3+</sup>/Tb<sup>3+</sup>-Doped  $\text{La}_2\text{O}_2\text{CO}_3/\text{La}_2\text{O}_3$  Nano/Microcrystals with Multiform Morphologies: Facile Synthesis, Growth Mechanism, and Luminescence Properties. *Inorg. Chem.* **2010**, *49*, 10522-10535
- (53) Yoo, H. S.; Jang, H. S.; Bin Im, W.; Kang, J. H.; Jeon, D. Y. Particle size control of a monodisperse spherical  $\text{Y}_2\text{O}_3 : \text{Eu}^{3+}$  phosphor and its photoluminescence properties. *J. Mater. Res.* **2007**, *22*, 2017-2024
- (54) Zhao, Y.; Toyama, M.; Kita, K.; Kyuno, K.; Toriumi, A. Moisture-absorption-induced permittivity deterioration and surface roughness enhancement of lanthanum oxide films on silicon. *Appl. Phys. Lett.* **2006**, *88*,
- (55) Li, X. L.; Tsoutsou, D.; Scarel, G.; Wiemer, C.; Capelli, S. C.; Volkos, S. N.; Lamagna, L.; Fanciulli, M. Chemical and structural properties of atomic layer deposited  $\text{La}_2\text{O}_3$  films capped with a thin  $\text{Al}_2\text{O}_3$  layer. *J Vac Sci Technol A* **2009**, *27*, L1-L7
- (56) Tsoutsou, D.; Scarel, G.; Debernardi, A.; Capelli, S. C.; Volkos, S. N.; Lamagna, L.; Schamm, S.; Coulon, P. E.; Fanciulli, M. Infrared spectroscopy and X-ray diffraction studies on the crystallographic evolution of  $\text{La}_2\text{O}_3$  films upon annealing. *Microelectron. Eng.* **2008**, *85*, 2411-2413

- (57) Gorller-Walrand, C.; Binnemans, K., Eds., *Rationalization of crystal-field parametrization*. In *Handbook on the Physics and Chemistry of Rare-Earths*. Elsevier Science B.V., 1996, p.^pp. Pages.
- (58) Yermolayeva, Y. V.; Tolmachev, A. V.; Korshikova, T. I.; Yavetskiy, R. P.; Dobrotvorskaya, M. V.; Danylenko, N. I.; Sofronov, D. S. Spherical Core-Shell Structured Nanophosphors on the Basis of Europium-Doped Lutetium Compounds. *Nanotechnology* **2009**, *20*, 325601
- (59) Gunawidjaja, R.; Myint, T.; Eilers, H. Synthesis of silver/SiO<sub>2</sub>/Eu:Lu<sub>2</sub>O<sub>3</sub> core-shell nanoparticles and their polymer nanocomposites. *Powder Technol.* **2011**, *210*, 157-166

## IX. APPENDIX

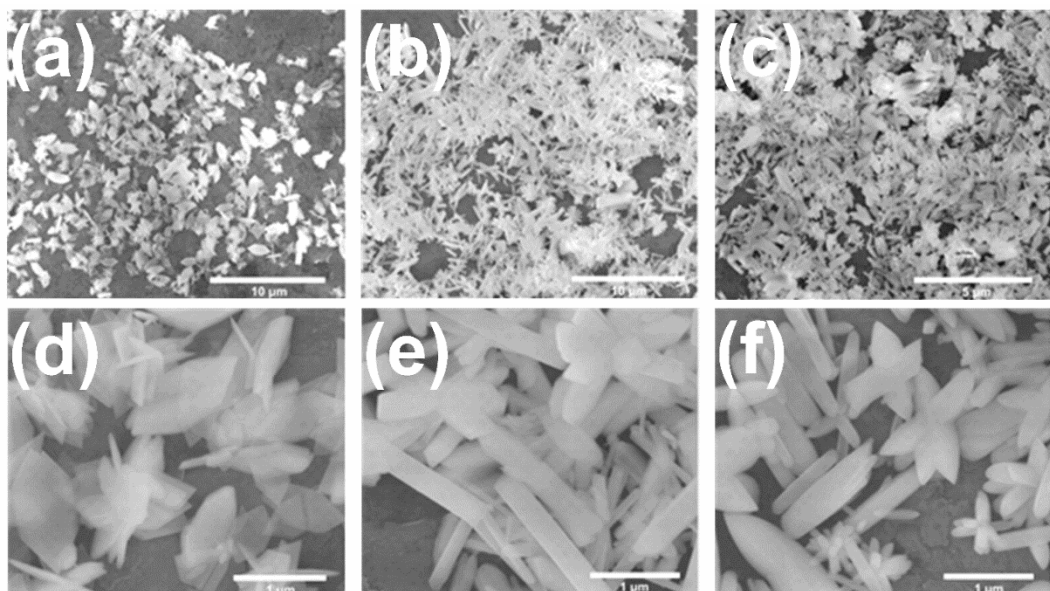
### A. Alternative Temperature Sensors

#### **Eu:La<sub>2</sub>O<sub>3</sub> – based materials**

Monodispersed spherical p-Eu:La<sub>2</sub>O<sub>3</sub> nanoparticles are obtained by heating an aqueous mixture of La(NO<sub>3</sub>)<sub>3</sub>·6H<sub>2</sub>O, Eu(NO<sub>3</sub>)<sub>3</sub>·6H<sub>2</sub>O, citric acid, and urea with salt/citric acid/urea ratio of 1/0.25/40 in a 90 °C thermostated oil bath for 3 h. The total metallic salt concentration is 0.005 M. Likewise, monodispersed spherical nanoparticles of p-Tb:Y<sub>2</sub>O<sub>3</sub> are obtained via homogeneous precipitation. An aqueous mixture of Yb(NO<sub>3</sub>)<sub>3</sub>·6H<sub>2</sub>O, Tb(NO<sub>3</sub>)<sub>3</sub>·6H<sub>2</sub>O, and urea with salt/urea ratio of 1/40 is heated under continuous stirring in a 90 °C thermostated oil bath. The total metallic salt concentration is 0.020 M.

Core/shell p-Eu:La<sub>2</sub>O<sub>3</sub>/p-Tb:Y<sub>2</sub>O<sub>3</sub> nanoparticles are prepared by repeating the homogeneous precipitation of p-Tb:Y<sub>2</sub>O<sub>3</sub> three times in the presence of p-Eu:La<sub>2</sub>O<sub>3</sub> nanoparticles. The salt concentration of the metallic salt is 0.005 M and the salt to urea ratio is 1/40. Likewise, the core/shell p-Tb:Y<sub>2</sub>O<sub>3</sub>/p-Eu:La<sub>2</sub>O<sub>3</sub> nanoparticles are prepared by repeating the homogeneous precipitation of p-Eu:La<sub>2</sub>O<sub>3</sub> in the presence of citric acid three times in the presence of p-Tb:Y<sub>2</sub>O<sub>3</sub> nanoparticles. The salt concentration of the metallic salt is 0.005 M and the salt/citric acid/urea ratio is 1/0.25/40.

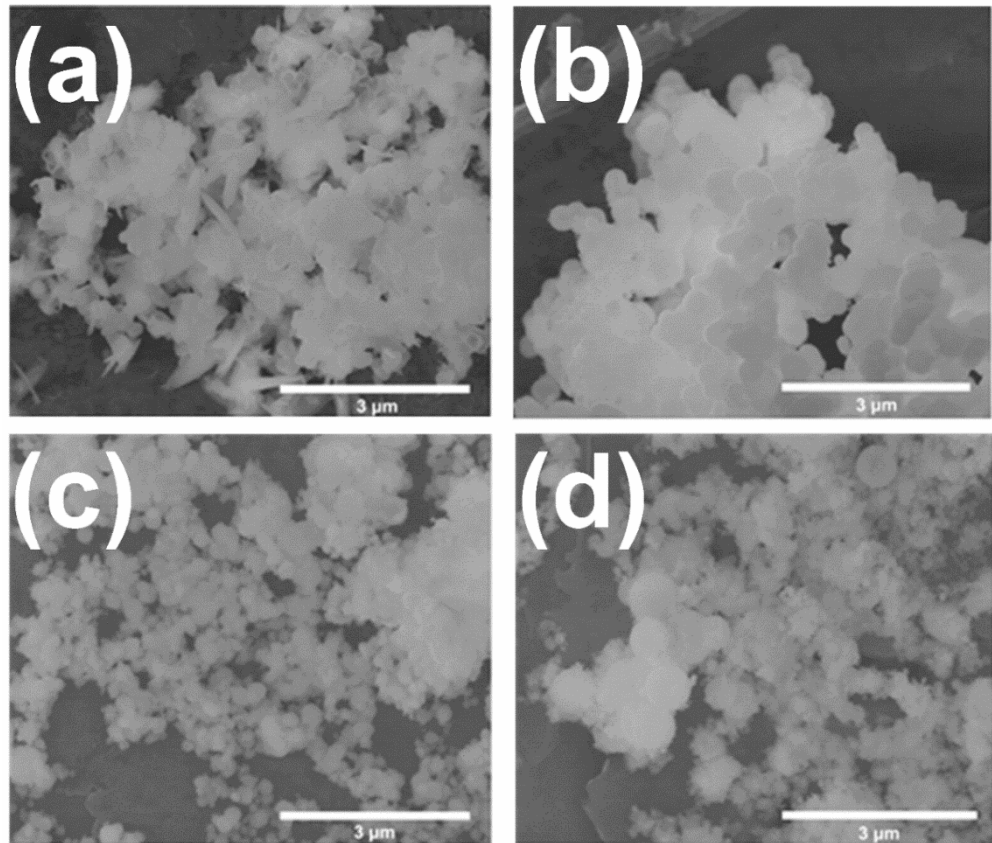
Figure 100 shows SEM images of p-Eu:La<sub>2</sub>O<sub>3</sub> prepared by homogeneous precipitation using variable amounts of urea. The anisotropy of the resulting structures increases with increasing urea concentration. A salt/urea ratio of 1/1, results in the formation of 2-D sheets, while salt/urea ratios of 1/40 and 1/200 result in the formation of 1-D structures with similar morphologies.



**Figure 100.** SEM micrographs of p-Eu:La<sub>2</sub>O<sub>3</sub> synthesized with (a, d) 1/1, (b, e) 1/40, and (c, f) 1/200 salt/urea ratios. In all cases the salt concentration is 20 mM.

Next, we perform a series of homogeneous precipitation of p-Eu:La<sub>2</sub>O<sub>3</sub> in the presence of citric acid as a capping agent at various salt to citric acid ratios, but keep the salt/urea

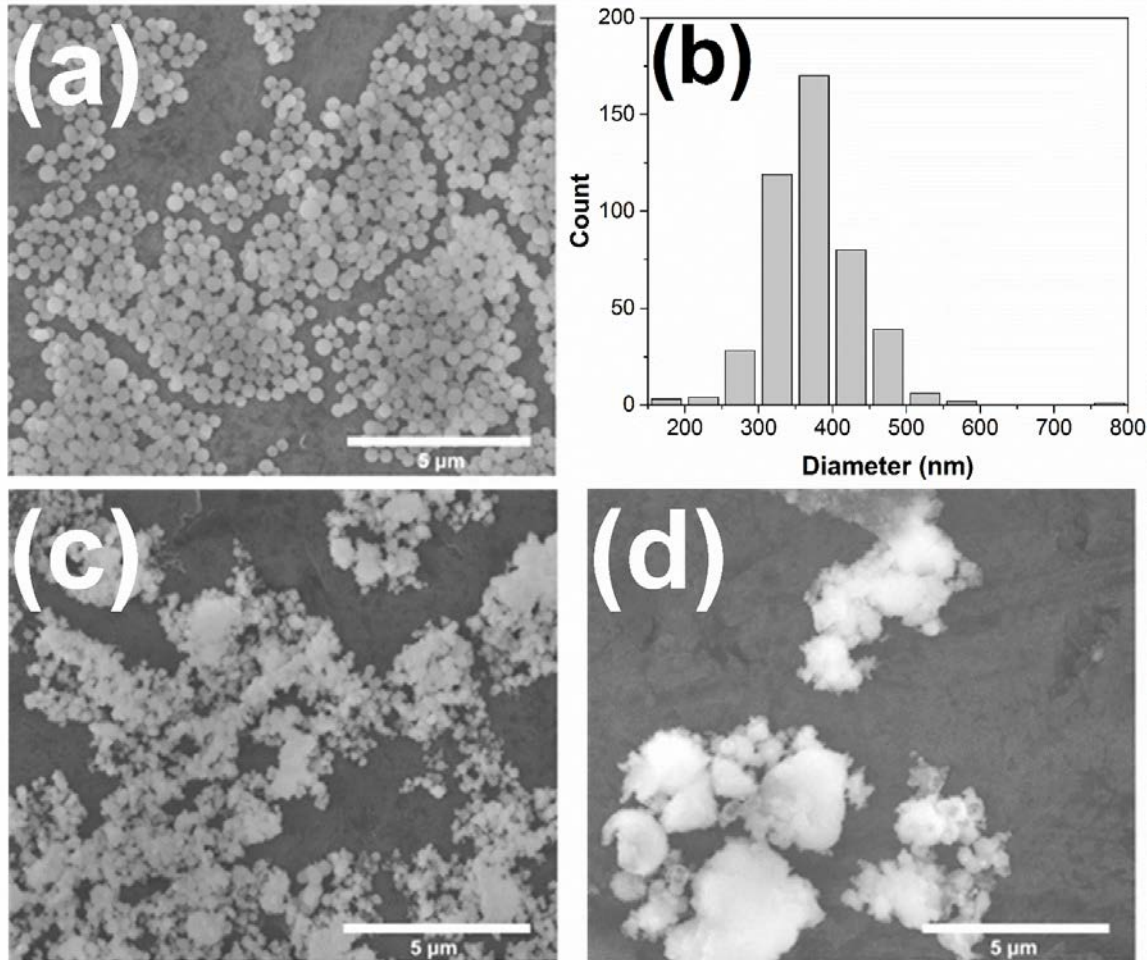
ratio fixed at 1/40. Figure 101 shows spherical nanostructures formed at a 1/0.05 salt/citric acid ratio, and a bimodal nanoparticle distribution at a 1/0.50 salt/citric acid ratio. When the salt/citric acid ratio is 1/2, the solution remains transparent, indicating no precipitation has taken place, after 3 h of heating at 90 °C (SEM micrographs not shown).



**Figure 101.** SEM micrographs of p-Eu:La<sub>2</sub>O<sub>3</sub> synthesized with (a) 1/0.05, (b) 1/0.10, (c) 1/0.25, and (d) 1/0.50 salt/citric acid ratio. In all cases the salt/urea ratio is 1/40. The salt concentration is 20 mM.

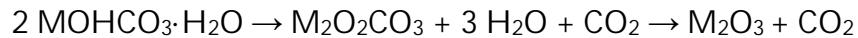
By comparing Figure 100 (b) and Figure 100 (e) with Figure 101, we see that the addition of citric acid reduces the formation of anisotropic structures. In the presence of citric acid, lanthanum-citric acid complexes form. The coordinated citric acid molecules suppress the preferential growth direction during precipitation.<sup>51</sup> In the case of the 1/0.25 salt/citric acid ratio the nanoparticles are more or less monodispersed and segregated, see Figure 101 (c). However, micrometer-sized aggregates can be seen as well. It is likely that the large particles form as a result of Ostwald ripening with adjacent nanoparticles fusing into larger particles. To further improve the monodispersity of the spherical nanoparticles, we vary the salt concentration. Figure 102 shows the quality of the nanoparticles at various salt concentrations. The salt/citric acid/urea ratio is fixed at 1/0.25/40. The extent of aggregation increases with increasing salt concentration. Relatively monodisperse spherical particles with an average diameter of (375 ± 60) nm form at a salt concentration of 5 mM, see Figure 102 (a). All further discussion is limited to p-Eu:La<sub>2</sub>O<sub>3</sub> nanoparticles synthesized with a salt/citric acid/urea ratio of 1/0.25/40 and a salt concentration of 5

mM. In addition, precursor Tb:Y<sub>2</sub>O<sub>3</sub> (p-Tb:Y<sub>2</sub>O<sub>3</sub>) is also prepared by means of homogeneous precipitation, but without citric acid.



**Figure 102.** SEM micrographs of p-Eu:La<sub>2</sub>O<sub>3</sub> synthesized using various salt concentrations: (a) 5 mM (b) its corresponding size distributions, (c) 20 mM, and (d) 80 mM. The salt/citric acid/urea ratio is fixed at 1/0.25/40.

Figure 103 shows a simultaneous TGA/DSC measurement of p-Eu:La<sub>2</sub>O<sub>3</sub> and p-Eu:Y<sub>2</sub>O<sub>3</sub>. The TGA graphs show a mass loss of 34% and 35% for p-Eu:La<sub>2</sub>O<sub>3</sub> and p-Tb:Y<sub>2</sub>O<sub>3</sub>, respectively. These losses can be ascribed to the endothermic decomposition of LaOHCO<sub>3</sub>·H<sub>2</sub>O and YOHCO<sub>3</sub>·H<sub>2</sub>O. MOHCO<sub>3</sub>·H<sub>2</sub>O compounds undergo multi-stage decomposition towards M<sub>2</sub>O<sub>3</sub>, which proceeds as follows:<sup>52, 53</sup>



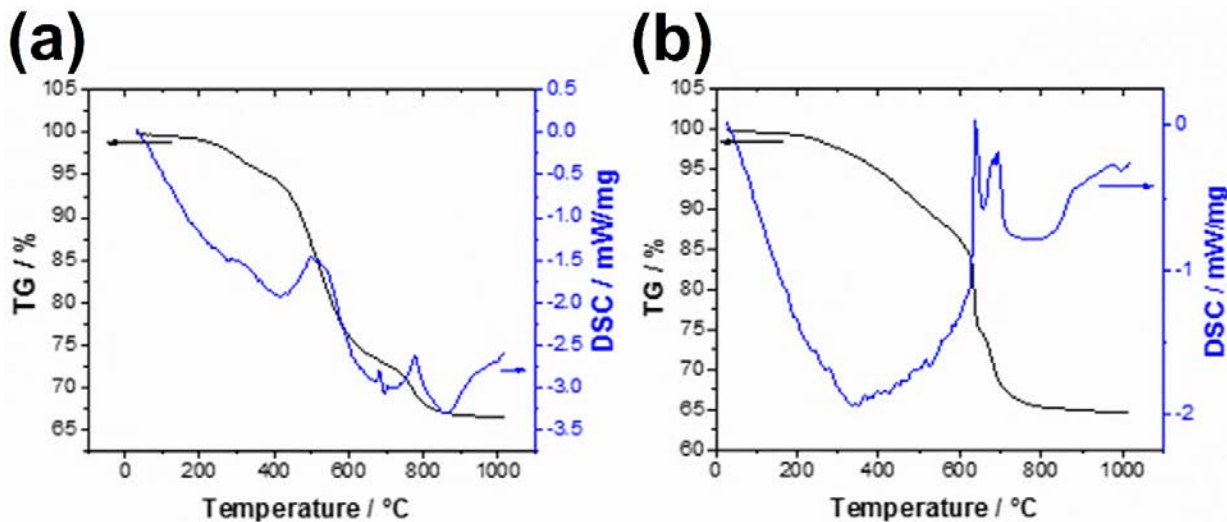


**Figure 103.** DSC/TGA graph of (a) p-Eu:La<sub>2</sub>O<sub>3</sub> and (b) p-Tb:Y<sub>2</sub>O<sub>3</sub> nanoparticles.

Table 11 compares the calculated mass loss with those derived from TG measurement while assuming that the starting compound is MOHCO<sub>3</sub>·H<sub>2</sub>O. The experimental results indicate good agreement with the proposed decomposition channel.

**Table 11.** Calculated and measured mass loss assuming that the starting compound is MOHCO<sub>3</sub>·H<sub>2</sub>O.

Assumed compound	Calculated mass / %	Measured mass / %	Assumed compound	Calculated mass / %	Measured mass / %
LaOHCO <sub>3</sub> ·H <sub>2</sub> O	100	100	YOHCO <sub>3</sub> ·H <sub>2</sub> O	100	100
La <sub>2</sub> O <sub>2</sub> CO <sub>3</sub>	79	74	Y <sub>2</sub> O <sub>2</sub> CO <sub>3</sub>	73	74
La <sub>2</sub> O <sub>3</sub>	70	66	Y <sub>2</sub> O <sub>3</sub>	61	65

The p-Eu:La<sub>2</sub>O<sub>3</sub> nanoparticles are heated to temperatures between 300 °C and 900 °C for 3 h. The corresponding x-ray diffraction patterns show crystalline phase formation in the samples heat treated  $\geq$  500 °C/3 h. The crystalline phases of the samples heat treated at 500 °C/3 h, 600 °C/3 h, and 700 °C for 3 h, can be assigned to m-La<sub>2</sub>O<sub>2</sub>CO<sub>3</sub> (PDF 00-048-1113), h-La(OH)<sub>3</sub> (PDF 01-083-2034), and h-La<sub>2</sub>O<sub>3</sub> (PDF 01-074-1144), respectively, see Figure 104 (a). All of the carbonate phases of samples heat treated at 900 °C/3 h are expected to have transformed into the h-La<sub>2</sub>O<sub>3</sub> phase. However, this h-La<sub>2</sub>O<sub>3</sub> phase readily hydrolyzes into the La(OH)<sub>3</sub> phase at ambient conditions in air.<sup>54</sup> As a result, and depending on its humidity exposure history, varying degrees of mixed La<sub>2</sub>O<sub>3</sub>/La(OH)<sub>3</sub> phases may be observed.

The susceptibility of the h-La<sub>2</sub>O<sub>3</sub> phase to moisture absorption is widely reported in the literature.<sup>54-56</sup> Annealing may be used to transform the hydrated La<sub>2</sub>O<sub>3</sub> species back into the La<sub>2</sub>O<sub>3</sub> phase. Also, a protective layer may be incorporated to minimize hydration in air.<sup>56</sup> Figure 104 (a) shows that the phase of the sample heat treated at 500 °C/3 h is mainly m-La<sub>2</sub>O<sub>2</sub>CO<sub>3</sub>. Samples heat treated at  $\geq$  600 °C/3 h consist of mixtures of the m-La<sub>2</sub>O<sub>2</sub>CO<sub>3</sub>, h-La(OH)<sub>3</sub>, and La<sub>2</sub>O<sub>3</sub> phases. The majority of the sample heat treated at 600

$^{\circ}\text{C}/3\text{ h}$  is m- $\text{La}_2\text{O}_2\text{CO}_3$ , while the sample heat treated at  $900\text{ }^{\circ}\text{C}/3\text{ h}$  consists of the h- $\text{La(OH)}_3$  and  $\text{La}_2\text{O}_3$  phases. The sample heat treated at  $700\text{ }^{\circ}\text{C}/3\text{ h}$  contains all three phases.

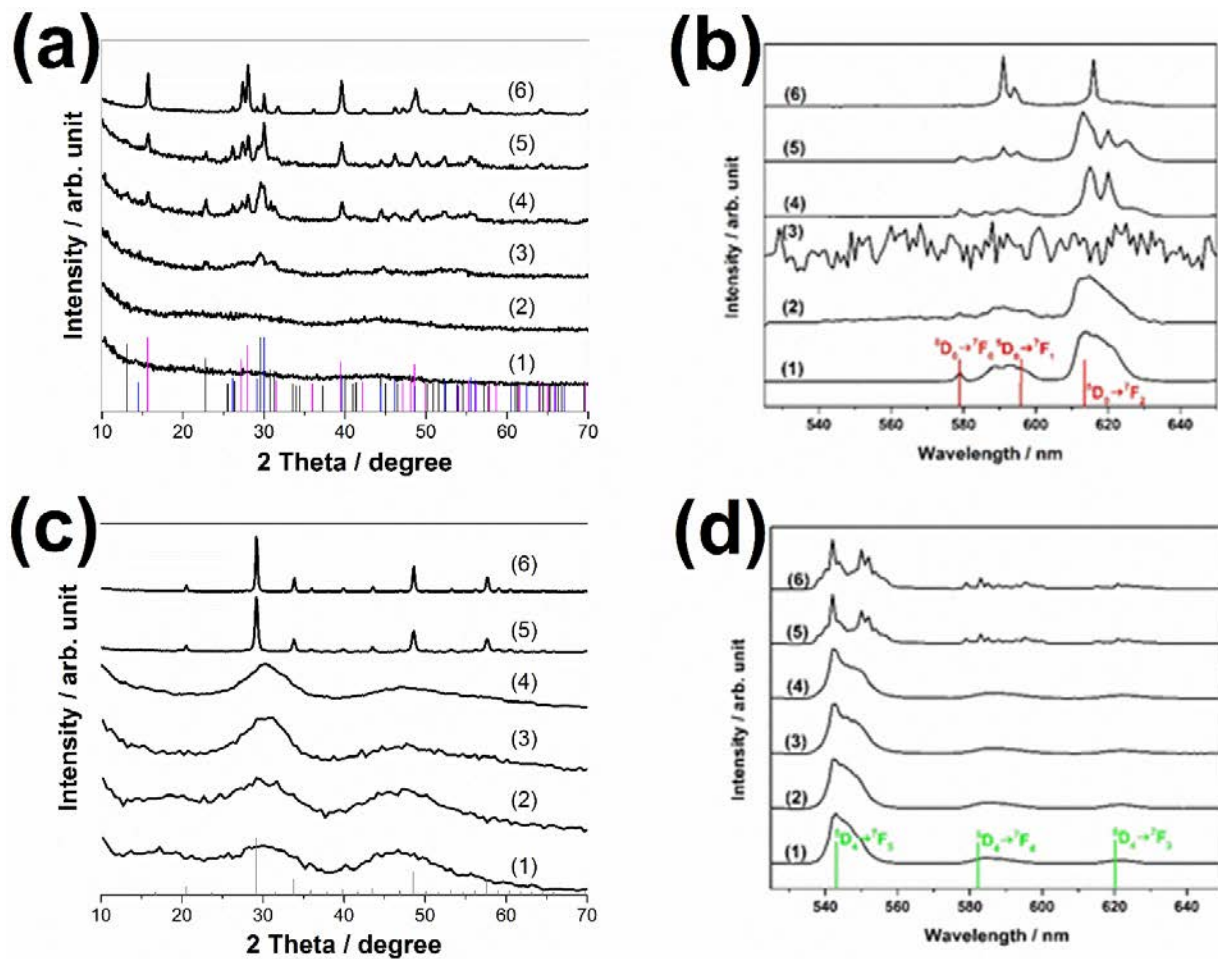


**Figure 104.** (a, c) XRD and (b, d) fluorescence of (a, b) p-Eu:La<sub>2</sub>O<sub>3</sub> and (c, d) p-Tb:Y<sub>2</sub>O<sub>3</sub> heated to: (Uncalcined, 300, 500, 600, 700, 900)  $^{\circ}\text{C}/3\text{ h}$ . Markers in (a) and (c) correspond to: m- $\text{La}_2\text{O}_2\text{CO}_3$  (black), h- $\text{La(OH)}_3$  (magenta), h- $\text{La}_2\text{O}_3$  (blue), and c- $\text{Y}_2\text{O}_3$  phase (gray).

Figure 104 (b) shows the fluorescence spectra of the p-Eu:La<sub>2</sub>O<sub>3</sub> samples with peaks corresponding to the Eu<sup>3+</sup>  ${}^5\text{D}_0 \rightarrow {}^7\text{F}_J$  ( $J=0-3$ ) transitions, and markers for the positions of the Eu<sup>3+</sup> free ion transitions. The emission spectra reflect the site symmetry of the Eu<sup>3+</sup> ions in the various phases. The inhomogeneous peak broadening reflects the amorphous nature of the p-Eu:La<sub>2</sub>O<sub>3</sub> samples in which the Eu<sup>3+</sup> ions are surrounded by disordered ligands. Following heat treatments at  $300\text{ }^{\circ}\text{C}/3\text{ h}$  and  $500\text{ }^{\circ}\text{C}/3\text{ h}$ , the color of the p-Eu:La<sub>2</sub>O<sub>3</sub> samples change from white to black due to the decomposition of the p-Eu:La<sub>2</sub>O<sub>3</sub> and the formation of carbon ash. No emission peaks characteristics of Eu<sup>3+</sup> ions are observed for the sample heat treated at  $500\text{ }^{\circ}\text{C}/3\text{ h}$  because the ash absorbs most of the excitation and fluorescence light. As suggested by the formation of narrow diffraction peaks in their XRD spectra, the samples heat treated at or above  $600\text{ }^{\circ}\text{C}/3\text{ h}$  have transformed into a crystalline phases such as Eu:La<sub>2</sub>O<sub>2</sub>CO<sub>3</sub>, Eu:La(OH)<sub>3</sub>, and Eu:La<sub>2</sub>O<sub>3</sub>.<sup>52</sup>

The spectra of the sample heat treated at 900 °C/3 h shows strong emission in the  $^5D_0 \rightarrow ^7F_1$  transitions compared to the  $^5D_0 \rightarrow ^7F_2$  transitions, indicating a high degree of spherical site symmetry. According to the powder diffraction file, the site symmetry of the La<sup>3+</sup> cations in a h-La<sub>2</sub>O<sub>3</sub> phase is C<sub>3</sub> and the site symmetry of the La<sup>3+</sup> cations in a h-La(OH)<sub>3</sub> phase is C<sub>3h</sub>. By assuming that the Eu<sup>3+</sup> cations replace the La<sup>3+</sup> host cations and possess the same site symmetries, the number of energy levels of the  $^7F_J$  may be derived in terms of the irreducible representations, see Table 12.<sup>57</sup>

**Table 12.** Irreducible representations for  $^7F_J$  levels in La<sub>2</sub>O<sub>3</sub> and La(OH)<sub>3</sub>.

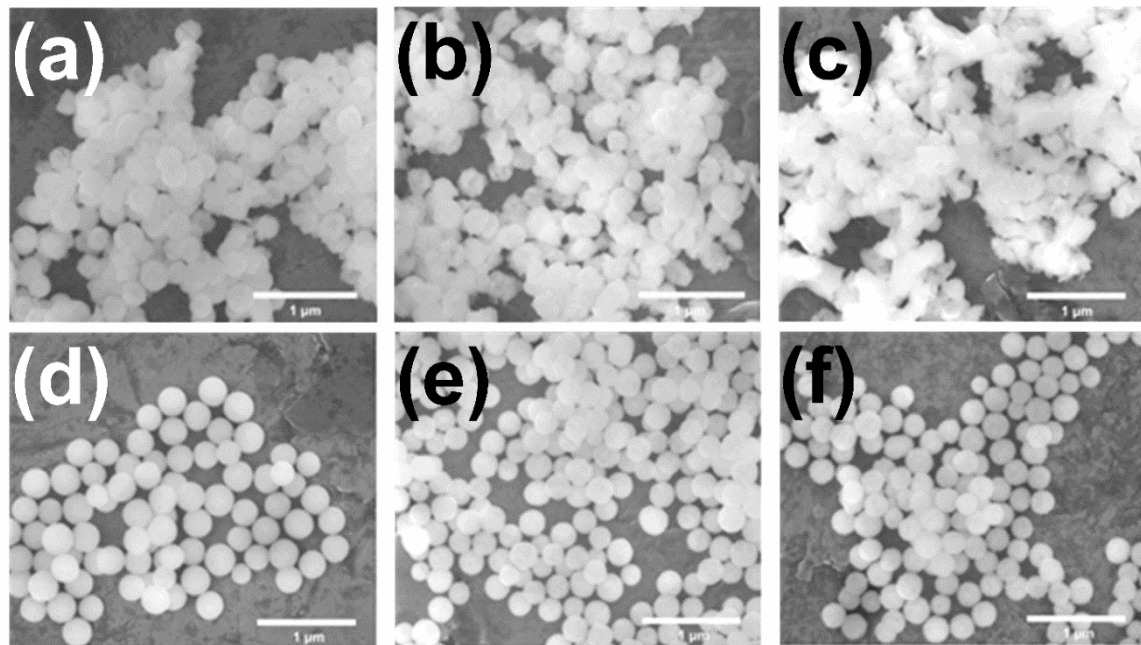
J	C <sub>3</sub> site	C <sub>3h</sub> site
0	$\Gamma_1$	$\Gamma_1$
1	$\Gamma_1 + \Gamma_2 + \Gamma_3$	$\Gamma_1 + \Gamma_{5,6}$
2	$\Gamma_1 + 2\Gamma_2 + 2\Gamma_3$	$\Gamma_1 + \Gamma_{2,3} + \Gamma_{5,6}$

Figure 104 (c) and Figure 104 (d) show the x-ray diffraction patterns and fluorescence spectra of p-Tb:Y<sub>2</sub>O<sub>3</sub>, respectively, following heat treatments between 300 °C/3 h and 900 °C/3 h. Figure 104 (c) shows that the crystalline Y<sub>2</sub>O<sub>3</sub> phase is observed only for the samples heat treated at 700 °C/3 h and 900 °C/3 h. Their XRD patterns can be matched with the cubic Y<sub>2</sub>O<sub>3</sub> phase (PDF 01-083-0927). No diffraction peaks other than those due to the cubic Y<sub>2</sub>O<sub>3</sub> phase are observed. According to the powder diffraction file, the site symmetries of the Y<sup>3+</sup> cations are C<sub>2</sub> and S<sub>6</sub>≡C<sub>3i</sub>. In rare-earth doped Y<sub>2</sub>O<sub>3</sub>, the rare earth ion is known to substitute for the Y<sup>3+</sup> cations.<sup>58</sup> By assuming that the Tb<sup>3+</sup> cations replace the Y<sup>3+</sup> host cations and maintain the same site symmetries, the number of the  $^7F_J$  energy levels may be derived in terms of the irreducible representations, see Table 13.<sup>57</sup>

**Table 13.** Irreducible representations for  $^7F_J$  levels in Y<sub>2</sub>O<sub>3</sub>.

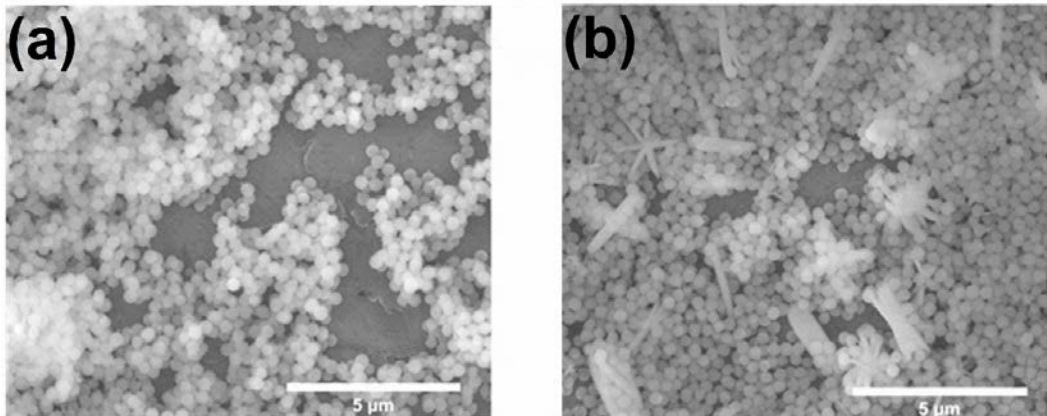
J	C <sub>2</sub> site	C <sub>3i</sub> site
5	$5\Gamma_1 + 6\Gamma_2$	$3\Gamma_1 + 4\Gamma_2 + 4\Gamma_3$
4	$5\Gamma_1 + 4\Gamma_2$	$3\Gamma_1 + 3\Gamma_2 + 3\Gamma_3$
3	$3\Gamma_1 + 4\Gamma_2$	$3\Gamma_1 + 2\Gamma_2 + 2\Gamma_3$

Figure 105 shows the SEM micrographs of polycrystalline Eu:La<sub>2</sub>O<sub>3</sub> and Tb:Y<sub>2</sub>O<sub>3</sub> nanoparticles heat treated between 600 °C/3 h and 900 °C/3 h. The Tb:Y<sub>2</sub>O<sub>3</sub> nanoparticles are segregated and remain spherical when heated. However, due to necking and sintering, the Eu:La<sub>2</sub>O<sub>3</sub> nanoparticles gradually form hard aggregates as the temperature increases and they lose their spherical morphology when heat treated at 900 °C/3 h. This difference is due to the lower crystallization temperature of the p-La<sub>2</sub>O<sub>3</sub> phase compared to the p-Y<sub>2</sub>O<sub>3</sub> phase, see Figure 104 (a) and Figure 104 (c).



**Figure 105.** SEM micrographs of the polycrystalline Eu:La<sub>2</sub>O<sub>3</sub> (a, b, c) and polycrystalline Tb:Y<sub>2</sub>O<sub>3</sub> (d, e, f) nanoparticles heat treated at (a, d) 600 °C/3 h, (b, e) 700 °C/3 h, and (c, f) 900 °C/3 h.

Oxide nanoparticle precursors synthesized via homogeneous precipitation can be grown over core templates.<sup>58, 59</sup> To assess the versatility of the modified homogeneous precipitation method we perform our synthesis procedure in the presence of SiO<sub>2</sub> nanoparticles (5 mg/mL) using salt/citric acid/urea ratios of 1/0.25/40 and 1/0/40. Figure 106 compares the results of the homogeneous precipitation of a p-Eu:La<sub>2</sub>O<sub>3</sub> shell in the presence and in the absence of citric acid. Figure 106 (a) shows that following the homogeneous precipitation in the presence of citric acid some of the SiO<sub>2</sub> nanoparticles exhibit rougher surface morphologies than others. In the absence of citric acid, a mixture of one-dimensional p-La<sub>2</sub>O<sub>3</sub> and spherical (SiO<sub>2</sub>) nanoparticles is obtained (see Figure 106). Figure 102 shows that increasing the concentration of the La(NO<sub>3</sub>)<sub>3</sub>·6H<sub>2</sub>O salt results in particle aggregation. In order to ensure that all of the core nanoparticles are covered with a p-La<sub>2</sub>O<sub>3</sub> shell the homogeneous precipitation is always repeated three times.



**Figure 106.** SEM micrographs of p-Eu:La<sub>2</sub>O<sub>3</sub> synthesized (a) in the presence and (b) in the absence of citric acid. Respectively, the salt/citric acid/urea ratio are 1/0.25/40 and 1/0/40.

To further demonstrate the usefulness of the modified homogeneous precipitation technique, we prepare Tb:La<sub>2</sub>O<sub>3</sub>/Eu:Y<sub>2</sub>O<sub>3</sub> and Tb:Y<sub>2</sub>O<sub>3</sub>/Eu:La<sub>2</sub>O<sub>3</sub> core/shell nanoparticles. Figure 107(a) and Figure 107 (d) show that the p-Tb:Y<sub>2</sub>O<sub>3</sub> and p-Eu:La<sub>2</sub>O<sub>3</sub> cores remain spherical during the formation of the respective p-Eu:La<sub>2</sub>O<sub>3</sub> and p-Tb:Y<sub>2</sub>O<sub>3</sub> shells via homogeneous precipitation. The core-shell morphologies can be clearly seen in the TEM micrographs, see Figure 107 (b) and Figure 107 (e). The EDS spectra of the Tb:La<sub>2</sub>O<sub>3</sub>/Eu:Y<sub>2</sub>O<sub>3</sub> and Tb:Y<sub>2</sub>O<sub>3</sub>/Eu:La<sub>2</sub>O<sub>3</sub> core/shell nanoparticles confirm the presence of Y and La, see Figure 107 (c) and Figure 107 (f).

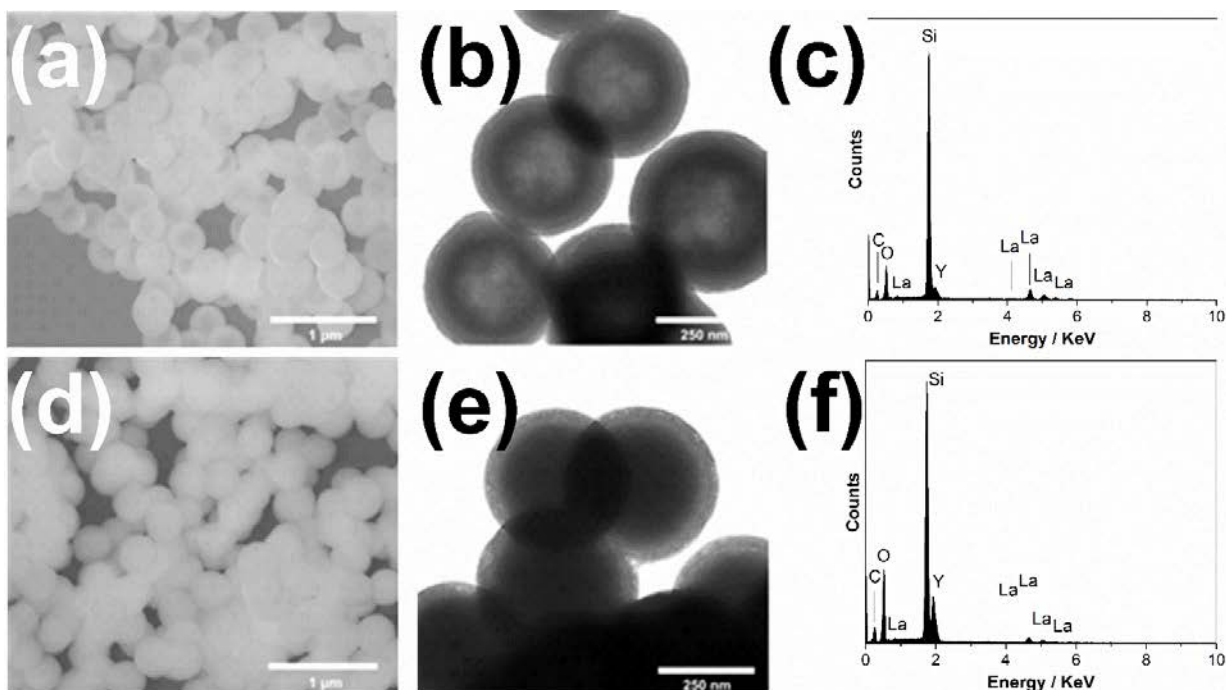


**Figure 107.** SEM and TEM micrographs of (a, b) p-Eu:La<sub>2</sub>O<sub>3</sub>/p-Tb:Y<sub>2</sub>O<sub>3</sub> and (c, d) p-Tb:Y<sub>2</sub>O<sub>3</sub>/p-Eu:La<sub>2</sub>O<sub>3</sub> core/shell nanoparticles, and (c, f) corresponding EDS spectra.

Figure 108 (a) and Figure 108 (c) show the x-ray diffraction patterns of heat treated (between 600 °C/3 h and 900 °C/3 h) p-Eu:La<sub>2</sub>O<sub>3</sub>/p-Tb:Y<sub>2</sub>O<sub>3</sub> and p-Tb:Y<sub>2</sub>O<sub>3</sub>/p-Eu:La<sub>2</sub>O<sub>3</sub>

core/shell nanoparticles, respectively. The peaks can be assigned to the m-La<sub>2</sub>O<sub>2</sub>CO<sub>3</sub>, h-La(OH)<sub>3</sub>, h-La<sub>2</sub>O<sub>3</sub>, and cubic Y<sub>2</sub>O<sub>3</sub> phases, compare with Figure 104. The peaks due to the La<sub>2</sub>O<sub>3</sub> related phases are more prominent than the Y<sub>2</sub>O<sub>3</sub> phase for p-Eu:La<sub>2</sub>O<sub>3</sub>/p-Tb:Y<sub>2</sub>O<sub>3</sub> nanoparticles. The opposite is true for the p-Tb:Y<sub>2</sub>O<sub>3</sub>/p-Eu:La<sub>2</sub>O<sub>3</sub> core/shell nanoparticles. These results indicate the dominance of the core.

As can be seen from Figure 108 (b) and Figure 108 (d), the fluorescence ( $\lambda_{\text{ex}}=488$  nm) from the uncalcined p-Eu:La<sub>2</sub>O<sub>3</sub>/p-Tb:Y<sub>2</sub>O<sub>3</sub> and from the uncalcined p-Tb:Y<sub>2</sub>O<sub>3</sub>/p-Eu:La<sub>2</sub>O<sub>3</sub> core/shell nanoparticles is dominated by emission from Tb<sup>3+</sup>. Simultaneous emission due to Tb<sup>3+</sup> and Eu<sup>3+</sup> is seen for the p-Eu:La<sub>2</sub>O<sub>3</sub>/p-Tb:Y<sub>2</sub>O<sub>3</sub> and the p-Tb:Y<sub>2</sub>O<sub>3</sub>/p-Eu:La<sub>2</sub>O<sub>3</sub> core/shell nanoparticles heat treated to (600, 700, 900) °C/3 h. Even though the nanopowder samples heat treated at 500 °C/3 h have a black appearance, some Tb<sup>3+</sup> emission is observed. While the emission from the shell components is clearly visible, the fluorescence spectra of the samples heat treated at 900 °C/3 h are dominated by the emission from the core components, indicating that the crystallization of the shell is not as efficient as the crystallization of the core.

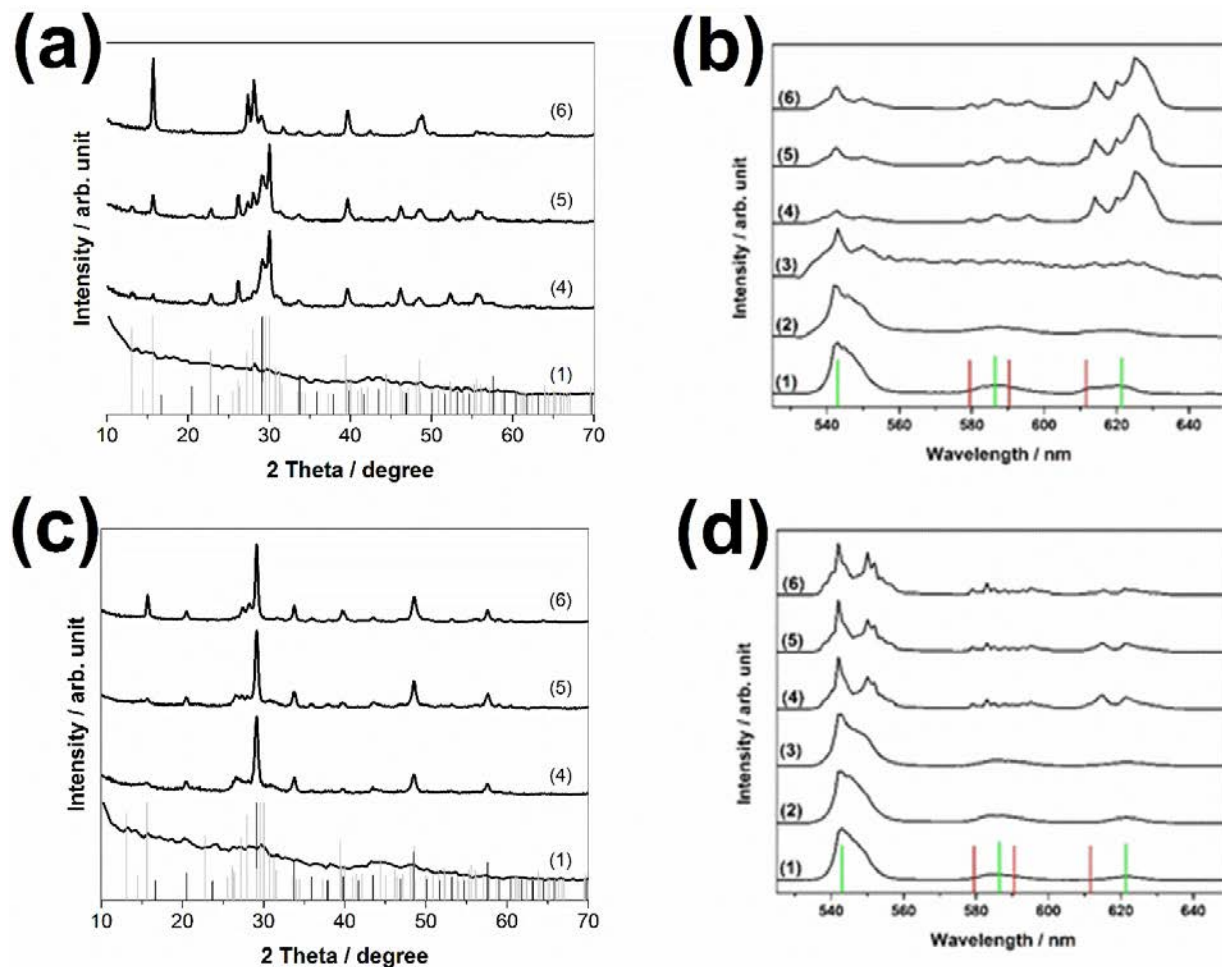


**Figure 108.** (a, c) XRD and (b, d) fluorescence of p-Eu:La<sub>2</sub>O<sub>3</sub>/p-Tb:Y<sub>2</sub>O<sub>3</sub> (a, b) and p-Tb:Y<sub>2</sub>O<sub>3</sub>/p-Eu:La<sub>2</sub>O<sub>3</sub> (c, d) heated to: (uncalcined, 300, 500, 600, 700, and 900) °C/3 h. Markers in (a) and (c) correspond to p-La<sub>2</sub>O<sub>3</sub> (gray) and the p-Y<sub>2</sub>O<sub>3</sub> phase (black).

Figure 109 shows the SEM and TEM micrographs of the polycrystalline Eu:La<sub>2</sub>O<sub>3</sub>/Tb:Y<sub>2</sub>O<sub>3</sub> and Tb:Y<sub>2</sub>O<sub>3</sub>/Eu:La<sub>2</sub>O<sub>3</sub> nanoparticles heat treated between 600 °C/3 h and 900 °C/3 h. In all cases, the polycrystalline Eu:La<sub>2</sub>O<sub>3</sub>/Tb:Y<sub>2</sub>O<sub>3</sub> nanoparticles remain segregated, whereas the Tb:Y<sub>2</sub>O<sub>3</sub>/Eu:La<sub>2</sub>O<sub>3</sub> nanoparticles show neckings and sintering following 900 °C/3 h heat treatment. This is reminiscent of the heat treated p-La<sub>2</sub>O<sub>3</sub> and p-Y<sub>2</sub>O<sub>3</sub>, compare with Figure 105. That is, the crystalline phases in the p-La<sub>2</sub>O<sub>3</sub> form much earlier than the crystalline phase in the p-Y<sub>2</sub>O<sub>3</sub>, see also see Figure 104.

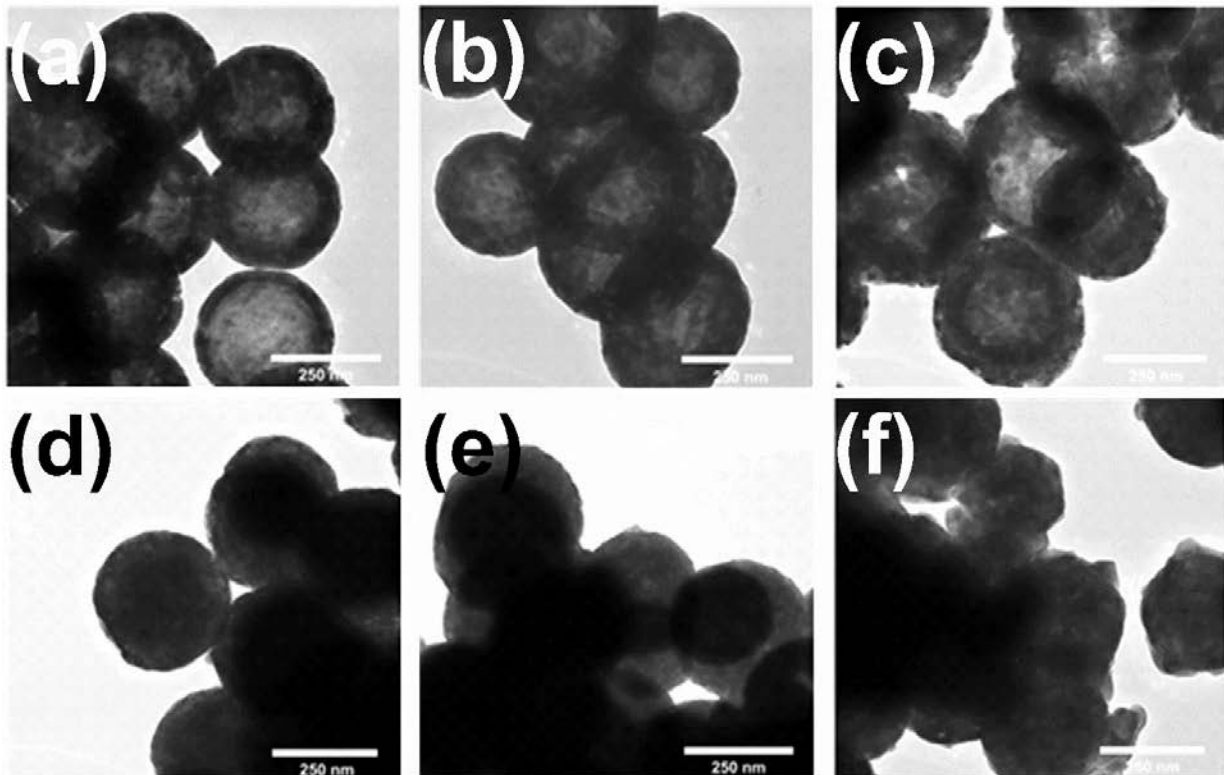


**Figure 109.** TEM micrographs of the polycrystalline Eu:La<sub>2</sub>O<sub>3</sub>/Tb:Y<sub>2</sub>O<sub>3</sub> (a, b, c) and Tb:Y<sub>2</sub>O<sub>3</sub>/Eu:La<sub>2</sub>O<sub>3</sub> (d, e, f) nanoparticles heat treated at 600 °C/3 h (left), 700 °C/3 h (center), and 900 °C/3 h (right).

Homogeneous precipitation of nanophase p-Eu:La<sub>2</sub>O<sub>3</sub> using La(NO<sub>3</sub>)<sub>3</sub>·6H<sub>2</sub>O as the salt precursor resulted in diverse morphologies, including sheets (2-D), rods (1-D), and spheres (0-D). Homogeneous precipitation in the presence of citric acid results in monodisperse spherical p-Eu:La<sub>2</sub>O<sub>3</sub> nanoparticles. The optimum salt/citric acid/urea ratio is 1/0.25/40 with 5 mM salt concentration. We have also demonstrated that the method can be used to synthesize core/shell morphologies with p-Eu:La<sub>2</sub>O<sub>3</sub> as either the core (e.g. p-Eu:La<sub>2</sub>O<sub>3</sub>/p-Tb:Y<sub>2</sub>O<sub>3</sub>) or the shell (e.g. SiO<sub>2</sub>/p-Eu:La<sub>2</sub>O<sub>3</sub> and p-Tb:Y<sub>2</sub>O<sub>3</sub>/p-Eu:La<sub>2</sub>O<sub>3</sub>). Heat treatments for 3 h for various temperatures leads to the formation of oxide phases. XRD and fluorescence data for the core/shell samples heat treated at 900 °C/3 h indicate the dominance of the core. The reported method of synthesizing monodisperse spherical shaped nanophosphor of p-Eu:La<sub>2</sub>O<sub>3</sub> is simple and low-cost. It requires a low heating temperature (90 °C) for 3 h in an aqueous solution in the presence of citric acid and urea. The h-La<sub>2</sub>O<sub>3</sub> phase is obtained following heat treatment of 900 °C/3 h. Due to the hygroscopic nature of the h-La<sub>2</sub>O<sub>3</sub> phase, it readily transforms into the

h-La(OH)<sub>3</sub> phase. Exposure to moisture should be minimized to preserve the h-La<sub>2</sub>O<sub>3</sub> phase. The variety of different phases make this material attractive as another sensor material.

## B. Eu:TiO<sub>2</sub> – based materials

Initial experiments were performed using Eu:TiO<sub>2</sub>. Figure 110 shows the fluorescence spectra excited at 464 nm and normalized for the emission peak at 592 nm and the peak intensity ratios as a function of temperature. The emission intensity at 612.5 nm decreases with increasing temperature indicating the increasing symmetry of the Eu site. This trend extends to temperatures at least as low as 80 °C, making this material promising as a wide-temperature range sensor.

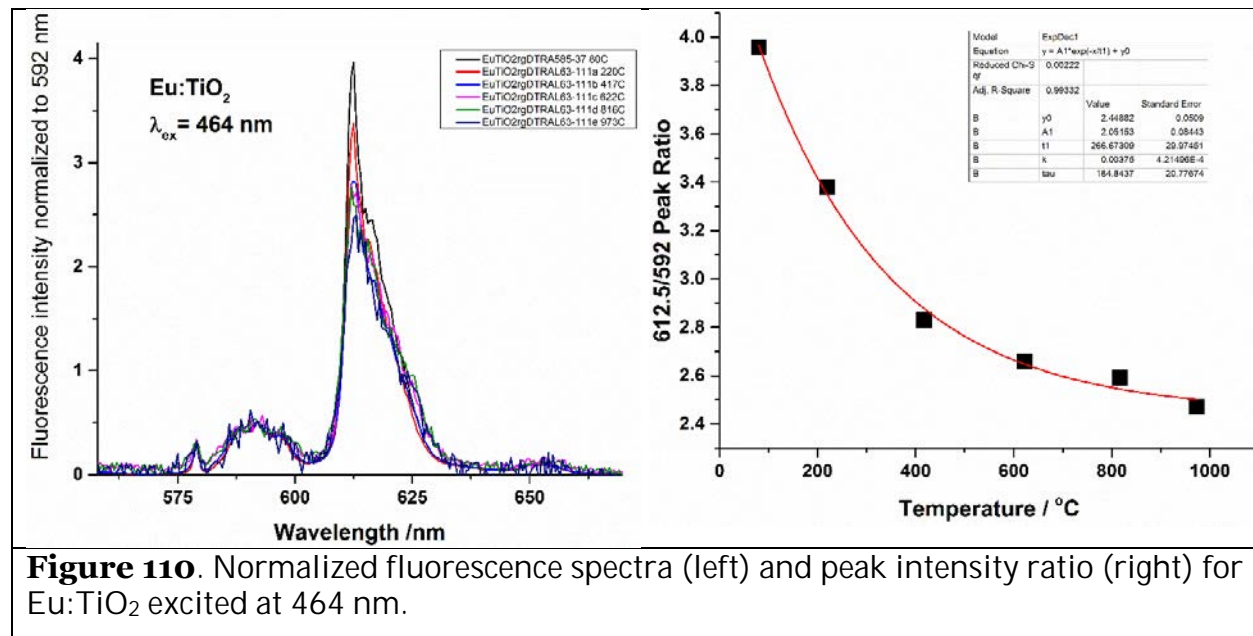


**Figure 110.** Normalized fluorescence spectra (left) and peak intensity ratio (right) for Eu:TiO<sub>2</sub> excited at 464 nm.

## C. Magnetic Core Sensors

Previous testing of our nanosensors has highlighted a potential problem related to the presence of debris. In some cases, a large amount (several grams) of powder was returned that contained only small amounts of sensor material, see Figure 111. While we were usually able to extract a fluorescent signal from these samples, the signal has been very weak. In order to enhance the S/N, we have developed an initial design that contains a magnetic core, Fe<sub>3</sub>O<sub>4</sub>. Having such a magnetic core, would allow us to use a magnet to extract our sensor materials from the debris. Figure 112 shows an SEM of Fe<sub>3</sub>O<sub>4</sub>/Y<sub>2</sub>O<sub>3</sub> core/shell nanoparticles.



**Figure 111.** Debris from explosion tests. Only a very small percentage of the debris is actual sensor material.

The magnetic properties of  $\text{Fe}_3\text{O}_4/\text{Eu}:\text{Y}_2\text{O}_3$  core/shell nanoparticles are demonstrated in Figure 113. All samples are magnetic, except the one heated to 950 °C. Further analysis is required to determine the exact cause.

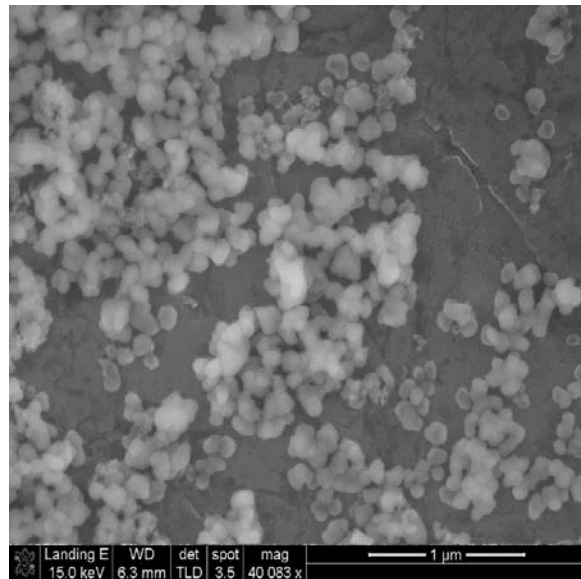


**Figure 112.** SEM of  $\text{Fe}_3\text{O}_4/\text{Y}_2\text{O}_3$  core/shell nanoparticles.



**Figure 113.** Images of  $\text{Fe}_3\text{O}_4/\text{Eu}:\text{Y}_2\text{O}_3$  core/shell nanoparticles in the presence of a magnet. Precursor (left), heated to 600 °C and 700 °C (center), and heated to 800 °C and 950 °C (right). All samples are magnetic, except the one heated to 950 °C.

Figure 114 shows the fluorescence spectra of  $\text{Fe}_3\text{O}_4/\text{Eu}:\text{Y}_2\text{O}_3$  core/shell nanoparticles heated to various temperatures for 5 s.

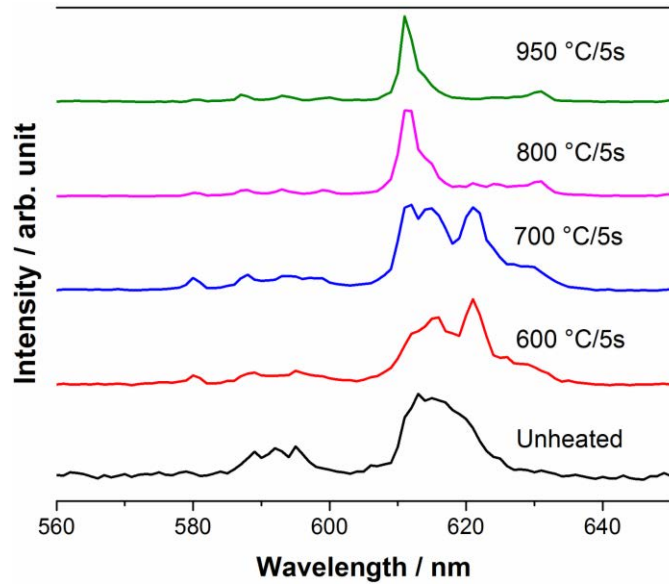


**Figure 114.** Fluorescence spectra of  $\text{Fe}_3\text{O}_4/\text{Eu:Y}_2\text{O}_3$  core/shell nanoparticles heated to various temperatures for 5 s.

## **X. LIST OF SYMBOLS, ABBREVIATIONS, AND ACRONYMS**

c-Ho:Y <sub>2</sub> O <sub>3</sub>	crystalline Ho-doped yttria
CO <sub>2</sub>	Carbon dioxide
DTRA	Defense Threat Reduction Agency
DSC	Differential Scanning Calorimetry
Dy	Dysprosium
EDS	Energy Dispersion Spectroscopy
Er	Erbium
Eu	Europium
Eu:Y <sub>2</sub> O <sub>3</sub>	Eu-doped yttria (1% unless otherwise indicated)
Eu:ZrO <sub>2</sub>	Eu-doped zirconia (1% unless otherwise indicated)
FTIR	Fourier Transform Infrared
FWHM	Full Width Half Maximum
Ho	Holmium
Ho:Y <sub>2</sub> O <sub>3</sub>	Ho-doped yttria
IH	Indian Head
IHEODTD	Indian Head Explosive Ordnance Disposal Technology Division
La <sub>2</sub> O <sub>3</sub>	Lanthanum oxide or lanthana
La(OH) <sub>3</sub>	Lanthanum hydroxide
Ln	Lanthanide
M <sub>2</sub> O <sub>3</sub>	Generic form for metal oxides (sesquioxides)
Nd	Neodymium
NSWC	Naval Surface Warfare Center
p-Eu:Y <sub>2</sub> O <sub>3</sub>	precursor of Eu-doped yttria
p-Eu:ZrO <sub>2</sub>	precursor of Eu-doped zirconia
Pr	Praseodymium
RE	Rare earth
SEM	Scanning Electron Microscopy
Sm	Samarium
Tb	Terbium
TC	Thermocouple
TEM	Transmission Electron Microscopy

TGA	Thermogravimetric Analysis
Tm	Thulium
XRD	X-ray diffraction
Yb	Ytterbium
$\text{Y}_2(\text{CO}_3)_3 \cdot n\text{H}_2\text{O}$	Yttrium carbonate
$\text{Y}_2\text{O}_3$	Yttrium oxide or yttria
$\text{ZrO}_2$	Zirconium dioxide or zirconia
$\text{Zr}(\text{OH})_4$	Zirconium hydroxide

**DISTRIBUTION LIST**  
**DTRA-TR-15-80**

**DEPARTMENT OF DEFENSE**

DEFENSE THREAT REDUCTION  
AGENCY  
8725 JOHN J. KINGMAN ROAD  
STOP 6201  
FORT BELVOIR, VA 22060  
ATTN: A. LYALIKOV

DEFENSE TECHNICAL  
INFORMATION CENTER  
8725 JOHN J. KINGMAN ROAD,  
SUITE 0944  
FT. BELVOIR, VA 22060-6201  
ATTN: DTIC/OCA

**DEPARTMENT OF DEFENSE  
CONTRACTORS**

QUANTERION SOLUTIONS, INC.  
1680 TEXAS STREET, SE  
KIRTLAND AFB, NM 87117-5669  
ATTN: DTRIAC